TECH LIBRARY KAFB, NM

0061326

NASA CONTRACTOR
REPORT

NASA CR

c.1

LOAN COPY: RETURN TO
AFWL (DOUL)
KIRTLAND AFB, N. M.

NASA CR-2034

# A COMPARISON OF OPTIMAL AND NOISE-ABATEMENT TRAJECTORIES OF A TILT-ROTOR AIRCRAFT

*by F. H. Schmitz, W. Z. Stepniewski,*
*J. Gibs, and E. Hinterkeuser*

*Prepared by*
THE BOEING COMPANY
Philadelphia, Pa.
*for U.S. Army Air Mobility R&D Laboratory, Ames Directorate*
*and Ames Research Center*

NATIONAL AERONAUTICS AND SPACE ADMINISTRATION • WASHINGTON, D. C. • MAY 1972

TECH LIBRARY KAFB, NM

0061326

1. Report No.
NASA CR-2034

2. Government Accession No.

3. Recipient's Catalog No.

4. Title and Subtitle
A Comparison of Optimal and Noise-Abatement Trajectories of a Tilt-Rotor Aircraft

5. Report Date
May 1972

6. Performing Organization Code

7. Author(s)
F.H. Schmitz, W.Z. Stepniewski, J. Gibs and E. Hinterkeuser

8. Performing Organization Report No.

9. Performing Organization Name and Address

The Boeing Company
Vertol Division
Philadelphia, Pennsylvania

10. Work Unit No.

11. Contract or Grant No.
NAS 2-5025

12. Sponsoring Agency Name and Address

National Aeronautics and Space Administration
Washinton, D.C. 20546

13. Type of Report and Period Covered
Contractor Report

14. Sponsoring Agency Code

15. Supplementary Notes

16. Abstract

The potential benefits of flight path control to optimize performance and/or reduce the noise of a tilt-rotor aircraft operating in the takeoff and landing phases of flight are investigated. A theoretical performance-acoustic model is developed and then mathematically flown to yield representative takeoff and landing profiles. Minimum-time and minimum-fuel trajectories are compared to proposed noise-abatement profiles to assess the reductions in annoyance possible through flight path control. Significant reductions are feasible if a nearly vertical-takeoff flight profile is flown near the landing site; however, the time expended and fuel consumed increase.

17. Key Words (Suggested by Author(s))
aircraft noise
tilt-rotor aircraft
tilt-rotor performance
optimal trajectories
noise abatement trajectories

18. Distribution Statement
UNCLASSIFIED-UNLIMITED

19. Security Classif. (of this report)
UNCLASSIFIED

20. Security Classif. (of this page)
UNCLASSIFIED

21. No. of Pages
165

22. Price*
3.00

*For sale by the National Technical Information Service, Springfield, Virginia 22151

# TABLE OF CONTENTS

Page

SUMMARY . . . . . . . . . . . . . . . . . . . . . . . . 1

I. INTRODUCTION . . . . . . . . . . . . . . . . . . . . 2

II. THEORETICAL TILT-ROTOR PERFORMANCE MODEL . . . . . 4

The Tilt-Rotor Aircraft . . . . . . . . . . . . . 4
Aerodynamics . . . . . . . . . . . . . . . . . . . 6
Performance Equations . . . . . . . . . . . . . . 19
Performance Constraints . . . . . . . . . . . . . 23
Performance Prediction Methodology . . . . . . . . 25

III. THEORETICAL TILT-ROTOR ACOUSTIC MODEL . . . . . . 35

Tilt-Rotor Noise Generation . . . . . . . . . . . 35
Propagation of Sound . . . . . . . . . . . . . . . 51
Subjective Measures of Noise . . . . . . . . . . . 52

IV. OPTIMIZATION TECHNIQUES . . . . . . . . . . . . . 53

Classification of Methods . . . . . . . . . . . . 54
AESOP (Automated Engineering Scientific Optimization Program . . . . . . . . . . . . . . . 56
Parametric Functional Expansion . . . . . . . . . 59

V. RESULTS AND DISCUSSION . . . . . . . . . . . . . . 60

General Results . . . . . . . . . . . . . . . . . 60
Detailed Presentation of the Results . . . . . . . 69
Review and Assessment of the Major Assumptions and Computational Techniques . . . . 120

VI. CONCLUSIONS & RECOMMENDATIONS . . . . . . . . . . . 123

APPENDICES:

A. Design Characteristics of the "Vertol 160" Tilt-Rotor Aircraft . . . . . . . . . . . . . . . . . . . 125

B. Numerical Solution of the Kinematic Performance Equations . . . . . . . . . . . . . . . . . . . . . 127

C. Solution of the Momentum Equation in Nonaxial Flight . . . . . . . . . . . . . . . . . . . . . . 131

D. Time & Fuel Minimization using a Simplified Kinematic Model . . . . . . . . . . . . . . . . . . 135

E. List of Symbols . . . . . . . . . . . . . . . . . . 155

References . . . . . . . . . . . . . . . . . . . . . . . . 162

# A COMPARISON OF OPTIMAL AND NOISE-ABATEMENT TRAJECTORIES OF A TILT-ROTOR AIRCRAFT

By F.H. Schmitz*, W.Z. Stepniewski,
J. Gibs and E. Hinterkeuser
The Boeing Company, Vertol Division

## SUMMARY

In this report, the possible benefits of flight path control to optimize performance and/or reduce the noise of a tilt-rotor aircraft operating in the takeoff and landing phases of flight are investigated. The Vertol Model 160 tilt-rotor aircraft, which has been designed primarily for the military transport mission, is used in this theoretical evaluation.

A mathematical model which describes the kinematic performance and acoustical characteristics of the aircraft is developed. The kinematic performance model governs the tilt-rotor in unaccelerated climbing and descending flight. Vehicle accelerations are enforced as inequality constraints, along with additional limits imposed by aerodynamic and structural considerations. The noise generated by the tilt-rotor aircraft is assumed to be produced entirely by the rotor. It is conveniently decomposed into the conventional classifications: rotational noise and broad-band noise. The latter is described by empirical methods, while a simplified theoretical development is used to describe the rotational noise of the tilt-rotor aircraft. Mathematical techniques are also formulated to assess subjectively the resulting noise spectrum.

A functional expansion technique is applied to the control time histories of this constrained performance and acoustic model of the tilt-rotor aircraft. Parameter optimization techniques are then used to locate optimal trajectories which minimize time and/or fuel during takeoff and landing. In addition, proposed noise-abatement trajectories are calculated by a judicious choice of the expansion parameters.

A comparison among optimal-performance and noise-abatement trajectories for the tilt-rotor aircraft is the major result of this report. Minimum-time and -fuel trajectories, along with proposed noise-abatement trajectories, are also presented in

---

*Now associated with the U.S. Army Air Mobility Research and Development Lab, Ames Directorate, Moffett Field, Calif.

detail. In particular, it is shown that by flying the noise-abatement trajectories, the noise level in the takeoff phase can be reduced up to 7 EPNdB* and as much as 10 EPNdB* during landing. For the considered tilt-rotor configuration, the associated fuel-consumed penalties (as compared with the minimum-fuel trajectory) amounted to 0.15 and 0.03 percent, respectively, of the gross weight.

## I. INTRODUCTION

For the past 20 years, vertical-takeoff and -landing (VTOL) aircraft have offered the promise of fast, efficient, and convenient transportation. Unfortunately, because of technical and operational problems, as well as lack of available funds, this promise has not been fulfilled. Most prototype and research aircraft built over the years demonstrated the technical feasibility of VTOL aircraft. However, other important factors have, up to now, always outweighed the projected advantages of VTOL flight. A successful VTOL aircraft designed for a military transport mission must successfully meet the operational requirements of the mission, be reasonably cost-effective, and be as quiet as possible to minimize detection. A commercial VTOL aircraft has to compete economically with other forms of transportation, satisfy safety requirements, and meet the proposed noise-annoyance criteria for commercial operations. In both cases, it is definitely desirable to maximize VTOL performance and minimize the generated noise throughout the flight, but especially in the terminal operation.

In this report, an attempt is made to understand the performance and noise tradeoffs associated with the operation of VTOL aircraft in their terminal phases of flight. This is done by using a specific VTOL aircraft; namely, the Vertol Tilt-Rotor Model 160 which has been designed primarily for a military mission. The major objectives of this analysis are to determine the minimum-time and minimum-fuel trajectories of this tilt-rotor aircraft and to assess the possible benefits of flight path control to reduce noise in the takeoff and landing phases of flight. To insure realistic flight trajectories, aerodynamic, structural, and operational constraints are included in the analysis. In addition, the possible penalties in performance (fuel and time) which result from the enforcement of noise constraints are investigated.

In order to provide as much clarity as possible, a simplified, but generalized, approach to describe a VTOL's performance is used. The advantages of such an approach are numerous. Performance is investigated with the help of a kinematic model, while in the acoustical model, rotor contributions as represented by the rotational and broad-band noise only, are considered. The methodology which emerges can be extended to other open-airscrew VTOL aircraft with slight modifications. The mathematical model which is developed can be used to predict the performance and noise of a rotary-wing VTOL aircraft where the wing is continuously immersed in the slipstream of the rotors. This flexibility can be used to describe the performance and noise characteristics of a compound helicopter and tilt-wing as well as the present tilt-rotor aircraft.

---

*The concept of EPNdB and its relationship to the more familiar PNdB is defined in Section III, p. 53.

Another distinct advantage which the simplified performance and acoustic model offers is the ease with which detailed sensitivity studies are undertaken. The cost of enforcing aerodynamic, structural, or noise constraints can be ascertained by theoretically flying the aircraft model with the specified constraints mathematically enforced.

Furthermore, due to the basic simplicity of treating performance and acoustics with kinematic models only, the computational techniques required to obtain an engineering optimum are less formidable. The physical implications of the resulting optimal trajectories are also more easily analyzed, affording the engineer a clearer insight into the practical implications of his work.

It should be mentioned at this point that, while in this report problems of noise reduction through management of the terminal flight trajectories are investigated analytically, there are also attempts to attack those problems experimentally. For instance, noise-reduction techniques for a small helicopter (less than 10 000 pounds) through control of helicopter operating conditions have been determined by a flight test program (ref. 1). These flight test results may contribute to a better understanding of the theoretical results of the present study.

In order to achieve its objectives, the remaining body of this report is structured in the following manner:

In Section II, a mathematical model of the tilt-rotor aircraft is developed which predicts the kinematic performance of the aircraft. For the sake of simplicity and clarity, sophisticated mathematical refinements are omitted from the analysis if they do not substantially influence the performance. By keeping the complicating factors to a minimum, a basic understanding of the vehicle's steady-state performance characteristics is developed. Vehicle structural and aerodynamic constraints are also represented in a simplified manner.

In Section III, an acoustic model of the tilt-rotor aircraft is developed. The noise is assumed to be generated entirely by the rotor and is conveniently decomposed into two classifications: rotational noise and broad-band noise. The latter is described by empirical methods. A simplified theoretical development is used to describe the rotational noise of the tilt-rotor aircraft. Mathematical techniques to assess subjectively the resulting noise spectrum are also presented in this section.

In Section IV, optimization techniques which can be used to solve this type of trajectory optimization problem are reviewed. A functional expansion technique is applied to the constrained kinematic performance model developed in the preceding sections of the report. This technique was chosen because of its relative ease of implementation.

In Section V, minimum-time and -fuel trajectories of the simplified theoretical model of the tilt-rotor aircraft are presented. Emphasis is placed upon a physical interpretation of the results, along with an analysis of the sensitivity of the solution to the important performance and acoustic constraints.

The last section of the report (Section VI) presents the conclusions and recommends areas of fruitful future investigations.

Finally, appendices are provided that elaborate on some computational techniques as well as give more physical insight into the problems of time and fuel minimization through a cursory analytical and graphical interpretation of the simplified kinematic model.

## II. THEORETICAL TILT-ROTOR PERFORMANCE MODEL

The first step in the analytical evaluation of possible tilt-rotor noise-performance tradeoffs through flight trajectory management has been the development of a simplified mathematical performance model. This mathematical model is capable of describing the aircraft performance and resulting trajectory in all modes of out-of-ground effect airborne flight. Aerodynamic, structural, and control power limits are used to constrain the permissible flight envelope.

### The Tilt Rotor Aircraft

In the present study, the developed performance methodology is applied to a particular tilt-rotor aircraft: the

Vertol Model 160. A brief outline of the 160 design characteristics needed for this analysis can be found in Appendix A. It may be emphasized at this point that the tilt-rotor aircraft which is considered in this analysis has been primarily designed for the transport mission. It is similar in its basic concept to the Bell XV-3 tilt-rotor aircraft which has undergone extensive flight testing. The basic configuration is depicted in the following illustration.

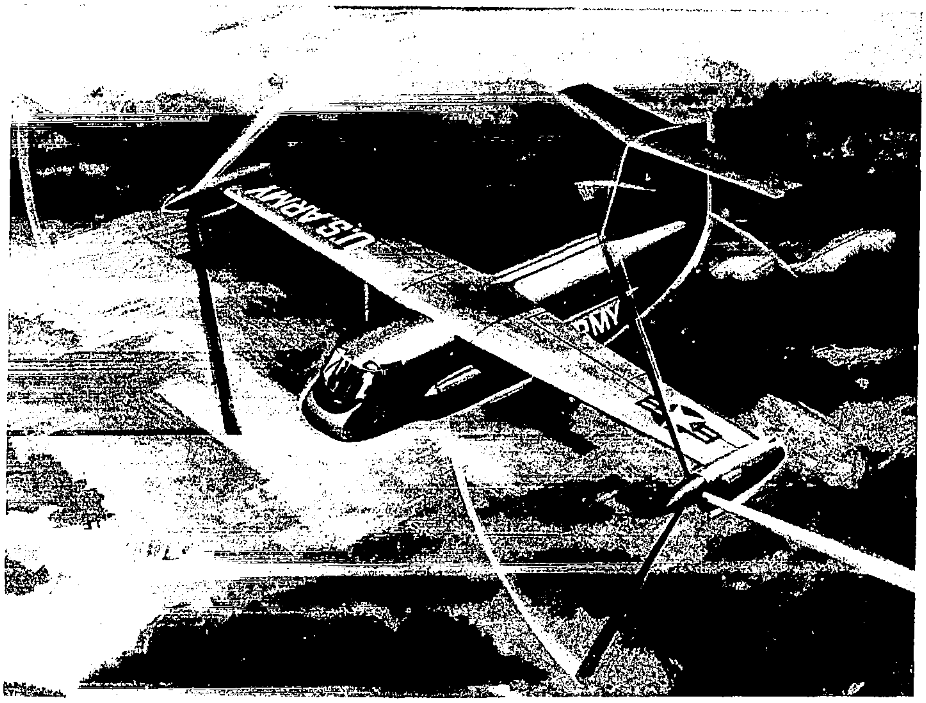

Figure II-1. Artist's Conception of a Tilt-Rotor Aircraft

The most prominent feature of this type of vehicle is its high fixed wing with tiltable nacelles at each wing tip. Each nacelle comprises a prop-rotor, a transmission, engine, and the necessary supporting structure. The nacelle is tilted by a hydraulic jack about a line near the prop-rotor thrust axis. During the conversion cycle, the rotor tilts through 90 degrees, while the wing remains fixed with reference to the fuselage.

The tilting rotor configuration promises good aerodynamic efficiency in hovering and in cruise flight. Advantage is taken of the high degree of freedom in selecting, somewhat independently, the rotor disc loading and the wing loading. The low disc loading rotor ($\sim$10 lbs/ft$^2$) is responsible for hovering performance of the aircraft which approaches that of the helicopter.

Moderately high speeds and favorable cruise performance are achieved through a high wing loading (∿80 lbs/ft$^2$).

The control system for the tilt-rotor aircraft in the helicopter configuration is typical of the side-by-side configurations: roll control is achieved through differential collective pitch, while simultaneous monocyclic input is used for pitch control. Differential cyclic provides the necessary yawing moment control. Collective pitch inputs, together with rotor rpm, govern thrust level. In cruise flight, normal airplane controls are used, and a mechanical unit programs the mixing of the controls during conversion.

## Aerodynamics

A significant portion of the tilt-rotor's flight envelope is spent in those regimes where aerodynamic interaction of the major aerodynamic forces is inevitable. Simplified theoretical models of the aerodynamic forces produced by the rotors, wing, and nacelles and their interaction are discussed below.

The low disc loading rotor in forward flight. - Obtaining an accurate assessment of the performance of a low disc loading rotor in forward flight is a formidable task. A detailed knowledge of the surrounding flow field as well as the design characteristics of the rotor is information needed à priori to accurately predict rotor performance. At present, there are many independent analyses which claim to predict nonaxial flight rotor performance. Unfortunately, the methods are all similar in one respect: they are rather complex and require digital computers for solutions to rotor performance.

Since the main interest of this work is in the gross aspects of rotor performance, the necessary generalized performance characteristics can be simply obtained by using a combination of classical simple momentum and blade element theories. More refined analytical methods do not appear justified for the considered case.

Simple momentum theory is used for prediction of the axial forces. Under the assumptions of simple momentum theory (uniform induced velocity over the whole disc area; no rotation of the slipstream, and no tip losses), the expression relating thrust, forward velocity, induced velocity, and inclination of the tip path plane becomes

$$T = \sqrt{\left(V \cos(\alpha_p) + v\right)^2 + \left(V \sin(\alpha_p)\right)^2}\,\left|2v\right|\rho A. \qquad \text{(II-1)}$$

Figure II-2 shows a vector diagram of the mai
interactions of the rotor disc.

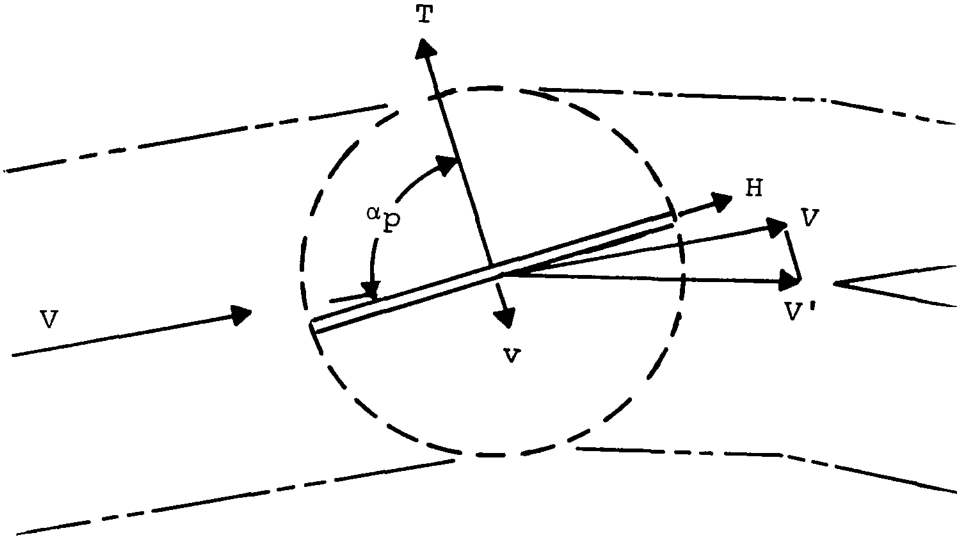

Figure II-2

In helicopter translational flight, the drag
blade is the cause of an effective in-plane force
It has been assumed that this "pseudo" H-force, wh
trated in Figure II-2, can be analytically approxi
following equation (ref. 2).

$$H = (3/8)\rho\sigma\pi\ R^2\ V_t^{\,2}\ \mu\ \bar{c}_{d_o}\ .$$

Wing-slipstream aerodynamic interactions. - Th
of aerodynamic forces and moments of a wing which
or fully immersed in the slipstream of a prop-roto
plex subject. An accurate determination of these
moments, which would probably require some detaile
of the flow field surrounding the lifting surface
the scope of this report. Instead, the overall as
wing fully immersed in a slipstream are approximat
plified analytical expressions.

The major assumption of this analysis is that
slipstream velocity covering the lifting surface c
approximately represented by the vector sum of the
velocity and the fully developed induced velocity
It is also assumed that: the thrusting rotor prod
form induced velocity distribution; the slipstream

the thrusting rotor is fully contracted and covers the entire wing; and rotational slipstream effects can be neglected.

A velocity diagram depicting the resulting aerodynamic interactions is shown below (Figure II-3)

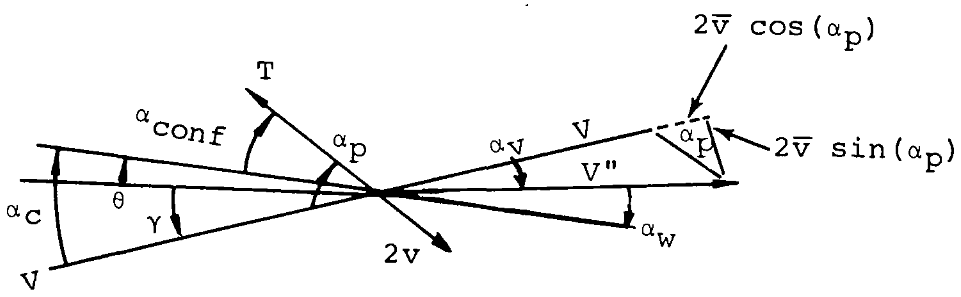
$2\bar{v}\ \cos(\alpha_p)$
T
$\alpha_{conf}$
$\alpha_p$
$\alpha_V$
V
$\alpha_p$
$2\bar{v}\ \sin(\alpha_p)$
V"
$\alpha_c$
$\theta$
$\gamma$
2v
$\alpha_w$
V

Figure II-3

From geometry,

$$\alpha_V = \sin^{-1}\left\{\frac{2v\ \sin(\alpha_p)}{V''}\right\} \qquad \text{(II-3)}$$

$$\alpha_w = \alpha_c - \alpha_V = \theta - \gamma - \alpha_V \qquad \text{(II-4)}$$

$$V''^2 = 4v^2 + 4v\ \cos(\alpha_p) + V^2 \qquad \text{(II-5)}$$

$$\alpha_{conf} = \alpha_p - \theta + \gamma \qquad \text{(II-6)}$$

It is further assumed that all of the aerodynamic lift is derived from the slipstream flow over an immersed wing. The total lift and drag of the aerodynamic surface is mathematically represented by the following equations:

$$L_s = (1/2)(\rho\ V''^2\ C_{L_s}\ S_w) \qquad \text{(II-7)}$$

$$D_S = (1/2)\ (\rho V''^2 C_{D_S} S_W) \qquad \text{(II-8)}$$

The wing of the Vertol Model 160 aircraft has two additional aerodynamic devices: a leading edge umbrella flap and a trailing edge flap (Figure II-4).

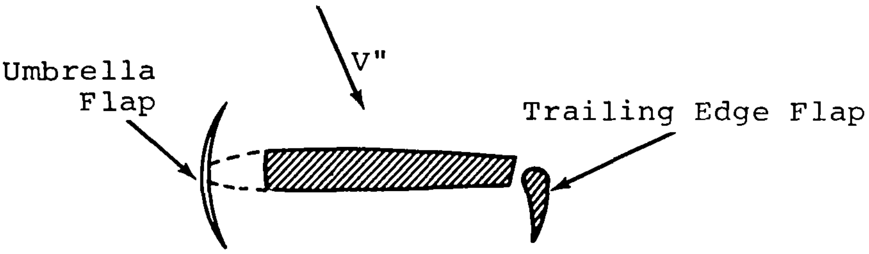

Figure II-4

The purpose of the leading edge umbrella flap is to reduce the download on the wing in the hovering and vertical climb modes of flight. As the aircraft acquires forward speed, the flap is quickly retracted. However, for the sake of simplicity, the umbrella flap has not been included in the analytical model. Therefore, the hovering and vertical climb performance results which are presented are slightly conservative.

The trailing edge flap system may be used to influence the performance of the aircraft in all modes of flight. An analytical representation of the performance characteristics of the trailing edge flap is included in this study.

The total wing area ($S_W$) of the tilt-rotor aircraft is composed of the basic wing area plus the area of the trailing edge flap system. At hover, when a download exists on the wing, the effective wing area and the resulting download may be reduced by lowering the trailing edge flap to its full 90° position. At small forward velocities, the trailing edge flap may be programmed to increase the performance of the vehicle. The effective area of the complete wing will, therefore, vary with flap position.

To simplify the analytical representation of the lift and drag coefficients of the aerodynamic surface, three distinct flow regimes were identified:

Regime I $-14° \leq \alpha_W \leq 15°$

Regime II $15° < \alpha_W \leq 90°$

Regime III $-90° \leq \alpha_W < -14°$

The lift coefficient for all three regimes is illustrated in Figure II-5. The solid lines indicate the assumed lift coefficient of the basic wing with zero flap deflection. The broken lines indicate the effect of deflecting the trailing edge flap.

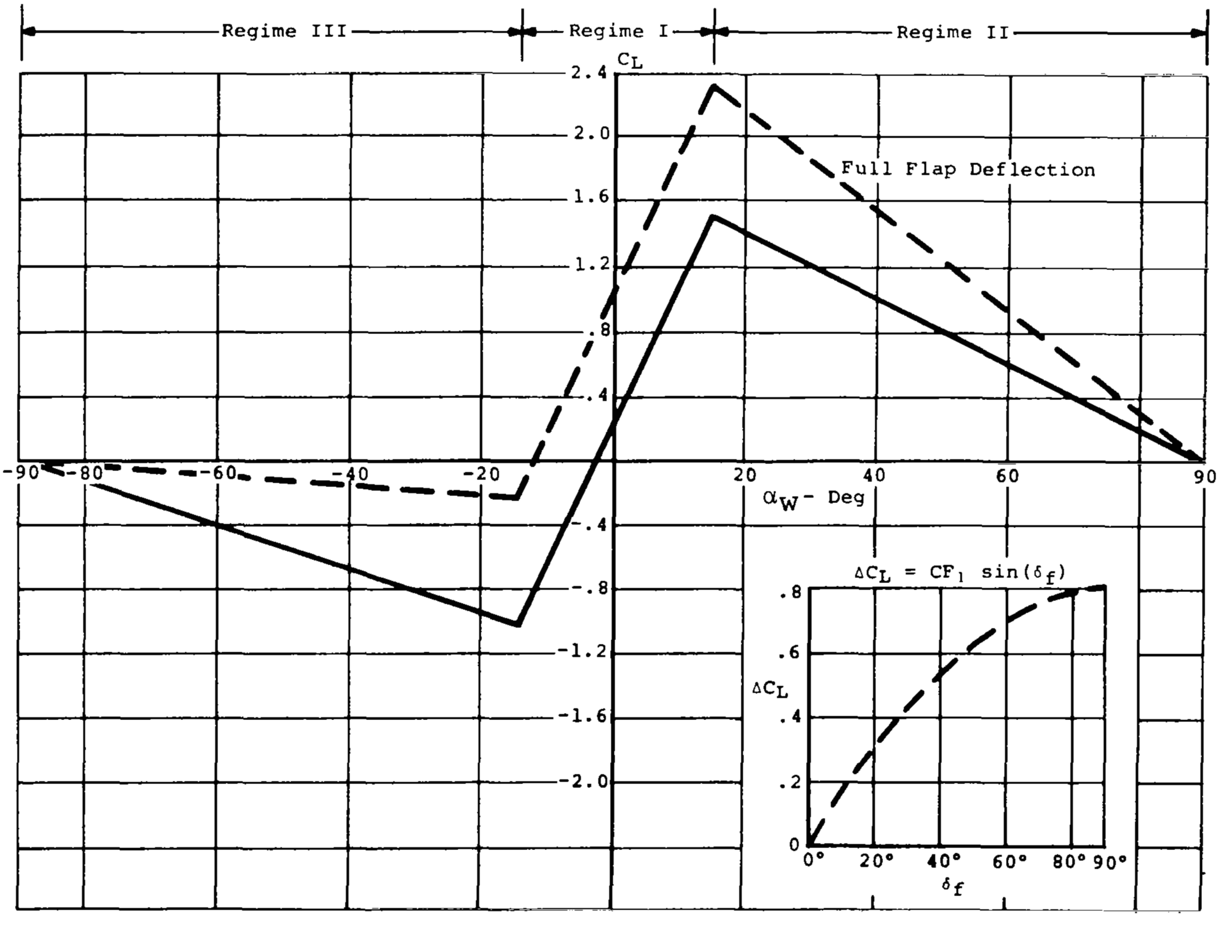

Figure II-5

In Regime I, $(-14° \leq \alpha_W \leq 15°)$, basic lifting line theory is used to predict the lift coefficient of the wing. The lift coefficient becomes:

$$C_L\big|_{\delta_f=0} = \frac{\partial C_L}{\partial \alpha_w}\left(\alpha_w - \alpha_{OL}\right) \quad .$$

where $\dfrac{\partial C_L}{\partial \alpha_w} \equiv$ lift curve slope of the basic wing = 5 $\text{rad.}^{-1}$

$\alpha_{OL} \equiv$ the angle of zero lift of the wing = -0.044 rad.

The increase in lift which occurs when the flap is deflected is given by the following expression:

$$\Delta C_L = CF_1 \ \sin(\delta_f)$$

where

$CF_1 \equiv \Delta C_L\big|_{\delta=90°} \equiv$ the maximum increase = 0.8 in lift coeff.

The numerical values shown are representative of the Vertol Model 160 configuration. The expression for the total aerodynamic lift coefficient becomes

$$C_L = 5(\alpha_w + 0.044) + 0.8 \sin(\delta_f) . \qquad \text{(II-9)}$$

The aerodynamic surface is assumed to be stalled in Regime II ($15° < \alpha_w \leq 90°$). When stall first occurs, the lift coefficient of the wing attains its maximum value which is equal to

$$C_{L_{max}} = C_L\big|_{\alpha_w=15°} = 1.52 + CF_1 \ \sin(\delta_f) .$$

When $\alpha_w = 90°$, it is assumed that no lift can be developed. It is also assumed that the lift coefficient in the intermediate states is a linear function of these two endpoints. The slope of the curve becomes

$$\frac{\partial C_L}{\partial \alpha_w}\bigg| = C_L\big|_{\alpha_w=15°} \ \left(\frac{-180°}{75°\cdot\pi}\right) = 0.764\left(1.52 + CF_1 \ \sin(\delta_f)\right).$$

The resulting lift coefficient is

$$C_L = 0.764(1.52 + CF_1 \sin(\delta_f))(\pi/2 - \alpha_W). \qquad \text{(II-10)}$$

In Regime III ($-90° \leq \alpha_W < -14°$), the wing is always operating at a negatively stalled angle of attack. This condition is quite prevalent in the tilt-rotor aircraft at small forward velocities. At the onset of negative stall, the lift coefficient attains its minimum value.

$$C_{L_{min}} = C_L\Big|_{\alpha_W=-14°} = -1.0 + CF_1 \sin(\delta_f).$$

Near hover, when $\alpha_W = 90°$, it is assumed that no lift can be developed. In intermediate states, a linear variation of the lift coefficient is assumed. The lift curve slope becomes

$$\frac{\partial C_L}{\partial \alpha_W} = C_L\Big|_{\alpha_W=-14°}\left(\frac{180°}{76°\cdot\pi}\right) = 0.754(-1.0 + CF_1 \sin(\delta_f)).$$

The lift coefficient for Regime III is

$$C_L = 0.754(-1.0 + CF_1 \sin(\delta_f))(\alpha_W + \pi/2). \qquad \text{(II-11)}$$

The drag coefficient in all three regimes is composed of two parts: an induced term and a profile term. It is assumed that in all three regimes of flight, the induced drag coefficient is equal to:

$$C_{D_i} = C_L^2/\pi AR e \qquad \text{(II-12)}$$

where $AR \equiv$ aspect ratio of the wing = 7.9
and $e \equiv$ Oswald's efficiency factor = 0.9.

The profile drag of the tilt-rotor wing is markedly different in each regime. In Regime I, it is assumed to be

$$C_{D_p} = f_{o_0} + f_{o_2}\delta_f^2. \qquad \text{(II-13)}$$

The boundaries of this regime are sketched in Figure II-6. The constant $f_{o_0}$ is the unflapped wing basic profile drag coefficient. The term which is parabolic in the flap deflection angle represents the profile drag coefficient which results when the flap is raised or lowered. The numerical values of $f_{o_0}$ (0.011) and $f_{o_2}$ (0.1) are representative of the Vertol Model 160 tilt-rotor aircraft.

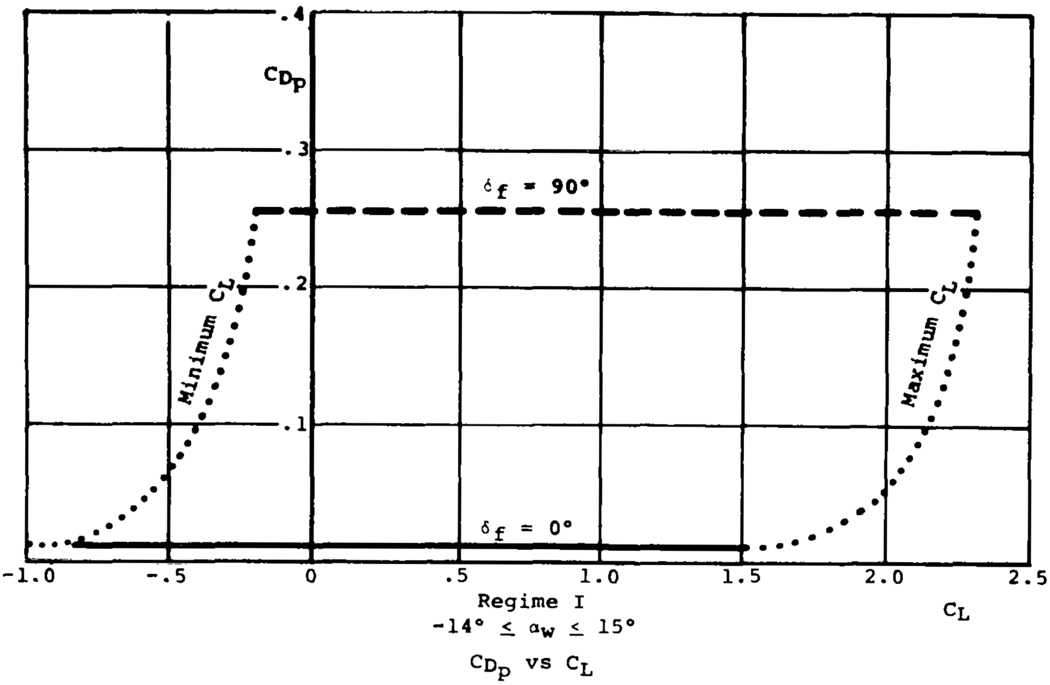

Figure II-6

The total wing drag coefficient for Regime I becomes

$$C_D = \underbrace{f_{o_0} + f_{o_2}\delta_f^{\,2}}_{\text{Profile}} + \underbrace{C_L^{\,2}/\pi AR\,e}_{\text{Induced}} \,. \tag{II-14}$$

When the wing is completely stalled, as in Regime II, the profile drag coefficient is assumed to be of the parabolic form

$$C_{D_p} = CF_3 - f_{s_1}C_L^{\,2}. \tag{II-15}$$

The maximum profile drag coefficient occurs when $\alpha_W$ = 90° ($C_L$ = 0). A realistic value for the constant $CF_3$ (0.731) has been evaluated from wind tunnel download tests (ref. 3). It is implicitly assumed in eq. (II-15) that deflecting the flap in the positive direction does not alter the basic drag characteristics of the aerodynamic surface. The factor $f_{s1}$ is evaluated by assuming that the drag coefficient is a continuous function and equating eqs. (II-13) and (II-14). The expression which results is

$$f_{s1} = \frac{CF_3 - fo_0 - fo_2\delta_f^2}{C_{L\,max}^2} \qquad \text{(II-16)}$$

where $C_{L_{max}} = 1.52 + CF_1 \sin(\delta_f)$.

The boundaries of Regime II are sketched in Figure II-7. The total wing drag coefficient becomes

$$C_D = \underbrace{CF_3 - f_{s1}C_L^2}_{\text{Profile}} + \underbrace{C_L^2/\pi AR e}_{\text{Induced}} . \qquad \text{(II-17)}$$

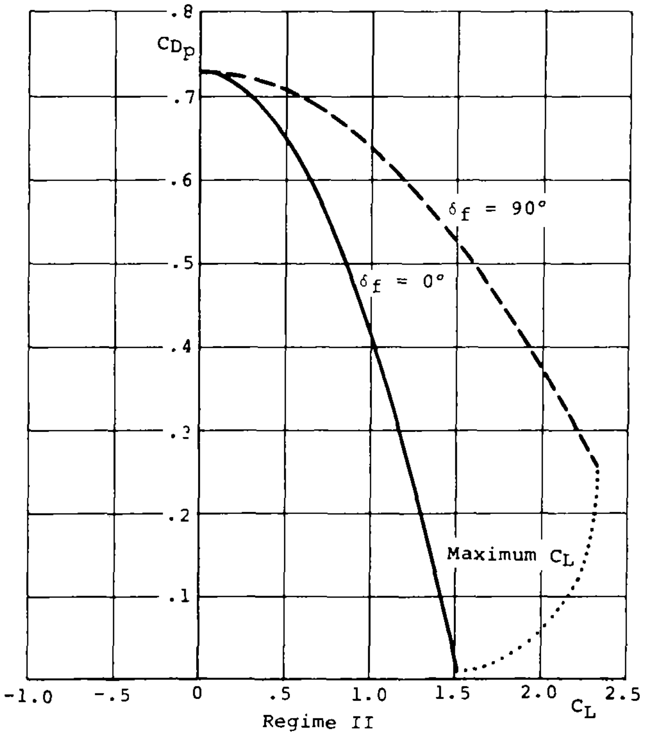

Regime II
15° < $\alpha_w \leq$ 90°
$C_{D_p}$ vs $C_L$

Figure II-7

In Regime III, a parabolic form is also assumed for the basic profile drag coefficient.

$$C_{D_p} = CF_3 - CF_2 \sin(\delta_f) - f'_{s1} \, C_L{}^2 . \qquad \text{(II-18)}$$

In this regime, dropping the trailing edge flap does reduce the download on the wing. From static download hover tests, realistic values for $CF_3$ (0.731), and $CF_2$ (0.325) have been determined. The factor $f'_{s1}$ can be found, as in Regime II, by equating the expressions for profile drag coefficient in Regimes I (eq. II-13) and III (eq. II-18) at a wing angle of attack of -14°.

$$\text{Thus, } f'_{s1} = \frac{CF_3 - CF_2 \sin(\delta_f) - fo_0 - fo_2 \delta_f{}^2}{C_L{}^2{}_{min}} \qquad \text{(II-19)}$$

where $C_{L_{min}} = -1.0 + CF_1 \sin(\delta_f)$.

The boundaries of the profile drag coefficient in Regime III are illustrated in Figure II-8.

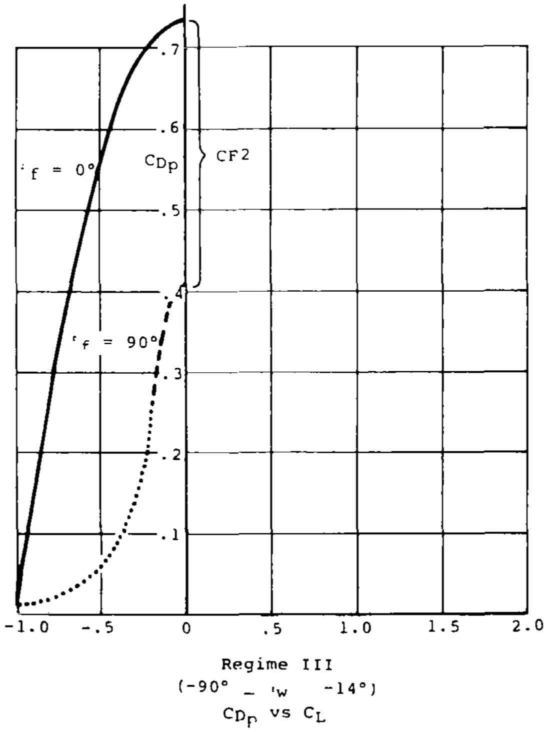

Figure II-8

The total wing drag coefficient becomes:

$$C_D = \underbrace{CF_3 - CF_2 \sin(\delta_f) - f'_{s1}\, C_L^2}_{\text{Profile}} + \underbrace{C_L^2/\pi \mathit{AR}e}_{\text{Induced}} \qquad \text{(II-20)}$$

A combined sketch of the assumed profile drag coefficients is given in Figure II-9.

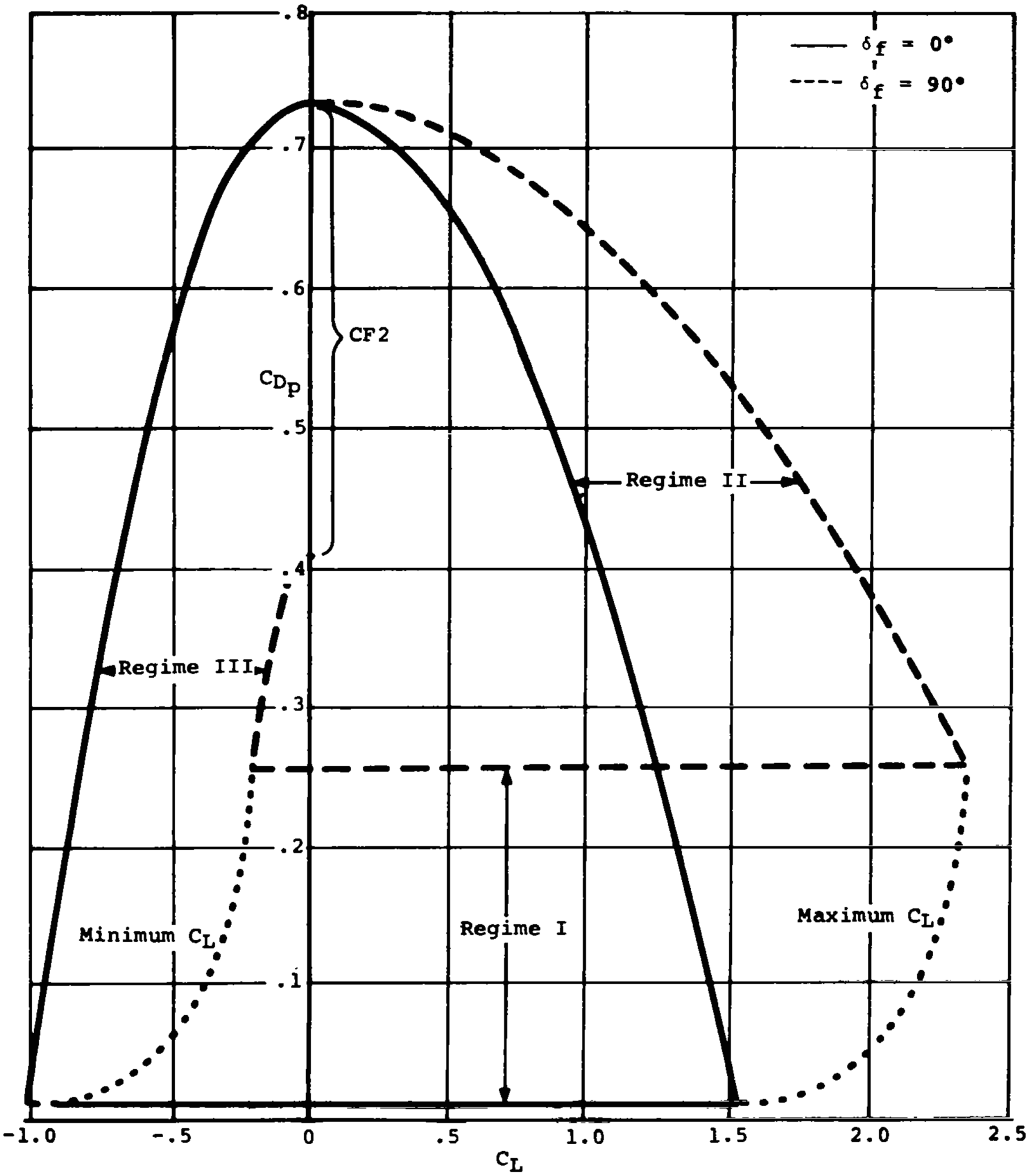

$-\pi/2 < \alpha_w < \pi/2$

$C_{D_p}$ vs $C_L$

Figure II-9

This figure summarizes the analytical efforts of the last few pages. Taken together with Figure II-5, the lift and drag characteristics of the wing operating between ± π/2 are completely specified. Mathematically, these characteristics are summarized below:

$$C_{L_S} = \begin{cases} .754\left(-1.0 + CF_1 \sin(\delta_f)\right)\left[\alpha_W + (3.14/2.0)\right] & -90^\circ \le \alpha_W < -14^\circ \\ 5.0(\alpha_W - \alpha_{OL}) + CF_1 \sin(\delta_f) & -14^\circ \le \alpha_W \le 15^\circ \\ .764\left(1.52 + CF_1 \sin(\delta_f)\right)\left[(3.14/2.0) - \alpha_W\right] & 15^\circ < \alpha_W \le 90^\circ \end{cases}$$

$$\left.\begin{aligned} C_{D_S} &= CF_3 - CF_2 \sin(\delta_f) - f'_{s_1} C_L^2 + C_L^2/\pi ARe \\ f'_{s_1} &= \left[\frac{CF_3 - CF_2 \sin(\delta_f) - f_{o_0} - f_{o_2}\,\delta_f^2}{C_{L\,\min}^2}\right] \\ C_{L_{\min}} &= -1.0 + CF_1 \sin(\delta_f)\,. \end{aligned}\right\} \quad -90^\circ \le \alpha_W < -14^\circ$$

$$\left. C_{D_S} = f_{o_0} + (C_L^2/\pi ARe) + f_{o_2}\delta_f^2 \right\} \quad -14^\circ \le \alpha_W \le 15^\circ$$

$$\left.\begin{aligned} C_{D_S} &= CF_3 - f_{s_1} C_L^2 + C_L^2/\pi ARe \\ f_{s_1} &= \left[\frac{CF_3 - f_{o_0} - f_{o_2}\,\delta_f^2}{C_{L\,\max}^2}\right] \\ C_{L_{\max}} &= 1.52 + CF_1 \sin(\delta_f) \end{aligned}\right\} \quad 15^\circ < \alpha \le 90^\circ$$

Other aerodynamic forces. - It has been assumed, for simplicity, that the remaining aerodynamic forces acting on the tilt-rotor aircraft can be treated as aerodynamic drag. Two additional sources of parasite drag are identified; drag due to nacelles and a residual drag reflecting the fuselage, empennage and interference drag.

When the nacelles of the tilt-rotor aircraft are in the vertical position ($\alpha_P = 90^\circ$), a large increase in the parasite drag occurs. This increase has been measured in the wind tunnel on a configuration similar to the Model 160. Typical values of parasite drag coefficient versus rotor pylon angle of attack ($\alpha_P$) for the Vertol Model 150 tilt-rotor aircraft are shown in Figure II-10 (ref. 4).

The increase of parasite drag coefficient with angle of attack above the airplane configuration was assumed to be representative for the theoretical model of a tilt-rotor aircraft which is considered in this report. This increase in basic parasite drag coefficient is analytically expressed by the following equation:

$$\Delta C_{D_{NAC}} = \left[\left(\Delta C_{D_{NAC}}\Big|_{max}\right)/2\right]\left[1 + \cos\left(2\alpha_p + \pi\right)\right] \qquad \text{(II-21)}$$

where $\Delta C_{D_{NAC}}\Big|_{max} = 0.139$

The increase in drag due to operation of the nacelles at large angles of attack becomes

$$\Delta D_{NAC} = (1/2)\ \rho\ V^2\ \Delta C_{D_{NAC}}\ S_w. \qquad \text{(II-22)}$$

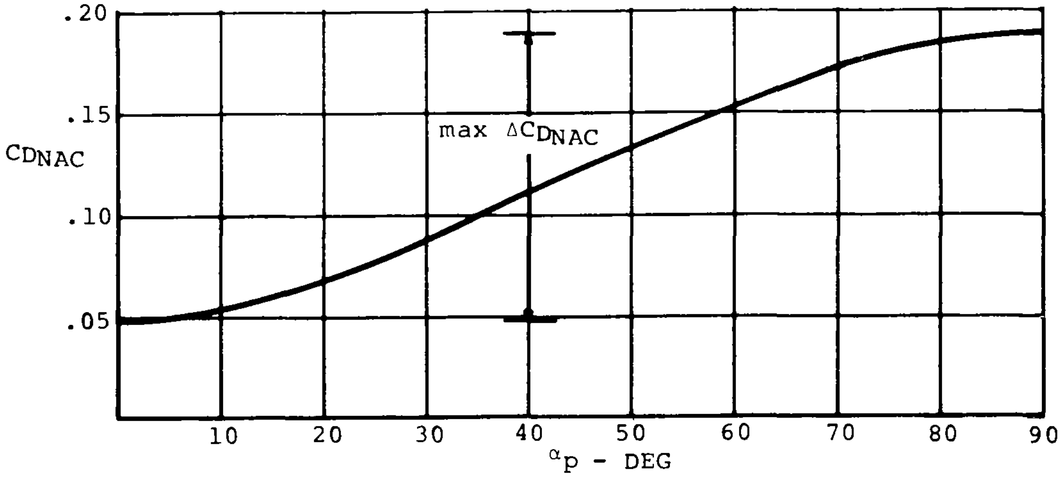

$C_{D_{NAC}}$ vs $\alpha_p$

Figure II-10

The total drag of the nacelles is found by summing the drag of the nacelles in the level flight aircraft mode and the increase in drag predicted by eq. (II-22). The drag coefficient for level flight in the aircraft configuration is calculated to be

$$C_{D_{O_{NAC}}} = 0.004.$$

The total drag of the nacelles becomes

$$D_{NAC} = (1/2)\,\rho\ V^2\ C_{D_{O_{NAC}}}\ S_w + \Delta D_{NAC} \qquad \text{(II-23)}$$

The residual parasite drag coefficient is defined to be the difference between the total parasite drag coefficient calculated in the aircraft mode (0.0316) and the sum of the calculated wing profile drag coefficient and nacelle parasite drag coefficient. For the Model 160 tilt-rotor aircraft, $C_{D_{RSL}} = 0.0166$, and thus, the corresponding drag force becomes:

$$D_{RSL} = (1/2)\rho V^2 C_{D_{RSL}} S_W . \qquad \text{(II-24)}$$

## Performance Equations

The basic aerodynamic and body forces are related to the overall performance of the aircraft by the longitudinal equations of motion. The two force balance equations and the scalar power equation govern the motion of the aircraft in space. The kinematic equations integrate this point performance to yield the spatial coordinates of the vehicle.

At this point, it should be noted that for the sake of simplicity, the moment balance equations are not included in the computational procedure. This was justified by the following: (a) in the case of the considered aircraft, sufficient control forces and/or moments are available from the rotor and the tail surfaces, thus permitting one to attain the necessary moment equilibrium, and (b) those control forces and moments would not significantly alter either the flight trajectory or aircraft acoustic characteristics established from the longitudinal equations of motion only.

For convenience and ease of interpretation, the point performance equations have been nondimensionalized. The chosen reference conditions are based upon hovering out-of-ground effect flight. As a result, a simple scaling parameter governs the effect of altitude, weight, and some design changes upon overall aircraft performance .

Force balance equations. - By summing forces in the longitudinal plane of motion, the dynamic trajectory equations of the tilt-rotor aircraft can be obtained. Figure II-11 illustrates the major aerodynamic and body forces considered.

Using a wind axis system and summing forces parallel and perpendicular to the relative wind, the following equations result:

Parallel (Drag Equation),

$$T\cos(\alpha_p) - L_s \sin(\alpha_v) - D_s \cos(\alpha_v) - D_f - D_{NAC}$$

$$- W\sin\gamma - H\sin(\alpha_p) = m(dV/dt) . \qquad \text{(II-25)}$$

Perpendicular (Lift Equation)

$$T \sin(\alpha_p) + L_s \cos(\alpha_v) - D_s \sin(\alpha_v) - W \cos \gamma + H \cos(\alpha_p) = mV(d\gamma/dt). \qquad \text{(II-26)}$$

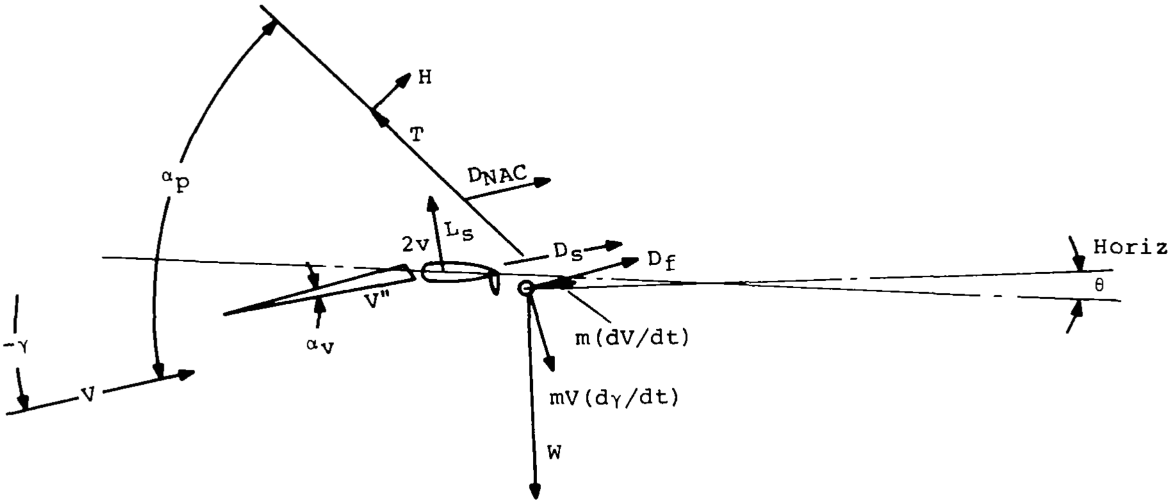

Figure II-11

In most atmospheric trajectory optimization problems, a wind axis system is used because some saving in mathematical complexity is realized. However, for VTOL aircraft, at zero forward velocity, the lift equation becomes singular, creating computational difficulties. To avoid this problem, the constraint that the velocity of the aircraft be greater than zero is enforced. In near hovering flight, a body axis system is used to evaluate the balance of forces.

Both sides of the two force-balance equations are nondimensionalized by dividing by the weight of the aircraft and by introducing the following definitions:

$\lambda_T \equiv T/W$ $\qquad \lambda_{L_s} \equiv L_s/W$ $\qquad \lambda_{D_s} \equiv D_s/W$

$\lambda_{D_f} \equiv D_f/W$ $\qquad \lambda_{D_{NAC}} \equiv D_{NAC}/W$ $\qquad \lambda_H \equiv H/W$

$\overline{V} \equiv V/V_r$ $\qquad \tau \equiv t/t_r$

where $V_r \equiv \sqrt{W/2\rho A}$ $\qquad t_r \equiv V_r/g.$

The resulting force balance equations become

(Drag)

$$\lambda_T \cos(\alpha_p) - \lambda_{L_S} \sin(\alpha_V) - \lambda_{D_S} \cos(\alpha_V) - \lambda_{D_f} - \lambda_{D_{NAC}} - \sin\gamma - \lambda_H \sin(\alpha_p) = d\bar{V}/d\tau \qquad \text{(II-27)}$$

(Lift)

$$\lambda_T \sin(\alpha_p) + \lambda_{L_S} \cos(\alpha_V) - \lambda_{D_S} \sin(\alpha_V) - \cos\gamma + \lambda_H \cos(\alpha_p) = \bar{V}(d\gamma/d\tau). \qquad \text{(II-28)}$$

Power balance equations. - For operation at constant rpm, the amount of power which is expended by the rotors must be equal to that delivered by the engines.

Thus, $\eta_c(\overline{HP})_{max.av.} + \bar{P}_{req} = 0$ (II-29)

where $\eta_c \equiv$ fraction of maximum horsepower available

$(\overline{HP})_{max.av.} = (HP)_{max.av.}$/hovering power required.

Using the previously described combination of simple momentum theory and blade element theory, the power required may be expressed as

$$P_{req} = T(V\cos(\alpha_p) + v) + P_{pro}(1.0 + \mu^2) \qquad \text{(II-30)}$$

where $P_{pro} \equiv$ profile power in hover

$\equiv (1/8)\sigma\, \pi\, R^2\, \rho\, V_t^{\,3}\, \bar{C}d_o$

and $\mu = (V\sin(\alpha_p)/\Omega R)$.

The power required is nondimensionalized by the ideal hovering power required. The resulting equation becomes

$$\bar{P}_{req} = \lambda_T(\bar{V}\cos(\alpha_p) + \bar{v}) + \bar{P}_{pro}(1.0 + \mu^2) \qquad \text{(II-31)}$$

where $\bar{P}_{req} \equiv P_{req}/P_r \quad \bar{P}_{pro} = P_{pro}/P_r \quad P_r = W^{3/2}\sqrt{2\rho A}$ .

Two Lycoming turboshaft "growth engines" (LTC-4B-12) supply the power-available for the Vertol Model 160 tilt-rotor aircraft. A complete discussion of the predicted characteristics of this engine is presented in ref. 5. The following equations were developed to approximate the horsepower available.

$$HP_{max.av.} = SHP_{max} \cdot \zeta_{tr} \tag{II-32}$$

$$SHP_{max} = 0.00348\left(\frac{V^2}{T/518.7}\right) + (4485. - 0.1313H + 1.064 \times 10^{-6} H^2) \tag{II-33}$$

where $H \equiv$ altitude (feet)
$V \equiv$ true airspeed (ft/sec)
$T \equiv$ temperature ($°R_k$)
$\zeta_{tr} \equiv$ transmission efficiency, also reflecting installation and accessory losses.

Kinematic equations. - The trajectory of an aircraft is usually described in an earth-fixed coordinate system. However, vehicle performance is analyzed in a wind axis system. The equations which relate the two coordinate systems are given below.

$$dH/dt = \bar{V}\, V_{ref} \sin\gamma = \bar{w}\, V_{ref} \tag{II-34}$$

$$dX/dt = \bar{V}\, V_{ref} \cos\gamma = \bar{u}\, V_{ref} \tag{II-35}$$

Two new variables, $\bar{u}$ and $\bar{w}$ are introduced which are defined to be the horizontal and vertical components of velocity measured in a ground-based axis system. In practice, these two variables can be used interchangeably with $\bar{V}$ and $\gamma$. They obey the following algebraic and trigonometric equations.

$$\bar{V}^2 = \bar{u}^2 + \bar{w}^2 \tag{II-36}$$

$$\gamma = \tan^{-1}(\bar{w}/\bar{u}) \tag{II-37}$$

It is possible to nondimensionalize the distance H and X. By following the procedure of the last few sections, the reference condition would be directly related to altitude. However, because density continually changes with altitude, such a nondimensionalization has little practical value.

International Standard Atmosphere. - The following algebraic equation governs density variations with altitude for the International Standard Atmosphere.

$$\rho = 0.00237[1.0 - 0.003566(H/518.7)]^{4.256}\ \text{slug/ft}^3 \qquad \text{(II-38)}$$

Weight equations. - The total gross-weight of the tilt-rotor aircraft decreases as fuel is consumed. The following differential equation quantifies this weight loss.

$$dW/dt = -W_f\ 1.05\ (1/3600)\ \text{lb/sec.} \qquad \text{(II-39)}$$

The equation below approximates the fuel flow rate characteristics of the Lycoming LTC-4B-12 engines (ref. 5).

$$W_f = 375 - 0.01367\ H + (0.495 - 2.11 \times 10^{-5}\ H + 1.283 \times 10^{-9} H^2) \times \eta_c\ SHP_{max} + (-0.156 + 1.13 \times 10^{-5}\ H + 2.96 \times 10^{-10}\ H^2)V \qquad \text{(II-40)}$$

## Performance Constraints

The overall performance of the tilt-rotor aircraft may be constrained by many additional factors besides the basic aircraft aerodynamic, weight and power characteristics. Structural integrity, stability and control requirements, dynamic instabilities, maximum permissible accelerations (as dictated by passenger comfort) etc., may influence the resulting flight profile of the aircraft.

A detailed investigation of any one of these design considerations could, in itself, be an extensive research effort. For this reason, this report has only enforced the following restricted set of performance constraints. A more detailed discussion is presented in ref. 6.

Pitching rate limit. - The moment-producing capability of the tilt-rotor aircraft, together with the vehicle's rate damping characteristics govern the magnitude of the pitching rate limit. A simple constant limit of

$$d\theta/dt \leq 0.25\ \text{rad/sec} \qquad \text{(II-40)}$$

has been assumed.

Structural "q" limit. - The airloads encountered by any aircraft in flight are proportional to dynamic pressure ($q = (1/2)\rho V^2$). In this report, an upper limit on dynamic pressure is assumed for the purpose of preserving the structural integrity of the aircraft.

Thus, $q = (1/2)\ \rho\ V^2 \leq q_{max} = 3500\ \text{lb/ft}^2$. (II-41)

This q constraint places a maximum velocity limit on the vehicle at any given altitude. As altitude increases, the maximum speed capability of the aircraft also increases.

Acceleration limits. - Acceleration constraints have been used to restrict the operating envelope of the tilt-rotor aircraft. Passenger comfort and stall-flutter boundaries may govern the magnitude of the limits chosen. For convenience, the constraints are expressed in a ground-based axis system, as:

$$|dw/dt| \leq 0.20g \qquad \text{(II-42)}$$

$$|du/dt| \leq 0.25g \qquad \text{(II-43)}$$

where $w = V \sin \gamma$ = the vertical velocity of the aircraft

$u = V \cos \gamma$ = the horizontal velocity of the aircraft.

Eqs. (II-42) and (II-43) do not allow the aircraft to accelerate or decelerate faster than 0.20g in the vertical direction, or 0.25g in the horizontal direction.

Touchdown velocity limit. - The landing gear design for the Model 160 limits the touchdown velocity to

$$w \geq -8 \text{ ft/sec.} \qquad \text{(II-44)}$$

Tilting rotor angle limits. - The angle that the engine nacelle makes with the mean aerodynamic chord of the main aerodynamic surface has been defined to be $i_p$. It is geometrically constrained to be within the following limits.

$$i_{p_{min}} \leq i_p \leq i_{p_{max}} \qquad \text{(II-45)}$$

where $i_{p_{min}} = 0$ and $i_{p_{max}} = 105°$.

Power limitation. - A nondimensional variable $\eta_c$ is used which is defined (see page 21) as the fraction of maximum available horsepower. By definition, the upper bound of $\eta_c$ is 1.

A lower constraint bound is introduced to insure that enough power is available to control the aircraft during descent. It is assumed that this lower bound is equal to 20 percent of the induced power required in hovering flight. If this additional constraint is expressed in terms of a percentage of the maximum available horsepower, both constraints may be mathematically expressed in the following manner:

$$\frac{.2\ (\text{Induced Power in Hover})}{\text{Maximum Available Power}} \leq \eta_c \leq 1.0. \qquad \text{(II-46)}$$

## Performance Prediction Methodology

In the preceding sections of this report, a simplified mathematical model has been developed which governs the performance of a tilt-rotor aircraft. The model consists of a set of algebraic and differential equations that may, or may not, be constrained by an auxiliary set of equations. The task of this section is to solve this system or a slightly modified system, of equations. The objective is to arrive at a description of tilt-rotor performance capability.

Finding a realistic solution to the complete set of dynamic performance equations may be a formidable task. Time histories of the physical control variables which meet the chosen initial and terminal boundary conditions of the problem are required. The determination of these control time histories may be difficult. Furthermore, a digital integration routine is needed to find a solution to the system of differential equations which result.

In this report, an approximate method of evaluating aircraft performance is investigated to highlight the important performance characteristics of the aircraft. These characteristics are then used to develop the so-called kinematic model of the basic tilt-rotor aircraft. This model is based on the steady-state solutions of the equations of motion. Thus, it represents time-independent relationships between the horizontal and the vertical (rate of climb, or descent) components of the total flight velocity vector at a given altitude, power setting and aircraft configuration. Because accelerations are only considered to be mathematical constraints which do not directly affect vehicle performance, it is relatively easy to physically interpret the results. Furthermore, if the aircraft accelerations are small, this kinematic performance model is a good representation of tilt-rotor performance. In most cases of interest, the simplified model is sufficiently accurate to estimate tilt-rotor performance.

Generalized kinematic performance. - The simplest description of tilt-rotor performance is governed by a kinematic mathematical model. The steady-state performance equations are the "core" of the mathematical kinematic model. The force balance equations, lift coefficient equation, and momentum equation must be satisfied at each point along the trajectory (App. B).

For purposes of discussion, it is convenient to represent these four equations in eight unknowns in a functional notation. They are, respectively, a drag equation, a lift equation, an equation relating $CL_s$ to the angle of attack, and the momentum equation.

Drag $f_1(\bar{u}, \bar{w}, \lambda_T, \alpha_p, C_{L_S}, \bar{v}, \quad , \delta_f) = P$ (II-47)

Lift $f_2(\bar{u}, \bar{w}, \lambda_T, \alpha_p, C_{L_S}, \bar{v}, \quad , \delta_f) = R$ (II-48)

$C_L$ $f_3(\bar{u}, \bar{w}, \quad , \alpha_p, C_{L_S}, \bar{v}, \theta, \delta_f) = S$ (II-49)

Momentum $f_4(\bar{u}, \bar{w}, \lambda_T, \alpha_p, \quad , \bar{v}, \quad , \quad ) = Q$ (II-50)

This system of four equations in eight unknowns has a degree of indeterminancy of four, which is eliminated by specifying the flight condition with $\theta$, $\bar{u}$, $\bar{w}$ and $\delta_f$. The independent variables are $\lambda_T$, $\alpha_p$, $\bar{v}$, and $C_L$. The right-hand variables, P, R, S and Q are dummies. In static force balance equilibrium, P, R, S and Q are identically equal to zero. Unfortunately, a simple explicit solution to this set of nonlinear algebraic equations does not exist. However, by using a Newton-Raphson iteration procedure to improve the solution guess so that $P = R = S = Q$ approach zero, a solution is approached.

The ability of the tilt-rotor aircraft to sustain equilibrium flight is also governed by the power balance equation which is represented in functional notation below.

Power Balance $f_5(\bar{u}, \bar{w}, \lambda_T, \alpha_p, \quad , \bar{v}, \quad , \quad , \eta_c, H) = Y = 0.$

(II-51)

The five algebraic equations which are functionally related to ten unknowns govern the point performance of the tilt-rotor aircraft. Four of the ten unknowns may be specified and can be thought of as "control variables."

There is a certain arbitrariness in the selection of control variables. It is desirable to have the chosen mathematical controls of this problem formulation correspond as closely as possible to the controlling inputs of the actual vehicle. If this criterion is met, it is usually easier to decide how to choose a reasonable set of flight controls. The attitude angle ($\theta$), the flap deflection angle ($\delta_f$), the rotor tilt that may be called the configuration angle ($\alpha_{config}$), and the fraction of maximum power available are all directly related to physical aircraft controlling imputs. However, choosing time histories of a configuration is a difficult task if the velocity profile is not specified à priori (which it can't be). Therefore, the horizontal velocity of the aircraft is assumed to be a control variable replacing the configuration angle time history. The control variables of the kinematic model of the tilt-rotor aircraft then become $\bar{u}$, $\eta_c$, $\theta$, and $\delta_f$.

The reference velocity ($V_r$) and power ($P_r$), which have been used to nondimensionalize the respective static performance and power equations, are a function of the density of air and the instantaneous gross weight of the aircraft.

Thus, $V_r = \sqrt{W/2\rho A}$, and $P_r = W^{3/2}/\sqrt{2\rho A}$.

Therefore, to find the true airspeed or power at a given altitude and weight, it is necessary to multiply the dimensionless quantity by the corresponding dimensional parameter referenced to that altitude and weight.

The density variation with altitude may be functionally represented by the following: $\rho = \rho(H)$.

As the tilt-rotor performs its mission, fuel is burned which reduces the instantaneous gross weight of the aircraft. The differential equation governing this weight decrease which relates the fuel flow to the altitude, forward velocity, and applied power of the aircraft may be functionally represented by

$$dW/dt = W(h, \eta_c, \bar{u}, \bar{w}).$$

The trajectory that the tilt-rotor performance model traces out in space is governed by the following kinematic equations

$$dH/dt = \bar{w}\, V_r \qquad \text{(II-52)}$$

$$dX/dt = \bar{u}\, V_r \quad . \qquad \text{(II-53)}$$

These differential equations or identities relate the trajectory to the steady-state performance of the aircraft.

The kinematic performance problem can now be stated in mathematical terms. There are nine independent equations (6 algebraic and 3 differential) in 14 unknowns ($\bar{u}$, $\bar{w}$, $\lambda_T$, $\alpha_p$, $C_{L_S}$, $\bar{v}$, $\theta$, $\delta_f$, $\eta_c$, H, X, $\rho$, W, t) which must be solved simultaneously. Time (t) is the independent parameter of this algebraic and differential system of equations. Four of the unknowns are called "control variables' ($\bar{u}$, $\eta_c$, $\theta$, $\delta_f$ and are assumed to be known as a function of time. The remaining 9 unknown time histories must be determined by solving the 9 governing equations. Appendix B presents the details of the chosen solution technique.

Point performance characteristics with specified "inner" controls. - The four independent controls, $\bar{u}(t)$, $\eta_c(t)$, $\theta(t)$ and $\delta_f(t)$ govern the trajectory of the tilt-rotor aircraft. At least one, and possibly two, of these controls are normally programmed to be a function of some geometric or performance parameter of the aircraft. If two of the four independent controls are assumed to be a function of the tilt-rotor performance state, significant savings in model complexity are achieved. Because only two independent control variables remain, a simple two-dimensional plot can be used to describe the performance state of the aircraft.

In this report, the inner loop controls, $\theta$ and $\delta_f$, are chosen to be functionally dependent upon the horizontal velocity of the aircraft. The functional dependence is chosen to minimize the level steady-state power required at each horizontal velocity and to realize a physical meaningful transition schedule. Only two of the inner loop controls may be arbitrarily specified. The configuration must change to allow the inner iteration loop to arrive at an equilibrium point. These inner loop control variables are chosen in the following manner:

Flap Control $\left(\delta_f(t)\right)$

The flap should be retracted as forward velocity is attained to minimize the steady level flight power required of the tilt-rotor aircraft (Figure II-12). It is also desirable to use some flap deflection to allow conversion to begin at lower horizontal velocities. This latter consideration is difficult to implement and is not considered in this study. The following function relationship for flap deflection angle is assumed.

$$\delta_f = \pi/4[1.0 + \cos(\bar{u}/3.0)\pi] \text{ if } 0 \le \bar{u} < 3.0 \qquad \text{(II-54)}$$

$$\delta_f = 0 \text{ if } 3.0 \le \bar{u}.$$

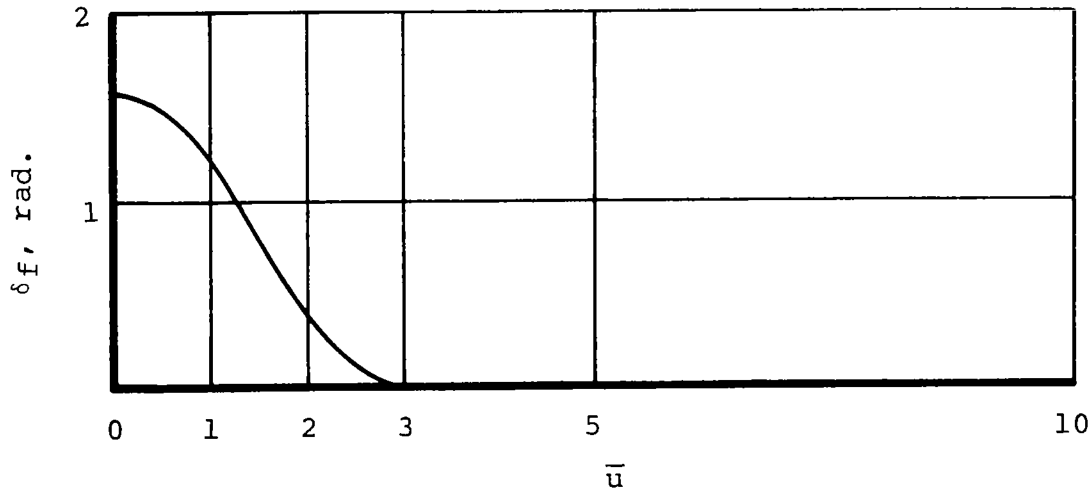

Figure II-12

### Attitude Angle ($\theta(t)$)

The attitude of the aircraft is chosen by specifying a wing lift-to-weight (L/W) transition schedule which is assumed to be a function of the tilt-rotor horizontal velocity. At low horizontal velocities ($\bar{u} \leq 3.0$), the attitude of the aircraft is ineffective at maintaining a prescribed lift-to-weight ratio. Therefore, a fuselage attitude of zero is assumed in this regime.

For velocities greater than 3.0, the attitude angle ($\theta$) is determined by solving eqs. (II-7) and (II-9) for a prescribed lift-to-weight ratio. The resulting expression is approximately given by

$$\theta \approx \gamma - \alpha_{OL} + (4.0/a)(A/S_W)(1.0/\bar{u}^2)(L/W) - \alpha_V$$

where $\bar{u}^2 \approx \bar{V}^2$ for $\bar{u} > 3.0$.

Because $\alpha_V$ is small, $\alpha_V \approx (2\bar{v}\sin(\alpha_p))/\bar{u}$.

$$\theta \approx \left[ \frac{\gamma - \alpha_{OL} + \left(\frac{4.0\ A\ L}{a\ S_W\ \bar{u}^2\ W}\right) + \left(\frac{2\bar{v}}{\bar{u}}\right)\sin(\alpha_{config} - \gamma)}{1 - \left(\frac{2\bar{v}}{\bar{u}}\right)\cos(\alpha_{config} - \gamma)} \right] \quad \text{(II-55)}$$

The attitude angle of the tilt-rotor aircraft can be found by solving eq. (II-55) when the following L/W conversion schedule is presented (Figure II-13).

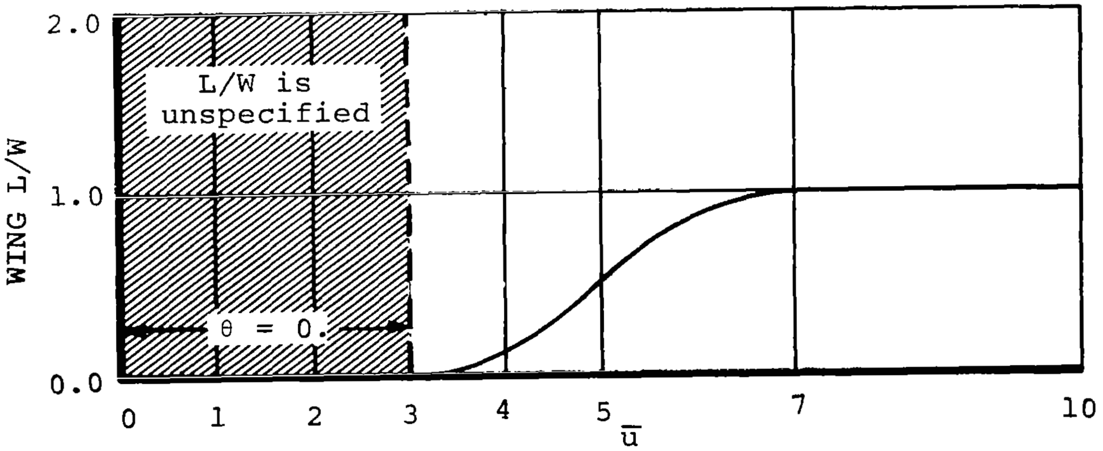

Figure II-13

| Horiz. Speed | Wing L/W | $\theta$ |
|---|---|---|
| $0 \leq \bar{u} < 3.0$ | Unspecified | 0° |
| $3.0 \leq \bar{u} < 7.0$ | $1/2\{\cos[\pi(\bar{u} - 3.0)/4.0 + \pi] + 1.0\}$ | Unspecified |
| $7.0 \leq \bar{u}$ | 1.0 | Unspecified |

An alternate "inner loop control" which may be specified is the configuration time history ($i_p(t)$). However, the governing equations must be rearranged to contain $i_p$ as one of the four independent control parameters. If this control is programmed as a function of horizontal velocity, the attitude of the aircraft may be left free to satisfy the algebraic performance equations. This alternate formulation of the inner loop controls allows other types of VTOL aircraft to be represented by the same mathematical performance model. For example, if $i_p = 0$ for all $\bar{u}$, a low disc loading tilt-wing aircraft is mathematically described by the governing performance equations. The added task of treating configurations other than the tilt-rotor has not been undertaken in this report.

The two independent controls ($\bar{u}$ and $\eta_c$) which have not been functionally specified govern the kinematic performance of the tilt-rotor aircraft. A graphical map of vehicle point performance may be obtained by solving the five equations in five unknowns for particular values of applied power and horizontal velocity. The power control, $\eta_c$, governs the rate of climb or sink of the aircraft at a chosen value of horizontal velocity ($\bar{u}$). $\eta_c$ has been defined to be the fraction of maximum power which is available.

The maximum performance climbing characteristics of the mathematical model of the tilt-rotor aircraft are illustrated in Figure II-14. The three curves which result are obtained by applying maximum power available ($\eta_c = 1.0$) at 0, 5000, and 10 000-foot altitudes and calculating the resulting climb performance. Altitudes of greater than 10 000 feet are not considered in the analysis. The results are nondimensionalized by the ideal induced velocity at the altitude considered.

Near hover at sea level ($0 \leq \bar{u} < 3.0$), the climbing tilt-rotor performance is not very sensitive to horizontal velocity variations. The maximum rate of climb is achieved at a horizontal velocity of 1.0. The surprisingly good vertical flight performance near hover arises because in near-vertical ascent, the mass flow through the rotor increases, thus reducing the effective power required. This beneficial effect decreases with increasing altitude. At 10 000 feet in this same speed range, significant increases in rate of climb performance can be realized by maintaining some horizontal velocity.

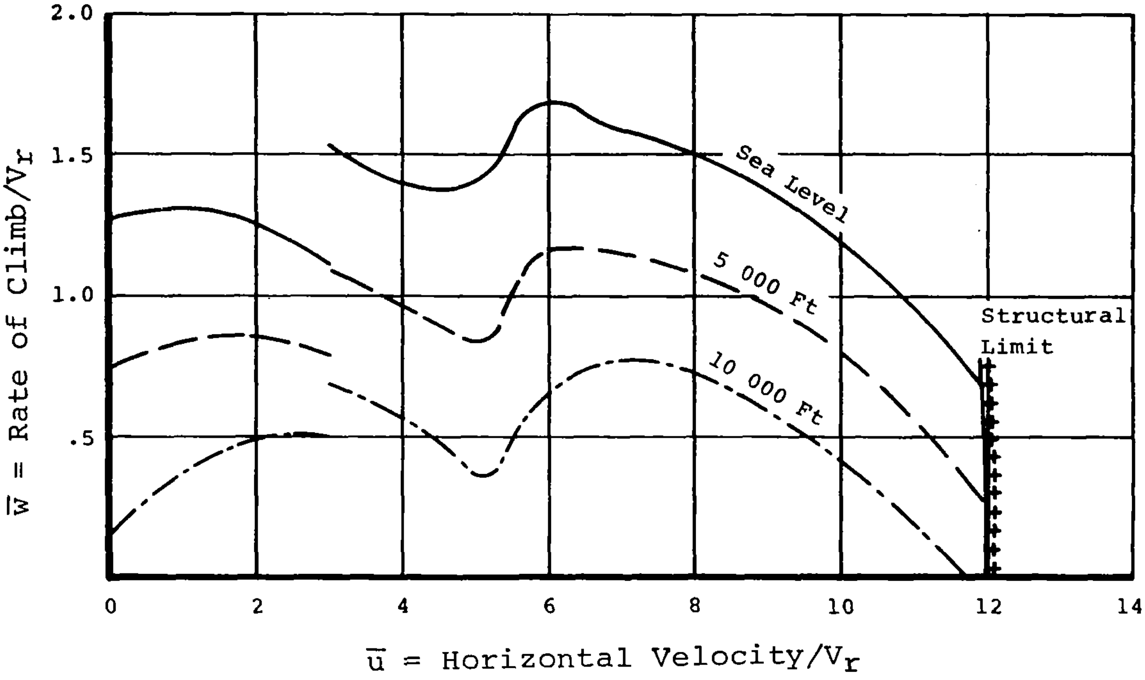

Figure II-14

At a nondimensional horizontal velocity of three, a discontinuity appears in the maximum performance curves. Because the attitude of the tilt-rotor aircraft has been arbitrarily set to zero until a horizontal velocity of three is attained, a considerable download on the wing is developed. At a velocity of three, a lift-to-weight ratio of zero is specified (Figure II-13). This discontinuity in wing download causes the abrupt change in the climbing performance characteristics which are continuous.

The attitude control, θ, which results from suddenly specifying the lift-to-weight ratio, is also discontinuous. However, a pitching rate limit of 0.25 rad/sec is enforced, thus prohibiting discontinuous climb performance. Because time is not one of the parameters of Figure II-14, the effect of a pitching rate constraint on rate of climb performance cannot be illustrated.

The best climb performance of the vehicle occurs in the aircraft mode of flight. The nondimensional horizontal velocity where the best rate of climb is attained is fairly insensitive to altitude variations. However, the actual horizontal velocity (ft/sec) increases as altitude increases.

The attitude of the aircraft was originally programmed in level steady-state flight to minimize the power required and to specify a transition schedule. It is not surprising that the programmed angle does not optimize performance during high rates of climb. To more fully optimize the tilt-rotor's climbing performance, the two inner controls ($\theta$ and $\delta_f$) should be chosen by the optimization procedure. A solution to this four-control optimum performance problem has not been attempted in this report.

A dynamic pressure limit ($q_{max}$) must be enforced to retain the structural integrity of the aircraft. This dynamic pressure limit (eq. II-56) is expressed in nondimensional notation by the following expression:

$$q = (\overline{V}^2/4.0)(W/A) \leq q_{max}. \qquad \text{(II-56)}$$

For a chosen disc loading ($W/A \approx T/A$), this dynamic pressure constraint becomes a high-speed nondimensional velocity constraint. The assumed constraint, which is illustrated in Figure II-14, permits maximum speeds at 10 000 feet of about 350 knots.

The descent characteristics of the mathematical tilt-rotor model are illustrated in Figure II-15. Lines of constant nondimensional applied power, which must be equal to the required power in descent, has been nondimensionalized by the tilt-rotor hovering power required. The resulting curves are independent of the engine characteristics and are valid for any altitude.

Previously, a lower limit on the applied power control was introduced to satisfy controllability requirements. It was assumed that 20 percent of the hovering power required is necessary to maintain control in descending flight. Therefore, the 0.2 nondimensional applied power curve of Figure II-15 becomes the maximum permissible rate of sink boundary of the tilt-rotor aircraft. Fully autorotative flight is not considered in this analysis.

There are three regimes where a rather high rate of sink can be maintained in this partial power condition. The first is an almost pure vertical descent where momentum theory indicates that high sink rates are possible. Unfortunately, finding a solution to the algebraic performance equations in partial power descent may be numerically difficult. At high rates of descent, the momentum equation may have more than one mathematical solution. The Newton-Raphson iteration procedure has difficulty locating any one particular solution. A discussion of these numerical interation difficulties is presented

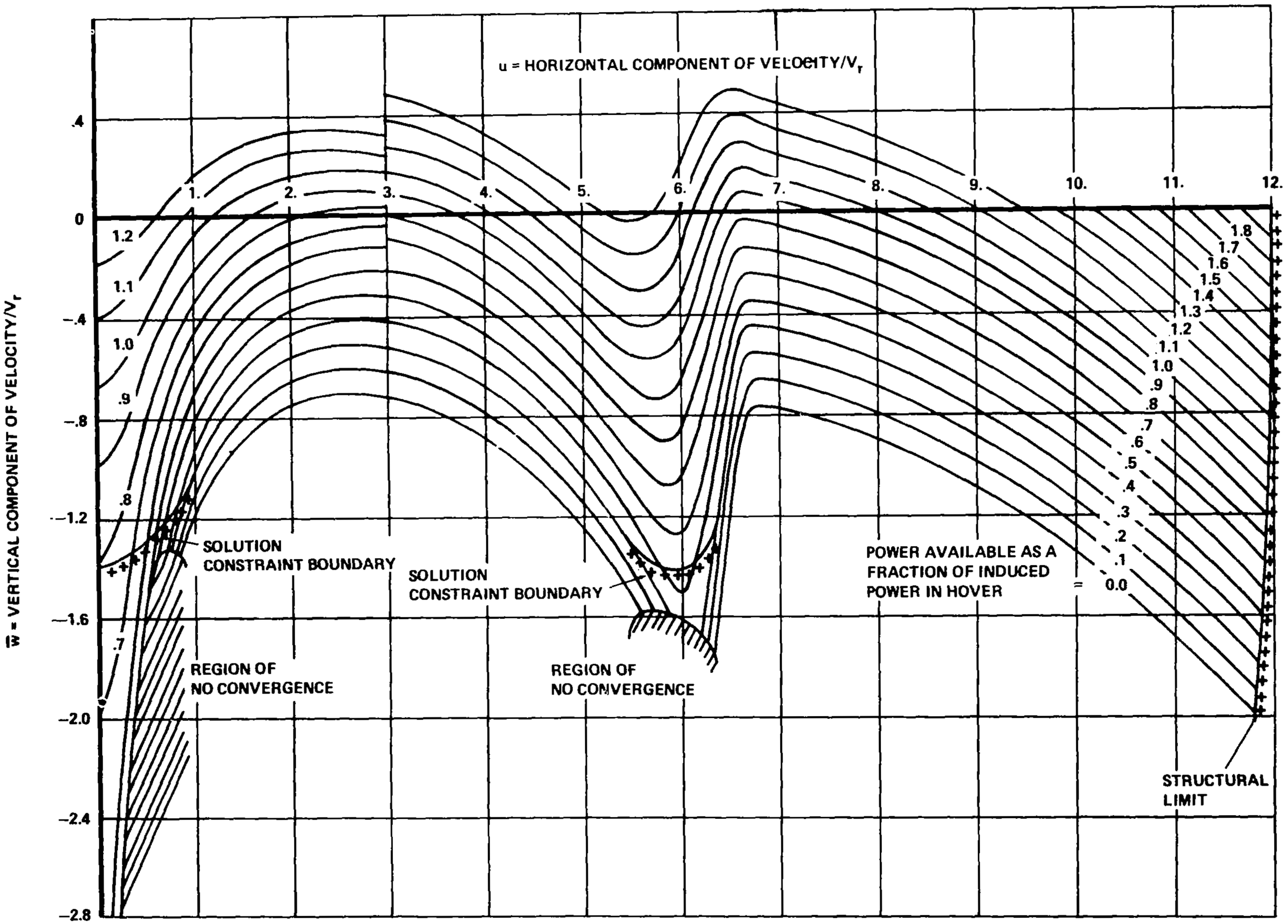
u = HORIZONTAL COMPONENT OF VELOCITY/V_r
w̄ = VERTICAL COMPONENT OF VELOCITY/V_r
.4
0
-.4
-.8
-1.2
-1.6
-2.0
-2.4
-2.8
1.
2.
3.
4.
5.
6.
7.
8.
9.
10.
11.
12.
1.2
1.1
1.0
.9
.8
.7
1.8
1.7
1.6
1.5
1.4
1.3
1.2
1.1
1.0
.9
.8
.7
.6
.5
.4
.3
.2
.1
0.0
SOLUTION CONSTRAINT BOUNDARY
SOLUTION CONSTRAINT BOUNDARY
REGION OF NO CONVERGENCE
REGION OF NO CONVERGENCE
POWER AVAILABLE AS A FRACTION OF INDUCED POWER IN HOVER
STRUCTURAL LIMIT

Figure II-15

in Appendix C. The locus of points where it is difficult and usually impossible to find solutions to the momentum equation by iterative techniques is labeled a "region of no convergence." The region is illustrated on a plot of nondimensional rate of sink versus horizontal velocity in Figure II-15 and in more detail in Figure C-4 (Appendix C). Notice that the assumed 20 percent fraction of hovering induced power constraint intersects the "region of no convergence. Therefore, the kinematic mathematical model of tilt-rotor performance must be more stringently constrained at small horizontal velocities.

In References 7 and 8, experimental data is given indicating the validity of using momentum theory to describe high sink rate conditions at zero forward velocities. It is shown that although the rotor is technically operating in the vortex ring state, as soon as descent begins, the momentum theory describes the actual descent performance quite well until nondimensional sinking velocities of 1.4 are attained. At this point, the vortex ring state is physically apparent and the simple theory no longer holds.

By now it is apparent that the 20-percent fraction of hovering induced power constraint passes into both the "nonconvergence region" and a region where simple momentum theory does not accurately describe rotor performance. To avoid these difficulties, a "solution constraint boundary," which is shown in Figure II-15 and in Figure C-4 of Appendix C, is assumed. The tilt-rotor aircraft is constrained to fly in steady-state equilibrium flight at rate of sink velocities which are above this assumed constraint function.

The second regime where high rates of steady-state sinking velocities can be maintained occurs at nondimensional horizontal velocities of about 5.5. The tilt-rotor aircraft is still flying in the helicopter mode but is about to convert to the airplane configuration. Because the rotor pylons create a lot of drag in the helicopter configuration, they act as a 'speed brake' causing high sinking velocities at partial power. Unfortunately, at very small power settings and horizontal velocities of about 6.0, the drag equation (eq. II-27) cannot be satisfied. The accelerating force of gravity caused by steep descent angles becomes larger than the total drag of the aircraft. The locus of points where equilibrium flight cannot be maintained is also labeled a "region of no convergence" as shown in Figure II-15. Notice that the assumed partial power constraint boundary intersects this region of no convergence. Therefore, a second solution constraint is assumed which is also illustrated in this same figure. Descending flight at sink rates which are above the solution constraint boundary are considered as possible operating states of the tilt-rotor aircraft.

High sinking velocities can also be maintained at high forward speeds under partial power in the airplane mode of flight. The basic drag of the tilt-rotor aircraft is sufficient to support steady equilibrium flight. However, the non-dimensionalized velocity constraint (eq. II-56) restricts the high-speed descent performance as shown in Figure II-15.

## III. THEORETICAL TILT-ROTOR ACOUSTIC MODEL

The acoustical properties of a tilt-rotor aircraft are mathematically modeled in this section of the report. The basic mechanisms which produce noise are reviewed, leading to the development of a simplified far-field acoustic model. Attenuation and propagation characteristics are also considered. The acoustical spectrum of sound generated by the tilt-rotor is then calculated at specified ground locations. Finally, some of the more applicable subjective evaluation criteria of the annoyance of the sound at these locations are presented.

### Tilt-Rotor Noise Generation

The noise generated by an open airscrew VTOL aircraft is typically classified by its generation mechanism. For a VTOL aircraft, driven by turboshaft engines, sound which is generated by aerodynamic forces often dominates in the far acoustic field. This aerodynamic sound includes various types of noise which are commonly classified as rotational noise, vortex noise (also called broad-band noise), and blade slap. Mechanical sources of sound which are produced by the transmission, gearbox, and vibrating components of the aircraft may also be of importance. Each source of sound has its own distinguishable characteristics. The type of sound which dominates is a function of the relative position between the sound source and the observer, the flight condition of the aircraft and many other factors. Nevertheless, at moderate distances from the tilt-rotor aircraft, some qualitative judgments about the relative importance of the different sound sources can be made. They are listed below in the order of decreasing importance for far-field considerations:

Blade slap (if it occurs)
Rotor rotational noise
Rotor vortex noise (broad-band noise)
Gearbox & transmission noise
Turbine engine noise.

Blade slap, if it occurs, is definitely the most offensive source of noise. The low frequency characteristic impulsive sound is not attenuated to any great extent by the atmosphere and can be heard at large distances from the source. The main rotor rotational noise is a lower frequency sound which is directly related to the integrated forces acting in the rotor blades. Rotor vortex noise, gearbox noise, and turbine engine noise are of higher frequency and are attenuated much faster by atmosphere. Each source of sound is subsequently discussed.

Rotational noise of a tilt-rotor in nonaxial flight. - The rotational noise produced by a tilt-rotor arises from the action of the rotor forces on the surrounding medium (air). Each element of the tilt-rotor has an elemental net force acting on it which may be decomposed into a thrust and a drag force. These elemental forces may be integrated along the rotor blade and around the azimuth to yield the total thrust and torque of the tilt rotor. These elemental blade forces cause an equal, but opposite force to be applied to the medium. Assume, for the moment, that the resulting pressure field on the air in the rotating frame is steady (this assumption is valid for a propeller in axial flight). The pressure measured at any fixed location on the rotor disc appears oscillatory. A sketch of this oscillating pressure field is shown in Figure III-1.

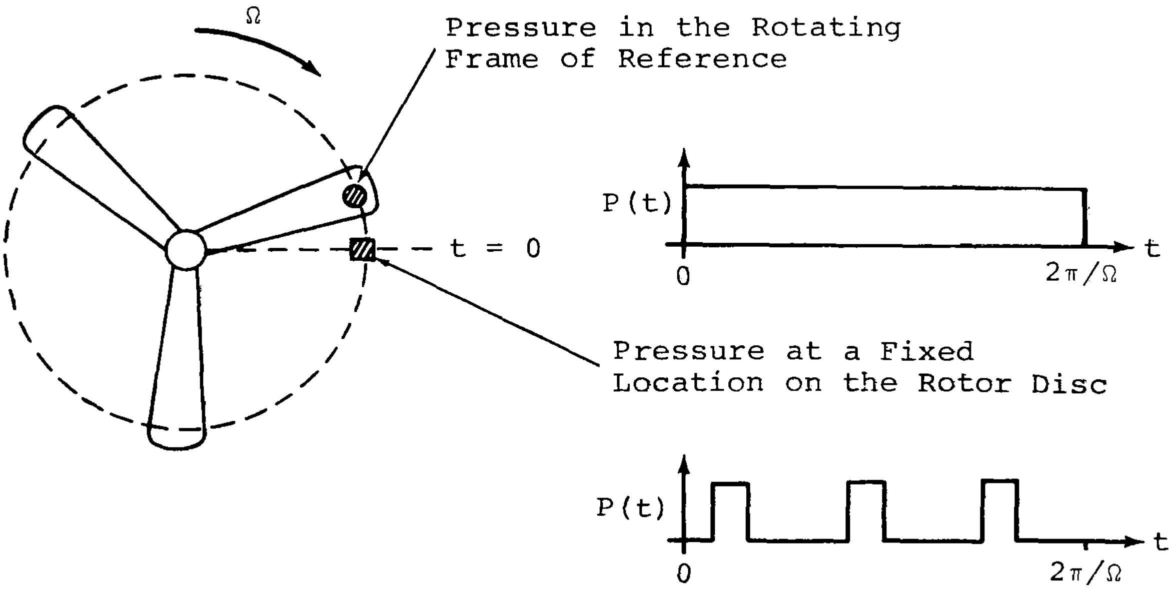
Ω
Pressure in the Rotating Frame of Reference
P(t)
0
2π/Ω
t
t = 0
Pressure at a Fixed Location on the Rotor Disc
P(t)
0
2π/Ω
t

Figure III-1

The pressure over each blade chord is assumed to be constant in this simplified illustration. The frequency of the oscillating pressure field at a point in the rotor disc plane is proportional to the frequency with which the blades pass that point.

This simplified model of oscillating forces and pressures is the cornerstone of present rotational noise analysis. Gutin (ref. 9) was the first to represent the oscillating force field of a propeller in a Fourier series. The components of this series sum to yield the thrust and torque. The rotational noise of the propeller is determined by treating this oscillating force field as an array of dipole sources from which the acoustic field can be calculated.

Garrick and Watkins (ref. 10) extended these concepts to an axially moving propeller. Because the propeller is in motion and the observer is stationary, frequency and retarded time corrections must be applied. In their derivation, an axis system fixed in the propeller was assumed.

Recently, Lowson & Ollerhead (refs. 11 and 12) have presented a theory for helicopter rotational noise which is very similar to Garrick & Watkin's moving propeller analysis. They derived their equations in an axis system fixed in space and included the effect of rotor coning. Their very complete analysis goes on to show that helicopter rotational noise is very dependent upon the higher harmonic airloads. The pressure field of the air in the rotating frame of a helicopter is, in general, not steady. The induced flow field, nonuniform inflow velocities, and nonaxial translation of the rotor plane all produce time-varying blade force and pressure fields. They also point out that an analytic description of the higher harmonic airloads is presently a formidable, if not impossible, task. However, by curve fitting existing measured and Fourier analyzed airload data (see refs. 13 and 14), Lowson and Ollerhead were able to develop a simplified rotational noise prediction technique that does consider higher harmonic airload data. Their comparison with measured acoustical data was encouraging.

In the introduction of the acoustical section of this report, blade slap was listed as the most offensive source of noise. It was treated as a totally separate phenomenon. In reality, it arises because of rapidly changing blade pressures due to either blade vortex interactions or advancing blade compressibility effects. These impulsive airloads, which imply high levels of harmonic content, are interpreted acoustically as blade slap. However, some acousticians (ref. 11) classify blade slap as a special case of rotational noise.

The tilt-rotor aircraft is, in many respects, very much like the single rotor helicopter. For this reason, a modification of Lowson & Ollerhead's simplified rotational noise analysis is chosen for this study. The basic program, which is described in ref. 11 is modified to accommodate arbitrary rotor plane inclinations with respect to the aircraft's velocity and loading laws which are a function of the operating state of the rotor. The theory which results reduced to Garrick and Watkin's analysis when the rotors are acting as conventional propellers in airplane flight. These necessary modifications are presented in the following two subsections of this report.

Acoustic far-field equations: On a tilt-rotor aircraft, the rotor disc plane may assume any angle with respect to the freestream velocity of the aircraft. A convenient axis system in which to derive the acoustic equations is illustrated in Figure III-2. The chosen set of orthogonal axes are fixed in space at the time the sound was first emitted and the $X_n$ axis is aligned with the thrusting axis of the rotor.

This same axis system was used in the development (ref. 11) of the rotational noise equations of a helicopter operating in level steady-state flight. By differentiating this source in the appropriate directions, the resulting dipole radiation for fluctuating axial, circumferential, and radial components of force can be expressed.

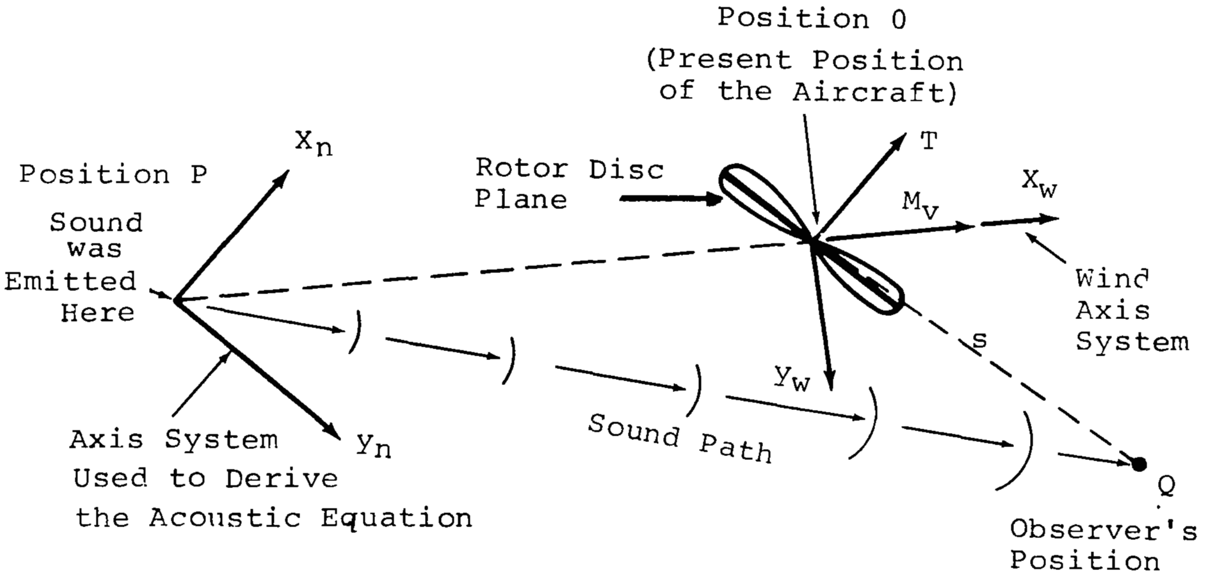
Position 0
(Present Position
of the Aircraft)
$X_n$
Position P
Sound was Emitted Here
Rotor Disc Plane
T
$M_V$
$X_W$
Wind Axis System
S
$Y_W$
Sound Path
Axis System Used to Derive the Acoustic Equation
$Y_n$
Q
Observer's Position

Figure III-2

The equation which governs the rotational noise of a rotor operating in nonaxial flight becomes, as derived in ref. 11:

$$\begin{aligned} C_n &= a_n + ib_n \\ &= \sum_{\lambda=0}^{+\infty} \frac{i}{4\pi}^{-(n-\lambda)} \left\{ \frac{n\Omega X_n}{a_o s^2} \left\{ +ia_{\lambda T}\left(J_{n-\lambda} + (-1)^{\lambda} J_{n+\lambda}\right) - b_{\lambda T}\left(J_{n-\lambda} - (-1)^{\lambda} J_{n+\lambda}\right) \right\} \right. \\ &\qquad - \left\{ \frac{ia_{\lambda D}}{R's}\left((n-\lambda)J_{n-\lambda} + (-1)^{\lambda}(n+\lambda)J_{n+\lambda}\right) \right. \\ &\qquad \left. - \frac{b_{\lambda D}}{R's}\left((n-\lambda)J_{n-\lambda} - (-1)^{\lambda}(n+\lambda)J_{n+\lambda}\right) \right\} \\ &\qquad \left. + \frac{n\Omega y_n}{a_o\, s^2} \left\{ a_{\lambda C}\left(J'_{n-\lambda} + (-1)^{\lambda} J'_{n+\lambda}\right) + ib_{\lambda C}\left(J'_{n-\lambda} - (-1)^{\lambda} J'_{n+\lambda}\right) \right\} \right\} \end{aligned} \tag{III-1}$$

where

$C_n$ = the nth sound harmonic at position Q when the tilt rotor aircraft is presently at 0.

$n$ = mB ≡ harmonic number × number of blades

$\lambda$ = loading harmonic number

$\Omega$ = rotational speed of rotor, radians/sec

$X_n$ = acoustic axis perpendicular to tip path plane with the positive direction forward of the tip path plane

$a_o$ = speed of sound in free air, ft/sec

$s$ = distance of the observer from the rotor hub

$a_{\lambda T}$, $b_{\lambda T}$; $a_{\lambda D}$, $b_{\lambda D}$; $a_{\lambda C}$, $b_{\lambda C}$ = the thrust, drag and radial force harmonic components

$J = J(nMy_n/s)$ ≡ Bessel function of argument $(nMy_n/s)$

$R'$ = radius of point source on rotor

$y_n$ = acoustic axis parallel to tip path plane with the positive direction below the axis of rotation

$J'$ = derivative of Bessel function

$M$ = Mach number at the radial station of the point source

The root mean square pressure of the $n^{th}$ harmonic of rotational noise is found by substituting eq. (III-1) into

$$C_n = (a_n{}^2 + b_n{}^2)^{1/2} \qquad \text{(III-2)}$$

These basic results are independent of the direction of motion of the sound source.

Lowson & Ollerhead (ref. 11) used eqs. (III-1) and (III-2) to predict the rotational noise of a helicopter operating in level steady-state flight. These same equations are used in this analysis to preduct the rotational noise of a tilt-rotor aircraft. However, the tilting plane of the rotors is allowed to assume an angle, $\alpha_p$ with respect to the freestream velocity of the aircraft (see Figure III-3).

It is, therefore, necessary to relate the flight condition of the tilt-rotor aircraft to the $x_n$, $y_n$ axis system. The following geometrical relationships can be deduced by inspection of Figure III-3.

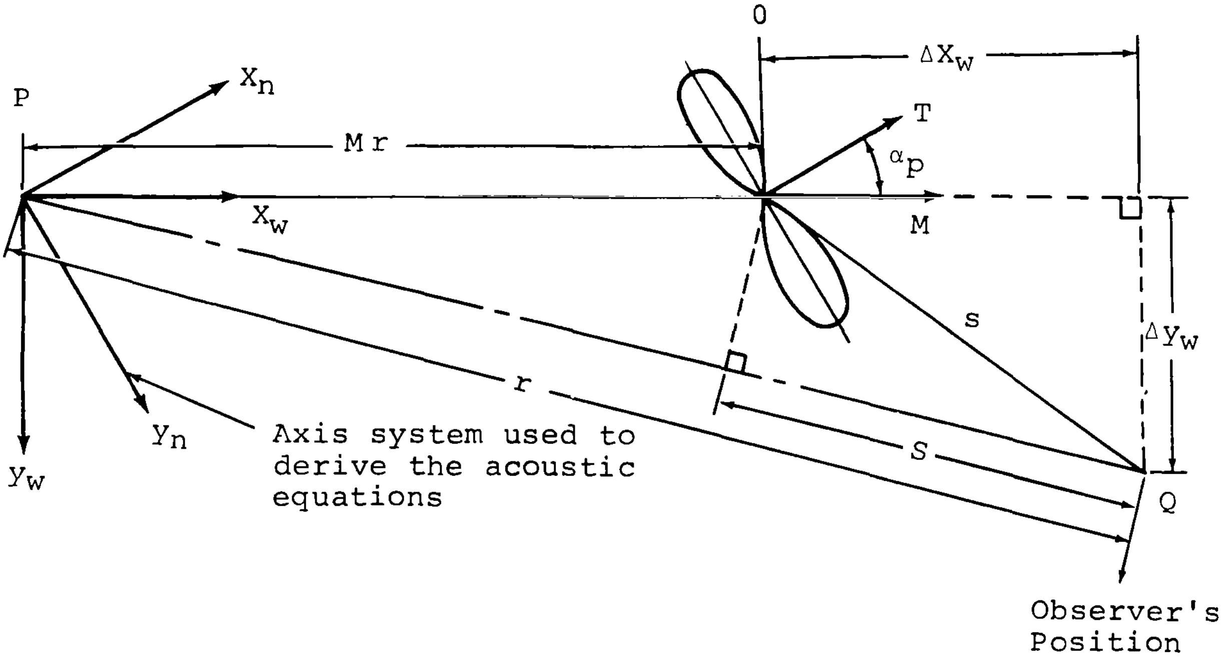

O
$\Delta X_w$
P
$X_n$
T
Mr
$\alpha_p$
$X_w$
M
s
$\Delta y_w$
r
$y_n$
Axis system used to derive the acoustic equations
S
$y_w$
Q
Observer's Position

Figure III-3

$$x_n = x_w \cos(\alpha_p) - y_w \sin(\alpha_p) \qquad \text{(III-3)}$$

$$y_n = x_w \sin(\alpha_p) + y_w \cos(\alpha_p) \qquad \text{(III-4)}$$

$$z_n = z_w \qquad \text{(III-5)}$$

where $$X_w = \Delta X_w + Mr \qquad \text{(III-6)}$$

$$y_w = \Delta y_w \qquad \text{(III-7)}$$

and phase radius, $$r = \frac{M\,\Delta X_w + S}{\beta^2} \qquad \text{(III-8)}$$

while $$S = \sqrt{\Delta X_w{}^2 + \beta^2(\Delta y_w{}^2 + Z_w{}^2)} \qquad \text{(III-9)}$$

$$\beta^2 = 1 - M^2 \qquad \text{(III-10)}$$

The variable $Z_n \equiv Z_w$ has been introduced to allow the observation point to be moved to specified "side-line" positions. A derivation of eqs. (III-6) through (III-10) is presented in detail in ref. 10.

Eqs. (III-1) through (III-10) predict the rotational noise of the tilt-rotor aircraft for specified flight conditions and corresponding values of the harmonic force coefficients. A method of specifying the harmonic force coefficients is presented in the next subsection.

Aerodynamic loading laws of the prop-rotor: It has been established by many authors that blade loading harmonic data is important in being able to predict rotational noise of a helicopter. Unfortunately, adequate theoretical prediction techniques and/or sufficiently reliable experimental data to quantitatively define the higher loading harmonics is lacking at the present time. To surmount this difficulty for the helicopter, Lowson & Ollerhead (ref. 11) developed the concept of a "rotor loading law." They hypothesized that the higher harmonic airloads decrease by some power of the harmonic number. This exponent is referred to as the "loading law" and is designated by the symbol "n". By empirically fitting airload data of helicopters in level steady-state flight, a numerical value of 2 was thought to be representative. If the phase of the loading harmonics is assumed to be random, the following expression results:

$$F = F_{steady}/\lambda^{(n+0.5)}$$

where $n = 2.0$
$F \equiv$ harmonic airloads
$\lambda \equiv$ loading harmonic number.

It is assumed that the higher harmonic airloads of thrust, drag, and radial force all obey the same loading law.

Thus, $C_{\lambda T} = C_{OT}/\lambda^{(n+0.5)}$ (III-11)

$C_{\lambda D} = C_{OD}/\lambda^{(n+0.5)}$ (III-12)

$C_{\lambda C} = C_{OC}/\lambda^{(n+0.5)}$ (III-13)

where $n = 2.0$.

If eqs. (III-11), (III-12), and (III-13) are substituted in eqs. (III-1) through (III-10), the rotational noise generated by a helicopter in level steady-state flight is completely determined.

The concept of a "loading law" which describes the blade loading of any rotor is an attractive one. It simplifies much of the necessary mathematics but still should retain the character of the solution. However, the question of how this blade loading varies as a function of forward speed and rotor angle of attack is still unanswered. At the present time, Vertol, in conjunction with the Ames Directorate of AMRDL, is reducing the pressure data on a wind tunnel model rotor test to help establish these loading laws (ref. 16). In the next few paragraphs, a framework which can be used to accept this data is developed. Preliminary data from ref. 16 and some loading data from ref. 13 are used to estimate how the operating state of the rotor influences the slope of the assumed loading law. By adopting the concept of a loading law which is only a function of the rotor's operating state, a single approximate noise prediction methodology is developed which can be used for rotors and propellers.

Physically, it may be argued that the higher harmonic airloads of a rotor in axial flight may be dependent on the proximity of a rotor blade to the tip vortex of the preceding blade and to the strength of this trailed vortex. Thus, it would appear as if the loading laws should be partially based upon the distance "$d_n$" shown in Figure III-4. This distance may be calculated by considering the mass flow rate which is normal to the disc plane. Thus, from simple momentum theory, the inflow normal to the tip-path plane becomes

$$\text{Normal inflow} = V \cos(\alpha_p) + v.$$

The distance "$d_n$" is, therefore, given by

$$d_n = 2\pi(V \cos(\alpha_p) + v)/\Omega B$$

where $B \equiv$ number of blades.

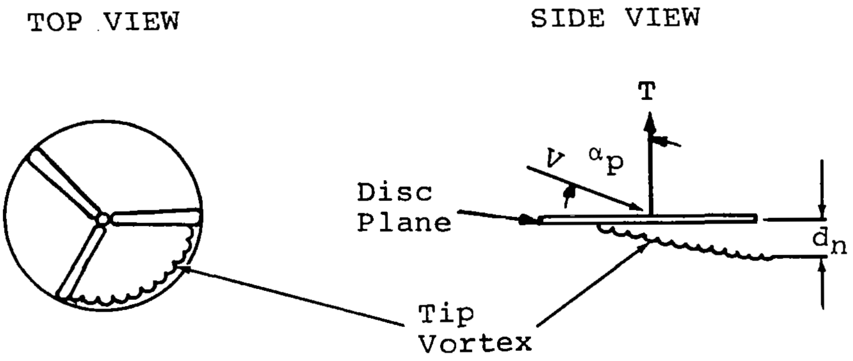

Figure III-4

The major usefulness of the concept of an effective "$d_n$" lies in its ability to approximately relate the influence of the trailing vortices to the higher harmonic loading distribution on the lifting rotors. The local induced velocity caused by a trailing tip vortex on one rotor blade can be approximated as

$$\Delta v_i \sim (1.0/B)(\Delta\Gamma/2\pi d_n) = \Delta\Gamma/2\pi B d_n$$

where $\Delta\Gamma$ is the total vorticity of the tip vortex of one rotor blade.

However, the average vorticity of the lifting rotor is approximately related to the total thrust by the following analytical expression

$$\Gamma \sim 2T/\rho\Omega R^2$$

It is also assumed for convenience that the vorticity of the tip vortex of the preceding blade is proportional to the average vorticity of one blade. Therefore, $\Delta\Gamma$ is proportional to $\Gamma$. Thus, the induced velocity which results from the passage of the preceding blade measured at the rotor plane becomes

$$v_i \sim T/\pi B d_n \; \rho\Omega R^2 .$$

Therefore, the loads which are induced by the trailing vortex system can be grossly approximated by

$$\begin{array}{l}\text{Higher Harmonics Induced} \\ \text{Load on One Blade}\end{array} \sim \int_0^R (1/2)\rho(\Omega r)^2 \; a(v_i/\Omega r)c \; dr.$$

Integrating and dividing by the total thrust, one obtains

$$\Delta I_{\ell}/T \sim (\sigma a/16\pi)(1/\lambda_H) .$$

The influence of the trailing vortex system on the "loading law" of the rotor is hypothesized to be correlated to this simplified calculation of the higher harmonic induced load on one rotor blade. A new parameter ($XP_{\ell\ell}$) which is defined to be the inverse of $\Delta I_{\ell}/T$ is introduced to facilitate this correlation.

Thus, $$XP_{\ell\ell} \equiv \frac{1}{\Delta I_{\ell}/T} = \frac{16\pi\ \lambda_H}{\sigma a} \qquad \text{(III-14)}$$

where $\sigma$ = Blade Area/Disc Area
$\lambda_H = (V \cos(\alpha_P) + v)/\Omega R$
$a$ = lift curve slope of one rotor blade = 5.

Loading data from ref. 13 and from a preliminary analysis of a model rotor operating in a wind tunnel (ref. 16) has been plotted versus the computed parameter $XP_{\ell\ell}$ in Figure III-5. A general trend toward larger values of n does exist for larger values of $XP_{\ell\ell}$. The loading law "n" which is used in this report has been approximated to be a linear function of $XP_{\ell\ell}$ as shown in Figure III-5. It is mathematically expressed by the equation

$$n = 0.0485|XP_{\ell\ell}| + 1.3 . \qquad \text{(III-15)}$$

Although much of the preceding analysis is conjecture at this time, it is interesting to look at some of the physical implications of this proposed loading law. In the helicopter mode, near hover, the loading law exponent has been chosen to be equal to 2. The corresponding value for $XP_{\ell\ell}$ is 14.4. As forward speed is attained, the rotor induced velocity decreases, thereby decreasing the net inflow through the tip path plane. The resulting close proximity of the trailing tip vortices to the rotor tip path plane is accounted for by a decrease in $XP_{\ell\ell}$. Therefore smaller values of "n" result. At higher speeds in the helicopter configuration, the rotor tip path plane tilts forward to balance the increasing drag. The large inflow which results causes large values of $XP_{\ell\ell}$ to be calculated. Larger values of "n" result.

In the propeller configuration ($\alpha_P = 0°$), the thrust ($\lambda_T$) is reduced while the inflow through the disc plane increases, resulting in very large values of $XP_{\ell\ell}$. The large values of

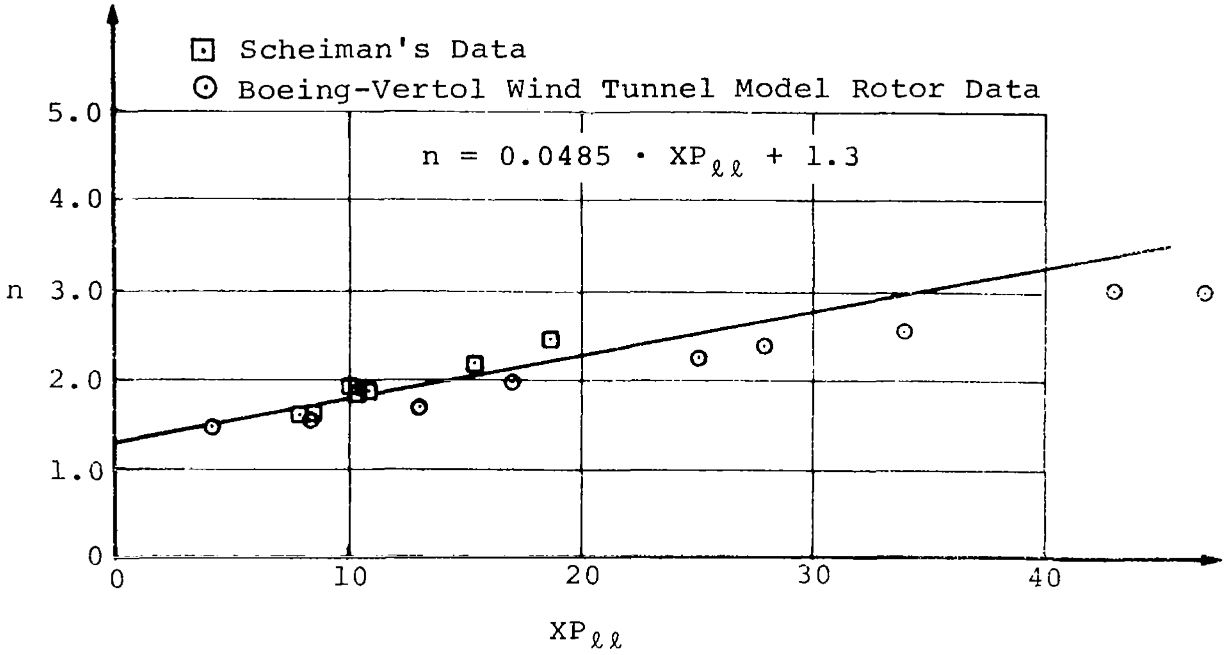

Figure III-5

n which result indicate the relative unimportance of higher harmonic loading for propellers.

With a large value of thrust, a low solidity ratio, or a small inflow velocity, low values of $XP_{\ell\ell}$ result. The corresponding small value of n indicates the importance of higher harmonic blade loading in being able to predict the rotational noise of the rotor.

Vortex noise (broad-band noise). - Examination of rotor and propeller noise spectra reveals that they consist of a number of peaks or line spectra occurring at the fundamental blade passage frequency and its harmonics. In between these is a continuous spectrum characteristic of sources which are random in nature. These are primarily of two types: dipole sources from the random force fluctuations on the rotor blades and quadrupole sources from the turbulent flow within the blade wakes. In the case of rotors and propellers, the random noise produced as dipole sources dominates under the usual operating conditions.

With the tilt-rotor at low thrust, rotational noise becomes comparatively weak and is only slightly higher than vortex noise. Considering that vortex sound is made up of a continuous spectrum, instead of line spectra like the rotational noise, it can be expected that vortex noise is the major contributor to the overall acoustic power levels under these conditions. At normal or high thrust conditions, the overall vortex noise level may be 20 to 30 dB below the overall rotational noise level. However, above 250 Hz, the level of the rotational noise harmonics falls off quite rapidly under normal rotor operating conditions, while the spectrum level of vortex noise is, in most instances, on the upswing toward a maximum level determined by the rotor blade Strouhal frequency.

Since the characteristic vortex noise is easily distinguishable from rotational noise by instrumental and aural analysis, it also lends itself to a separate prediction method which is described below. These methods are included in the analytical model of the tilt-rotor aircraft because of the importance of this sound in determining the aural acceptability or annoyance and aircraft detection.

Generalization of empirical data: Prediction of overall sound pressure level of vortex noise is based on considerable extension of the work of Yudin (ref. 17) with rotating rods. This development led to the relationship where the total acoustic power generated by this mechanism is, among other things, proportional to the rotor blade tip speed raised to the sixth power. The other factors on which this noise level primarily depends are the lift of the rotor and the area of the blades. With suitable empirical constants added to match measured rotor noise data, Schlegel (ref. 18) gives the following expression for the overall vortex noise level at a distance of 500 feet from the rotor and 20 degrees below the rotor disc plane:

$$dB_{500} = 20 \log V_t + 20 \log T - 10 \log S_b - 43dB \qquad \text{(III-16)}$$

where $dB_{500}$ = overall vortex noise in decibels at 500 feet
$V_t$ = rotor blade tip speed in feet per second
$T$ = thrust in pounds
$S_b$ = total blade area in sq. ft.

For the Model 160 tilt-rotor aircraft overall vortex noise level prediction, 5 decibels have been added to compensate for the generally low estimate arrived at by the use of eq. (III-16). Lowson & Ollerhead's rationale (ref. 11) for adding 5 decibels is to compensate for the increased number of blades (5 and 6) used by Schlegel, whereas most rotors have 3 to 4 blades like the Model 160 aircraft. Other data in the process of being reduced under an ARO Research Contract (ref. 19) by Vertol indicate that the addition of 5 dB is, perhaps, still too conservative.

Since vortex noise has been assumed to be primarily of the dipole type, with maxima on the rotor axis above and below the disc plane and a minimum in the disc plane, an expression for this distribution has been described in ref. 12 as follows:

$$D = 10 \log \left( \frac{\cos^2 \phi + 0.1}{\cos^2 70^\circ + 0.1} \right) \quad \text{dB} \qquad \text{(III-17)}$$

where $\phi$ is the angle measured from the rotor shaft axis. The expression yields a zero dB correction for an angle 20 degrees below the rotor disc plane which means that eq. (III-17) is simply added to the results of eq. (III-16) to spatially correct the predicted overall vortex noise level. A difference of approximately 10 dB exists by the use of the directivity formula between the level of the maxima and minimum.

Reference was made several paragraphs ago to the rotor blade Strouhal frequency where the peak of the vortex noise occurs. This frequency is given by the following formula (ref. 12) which relates to the blade speed and radius:

$$f_o = (V_t/KR_0) \qquad \text{Hz} \qquad \text{(III-18)}$$

In eq. (III-18), $V_t$ is the rotor blade tip speed in ft/sec, and $R_0$ is the rotor radius in feet. The constant K is derived from Schlegel's data as 0.035.

In order to predict the general spectrum shape of the continuously varying level of the broad-band vortex noise, Ollerhead & Lowson (ref. 12) assume a basic spectrum shape formula which, when properly modified for the frequency modulation effects of blade rotation and expressed for purposes of one-third octave band noise level prediction, yields the following expression (giving results in dB) to be added to the results of Eq. (III-16):

$$S = 10 \log \left\{ \frac{\ln \left[ \left( \frac{1 + (1 + M_t)^2 (f_2'^2)}{1 + (1 - M_t)^2 (f_2'^2)} \right) \left( \frac{1 + (1 - M_t)^2 (f_1'^2)}{1 + (1 + M_t)^2 (f_1'^2)} \right) \right]}{\ln \left[ \frac{1 + M_t}{1 - M_t} \right]^2} \right\} \qquad \text{(III-19)}$$

In this formula, $M_t$ is the blade tip Mach number and $f_1'$ and $f_2'$ are the Doppler shifted (ref. 20) lower and upper one-third octave band frequency limits respectively, divided by the vortex noise center frequency $f_o$ given by eq. (III-18). Expressed in mathematical notation:

$$f_1' = f_L'/f_o \text{ and } f_2' = f_H'/f_o.$$

The effect of the Doppler shift comes in two parts: first, a term to correct the overall vortex sound pressure level (eq. (III-16)) for the effective change in measured bandwidth, expressed in dB, by;

$$B = 10 \log \frac{\text{Bandwidth corrected for Doppler Shift}}{\text{Original Bandwidth}} \qquad \text{(III-20)}$$

Here, the "Original Bandwidth" term in the denominator corresponds to the difference in Hertz between the upper ($f_H$) and the lower ($f_L$) one-third octave filter cut-off frequencies and is equal to 23 percent of the center frequency of any one particular filter. The energy originally in this bandwidth is now assigned to a new bandwidth corresponding to 23 percent of the new or Doppler shifted center frequency. This new bandwidth corresponds to the numerator in eq. (III-20). The relationships between the cutoff frequencies and the one-third octave center frequency are as follows:

$$f_C = (f_L \; f_H)^{1/2} \; ; \qquad f_H = 2^{1/3}(f_L);$$

and $f_L = (f_C/2^{1/6})$ .

The second effect due to Doppler shift is from the effective shift in frequencies which occurs when the sound source approaches or recedes from the observer. This has the analytical effect of dividing the three expressions, immediately given above for the filter frequencies, by the term

$(1 - M \cos \theta)$. Here, M is the flight Mach number of the aircraft and $\theta$ is the angle between the flight path and a line connecting the sound source with the observer.

It is the thus modified, or Doppler shifted, filter frequency limits $f'_H$ and $f'_L$ denoted by the primed (′) symbols and the normalized filter frequency limits $f'_1$ and $f'_2$ in eq. (III-19) which are used to calculate the one-third octave band vortex noise spectral distribution.

Eq. (III-19) has been evaluated for three different rotor tip speeds of the CH-3C helicopter rotor and the octave band results are shown in Figure III-6. The broadening of the predicted spectrum toward the higher frequencies as blade tip speed increases is readily apparent. However, it should be pointed out that as blade tip Mach numbers of 0.8-0.9 are approached, vortex noise is no longer a primary contributor to the far-field noise produced by the helicopter.

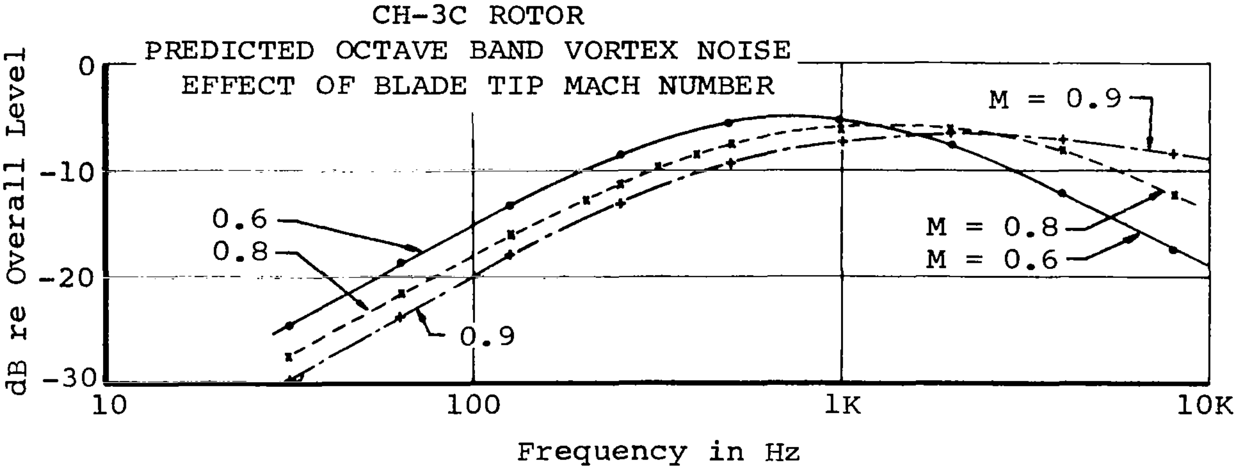

Figure III-6

Several of the foregoing expressions require a modification for specific application to the Model 160 tilt-rotor aircraft. This is due to the changes in rotor disc plane attitude which occur as the aircraft converts from the helicopter rotor mode to airplane propeller mode at takeoff, and vice-versa during landing. It is assumed that the local flow over the blade is responsible for the magnitude of the resultant noise and can be thought of as consisting of two components: one aligned with the tip velocity vector $V_t$ and another parallel to the aircraft velocity vector V. If $\alpha_p$ is the angle between the rotor shaft axis and the direction of the aircraft velocity vector V, the effective advancing rotor tip speed can be expressed by:

$$V_E = \left[\left(V + V_t \sin(\alpha_p)\right)^2 + \left(V_t \cos(\alpha_p)\right)^2\right]^{1/2} \quad \text{ft/sec} \qquad \text{(III-21)}$$

Eq. (III-21) is substituted for the symbol $V_t$ occurring in Eqs. (III-16), (III-18), and in the calculation of $M_t$ in Eq. (III-19) for the prediction of the tilt-rotor vortex noise.

Other noise sources. - In addition to the rotor rotational and vortex noise sources, other sources that arise are of a mechanical or aerodynamic nature. Under the first, the mechanical noise sources, fall the noises emitted by the rotor transmissions and gearboxes. In addition, any structure such as an aircraft fuselage panel attached to the reciprocating or rotary parts is subject to vibration and the result is further air excitation, as noise, by these vibrating parts. These mechanical noise sources receive considerable attention from the acoustical engineer in the final aircraft design stages to provide a useful aircraft interior acoustical crew environment. They are not, however, of any consequence in the acoustic far-field from the annoyance or detection viewpoint. In certain rare cases, it may be that such sources necessitate treatment because the acoustic near-field of the aircraft is part of the ground or service crew environment.

Other aerodynamic noise sources from the aircraft consist of boundary layer noise and powerplant noise. Boundary layer noise is, again, almost exclusively a problem from the viewpoint of the acoustical interior of the aircraft fuselage. It most certainly does not propagate beyond the aircraft acoustic near-field due to its relatively low energy and high frequency distribution. On the other hand, turboshaft powerplant noise could be a problem in the far-field, but is generally not, because of the following: exhaust noise caused by the small engine exhaust velocity is negligible because most of the gas energy has already been expended in the conversion from thermodynamic and kinetic to mechanical energy, so that what is available to produce noise is over-shadowed by the dominant rotor vortex turbulent noise in the far field. Inlet noise, because of its pure tone content, appears on the surface, to be a dominant noise source, but is subject to several mitigating influences. One is that high frequency noise attenuates rapidly with distance. Also, the state of the art in engine inlet noise control has advanced considerably within the past five years to a point where from 15 to 20 decibels of noise reduction have been proven feasible on model and full-scale powerplants. In addition, the tilt-rotor aircraft's commercial application is such that during the noise sensitive approach to landing and takeoff, the axially and forward oriented engine inlet noise is directed up and away from the ground. These factors primarily account for the relative unimportance of powerplant noise in the far-field and is the reason it has not been included in the Model 160 tilt-rotor acoustic model.

## Propagation of Sound

Fortunately for the aircraft designer and builder, operator and user, the sound generated by the aircraft is rapidly reduced in several ways: by spatial and atmospheric effects, and absorption due to vegetation. Spatial effects are those of directivity, already discussed, and straightforward distance between source and observer. Atmospheric effects include such things as changes in the speed of sound due to temperature, humidity, and wind. Sound propagation is also affected by the geometry of the surrounding terrain: hills may provide a sound shadow or reflect sound, perhaps even focus it; built-up areas in cities may redirect the sound many times, giving it a reverberant quality which can hide the original subjective character of the sound. These latter effects are extremely hard to quantify, and lend themselves only occasionally to ray-tracing solutions. They have not been included in this tilt-rotor analytical model. The following effects, however, are included:

Spatial effects (distance). - In the far field, the sound of the tilt-rotor aircraft is assumed to decay uniformly, at all frequencies and in all directions, at the rate of 6 dB per doubling of distance, due to spherical spreading:

$$\Delta dB_1 = -20 \log (D/D_r) \qquad \text{(III-22)}$$

where D = distance (feet) at which the predicted noise is sought; and Dr = reference distance (feet) at which a noise formula gives a certain noise level.

Atmospheric effects. - In addition to the spatial effect shown above, a frequency-dependent attenuation of sound takes place during sound propagation: the higher the frequency, the more relative attenuation takes place. Analytically, this is expressed as follows (ref. 21):

$$\Delta dB_2 = -(1.55 \times 10^{-6})(D - D_r)\ f \qquad \text{(III-23)}$$

Here, D and $D_r$ are as defined for Eq. (III-22); f is the sound frequency in Hz; and the numerical factor is derived from experimental observations - being $(1.55 \times 10^{-6})$ for sea-level, standard day conditions (for other conditions, see ref. 21).

Eqs. (III-22) and (III-23) are used to modify the results of the noise prediction formulae to derive the noise level spectrum at any distance. At present, the analytical model is limited to those two effects, although the effects of excess ground attenuation due to vegetation or other ground covers could be incorporated in a future refinement of the overall model for purposes of evaluating detection times or distances, for example (refs. 22 and 23).

## Subjective Measures of Noise

A subjective measure of the noise produced by the Model 160 tilt-rotor has been incorporated in the analytical program so that the benefits or lack thereof, of particular noise-sensitive flight profiles may be evaluated. The subjective measure chosen to describe the acoustic properties of the aircraft is Perceived Noise Level (ref. 24). It incorporates the effects of noise amplitude and frequency, an observer's non-linear hearing response, and the concept of an annoyance criteria in a single number rating scheme as determined by

$$PNL = 40 + 33.3 \log\{[N_{max} + 0.15(\Sigma N - N_{max})]\} \qquad \text{(III-24)}$$

where PNL = Perceived Noise Level in PNdB
$N_{max}$ = Number of noys in the noisiest 1/3-octave band
$\Sigma N$ = Sum of the noy values in all bands.

The constants in Eq. (III-24) as well as the noy values for each third-octave band at any given sound pressure level have been determined experimentally in subjective response experiments and related to objective acoustic measures. In order to calculate the Perceived Noise Level, it is usually necessary to look up many of the approximately 2500 different noy values for any given combination of level and frequency in a table. In the interest of efficient computer storage usage, however, a mathematical approximation of the noy table has been adopted in this tilt-rotor noise evaluation program according to the procedures in ref. 25. This consists of a series of straight lines relating the sound pressure level and the noy values of a 1/3-octave bandwidth. Use of the slopes of these lines and their intercept values greatly simplifies the computational process and introduces an uncertainty of ±0.5 PNdB.

The lowest one-third octave ($f_C$ = 50 Hz) for which experimentally derived noy values are available falls considerably above the frequencies at which the maximum aircraft rotational noise levels occur. An extrapolation has, therefore, been performed of the slopes and intercept values of the three next lower, 1/3 octaves (40 Hz, 31.5 Hz and 25 Hz) to give the perceived noise calculation more relevancy in the tilt-rotor noise evaluation.

It is recognized that in addition to the factors incorporated in a noise evaluation by the perceived noise level technique, that additional factors such as duration, frequency of occurance of the noise, background noise, and the presence of pure tones are necessary to more completely describe the total annoyance value of a sound. Of these, the effects of sound duration are of particular interest in the tilt-rotor aircraft case which, as any V/STOL aircraft, may alter its flight trajectory with considerably more freedom than fixed-wing aircraft. These changes in V/STOL flight profiles can account for large differences in the lengths of time during which the aircraft noise is causing an annoyance on the ground. Effective Perceived Noise Level, in EPNdB, is used to penalize for excessively long loitering near the ground, or vice versa, give credit to a fast get-away. Hence, the following noise level duration correction is added to the perceived noise level

$$\Delta \mathrm{PNdB} = 10 \log(t/15). \qquad \text{(III-25)}$$

In this equation, t is the length of time in seconds during which the perceived noise level at the observer remains within 10 PNdB of its maximum value. The constants 10 and 15 in Eq. (III-25) are based on both subjective experiments and experience with fixed-wing aircraft annoyance. The adequacy of the known effects of duration on annoyance was the subject of a NASA-sponsored psychoacoustic study at The Boeing Company Vertol Division. This study was completed in May 1971 (ref 26).

## IV. OPTIMIZATION TECHNIQUES

The field of optimization has grown significantly during the last 10 years. Although the basic mathematical theory has not changed, several numerical optimization algorithms have been developed which can be quite useful to the engineer. A cursory review of some of these algorithms is presented in this section of the report.

It should be emphasized that optimization is beneficial, in an engineering sense, when it contributes to the solution of a well-posed problem. It is a tool, like calculus, to be used to better understand and model a physical process. In this report, optimization techniques are used to locate (within engineering accuracy) and to explore the optimum performance of the tilt-rotor aircraft. Time and fuel to takeoff and land are the parameters of interest.

## Classification of Methods

There are two classes of optimization problems that consistently appear in aircraft design and performance evaluation.

The simplest class represents those cases where the quantity to be optimized can be expressed directly as a number of independent variables:

$$J = J(v_1, \ldots, v_m)$$

The quantity J is called the payoff function while its arguments are usually called parameters or controls.

An additional set of algebraic equations and corresponding variables often exists which mathematically describes the performance of the vehicle:

$$\begin{array}{ll} f_1(x, \ldots, x_n, \; v, \ldots, v_m) = 0 & \\ f_2( \qquad\qquad , \qquad\qquad\qquad ) = 0 & \\ \cdot & \qquad (IV-1) \\ \cdot \qquad\qquad\qquad\qquad\qquad\qquad\qquad \cdot & \\ f_n( \qquad\qquad\qquad\qquad\qquad ) = 0 & \end{array}$$

This set of equations in (n + m) unknowns comprises the mathematical model to be optimized. The new variables ($x_1$, $x_2$, $x_n$) are implicit problem variables which are completely determined by Eq. (IV-1).

In most practical cases, some limitations (constraints) are also imposed on the parameters or other problem variables. As each additional constraint is enforced, the number of independent parameters (m) is correspondingly reduced.

The task of optimization can now be defined as that of selecting the $v_i$ values (subject to possible constraints) in such a way that J takes on its maximum or minimum value. The name "parameter optimization" is associated with this class of problems.

The second class of optimization problems which occurs frequently is usually described by a system of ordinary differential equations:

$$
\begin{aligned}
dx_1/dt &= f_1(x\ , \ldots, x_n, v_1, \ldots, v_m) \\
&\vdots \\
dx_n/dt &= f_n(x_1, \ldots, x_n, v_1, \ldots, v_m)
\end{aligned}
$$

The variables $(x_1, \ldots, x_n)$ are called state variables because they describe the time history of the state of the process. The time history of the control parameters $(v_1, \ldots, v_m)$, simply called controls, directly influence the course of the process. The payoff function

$$J = \int_{t_i}^{t_f} f_0(x_1, \ldots, x_n, v_1, \ldots, v_m)dt$$

measures the desired performance of the system. Because the state of the system is described by a set of differential equations, initial and final conditions can also be specified. The object of the optimization procedure is to find the control time histories which maximize or minimize the chosen performance index. Because differential equations describe the vehicle performance, the numerical procedures used to find optimal solutions are called "dynamic optimization techniques."

This latter class of problems is considerably more difficult to optimize. The necessary conditions for extremals of this system of differential equations are also of a differential nature. In fact, in the most general case, application of optimization theory yields a system of second-order differential equations along with m auxiliary equations which must be solved simultaneously. At both initial and terminal times, n boundary conditions must be satisfied. The resulting two-point boundary value problem has received much attention in recent years. Probably its most noteworthy feature is the degree to which a solution of this boundary value problem is a function of the process being optimized. Optimal space-flight trajectories, optimal blade design, and optimal atmospheric trajectories of an aircraft all may require different optimization algorithms for an efficient solution. These algorithms are not trivially different--some work and some just will not work on a particular problem.

On the other hand, parameter optimization problems are relatively straightforward. Many basic algorithms exist which can be set up easily on a digital computer. Some techniques are more suited to particular classes of problems than others. However, because each parameter optimization technique is relatively easy to perform, rapid evaluations of many parameter variations are possible.

In this report, use is made of a parameter optimization program called AESOP (Automated Engineering Scientific Optimization Program). Although the governing equations are differential, the control time history has been parameterized. Before discussing how this was accomplished, a brief description of AESOP is in order.

## AESOP (Automated Engineering Scientific Optimization Program)

AESOP was developed by The Boeing Company under a NASA-sponsored contract (ref. 27). One of the primary purposes of AESOP is to give the uninitiated engineer easy access to a variety of optimization techniques. Only a minimal amount of computer programming is required. A total of nine different parametric optimization algorithms are included in the AESOP package (Figure IV-1). A complete description of each parametric search technique is given in refs. 27 and 28.

The algebraic equations making up the mathematical model whose payoff function is being optimized are solved as an entity without being an integral part of AESOP's processes. AESOP changes the control parameters in a manner dictated by the particular search technique used. Then, from resulting changes in the performance of the model, AESOP determines the combination of control parameters that result in optimum performance. A schematic diagram of the system described above is shown in Figure IV-2.

Constraints can be applied to the optimization by two techniques: one method is to incorporate the constraints as part of the model, and the other is to enforce the constraints using AESOP's penalty function approach (described in ref. 27). Any combination of AESOP's nine search procedures may be called upon to locate the extremum of the chosen problem. Access to a variety of parametric optimization searches, the ability to easily change from one combination of searches to another, and the availability of the AESOP program are the reasons for AESOP being applied to the tilt-rotor trajectory problem.

It was previously shown in Section II that the evaluation of tilt-rotor performance is, by itself, a rather difficult

## BASIC SEARCH ALGORITHMS CONTAINED IN PROGRAM AESOP

1. Sectioning - Succession of one-dimensional optimization calculations parallel to coordinate axes. Variables may be perturbed in random or natural order.
2. Pattern - A Ray Search in the gross direction defined by a previous search or search combination.
3. Magnification - Straightforward magnification or diminution about the origin.
4. Steepest Descent - Search along the weighted gradient-direction. Several weighting options available.
5. Adaptive Creeping - Search in small incremental steps parallel to the coordinate axes. Step-size adjusted automatically in the algorithm. Variables may be perturbed in random or natural order.
6. Quadratic - Second-order multivariable curve fit to the function being optimized, followed by search in direction of second-order surface optimum.
7. Davidon's Method - An attempt to achieve the advantages of second-order search from an ordered succession of first-order (steepest-descent) searches.
8. Random Point - Function to be optimized is evaluated at a set of uniformly distributed random points in a specified region.
9. Random Ray Search - Function is optimized by search along a sequence of random rays having a uniformly distributed angular orientation in the multivariable parameter space.

Figure IV-1

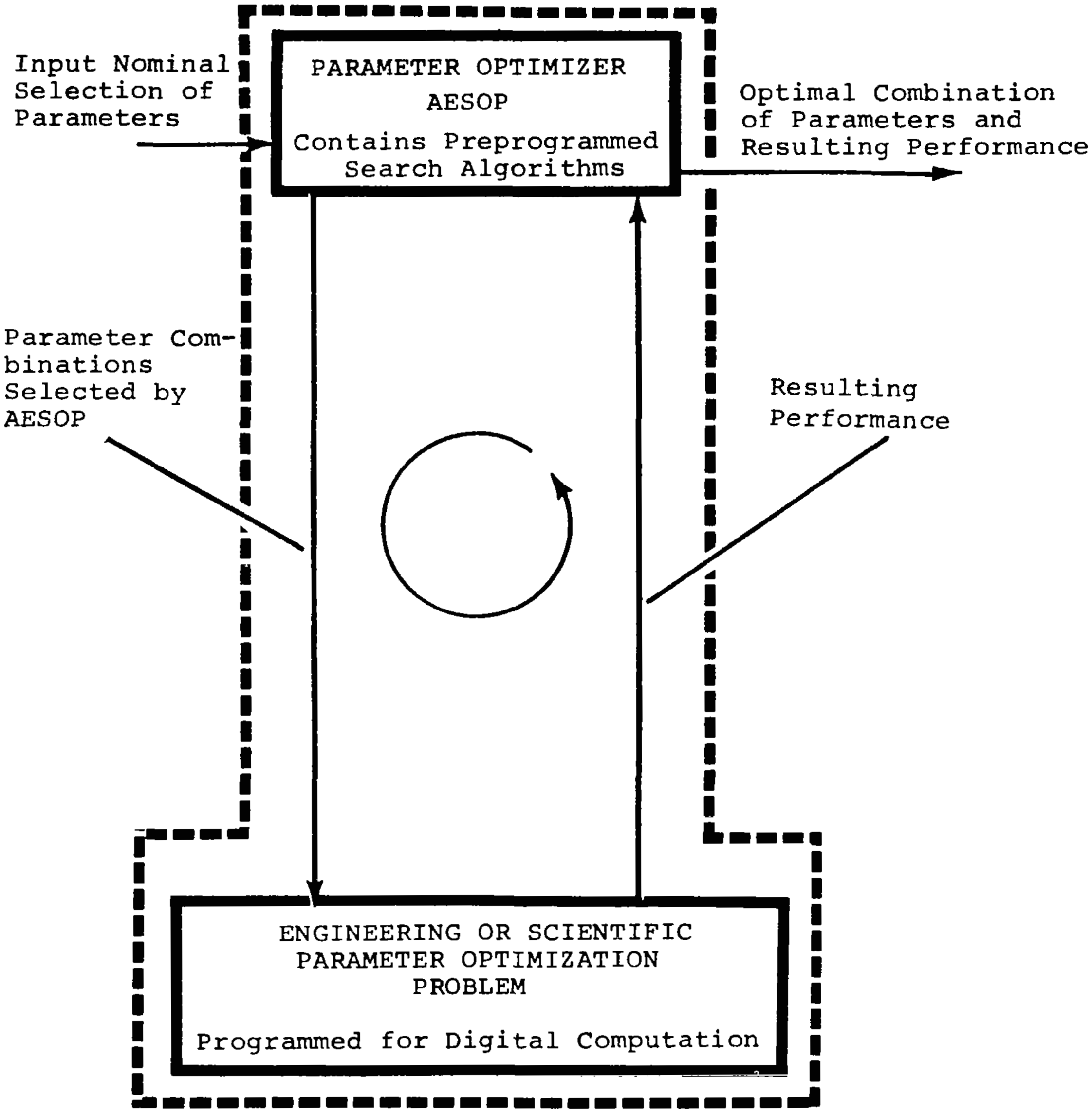
Input Nominal Selection of Parameters
PARAMETER OPTIMIZER
AESOP
Contains Preprogrammed Search Algorithms
Optimal Combination of Parameters and Resulting Performance
Parameter Combinations Selected by AESOP
Resulting Performance
ENGINEERING OR SCIENTIFIC PARAMETER OPTIMIZATION PROBLEM
Programmed for Digital Computation

SCHEMATIC OF PARAMETER OPTIMIZATION PROBLEM

Figure IV- 2

task. Iteration techniques are required which may, or may not, converge depending upon the chosen flight condition.

Using parametric techniques to optimize tilt-rotor performance results in the evaluation of model performance and the determination of the optimum performance or payoff being treated as two separate problems. This enables the physical implications of each improvement in the optimization process to be more visible to the engineer.

## Parametric Functional Expansion

The tilt-rotor kinematic performance model is composed of algebraic equations which describe the point performance of the aircraft and differential equations which relate the wind axis system of the aircraft to a fixed ground-based axis system. The problem of locating the minimum time and fuel trajectories is, by definition, a "dynamic optimization" problem. However, by a judicious choice of the form of the independent control time histories, the problem may be solved by parameter optimization techniques.

The mathematical model which was developed in Section II describes tilt-rotor performance if two independent control time histories are assumed. The applied power fraction $\eta_c(t)$ and the nondimensional horizontal velocity $\bar{u}(t)$ are the chosen controls. To parameterize the problem, the control time histories are expanded in an orthogonal series. The following Fourier series were chosen for convenience.

$$\eta_c(t) = \eta_0 + \eta_1 \sin(2\pi\, \omega_\eta t + \zeta_\eta) + \ldots + \eta_s \sin(s2\pi\, \omega_\eta t + \zeta_\eta) \tag{IV-2}$$

$$\bar{u}(t) = \bar{u}_0 + \bar{u}_1 \sin(2\pi\, \omega_u t + \zeta_u) + \ldots + \bar{u}_p \sin(p2\pi\, \omega_u t + \zeta_u) \tag{IV-3}$$

The coefficients of this functional expansion are the parameters of the optimization problem. The resulting 6 + s + p parameters are chosen to optimize tilt-rotor performance and, at the same time, satisfy necessary equality and inequality constraints. The number of terms needed in each control expansion is entirely problem dependent. When additional parameters do little to improve system performance, the corresponding terms can be omitted from the series.

In any realistic performance problem, constraints upon allowable parameter variations exist. These constraints can be enforced in two alternate ways: the control time history may be prohibited from entering restricted regions or a penalty may be attached to the performance index for a violation of these restrictions. In this analysis, parameter variations which violated the stated restrictions were not allowed. Limits were placed on the vertical and horizontal accelerations and applied power. If the control at a particular instant in time exceeded the constraint, the value of the constraint function was used as the control input. The allowable control space was, therefore, bounded by the inequality constraints of the control variables.

The initial boundary conditions on the vertical and horizontal velocities of the takeoff problem and the terminal conditions on the velocities of the landing case* were specified by adjusting the parameters $\eta_0$ and $\bar{u}_0$.

These parameters were no longer available for optimization. AESOP was applied to the resulting 4 + s + p parameter optimization problem. In the landing problem, additional boundary conditions which specify the initial velocities were enforced by using standardized penalty function techniques (ref. 27).

There is very little theoretical justification for the apparent success of the functional expansion approach. It is, mathematically speaking, not at all rigorous. However, there have been examples where this same type of approach has achieved some degree of success (refs. 28 and 29). It is usually possible for the engineer working the problem to choose, from his experience, the form of the orthogonal expansion which most easily optimizes the problem. Therefore, the parametric optimization problem includes a certain degree of engineering judgment. The optimization methods are then used to refine the engineering guess at the optimum solution.

## V. RESULTS AND DISCUSSION

### General Results

Before a detailed analysis of each tilt-rotor trajectory which has been explored is presented, it is instructive to review some of the more general results of this investigation.

---

*Time was run backwards; thus allowing the terminal conditions or velocity to become initial conditions of this new problem.

Several different possible takeoff and landing trajectories are compared and evaluated in terms of the time of flight, the fuel consumed, and the noise heard at specific locations on the ground plane. The degree of success in applying parameterized optimal control techniques to this class of problems is also discussed.

Takeoff and Climb. - For convenience, the optimization problem of determining how to climb to cruise altitude (10 000 feet) to minimize time, fuel, or noise exposure has been divided into two distinct flight segments. The first segment is arbitrarily chosen to begin at sea level with the aircraft in the helicoper configuration and terminates when the tilt-rotor attains an altitude of 3000 feet. The second flight path segment begins at 3000 feet with initial conditions which are the terminal conditions of the first segment. Steady cruising flight at 10 000 feet are the terminal conditions of the second segment.

In the first takeoff segment, optimization theory is a useful tool which was used in the exploration of minimum time and fuel trajectories. By the time the 3000-foot altitude is attained, maximum steady-state tilt-rotor performance is realized. Therefore, the second segment of the optimized trajectory is flown at those conditions which optimize conventional steady-state tilt-rotor performance. It can be shown that minimum time and fuel trajectories are achieved when the tilt rotor climbs in the aircraft mode at the best rate of climb speed with maximum available power. Although these conditions do vary slightly with altitude, the results are generally known and are not in themselves a significant research topic. Furthermore, the noise produced by a tilt-rotor aircraft flying in the airplane mode above 3000 feet is not of primary concern in commercial applications. For these reasons, this report has concentrated on determining optimum takeoff performance for the first flight path segment only.

The time, fuel consumed, and effective perceived noise level of four distinct trajectories which begin at sea level and terminate at an altitude of 3000 feet are listed in Table V-1.

The trajectory which minimizes the time to climb to 3000 feet is performed in the following manner: the tilt-rotor accelerates at the maximum vertical and horizontal acceleration limits in the helicopter configuration until the maximum rate of climb limit is attained. At this point, the rate of climb is held at its maximum value as maximum horizontal acceleration is also maintained. As forward speed increases, the tilt-rotor makes the conversion to the airplane mode of

|  |  |  | EFFECTIVE PERCEIVED NOISE LEVEL - EPNdB |  |  |
|---|---|---|---|---|---|
|  | TIME SECS | FUEL LBS. | DISTANCE FROM TAKEOFF |  |  |
|  |  |  | 400 Ft | 1600 Ft | 6400 Ft |
| (Max R/C Power Used/ Max Power Avail) = 1. | 54.2 | 75.4 | 112.6 | 101.2 | 76.4 |
| (" " " ") = 0.8 | 71.7 | 84.0 | 113.5 | 103.2 | 78.8 |
| Vertical Climb* | 62.8 | 87.2 | 106.1 | 91.8 | 69.2 |
| Vertical Climb & Horiz. Flight* | 106.0 | 143.9 | 106.1 | 92.8 | 77.2 |

*Suggested Noise Abatement Profiles

Table V-1

flight. The aircraft continues to accelerate horizontally until the maximum rate of climb speed is attained. The tilt-rotor continues to fly at the best rate of climb speed until 3000 feet altitude.

In Appendix D, minimum time and fuel trajectories were proven to be synonymous. Nevertheless, a second trajectory is considered which is further constrained to 80 percent of the maximum power available. The resulting minimum time of flight path has a similar character but results in increased time, fuel expended, and noise exposure.

The last two trajectories listed in Table V-1 are proposed "noise abatement" profiles. No one measure of total noise exposure was felt to be sufficiently well defined to be minimized. Instead, two trajectories which have been suggested by many researchers to reduce the ground area exposed to excessive noise were flown. A simple vertical climb at the tilt-rotor's performance limits in the helicopter mode is the first of these trajectories. The helicopter configuration is maintained throughout the maneuver. An initial maximum vertical acceleration is followed by steady vertical acceleration at full power available to 3000 feet altitude. The resulting time, fuel and effective perceived noise level are given in Table V-1.

The second proposed "noise abatement" profile which is considered in this study is very similar in concept to the first. A vertical takeoff is commenced at the tilt-rotor's maximum vertical acceleration limit. Maximum rate of climb is then maintained in the helicopter configuration. At an altitude of 2750 feet, maximum horizontal acceleration is begun. As forward velocity increases, the applied power is reduced to maintain level flight at 3000 feet. The tilt-rotor also commences transition and finally attains the horizontal velocity where the best rate of climb occurs. This horizontal velocity is maintained until the horizontal distance of the minimum time climb trajectory is achieved. The terminal conditions of this trajectory are identical to the terminal conditions of the minimum time (fuel) trajectory. This fact allows meaningful comparisons between the two trajectories to be made.

Some very general conclusions can be drawn from Table V-1 for tilt-rotor aircraft operating procedures. The total fuel consumed in all of the maneuvers is relatively small because of the low disc loading rotors and is probably not a primary operational consideration. However, the time to attain 3000 feet does vary significantly according to pilot technique. Because this time can be thought of as "exposure time" in a military sense, it is desirable to have it minimized.

Commercially, the quietest flight path is seen to be the pure vertical climb. The second noise abatement profile which can be directly compared with the maximum performance trajectory also shows significant (up to 7 EPNdB) noise reductions at the ground positions close to the takeoff point. However, the time and fuel expended to achieve these end conditions is almost doubled.

Because the actual quantity of fuel is small, this is probably a secondary performance consideration. Notice also that applying less than full power actually increases the EPNL at two measuring locations for an aircraft of a given gross weight. The inference is that more installed power will increase performance and reduce the measured ground noise.

Descent and Landing. - In Appendix D, a discussion of the relation between minimum time and minimum fuel landing trajectories was presented. It was indicated that they are synonymous if the initial conditions of velocity and altitude are specified but the initial horizontal distance is left unspecified. The remainder of this chapter only considers solutions to this somewhat restricted problem formulation.

One additional comment, concerning those optimal problem formulations which arise when the initial velocity, altitude, and horizontal distance are all specified, is in order. In this case, the trajectory which minimizes time may not be identical to the trajectory which minimized fuel. Furthermore, it can be shown that because of the additional initial condition on horizontal distance, the resultant fuel consumed and time expended always equals or exceeds the case with the unspecified initial horizontal distance. Although this further constrained optimization problem is interesting, the added complexity of introducing a new independent parameter is beyond the scope of this present effort.

The trajectory which minimizes time and fuel in descent and landing can be qualitatively described as the trajectory which maximizes the aircraft's rate of sink for the longest period of time. The resulting optimal trajectory consists of the following operational segments: descent is begun in the airplane configuration at 10 000 feet in a high-speed dive at the aircraft's structural limit. The applied power is maintained at the minimum level necessary to control the aircraft throughout the entire descent in equilibrium flight. The rate of descent in this configuration is initially about 80 feet per second and decreases slightly with altitude. At about an altitude of 2000 feet, the tilt-rotor is decelerated horizontally at its maximum rate. As the vehicle's horizontal velocity decreases, the tilt-rotor makes the transition from the airplane to the helicopter mode of flight. Just before touchdown, the vertical sinking rate is decreased by applying power. Touchdown occurs at a rate of sink of 8 fps at zero forward velocity.

If, in addition to the initial altitude, the initial horizontal and vertical velocities are specified, the optimal trajectory only appears to change. The tilt-rotor then quickly attains those conditions which maximize the integral of the aircraft's rate of sink with respect to time. For all initial velocities in the airplane mode of flight at the 10 000-foot altitude level, the previously described maximum rate of sink trajectory is closely approximated. However, at small initial altitudes (i.e., less than 5000 feet) it may not be the most efficient procedure to accelerate to the horizontal velocity where the vehicle's maximum sink rate is attainable and then have to decelerate again to slower horizontal speeds. Too much time is spent in the connecting regions where only relatively small steady state sink rates are possible. A more efficient control policy would maintain steady flight in the high-speed helicopter configuration where fairly high sink rates can be maintained for long periods of time. A qualitative discussion of these tradeoffs is presented in Appendix D.

In most practical cases of interest, high-speed dives near the ground at the aircraft's structural limit are to be avoided. Flying this type of optimal trajectory requires a great deal of pilot skill and judgment. Small errors in the estimation of tilt-rotor performance boundaries at high speed would be fatal. Therefore, the additional constraint that the tilt-rotor's total velocity not be excessive upon nearing the ground is enforced. This constraint prohibits high-speed diving flight in the airplane configuration below the 3000-foot altitude. Although the time and fuel required to land are higher, the proposed constrained optimal trajectory is operationally more realistic.

This modified optimization problem may be conveniently broken into two distinct operational segments. The first segment begins at 10 000 feet and is arbitrarily chosen to end at an altitude of 3000 feet. An additional constraint upon the total velocity of the aircraft at the terminal conditions of this first segment is also enforced. The tilt-rotor's terminal horizontal velocity is chosen to be equal to the velocity where the best rate of sink in the helicopter configuration occurs. The trajectory which optimizes this first segment is one which begins in a high-speed steady-state descent at the tilt-rotor's design limit. After maintaining this maximum descent rate as long as possible, the aircraft is decelerated at its limit and converts to the helicopter configuration to meet the specified condition on horizontal velocity at an altitude of 3000 feet.

The second flight path segment begins at 3000 feet in the helicopter configuration. The resulting maximum rate of sink is maintained as long as possible. However, to meet the terminal conditions of zero horizontal velocity and an 8 fps rate of sink at sea level, maximum horizontal and vertical decelerations are necessary at the end of the maneuver.

The time and fuel consumed for both the optimal and restricted optimal problem formulations are given in Table V-2. Relatively small increases in time and fuel required to descend from 10 000 feet are registered if the restricted optimal flight path is followed. This results because the large equivalent flat plate area of the helicopter configuration causes sink rates which are almost as large as diving airplane flight.

Similar to takeoff, noise is only a problem to the landing area during the last 3000 feet of vertical descent. Above that altitude, the additional effective perceived noise level generated amounts to about one additional EPNdB. For this reason, the tradeoffs in noise and performance during descent and landing have only been evaluated during this last (second) segment of flight. Table V-3 compares five possible flight profiles and their resulting noise.

| | TIME | FUEL |
|---|---|---|
| OPTIMAL | 161.8 sec. | 54.2 lbs. |
| RESTRICTED OPTIMAL | 168.4 sec. | 58.7 lbs. |

TABLE V-2

| | TIME SEC. | FUEL LBS. | EFFECTIVE PERCEIVED NOISE LEVEL - EPNdB | | |
|---|---|---|---|---|---|
| | | | DISTANCE FROM LANDING | | |
| | | | 400 Ft | 1600 Ft | 6400 Ft |
| High-Speed Dive | 74.0 | 21.5 | 117.4 | 108.4 | 75.4 |
| High-Speed Helicopter Descent | 64.4 | 26.0 | 116.0 | 107.5 | 77.2 |
| Pure Vertical Descent* | 52.9 | 36.3 | 107.0 | 93.3 | 78.0 |
| Level Flight followed by Pure Vertical Descent* | 99.0 | 60.0 | 107.1 | 94.4 | 79.2 |
| A Nonoptimum Noise Performance Descent Path* | 67.7 | 27.1 | 109.7 | 103.6 | 80.2 |
| *Suggested Noise Abatement Profiles | | | | | |

TABLE V-3

A comparison of the nature and resulting performance of the optimal (high-speed dive) and restricted optimal (high-speed helicopter descent) from an altitude of 10 000 feet has been presented. Table V-3 compares the noise and performance variables of these same two trajectories from an altitude of 3000 feet. It can be seen from this table that descents from this specified altitude can be made more quickly in the helicopter configuration. Less time is spent in regions connecting high rate of sink conditions resulting in an overall improvement of descent performance.

The fuel consumed during the restricted optimal descent (high-speed helicopter descent) is greater than the fuel consumed in the high-speed diving trajectory. This is a result of the larger power required during high-speed helicopter descent. In descent, the Model 160's fuel consumption is more sensitive to power required than tc elapsed time.

The noise produced by flying either of these two trajectories is almost indistinguishable. Some slight reductions of EPNdB are noted by flying a helicopter descent at the 400 and 1600-foot ground locations because of the vehicle's higher position above the ground. However, at the 6400-foot ground location, a high-speed descent in the aircraft mode is quieter because of the smaller required thrust levels and favorable directivity effects.

Three trajectories which help reduce the noise level which is measured on the ground are also listed in Table V-3. Maximum vertical rates of sink in the helicopter configuration at zero forward velocity is the first noise abatement profile considered. Increases in power above that required to control the aircraft are necessary near the terminal time to sustain the maximum vertical deceleration necessary to meet the condition on the tilt-rotor's terminal rate of sink. Significant reductions in EPNdB are realized at all three noise measuring locations.

A comparison between the performance of the "pure vertical descent" trajectory from 3000 feet and the maximum performance trajectories from that same altitude is not really fair. Significant time must be spend converting to the helicopter configuration at zero horizontal velocity before the 3000-foot altitude level is achieved. The associated lower sink rates in the connecting regions at these higher altitudes increase the time to descend and the fuel consumed during the descent trajectory. Nevertheless, performance and acoustical characteristics of this pure vertical descent segment are interesting by themselves.

The second noise abatement profile which is listed in Table V-3 can be directly compared with the high-speed helicopter descent case. The initial altitude and horizontal distances are identical. The initial horizontal velocity is chosen to be equal to the velocity corresponding to the best lift-to-drag ratio of the tilt-rotor in the airplane mode of flight. This clean configuration is significantly quieter in steady level flight than other possible operational configurations. Steady-state horizontal flight is then maintained at the 3000-foot altitude level. Some time later the aircraft is decelerated horizontally at its maximum rate. As the horizontal velocity decreases, conversion from the airplane to helicopter mode of flight occurs. Near zero horizontal velocity, maximum negative vertical acceleration is initiated until the vehicle's maximum rate of sink is achieved. The remainder of the trajectory is identical to the pure vertical descent case previously considered.

The time of flight and fuel consumed have increased significantly over the optimum "high-speed helicopter descent" case. The increase in time is detrimental for military applications. Increased descent and landing times may increase the exposure of the aircraft to the hostile environments near the landing site.

The increase in consumed fuel is not really too significant. Because of the low disc loading rotors, the largest amount of fuel consumed in all of the cases considered is less than one percent of the tilt-rotor's total fuel load for the design mission.

The noise produced by flying this second noise abatement profile is greatly reduced at the first two ground locations. At 200 feet up-range of the landing point, a 10 EPNdB reduction in annoyance is predicted. However, the noise evaluated at the last measuring location has a higher EPNdB than the optimal descent trajectories. The longer exposure time of the noise-abatement profile causes an increase in the EPNdB level at that particular location.

By comparing these last two noise abatement profiles, an estimate of the annoyance of the horizontal flight segment at 3000 feet can be made. The EPNdB of both trajectories is almost identical at 400 feet, is slightly greater for the second profile at 1600 feet, and is significantly greater for the second flight profile at 6400 feet up-range. This increasing difference in subjective assessment indicates that the horizontal steady-state flight segment only significantly influences the measured annoyance of tilt-rotor noise abatement trajectories at distances in excess of one mile from the touchdown point.

The last trajectory shown in Table V-3 is a near-optimum descent trajectory which is flown to alleviate some of the ground noise. The flight path is very similar to the restricted optimal descent (high-speed helicopter). However, deceleration to zero forward velocity is reduced from its maximum value near the terminal time. The resulting trajectory traces a near vertical descent in the last 1000 vertical feet. Some slight increases in time of flight and fuel consumed result over the "high-speed helicopter descent" case. However, a significant reduction in the calculated EPNdB is registered at the first ground measuring location.

Steepening the flight path to reduce a chosen subjective measure (EPNdB) of noise can be concluded to be an effective operational procedure. The cost in performance of achieving a 10 EPNdB reduction in annoyance at short distances from the touchdown point is estimated to be about a 50 percent increase in time of flight and fuel consumed. The increased time is important militarily, while the increase in fuel is only a small fraction of the total mission fuel. Commercially, the minimization of the area exposed to noise of disturbing intensity is most important. The increases in flight time and consumed fuel are probably secondary considerations for commercial operations of the tilt-rotor VTOL aircraft.

## Detailed Presentation of the Results

The general results presented in the previous section of this chapter do indicate the overall noise-performance tradeoffs which are possible with the tilt-rotor aircraft operating in the takeoff and landing modes of flight. This section contains a more detailed description of these same trajectories. Time histories of individual performance parameters such as power setting, velocity, configuration angle, etc., are presented to more clearly illustrate the transition performance of the aircraft. The resulting trajectories are graphically illustrated, showing six noise-measuring locations. A one-third octave band analysis of the resulting noise is also presented at the point of maximum annoyance for each chosen ground location.

Takeoff and Climb. - A geometric representation of a takeoff flight profile is illustrated in Figure V-1. Six different measuring locations (A, B, C, D, E and F) which are located directly below the flight path are also indicated on this figure. Position A was chosen to be 200 feet from the point of takeoff. The 5 remaining ground measuring locations were chosen to be twice the distance of the previous location. Therefore, location B is 400 feet from the point of takeoff; location C is 800 feet, etc. The last measuring location (F) was chosen to be 6400 feet from the initial point of takeoff. The primed letters (A', B', C', D', E', F') which are shown at specific flight path locations illustrate the position of the aircraft where the maximum predicted perceived noise level of

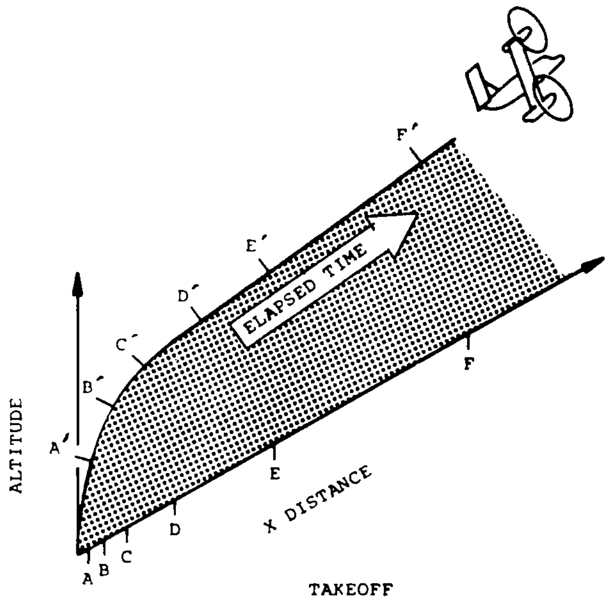

Figure V-1

each respective measuring location occurs. For example, an observer at location E would register the largest value of PNdB when the aircraft is at position E'. This notation is used throughout this section of the report to relate the performance state of the aircraft to a frequency analysis of the resulting predicted noise.

A one-third octave band frequency analysis of the sound pressure level is also calculated for each measuring location when the aircraft is in its respective primed position along the flight path. A representative SPL (sound pressure level) versus frequency plot is illustrated in Figure V-2. Labels at the top of the spectrum are: the measuring location at which this spectrum is received, the perceived noise level of the spectrum, and the elapsed time from takeoff when the predicted maximum perceived noise level occurred. A solid line connects those one-third octave bands in which rotational noise of the rotors predominate. Each measuring location has its own symbol for the one-third octave band sound pressure level (see below).

| LOCATION | A | B | C | D | E | F |
|---|---|---|---|---|---|---|
| SYMBOL | ○ | △ | □ | ◇ | ▽ | ◗ |

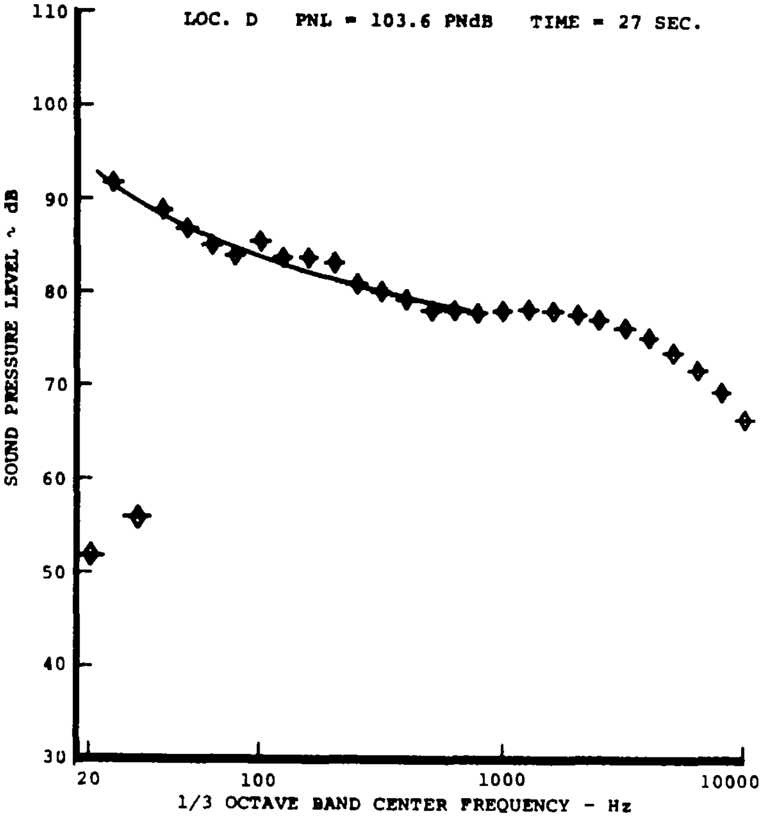

Figure V-2

None of the ambient and power train (engine, transmissions, etc.) noise that is normally present in 'real life' is shown in the predicted noise spectrum.

Detailed takeoff performance and acoustic data which has only been calculated for the first flight path segment is presented in the next few subsections.

Minimum Time and Fuel [Max. (R/C) Power Used/Max. Power Available = 1.0]: Figures V-3 through V-6 graphically illustrate the optimal takeoff performance problem up to a 3000-foot altitude. The takeoff profile trajectory which results is shown at the top of Figure V-3. Maximum horizontal and vertical acceleration limits are enforced at the time of takeoff (Figure V-6). The vertical acceleration constraint is enforced until the maximum applied power limit is intersected (Figure V-5). Maximum power is then applied for the remainder of the trajectory. The horizontal acceleration is maintained at its limiting value until the horizontal velocity which corresponds to the tilt-rotor's best rate of climb speed is attained. As horizontal velocity increases, the aircraft makes the conversion from the helicopter to the airplane configuration (Figure V-5). An additional limit upon the rate of change of the tilt-rotor's attitude with respect to time reduces the applied power slightly during conversion for a small time interval. The remainder of the trajectory is flown in the airplane configuration at the best rate of climb speed with maximum power applied.

Several interesting performance characteristics of the tilt-rotor's climbing transition to forward flight are illustrated in Figures V-5 and V-6. The rate of climb versus horizontal velocity curve is remarkably similar to the unconstrained constant altitude performance curves presented in Section II (Figure II-14). However, the kinematic performance which is illustrated in Figure V-5 has been further constrained by the dynamic performance constraints. The initial vertical acceleration constraint is directly responsible for low rates of climb near the takeoff point.

The second dip in the rate of climb versus horizontal velocity curve is observable in both Figure V-5 and II-14. It is directly attributable to the significant download on the wing which occurs at moderate forward speeds and high rates of climb. The last dip in the kinematic performance curve occurs in high-speed helicopter flight. The power expended to overcome the drag of the tilt-rotor aircraft in the helicopter configuration at high speeds reduces the power which is left to maintain high rates of climb.

Figures V-3 and V-4 illustrate the character of the noise which is heard at all six ground measuring positions. A plot of sound pressure level versus frequency is given (Figure V-3) at each ground location when the aircraft is registering its maximum perceived noise level (PNdB). The relative importance of the high frequency broadband noise is immediately obvious. The low frequency rotational noise drops off very rapidly with increasing frequency. The large inflow through the plane of the rotor in takeoff flight conditions reduces the importance of the higher harmonic rotor airloads, thus reducing the magnitude of higher harmonic rotational noise. The effect of varying the distance between the aircraft and the observer can also be seen. Besides the normal reduction of 6 decibels with a doubling of distance, a more rapid attenuation of high frequency noise with distance is observed. A time history of the perceived noise level which is heard at each measuring location is presented in Figure V-4. The initial peak in each of the curves occurs just before the tilt-rotor reaches the point of closest passage to the measuring location. Doppler shift, directivity effects, and conversion regime performance are reflected in these curves.

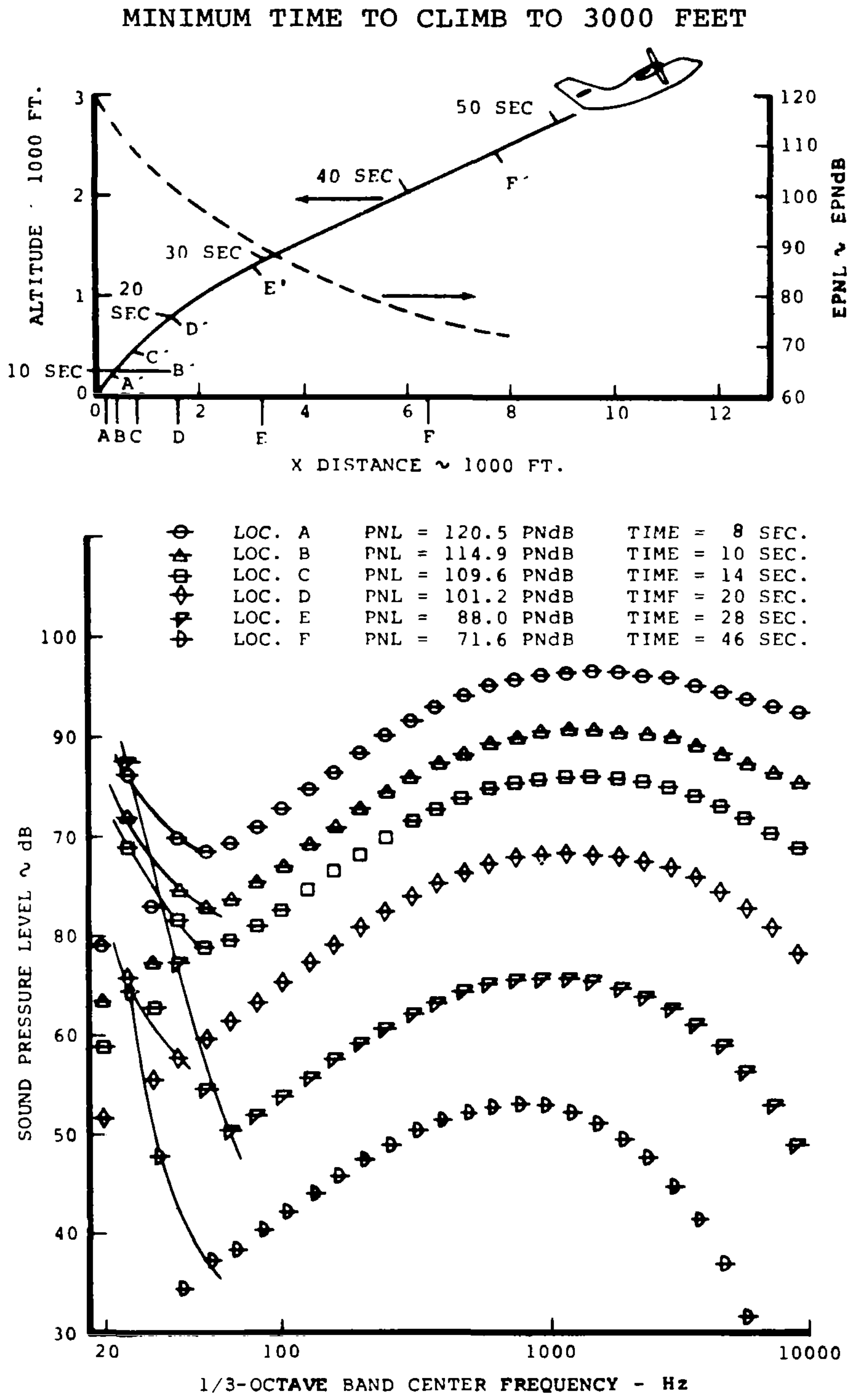
MINIMUM TIME TO CLIMB TO 3000 FEET

FIGURE V-3

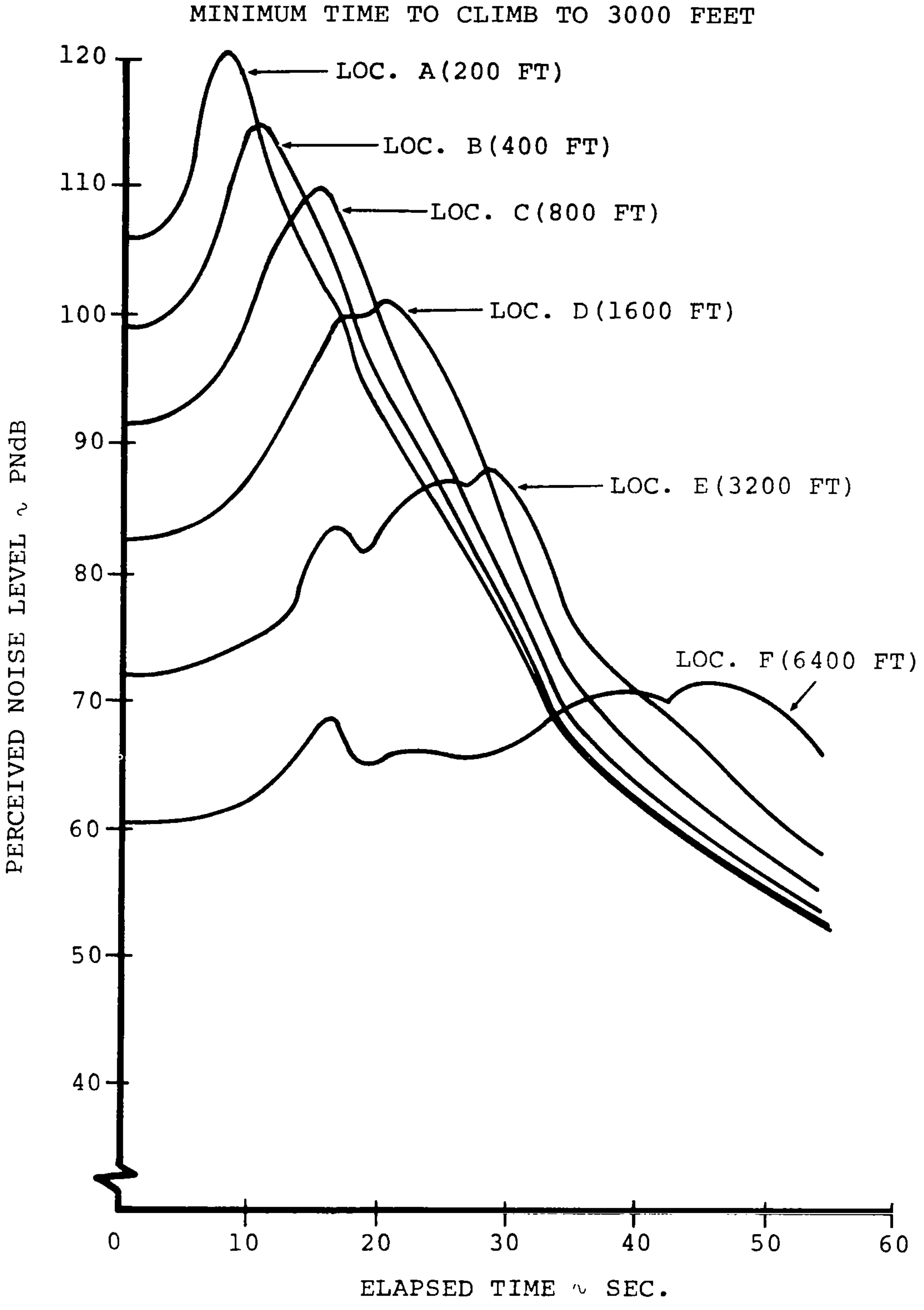
MINIMUM TIME TO CLIMB TO 3000 FEET
LOC. A(200 FT)
LOC. B(400 FT)
LOC. C(800 FT)
LOC. D(1600 FT)
LOC. E(3200 FT)
LOC. F(6400 FT)
PERCEIVED NOISE LEVEL ∿ PNdB
120
110
100
90
80
70
60
50
40
0
10
20
30
40
50
60
ELAPSED TIME ∿ SEC.

FIGURE V-4

MINIMUM TIME TO CLIMB TO 3000 FEET

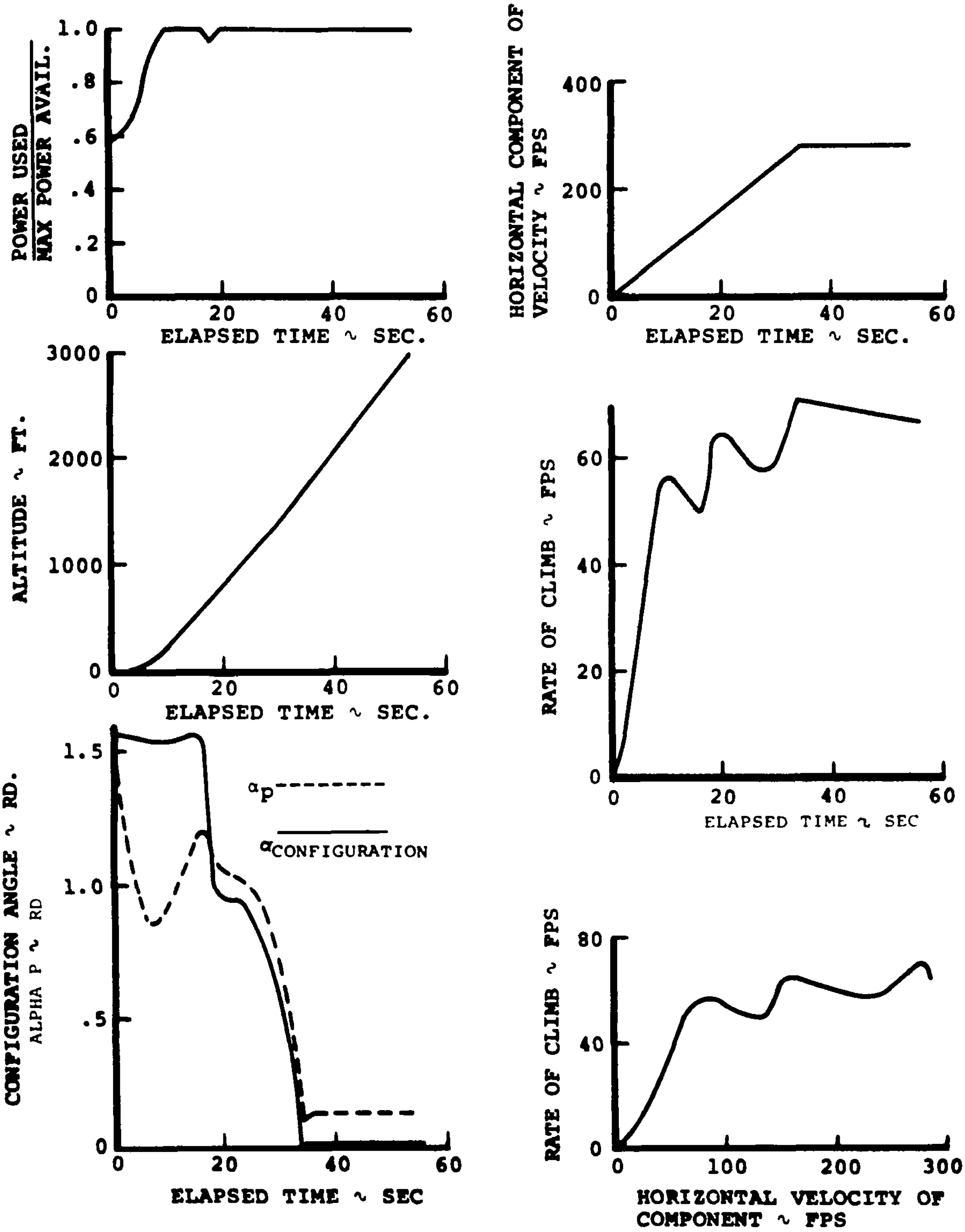

FIGURE V-5

MINIMUM TIME TO CLIMB TO 3000 FEET

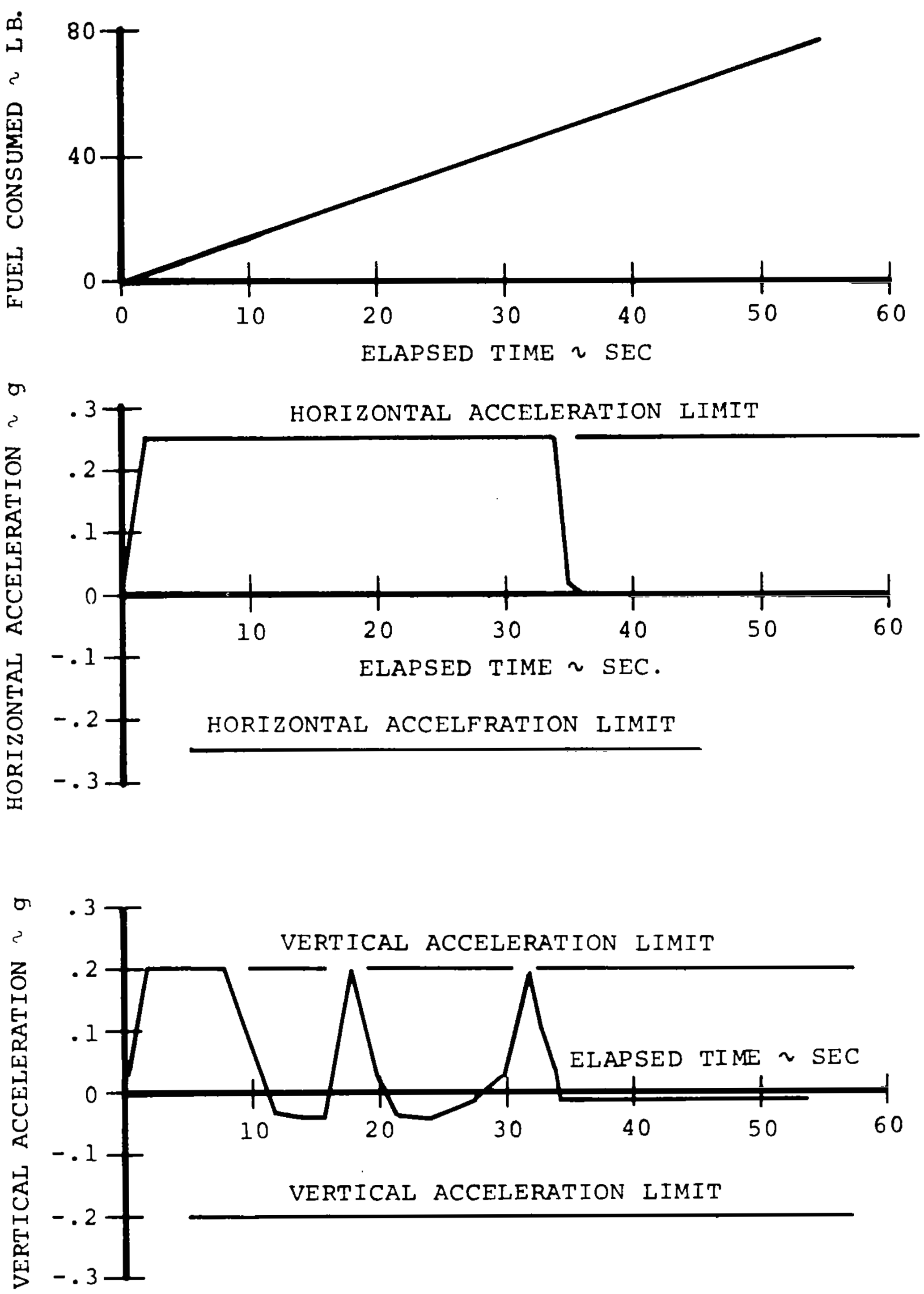

FIGURE V-6

Partial Power Takeoff and Climb [Max. (R/C); Power Used/ Max. Power Available = 0.8]: Figures V-7 through V-10 illustrate the performance takeoff and climb trajectory at 80 percent of maximum power. Although the flight path which is shown in Figure V-7 is shallower, the optimum trajectory and resulting noise characteristics are quite similar to the maximum power takeoff trajectory. Maximum horizontal and vertical acceleration limits are initially enforced (Figure V-10). When the 80 percent power limit is intersected, it is maintained throughout the takeoff maneuver (Figure V-9). Maximum permissible horizontal acceleration is applied until the best rate of climb speed is attained. Conversion to the airplane configuration from the helicopter configuration occurs naturally as the horizontal velocity increases. A constant velocity maximum rate of climb trajectory is then maintained to 3000 feet.

Reducing the applied power during takeoff has resulted in increased time and fuel required to climb to 3000 feet. The more shallow flight path which results from the power reduction also increases the overall level of noise heard at the 6 noise measuring locations (Figure V-7). Although the applied power has been reduced, the accompanying reduction in distance between the aircraft and the measuring locations causes an increase in the measured sound pressure level. Thus, reducing the applied power to reduce noise during a maximum performance takeoff only aggravates the situation.

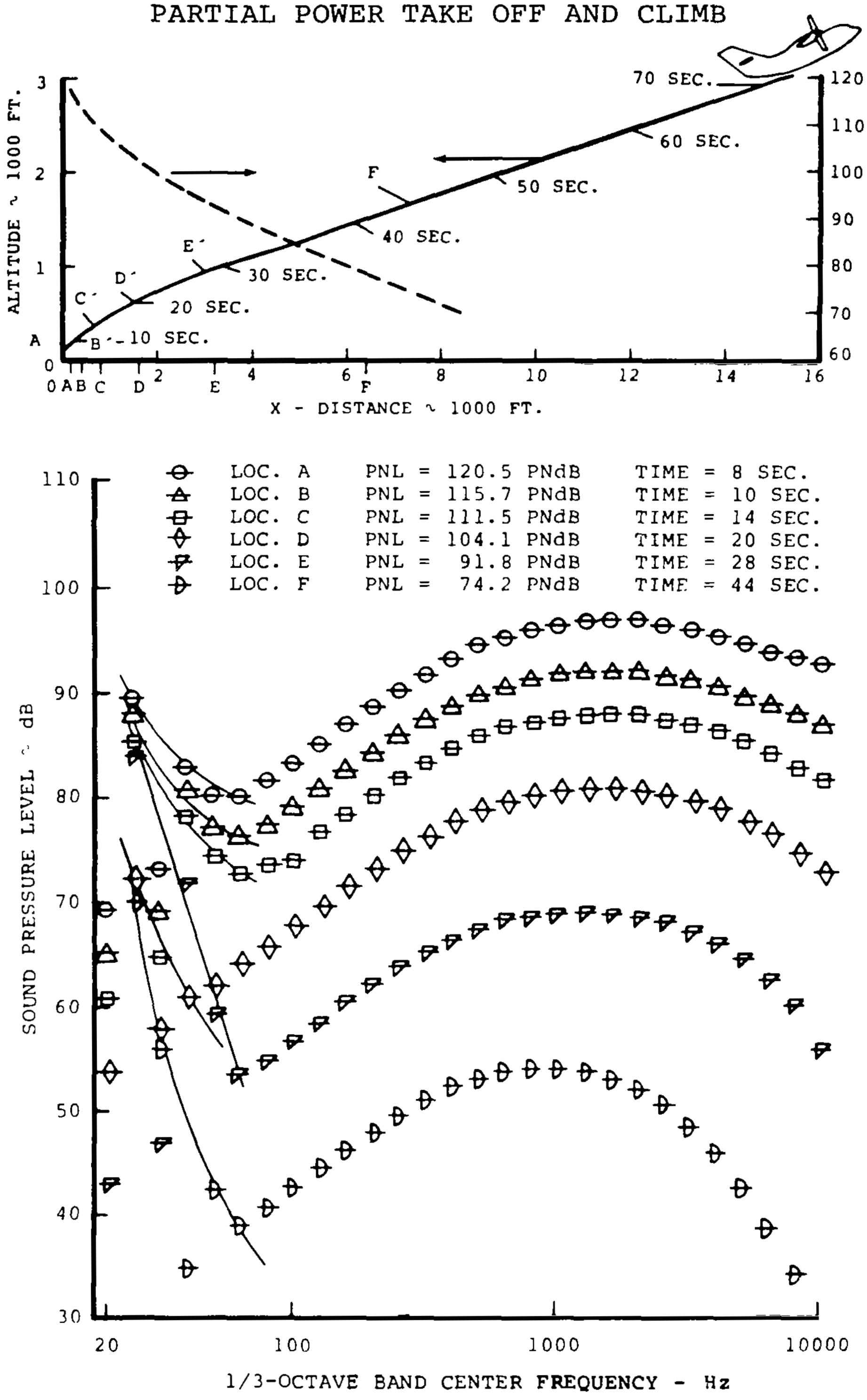
PARTIAL POWER TAKE OFF AND CLIMB

FIGURE V-7

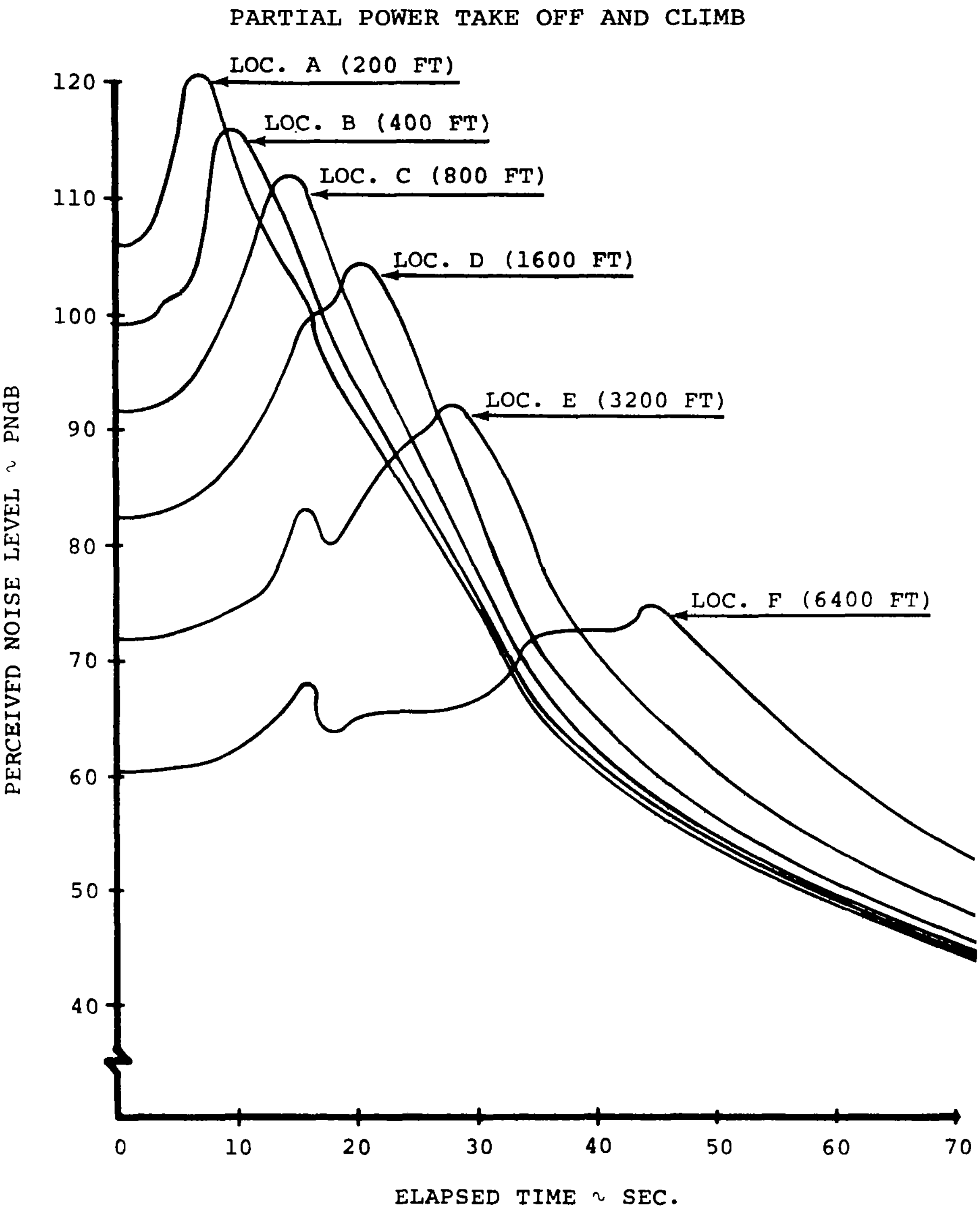
PARTIAL POWER TAKE OFF AND CLIMB
LOC. A (200 FT)
LOC. B (400 FT)
LOC. C (800 FT)
LOC. D (1600 FT)
LOC. E (3200 FT)
LOC. F (6400 FT)
PERCEIVED NOISE LEVEL ~ PNdB
120
110
100
90
80
70
60
50
40
0
10
20
30
40
50
60
70
ELAPSED TIME ~ SEC.

FIGURE V-8

## PARTIAL POWER TAKE OFF AND CLIMB

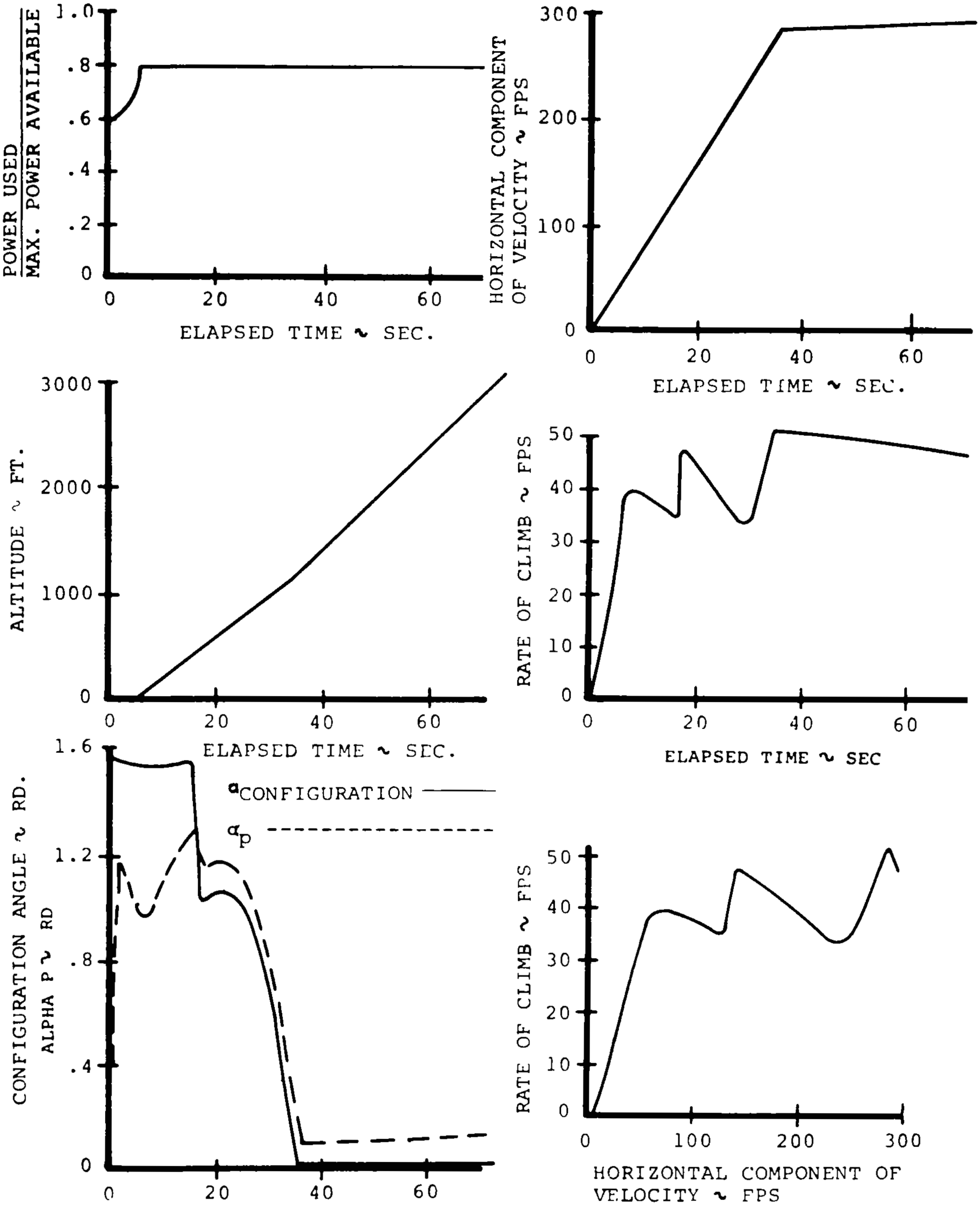

FIGURE V-9

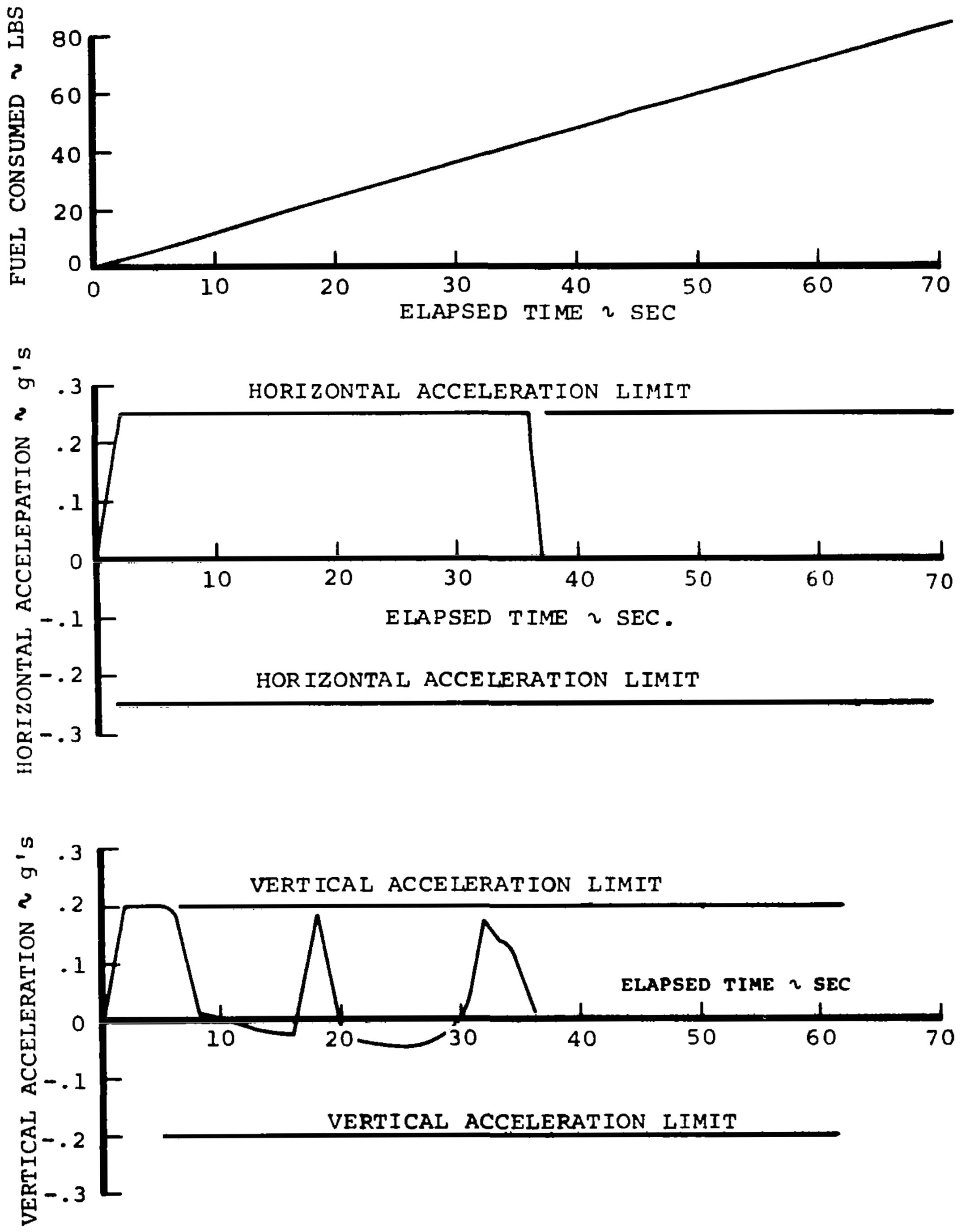

PARTIAL POWER TAKE OFF AND CLIMB

FIGURE V-10

Proposed Noise Abatement Profile. - The lack of any one weighted subjective measure of total tilt-rotor operational noise prohibits the formulation of a mathematical noise optimization problem in the strictest sense. However, to obtain some knowledge of the effects of the flight path on the tilt-rotor acoustical characteristics, some proposed noise abatement profiles have been chosen.

Many people in the technical community have been proposing takeoff flight profiles which take advantage of the VTOL's unique operational performance characteristics. One class of trajectories which has been seriously considered by British researchers incorporates initial pure vertical climbing trajectories. The lift-engine VTOL aircraft which they are considering benefit greatly from the increased distance between the source of noise and the chosen measuring locations at those positions close to the terminal. The higher frequency noise, which is the dominant source of noise in lift-fan engines, attenuates rapidly with distance due to atmospheric absorption. The proposed noise abatement trajectories which are considered in this report also contain at least one flight path segment of pure vertical climb. Although the atmospheric noise attenuation characteristics of the tilt-rotor aircraft are not as large as those of the jet-lift aircraft, the vertical takeoff profile still appears to offer the greatest potential for noise reduction.

PURE VERTICAL CLIMB: The first noise abatement trajectory which is considered is a pure vertical climb to 3000 feet. The resulting performance and acoustical characteristics are illustrated in Figures V-11 through V-14.

The takeoff begins with maximum allowable vertical acceleration. Horizontal acceleration is nulled and the applied power is increased until the power limit is attained. Maximum power is then applied, resulting in maximum rate of climb of the tilt-rotor aircraft in the helicopter configuration. This near constant rate of climb is sustained until the termination of the maneuver. Figures V-13 and V-14 illustrate the more important time histories of the performance variables for this trajectory.

As illustrated in Figure V-11, the SPL versus frequency curves which are generated at each measuring location when the tilt-rotor aircraft produces the maximum perceived noise level. Higher levels of rotational noise are calculated in the pure vertical takeoff as compared to the minimum time to climb case. The higher thrust-to-weight ratios of the helicopter configuration generate a significant amount of low frequency rotational noise. However, because the higher harmonics airloads which generate this noise decay rapidly with frequency under these large inflow conditions, the rotational noise quickly becomes less important at higher frequencies. The rapid attenuation of vortex noise with distance is also very noticeable (Figure V-11). A very smooth variation of PNdB versus time is illustrated in Figure V-12. The tilt-rotor remains in the helicopter configuration throughout the maneuver and the inflow is always axial, eliminating many of the possible larger changes in the perceived noise level time history.

VERTICAL CLIMB TO 3000 FEET

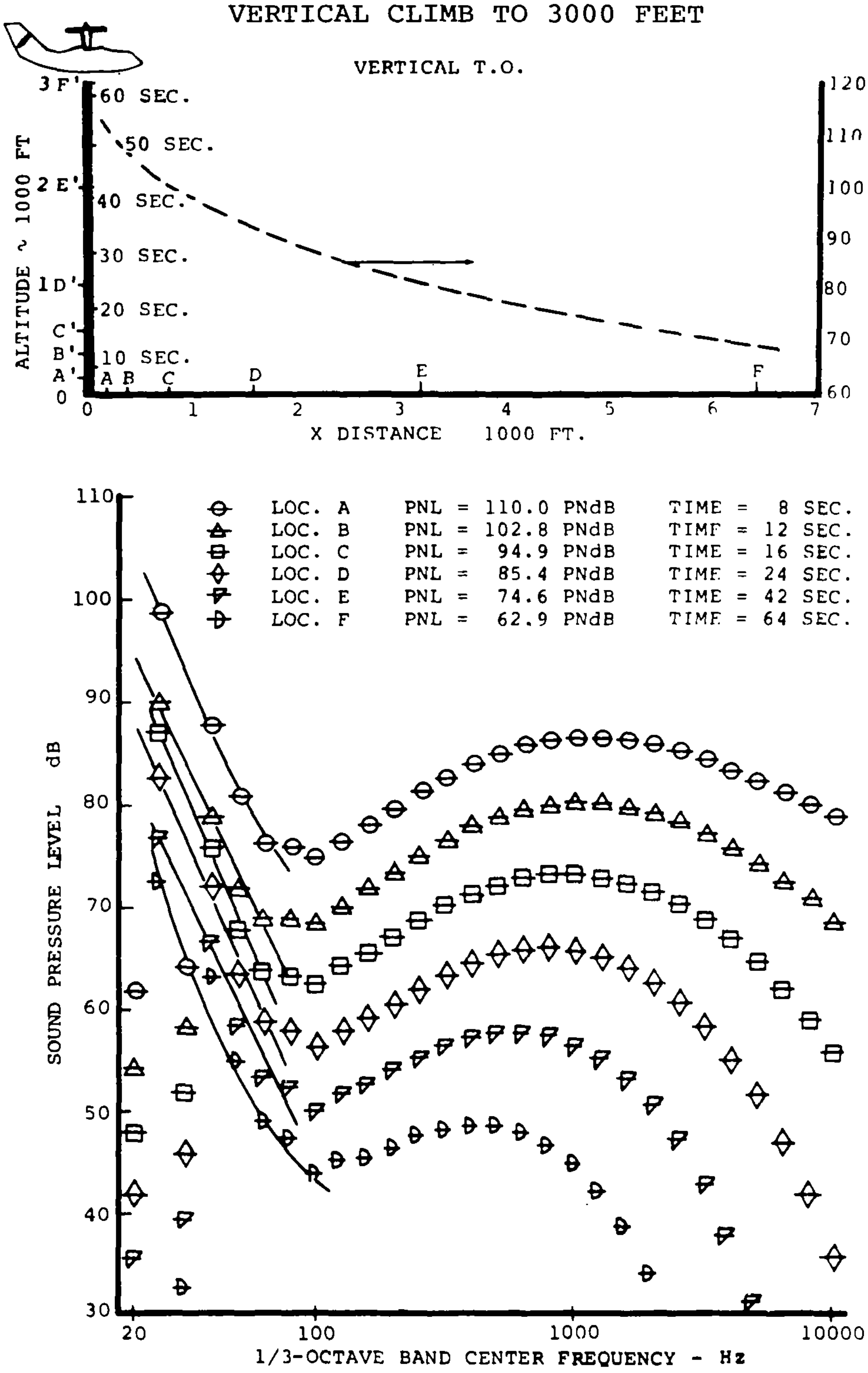

FIGURE V-11

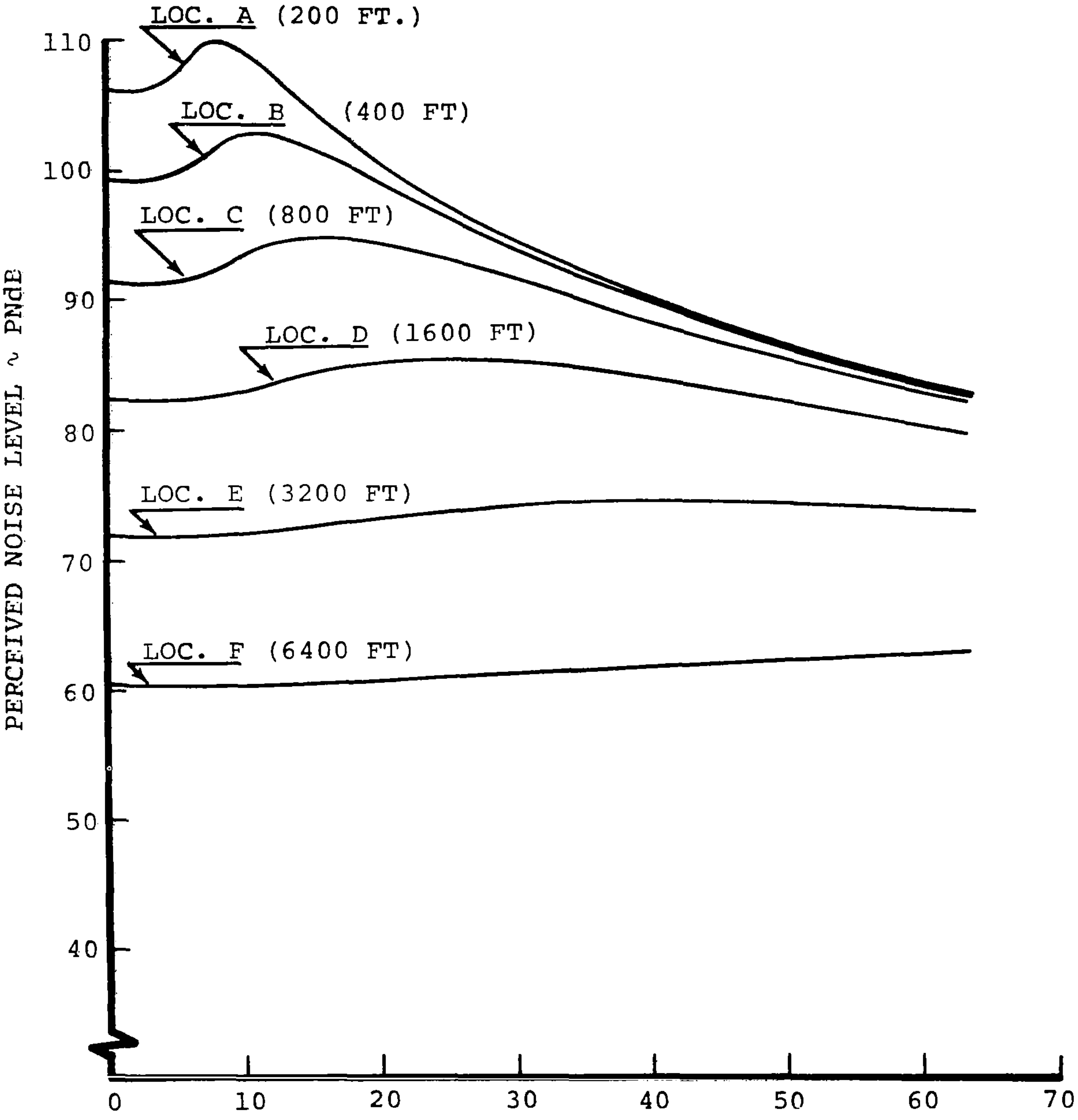

VERTICAL CLIMB TO 3000 FEET

FIGURE V-12

## VERTICAL CLIMB TO 3000 FEET

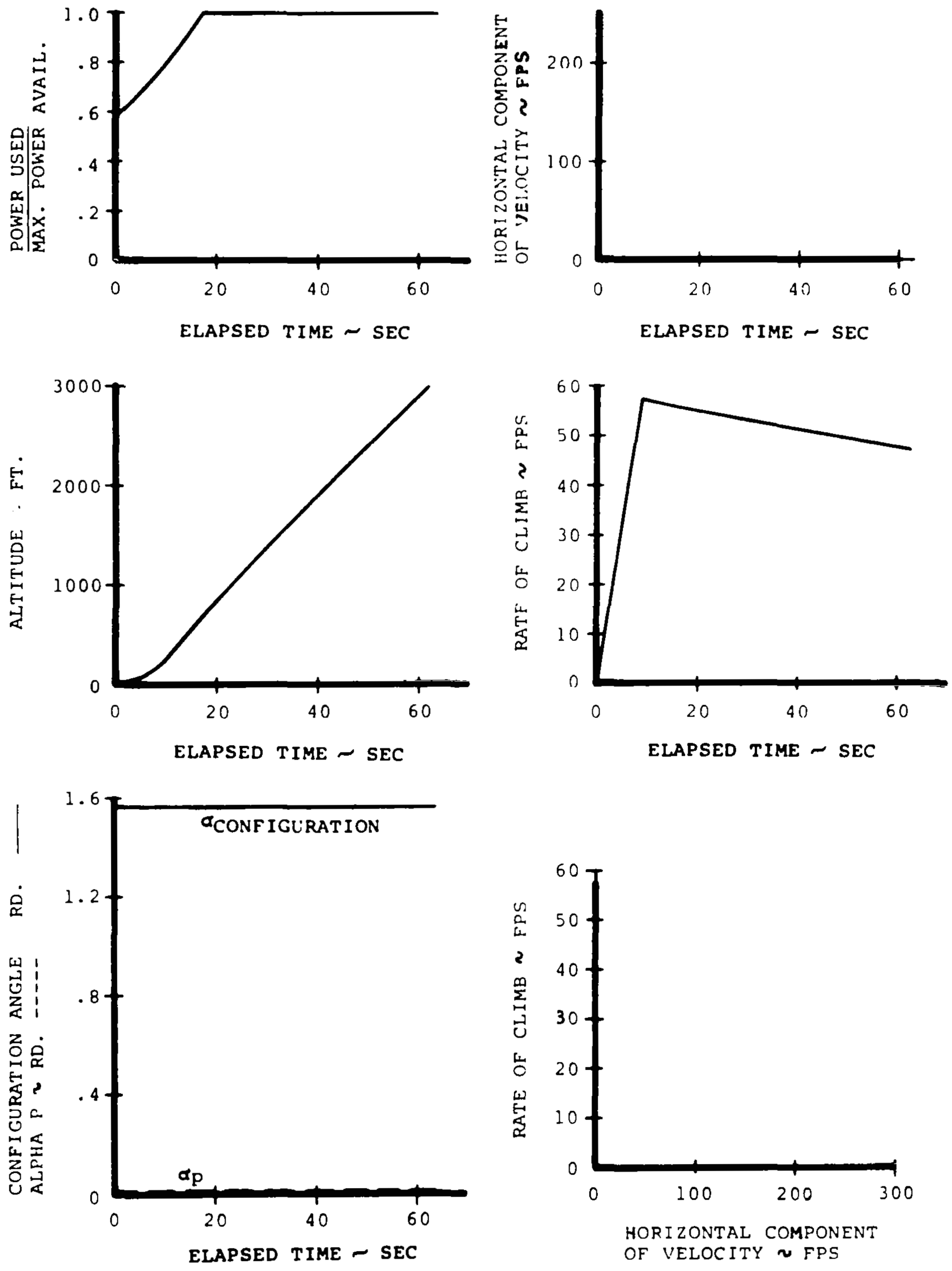

FIGURE V-13

VERTICAL CLIMB TO 3000 FEET

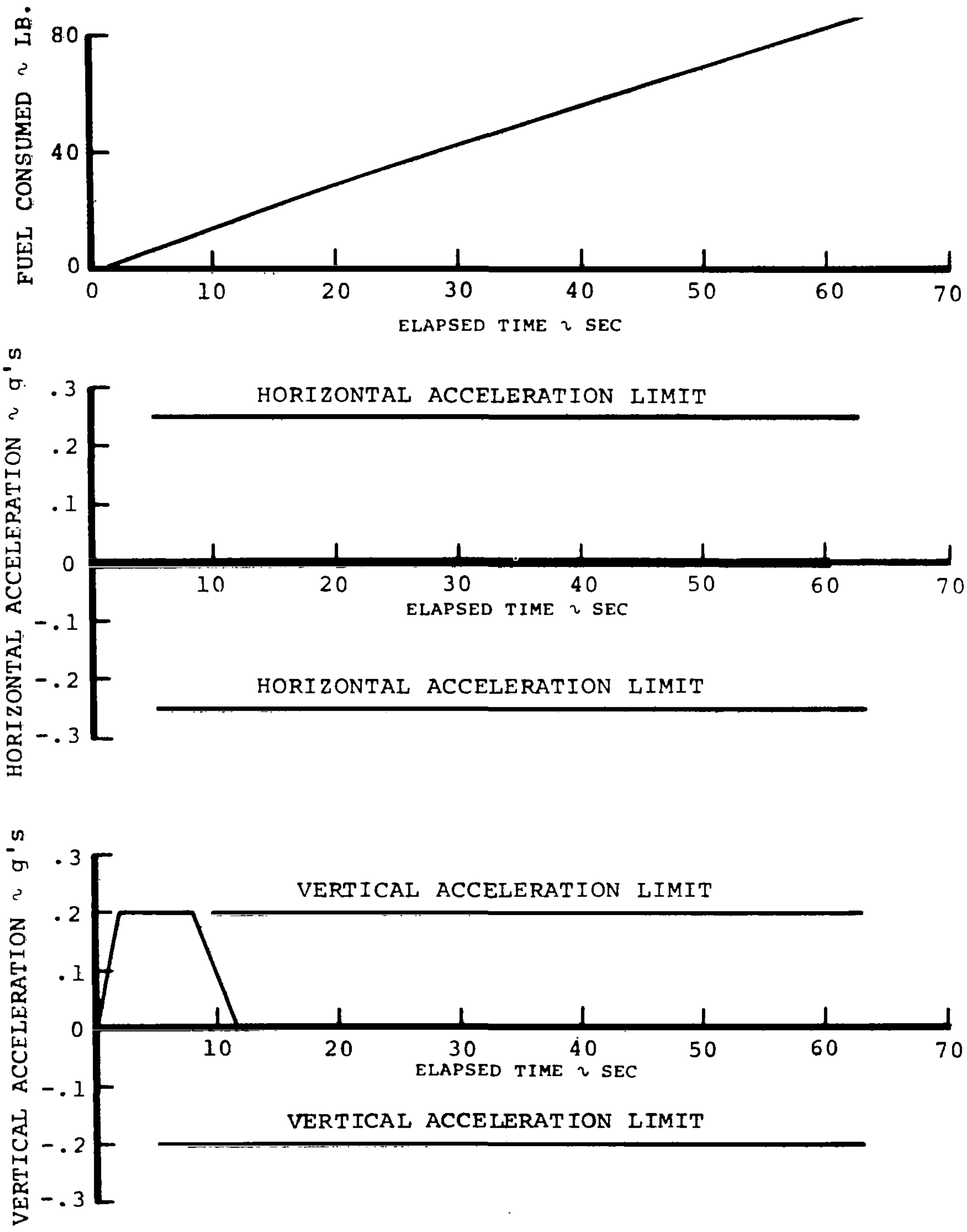

FIGURE V-14

Vertical Climb to Altitude Followed by Steady Horizontal Flight. - The second and last takeoff noise abatement profile which is treated in this report attains the same downrange position as the optimal performance trajectory. Therefore, the tilt-rotor aircraft must fly directly over the noise measuring locations. Thus, it has been possible to make a direct comparison of the noise and performance between the optimal performance trajectory and this second proposed noise abatement profile.

Figure V-15 graphically illustrates the frequency content of the noise which is heard on the ground when the vehicle flies this noise abatement profile. All of the previously observable characteristics of the pure vertical takeoff trajectory are also illustrated in these same figures. The addition of this constant altitude horizontal flight path segment has not significantly changed the characteristics of the resulting noise. The rapid conversion to airplane flight at low power settings and favorable Doppler effects produce very little additional noise. Figure V-16 illustrates the rapid decay in PNdB once the tilt-rotor converts to airplane configuration flight.

Figures V-17 and V-18 present the time histories of the more important performance variables. The first part of this second noise abatement profile is identical to the pure vertical climb trajectory. However, as the terminal altitude is approached (3000 feet), the applied power is reduced to maintain level flight. At the same time, the tilt-rotor accelerates horizontally at its maximum permissible limit. Conversion to the airplane configuration occurs as horizontal velocity increases. When the velocity which corresponds to the steady state, best rate of climb speed (minimum power required) is achieved, the tilt-rotor attains level steady-state flight. The maneuver ends when the tilt-rotor reaches the same downrange position as the minimum time to climb trajectory.

## VERTICAL T.O. TO 3,000 FT - HORIZ FLIGHT TO 11,400 FT DOWN RANGE

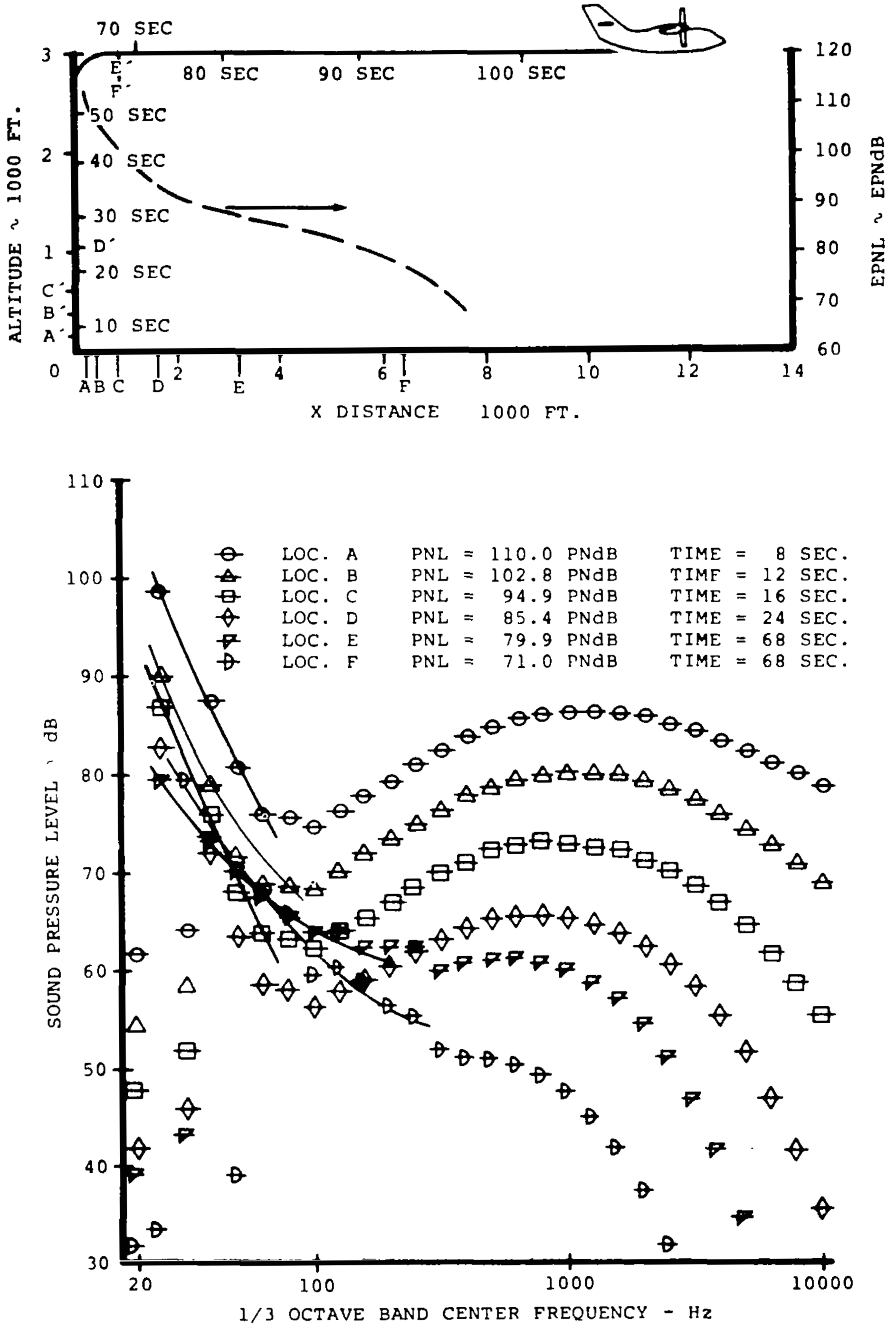

FIGURE V-15

VERTICAL T.O. TO 3,000 FT - HORIZ FLIGHT TO 11,400 FT DOWN RANGE

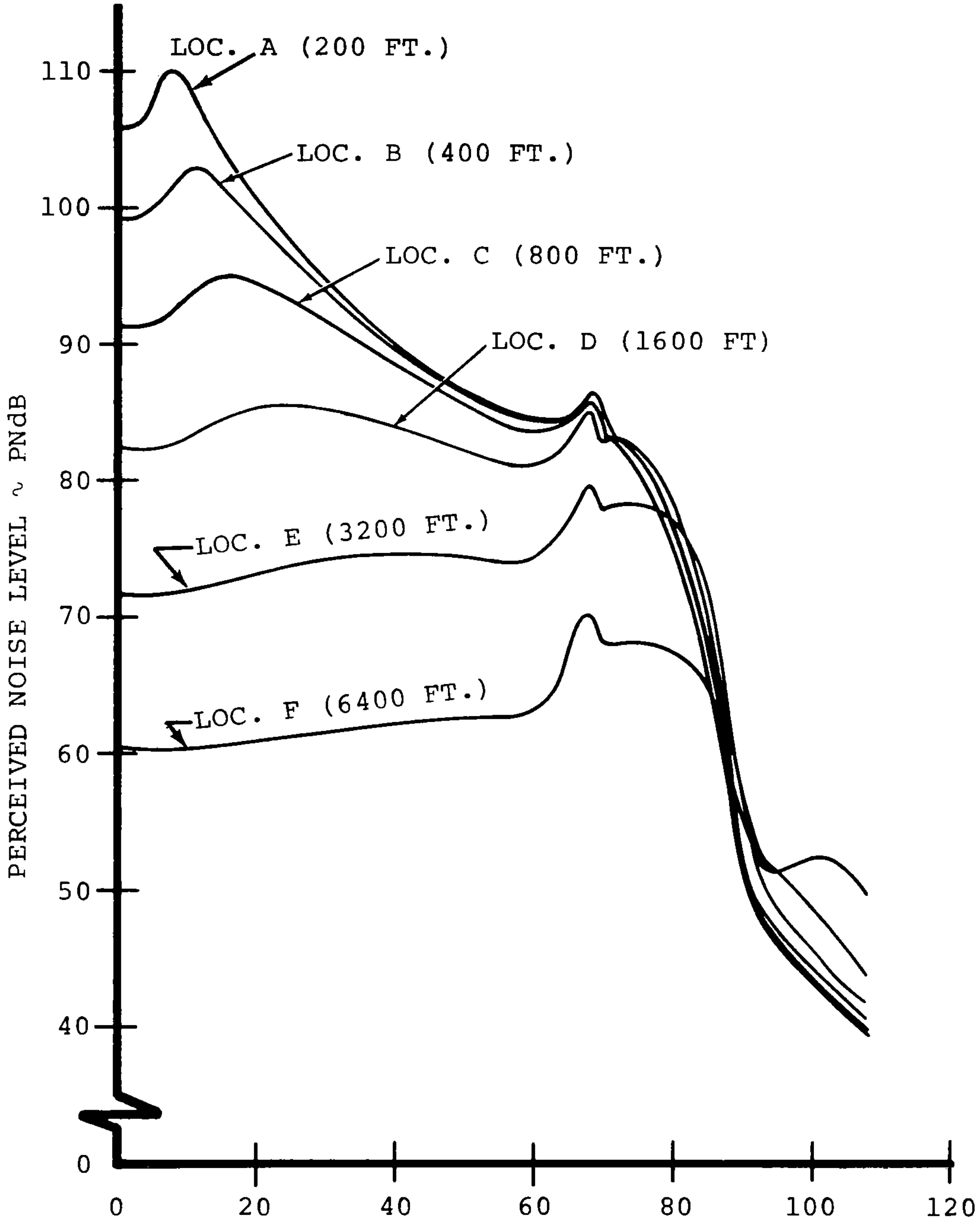

FIGURE V-16

VERTICAL T.O. TO 3,000 FT-HORIZ. FLIGHT TO 11,400 FT DOWN RANGE

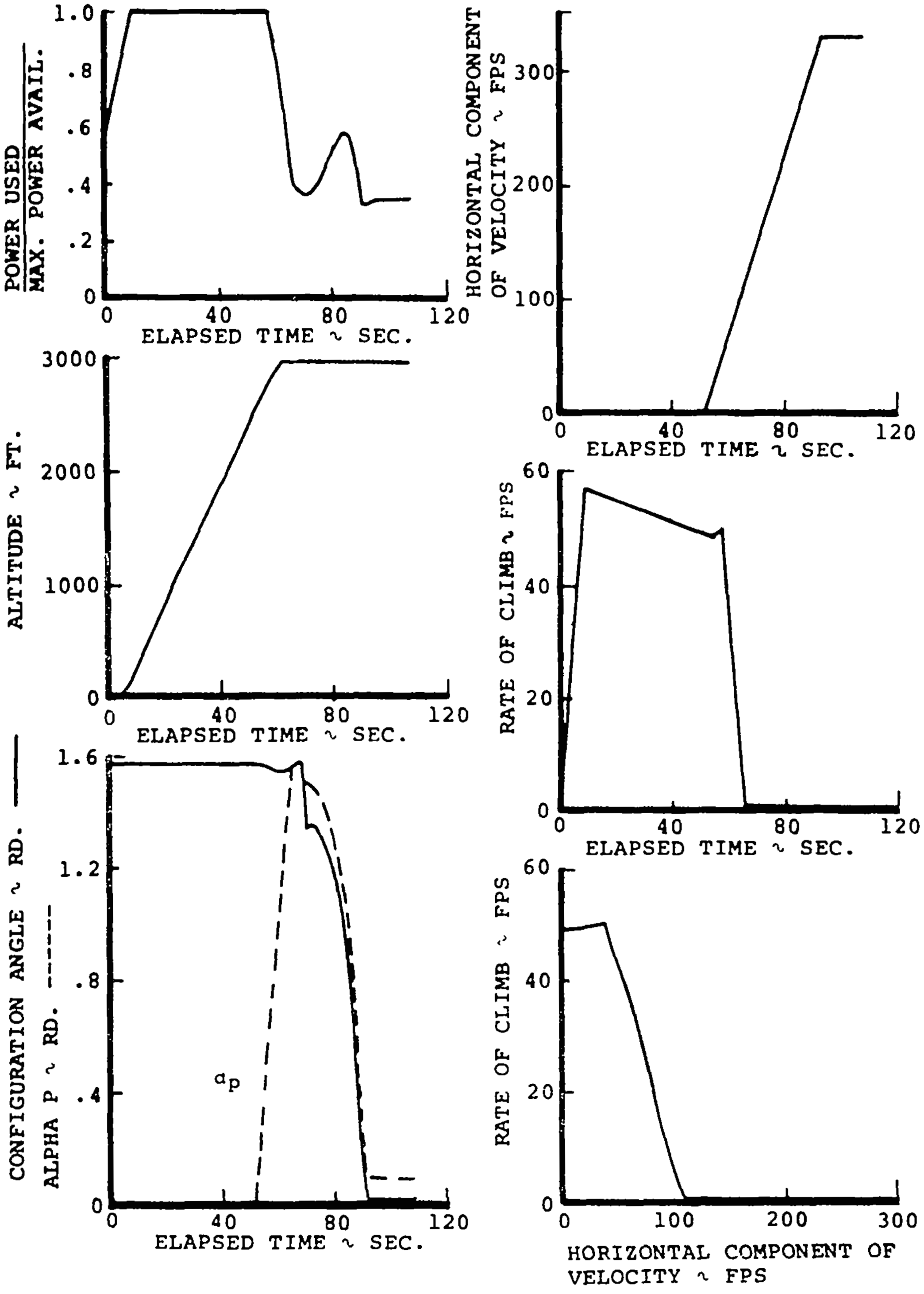

FIGURE V-17

VERTICAL T.O. TO 3,000 FT - HORIZ FLIGHT TO 11,400 FT DOWN RANGE

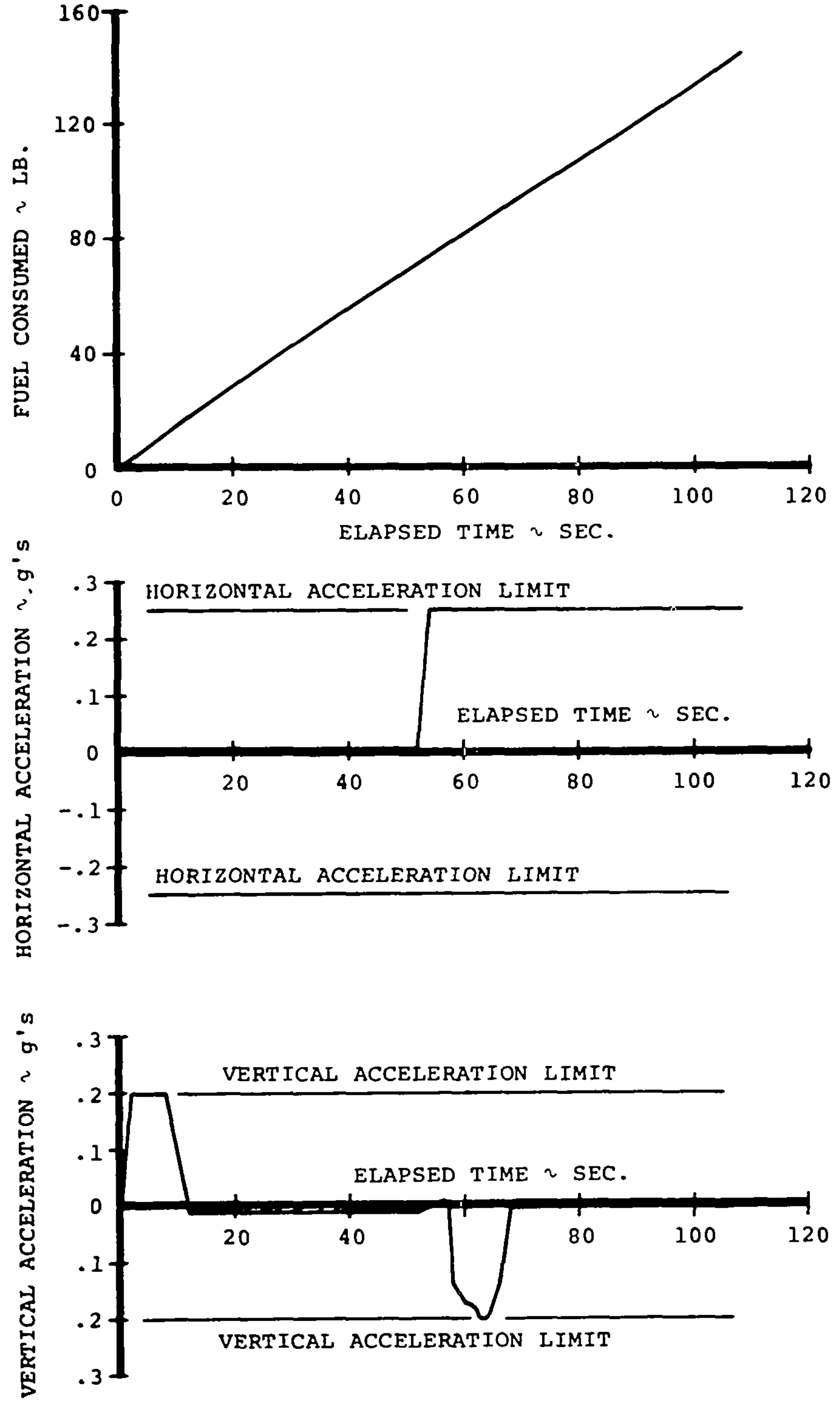

FIGURE V-18

Descent and Landing. - A two-dimensional illustration of a tilt-rotor landing profile is sketched in Figure V-19.

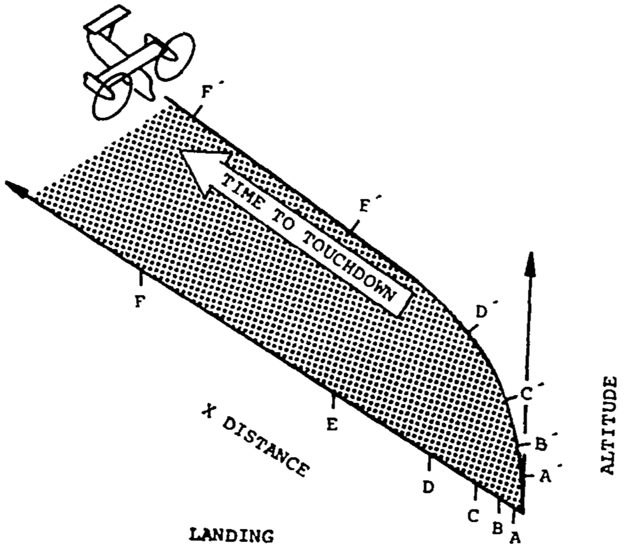

Figure V-19

For convenience, the landing point is assumed to remain fixed as the initial conditions are varied for each case which is considered. The trajectory computations have been performed in reverse time starting from the specified landing position. Therefore, the independent variable, time, was transformed to "time to touchdown" and is illustrated as such for each landing trajectory. The integration terminated when the desired altitude was attained. The horizontal distance between the initial and terminal conditions had not, in general, been specified. Thus, it was possible to easily obtain optimal landing trajectories from a specified altitude because no a priori constraints were placed upon the total horizontal distance flown.

Because the landing point is fixed, it was also easy to specify meaningful fixed ground noise measuring locations. They were chosen in a similar manner to the takeoff flight profile. The first location (position A) is 200 feet from the touchdown point and lies directly beneath the flight path. The five remaining ground measuring positions (B, C, D, E and F) were chosen to be twice the distance of the preceding position. The primed letters (A', B', C', D', E', and F'), which are also shown in Figure V-19, illustrate the position of the aircraft when the perceived noise level predicted at the corresponding unprimed position attains its maximum value.

Five possible tilt-rotor landing trajectories are presented in the next few sections of this chapter. The following analysis of the acoustic character of the "minimum time and fuel" trajectory to descend from 5000 feet resulted in the conclusion that it was not important above altitudes greater than 3000 feet. Therefore, the other descent trajectories presented herein start from 3000 feet in order to reduce the computations involved.

Minimum Time and Fuel (High-Speed Dive): Figures V-20 through V-22 describe optimal tilt-rotor landing performance during the last 5000 feet of descent. The perceived noise level time histories and the sound pressure level spectra of the resulting profile have not been presented because of their similarity to the restricted optimal landing problem which is discussed next. However, an effective perceived noise level contour provides the acoustical characteristics of the trajectory.

Steady flight at the tilt-rotor's maximum rate of sink, although not shown, has been maintained above the 5000-foot altitude level. As the aircraft descends below the 3000-foot level, these same high rate of sink conditions are maintained. Controllability requirements necessitate the expenditure of the minimum allowable applied power. When the tilt-rotor reaches an altitude of 2500 feet, maximum horizontal deceleration reduces the horizontal velocity to zero in minimum time. The applied power is maintained at its smallest allowable value during most of this horizontal deceleration maneuver as the vehicle follows its highest rate of sink versus velocity curve (Figure II-15). Conversion from airplane to helicopter flight occurs as the forward airspeed is reduced to zero. Near the point of landing, the applied power is increased above its minimum value to decelerate the aircraft at its maximum allowable limit to the required touchdown velocity (8 ft/sec).

Constrained kinematic performance of the tilt-rotor aircraft is governed by the rate of sink versus horizontal velocity curve (Figure II-15). An initial large rate of sink at high forward velocities in the airplane configuration is visible on both rate of sink versus velocity curves. Two additional local minima also exist. The largest corresponds to the high rate of sink conditions which can be maintained in the high-speed helicopter descent. The second dip represents the relatively high rate of sink conditions which can be maintained in near vertical descent. This last dip has been significantly decreased in magnitude (Figure V-21) by the requirement that the tilt-rotor decelerates to an 8 ft/sec vertical rate of sink at the terminal time.

The very rapid decay of effective perceived noise level with distance from the landing point (Figure V-20) is indicative that noise above the 3000-foot level is definitely of secondary importance. In fact, most of the noise which is calculated occurs during the later stages of transition in the helicopter configuration. The gradual reduction of wing lift with decreasing forward airspeed brings about the necessity for more thrust in order to maintain equilibrium flight. This increase in thrust produces more overall noise. A complete discussion of the source and character of the resulting noise is presented in the next section.

MINIMUM TIME AND FUEL DESCENT

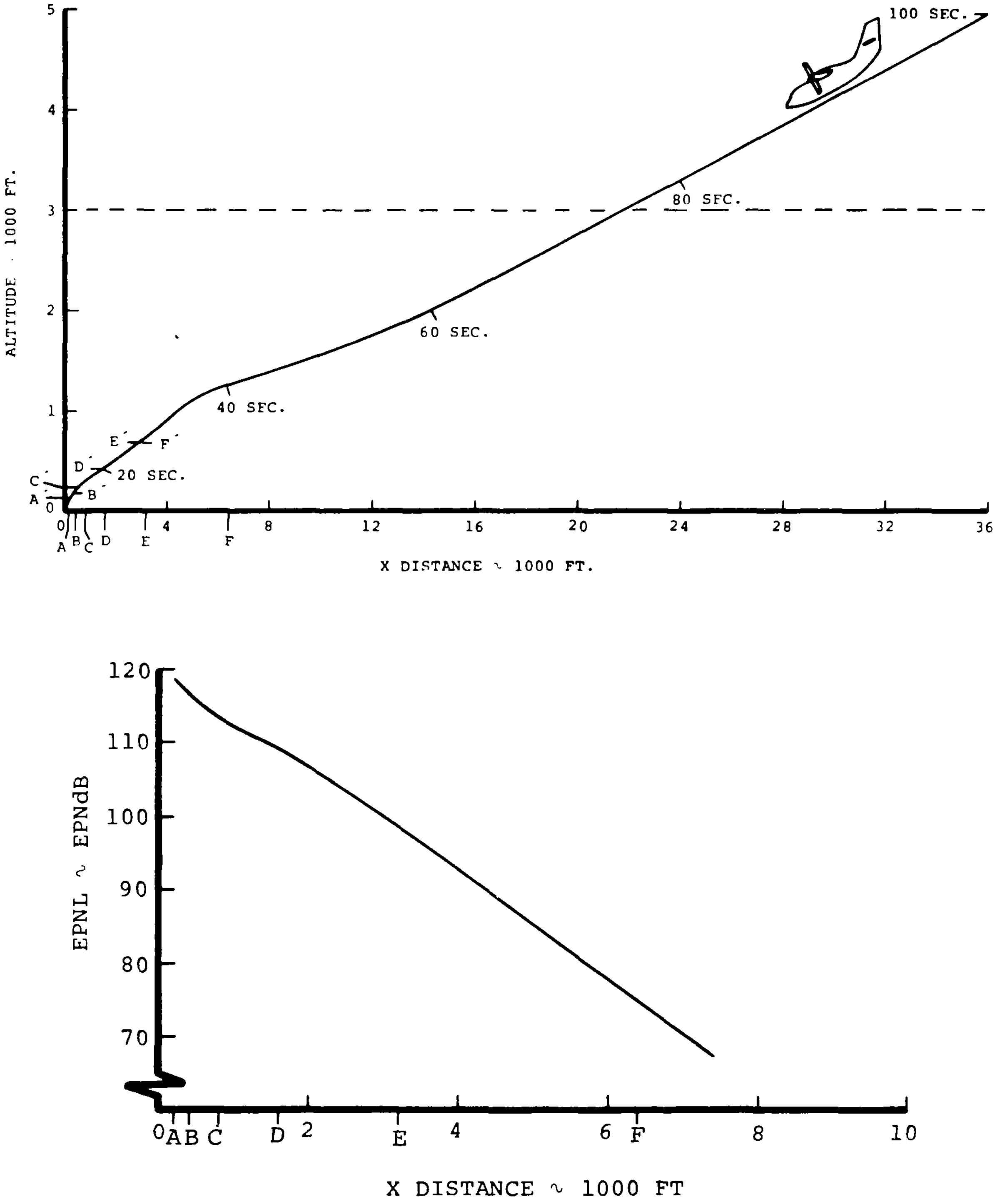

FIGURE V-20

# MINIMUM TIME AND FUEL - DESCENT

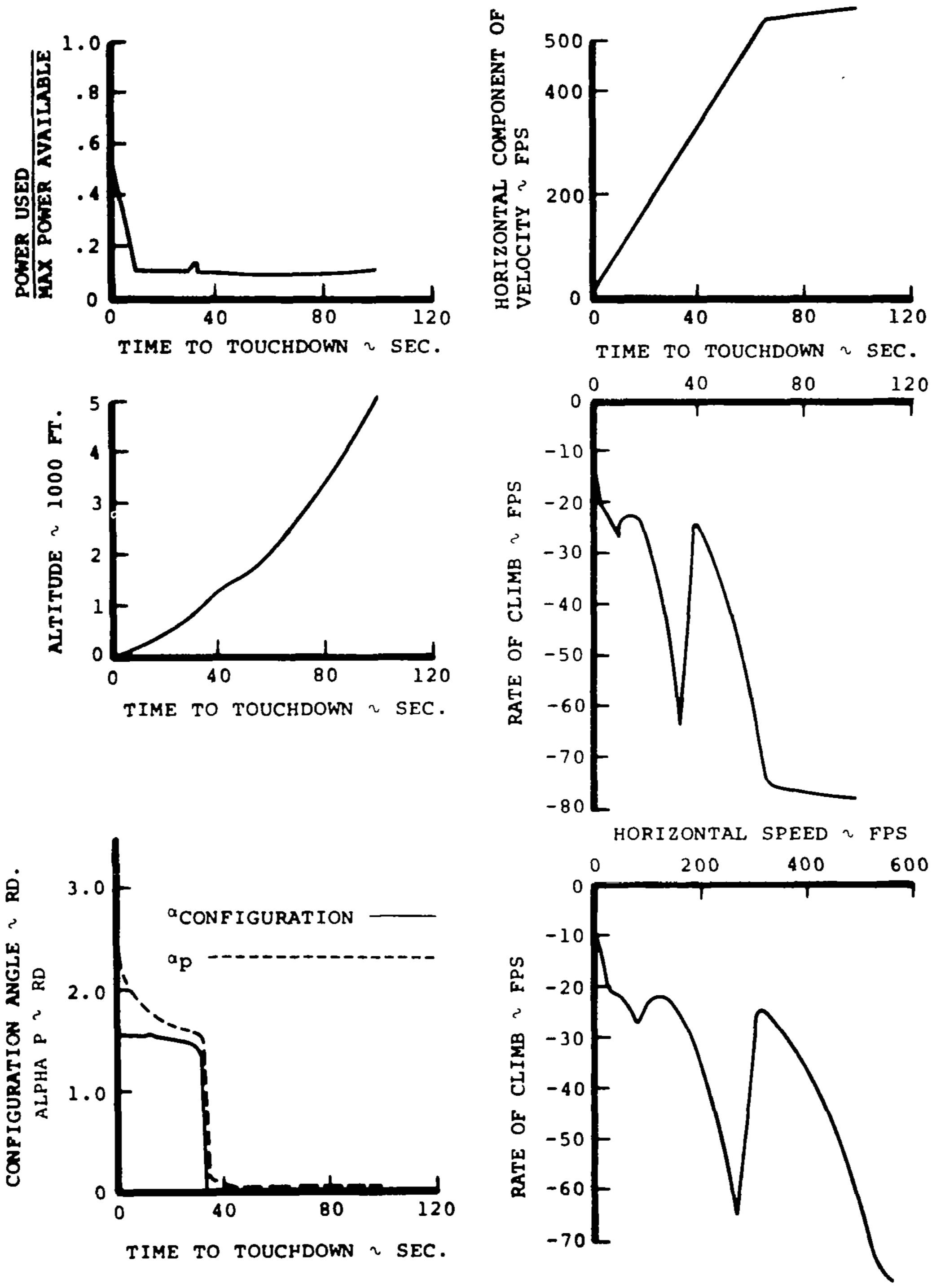

FIGURE V-21

MINIMUM TIME AND FUEL DESCENT

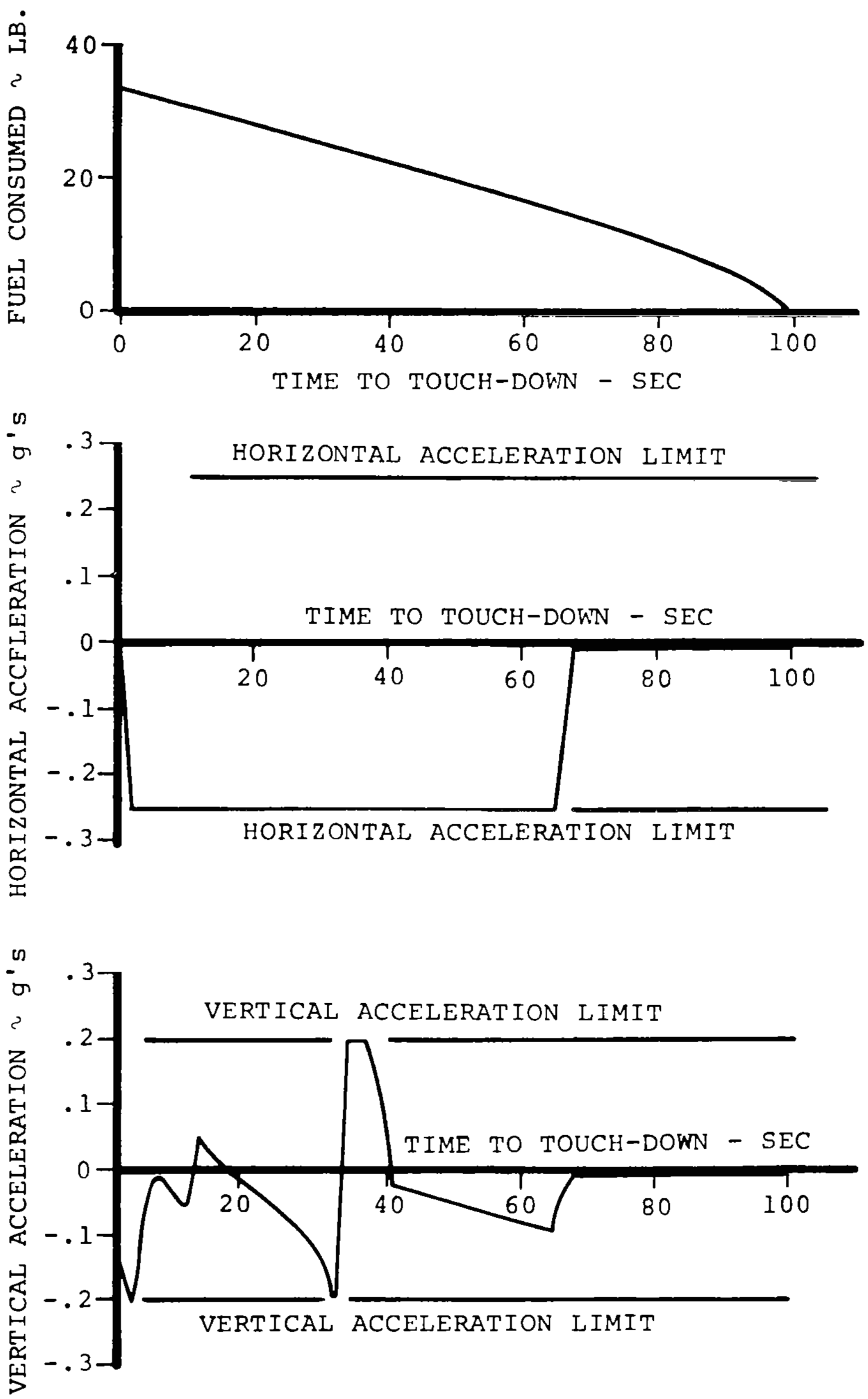

FIGURE V-22

Optimization of Time and Fuel with an Additional Flight Path Constraint (High-Speed Helicopter Descent): Maintaining high-speed flight at the tilt-rotor's structural limit in the airplane configuration near the ground is, at best, a risky operational procedure. By restricting these high-speed flight conditions to altitudes above 3000 feet and by applying optimization techniques to this further constrained problem, a near optimal trajectory is generated which is more easily flown. The last 3000 feet of the resulting restricted optimal trajectory is illustrated in Figures V-23 through V-26 along with a graphical presentation of the sound which is heard at each measuring location.

This second optimal trajectory problem formulation has been constrained to moderate forward velocities at altitudes below 3000 feet. An initial condition upon the horizontal velocity at the 3000-foot altitude level is directly enforced. The tilt-rotor aircraft must be in the helicopter configuration operating at the maximum rate of descent. The application of optimization techniques to this constrained minimum time and fuel problem causes the resulting optimal trajectory to maintain this high rate of sink condition (Figure V-26). Notice also that during this time interval, more than the minimum applied power is needed to restrict the tilt-rotor to equilibrium flight conditions for the helicopter configuration in high-speed descent (see page 64). At about 35 seconds from touchdown, the tilt-rotor begins to decelerate horizontally at its maximum allowable limit. This last portion of the restricted optimal trajectory is identical to the preceding unconstrained optimization problem. A comparison of Figures V-23 and V-20 below 1000 feet illustrates this fact. In both trajectories, the horizontal acceleration limit is enforced as the tilt-rotor gradually transfers lift from the wing to the helicopter rotor (Figure II-13). The applied power is maintained at its minimum permissible value as the horizontal velocity decreases at a constant rate. Near the final time, the applied power is increased to decrease the rate of sink to 8 ft/sec at touchdown.

Figure V-24 indicates that significant noise measurements are only obtained during the last phases of helicopter flight. Relatively little noise is generated when the tilt-rotor is flying in the high-speed helicopter descent condition. Nearly 85 percent of the aircraft weight is being supported by the wing at these forward speeds (Figure II-13). The reduced thrust levels which are required to maintain equilibrium flight generate low rotational and vortex noise levels.

Because most of the noise which is heard at any one of those six measuring locations is a result of the last 1000 feet of descent, the noise characteristics of both the restricted and unrestricted optimization problems are very similar. Figure V-23 presents detailed sound pressure level versus frequency plots for all six ground positions. Each individual curve shown illustrates the frequency content of the noise which causes the largest value of PNdB to be measured. The corresponding position of the aircraft at this instant of time is indicated on the top of Figure V-23 by the primed letters. The importance of the low frequency rotational noise at all of the measuring positions is readily apparent. The decay of rotational noise with increasing number of harmonics is much more gradual than for the takeoff flight profiles. Less inflow through the rotor disc plane causes higher harmonic airloads of significant magnitude to be generated which in turn, are responsible for the higher harmonic rotational noise. Significant amounts of vortex noise are also noticeable in all of the cases considered. However, the latter is rapidly attenuated with distance.

MINIMUM TIME HIGH-SPEED HELICOPTER DESCENT

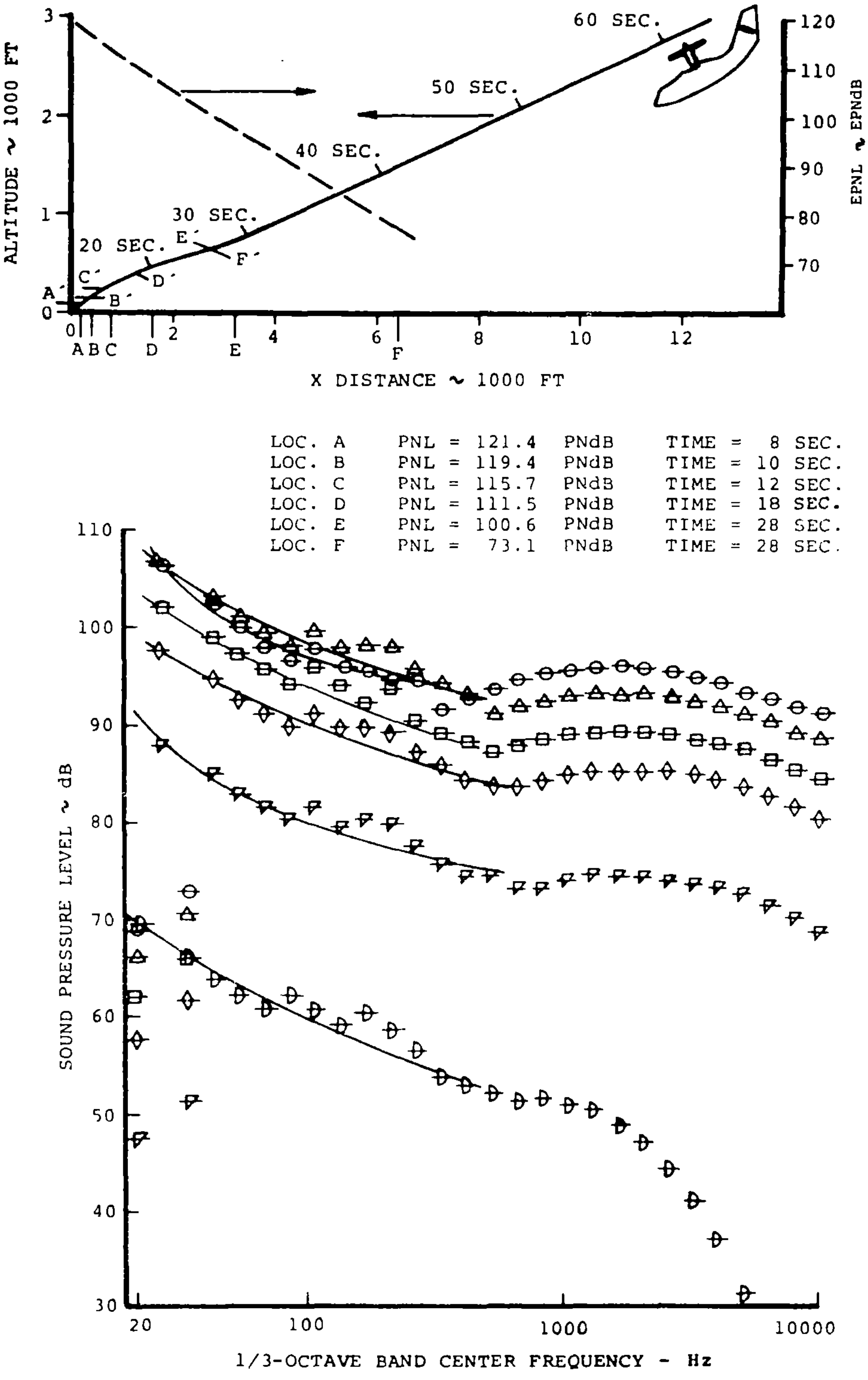

| | | | |
|---|---|---|---|
| LOC. A | PNL = 121.4 | PNdB | TIME = 8 SEC. |
| LOC. B | PNL = 119.4 | PNdB | TIME = 10 SEC. |
| LOC. C | PNL = 115.7 | PNdB | TIME = 12 SEC. |
| LOC. D | PNL = 111.5 | PNdB | TIME = 18 SEC. |
| LOC. E | PNL = 100.6 | PNdB | TIME = 28 SEC. |
| LOC. F | PNL = 73.1 | PNdB | TIME = 28 SEC. |

FIGURE V-23

MINIMUM TIME HIGH-SPEED HELICOPTER DESCENT

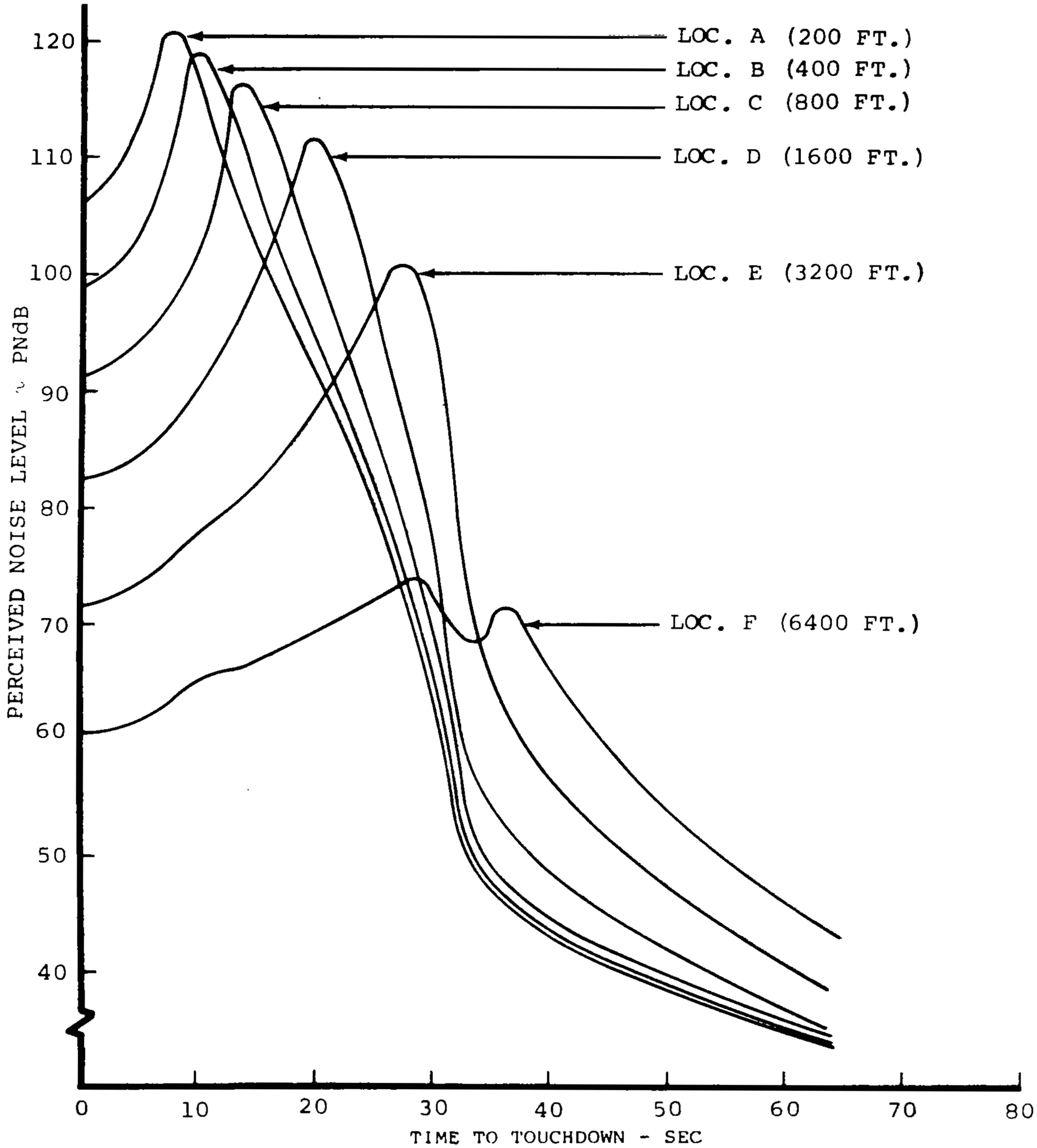

FIGURE V-24

MINIMUM TIME HIGH-SPEED HELICOPTER DESCENT

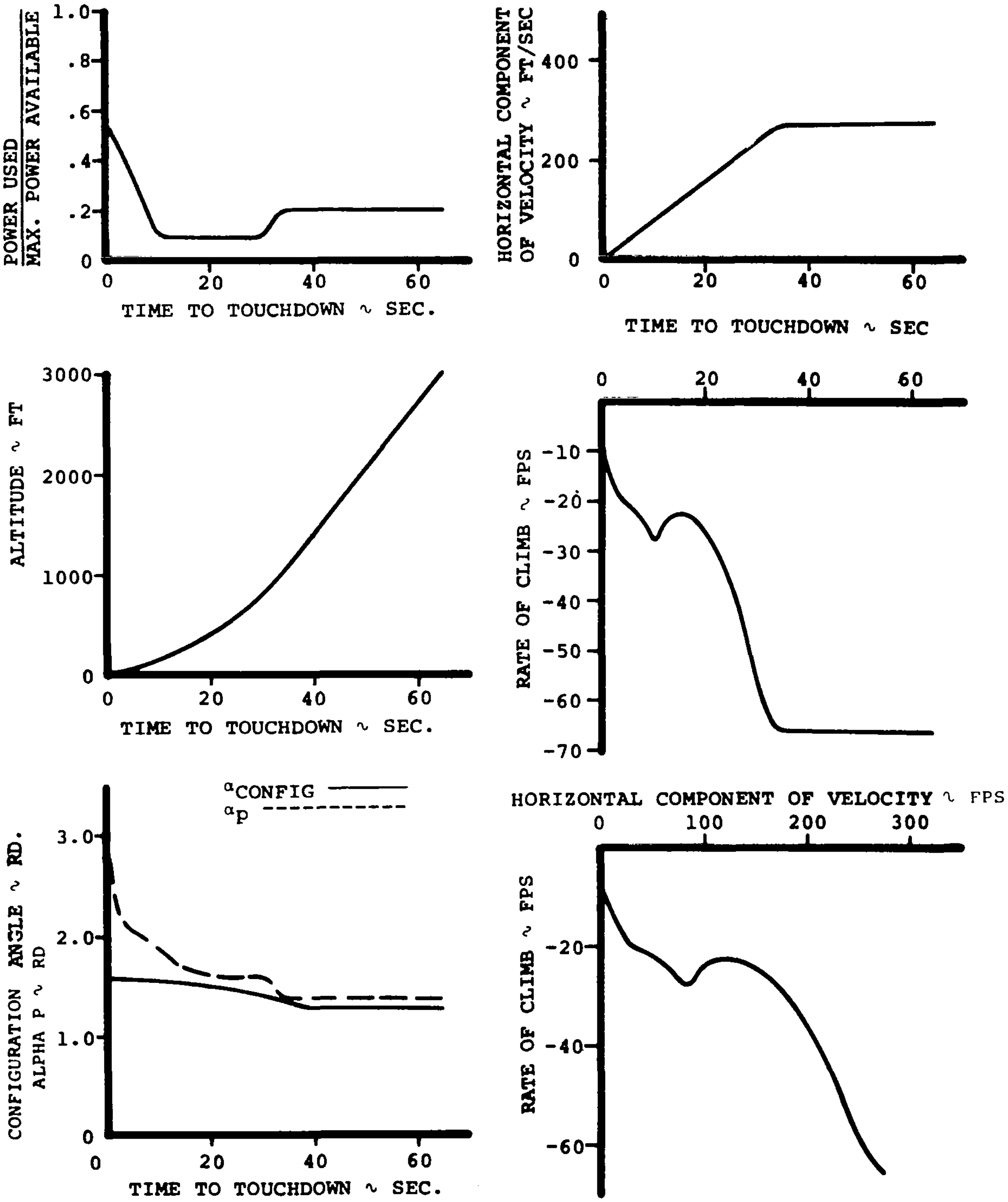

FIGURE V-25

MINIMUM TIME HIGH-SPEED HELICOPTER DESCENT

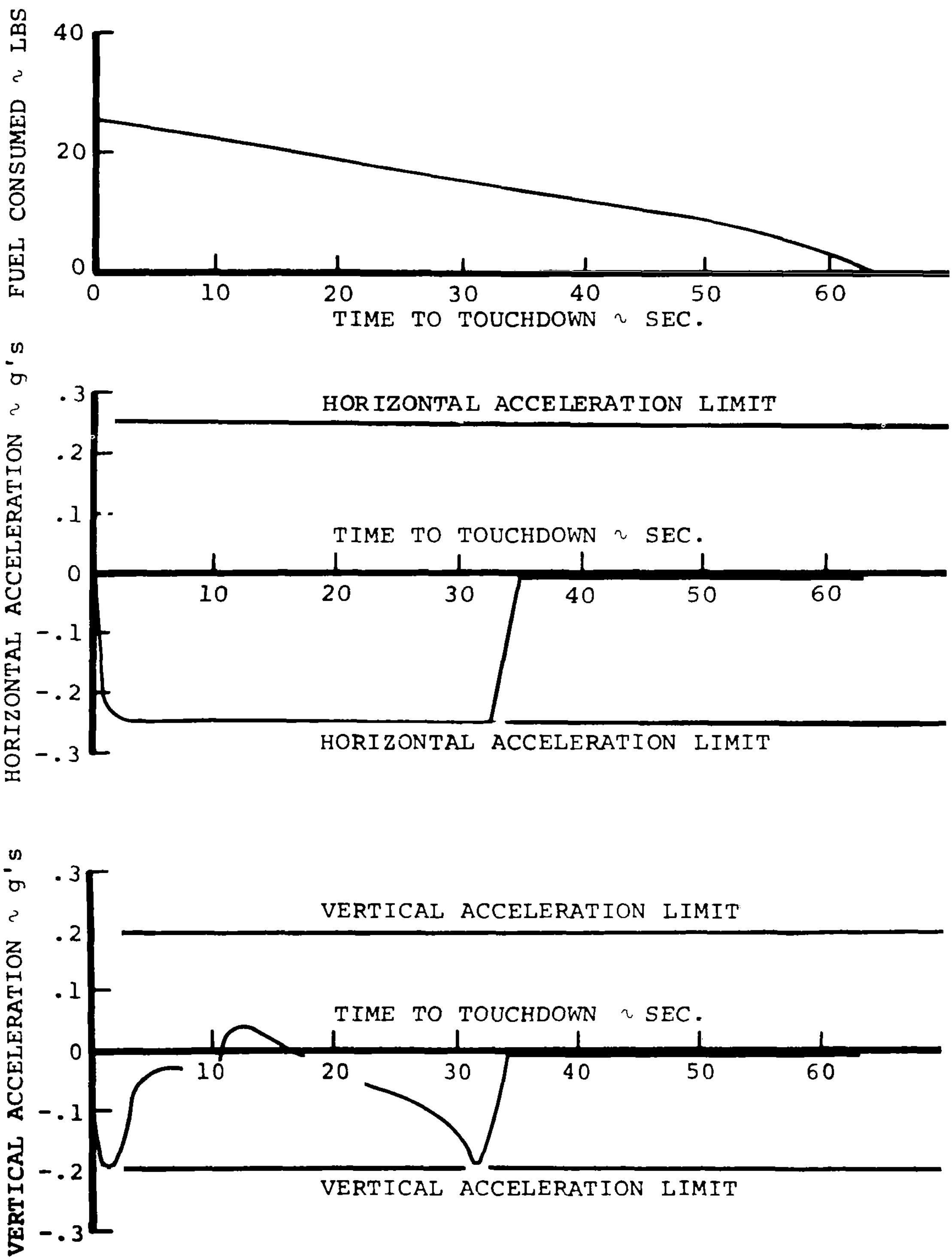

FIGURE V-26

Proposed Noise Abatement Profiles. - Flight paths which descend in a near vertical manner seem to offer the greatest potential annoyance reduction at distances which are close to the landing site. Therefore, each proposed landing noise abatement profile which is considered in this report incorporates a near vertical descent path as an integral part of its trajectory.

**PURE VERTICAL DESCENT:** Descent from 3000 feet in the helicopter configuration is the first noise abatement profile which is analyzed (Figures V-27 through V-30). The applied power is held at its minimum allowable value as the tilt-rotor maintains a steady sink rate at zero horizontal velocity. Near the landing point, maximum vertical acceleration is initiated and maintained to reduce the terminal rate of sink to 8 fps. Time histories of most of the important trajectory variables are illustrated in Figures V-29 and V-30. The rather large minimum applied power constraint is needed to prevent unrealistically high rates of pure vertical descent (see Appendix C).

Rotational noise constitutes a very important part of the acoustical spectrum (Figure V-27). Because low inflow conditions exist in this pure vertical descent trajectory, the sound pressure level of rotational noise decays slowly with increasing frequency. The rapid attenuation characteristics of vortex noise with increasing distance from the sound source is also clearly visible. Figure V-28 illustrates the very smooth variation in the perceived noise level with time at all six measuring locations. This is due to the fact that the tilt-rotor remains in the helicopter configuration for the duration of the vertical descent.

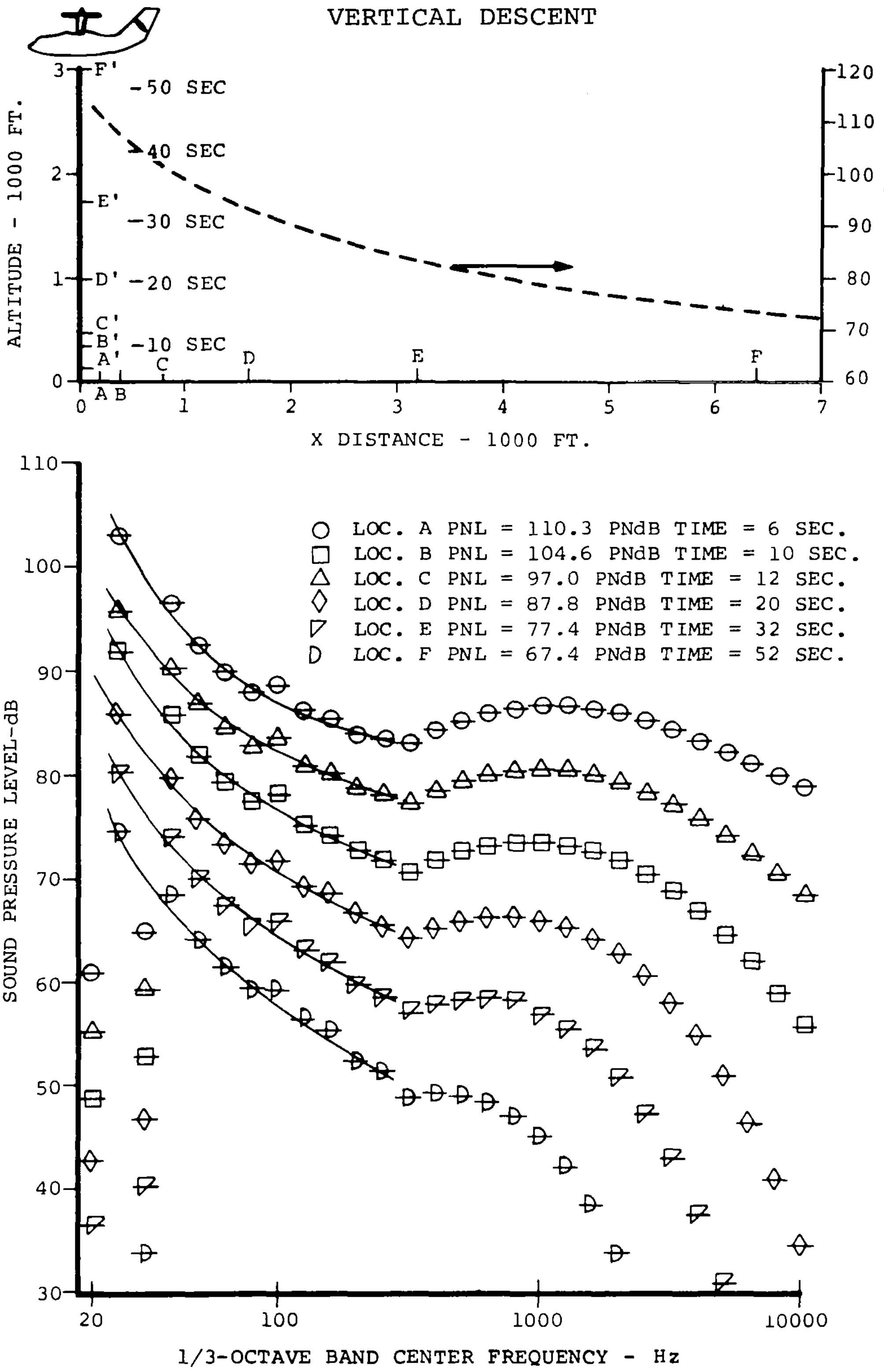
VERTICAL DESCENT

FIGURE V-27

VERTICAL DESCENT

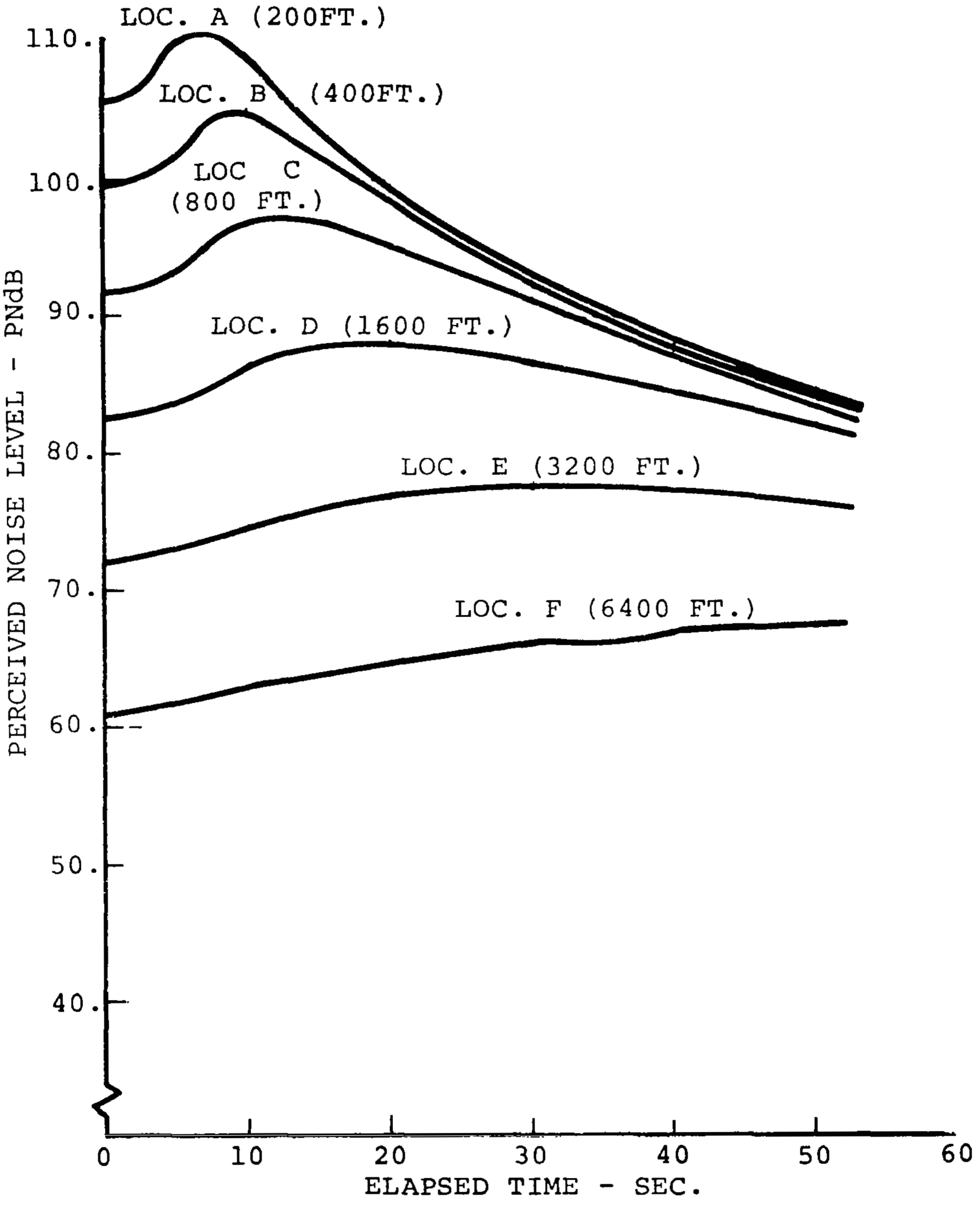

FIGURE V-28

VERTICAL DESCENT

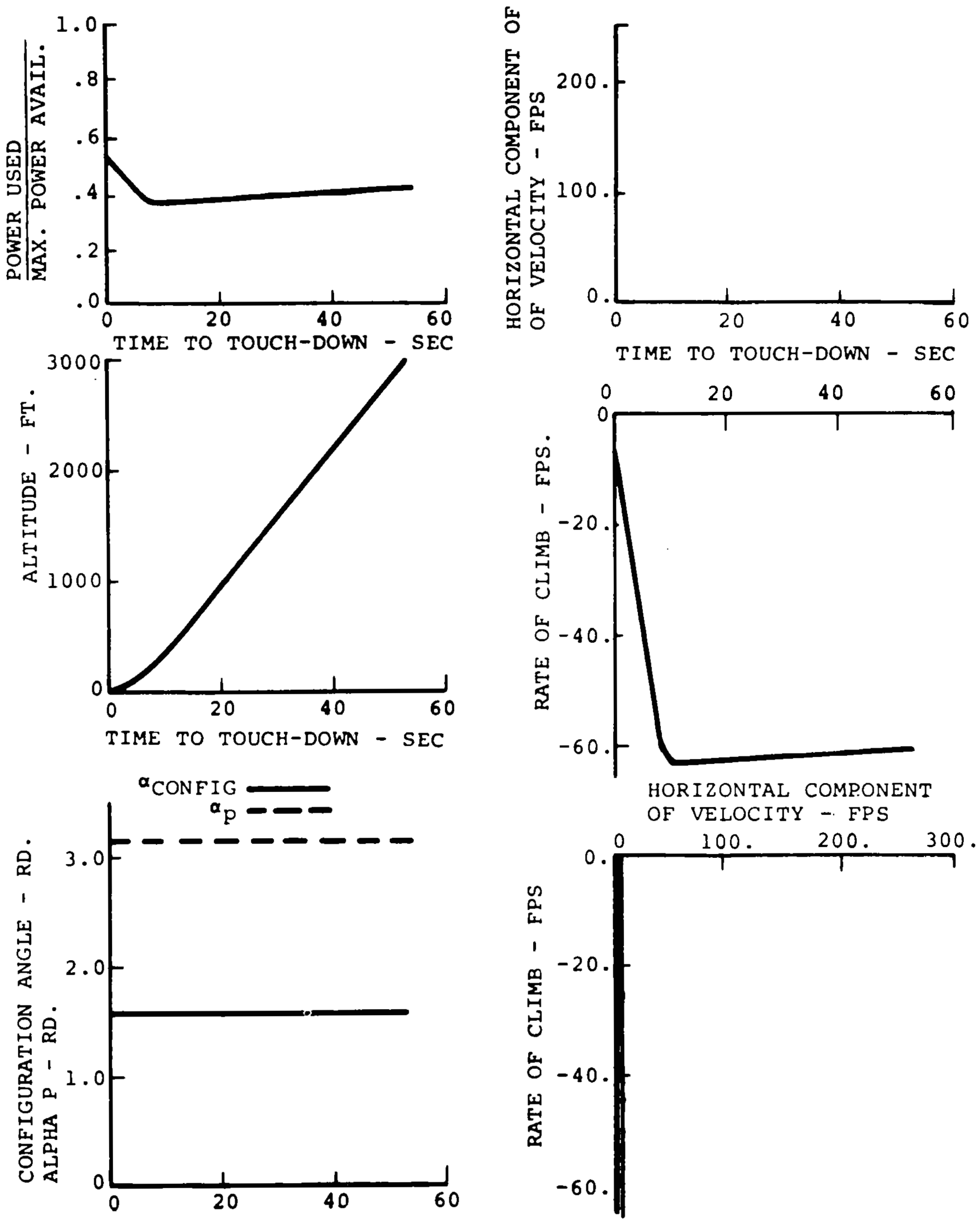

FIGURE V-29

VERTICAL DESCENT

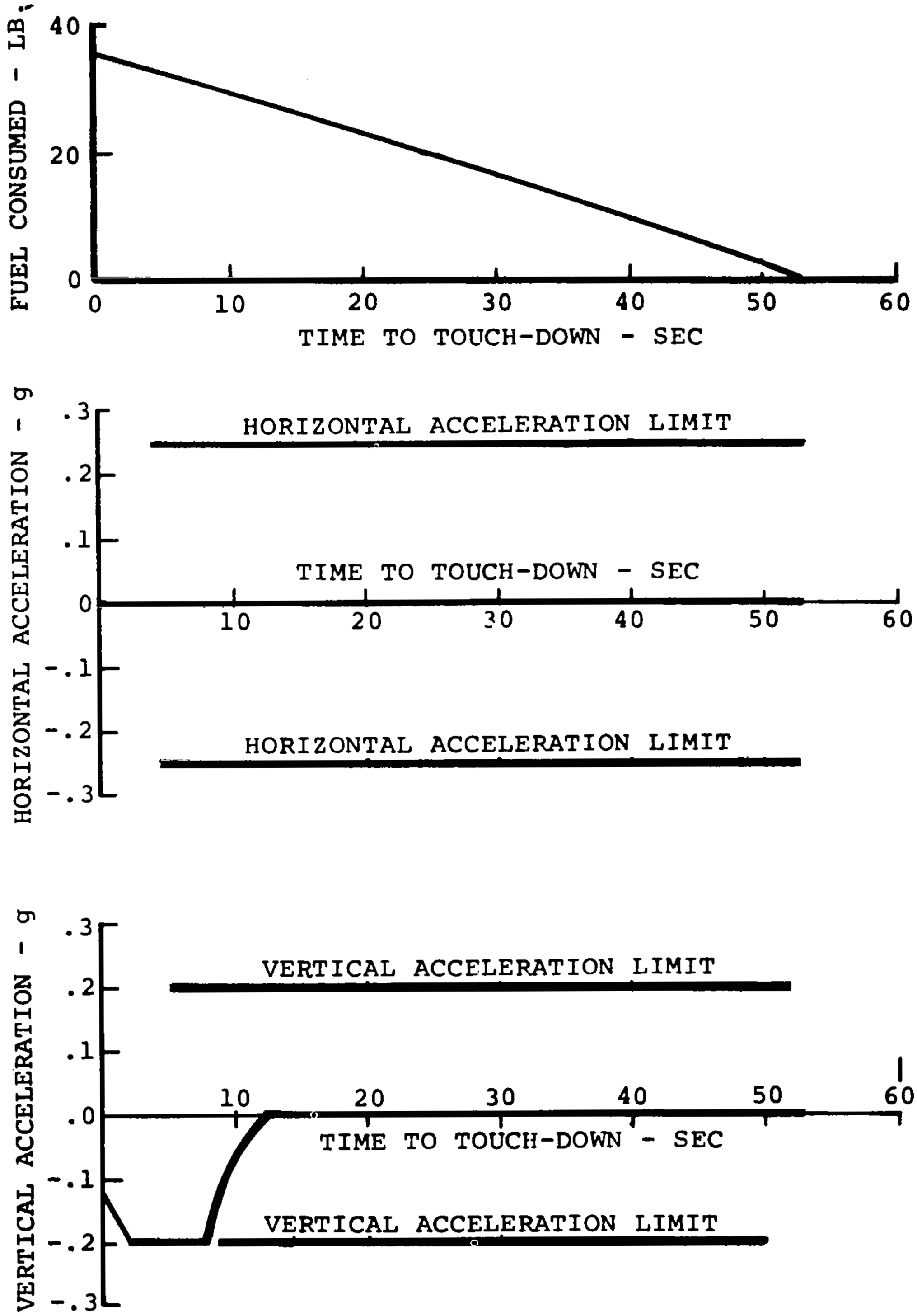

FIGURE V-30

Steady Horizontal Flight Followed by Vertical Descent: The second noise abatement landing profile which is considered in this report is graphically illustrated in Figures V-31 through V-34. It has, as one of its initial conditions, the horizontal distance from the landing point which results from flying the constrained optimal descent trajectory. Therefore, the resulting trajectory must pass directly over each noise measuring location. By directly comparing this second noise abatement profile with the restricted optimal trajectory, it is possible to evaluate the noise reduction benefits which arise by altering the flight path of the tilt-rotor aircraft.

Steady horizontal flight at 3,000-foot altitude in the aircraft configuration at the maximum lift-to-drag ratio of the aircraft is initially established (Figure V-33). At a later instant in time when the horizontal distance between the landing point and the position of the aircraft has been reduced, a maximum horizontal deceleration segment is initiated. Horizontal velocity decreases as the conversion from airplane to helicopter configuration occurs. The horizontal acceleration is reduced to zero at the instant in time when the vehicle has attained zero horizontal velocity directly above the landing site (Figure V-34). A maximum vertical acceleration maneuver is initiated slightly before zero horizontal velocity is achieved. The resulting flight path (Figure V-31) curves to a pure vertical descent segment in the last 44 seconds of flight. Maximum vertical descent rates are maintained until just before touchdown. The applied power is then increased, thus decreasing the terminal rate of sink at touchdown.

The last portion of this second noise abatement profile is identical to the preceding pure vertical descent case. Because most of the measured noise is generated in the low speed regime of the helicopter configuration, it is not surprising to notice that noise characteristics of both trajectories are quite similar (Figures V-27 and V-31). The slow decay of the amplitudes of rotational noise with frequency and the rapid attenuation of high frequency vortex noise with distance is apparent in both cases. The time history of perceived noise level (Figure V-32) for each measuring location illustrated the complex effects of performance during conversion and directivity. The many "peaks and valleys" in these curves are directly attributable to these complicating factors.

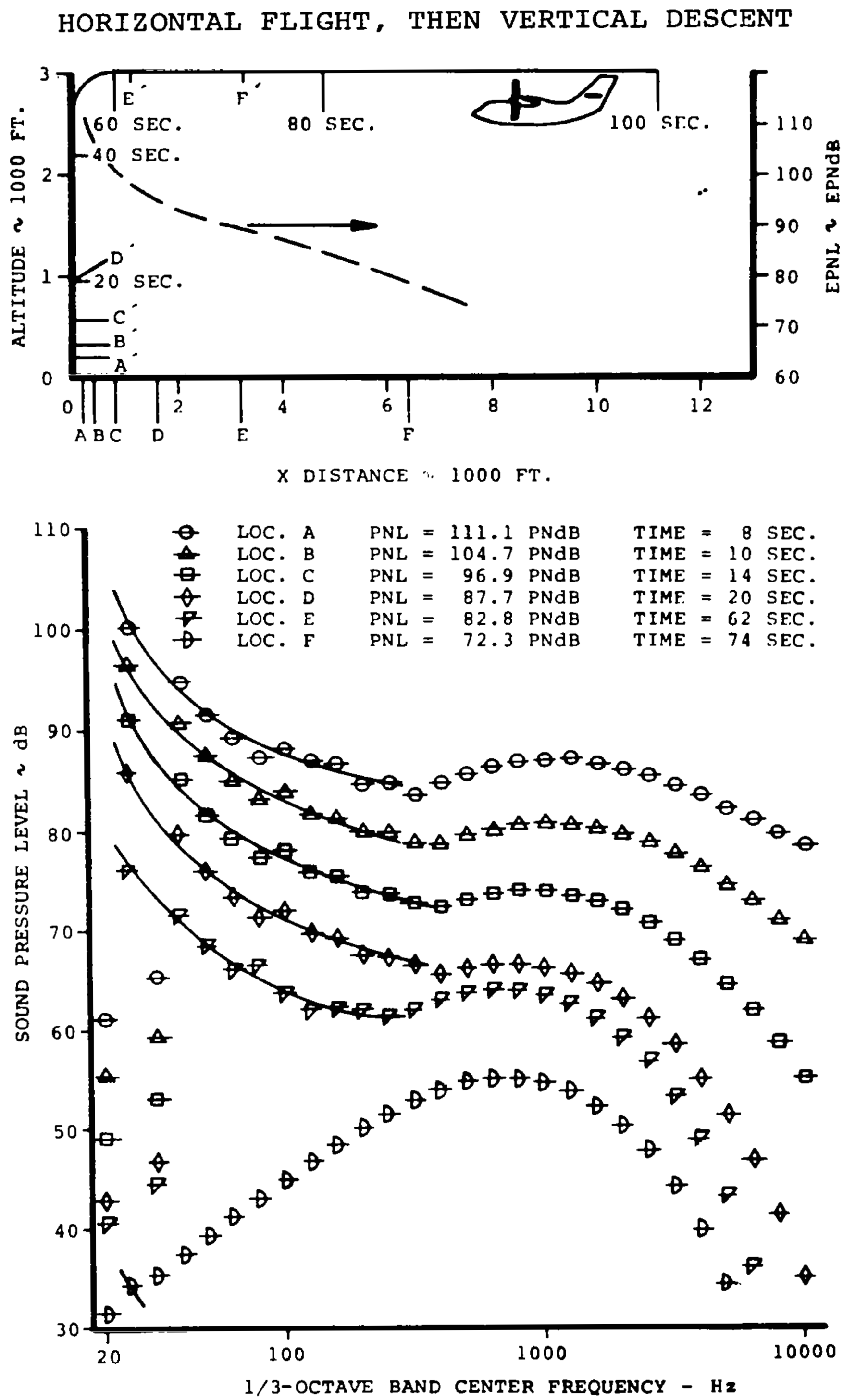
HORIZONTAL FLIGHT, THEN VERTICAL DESCENT

FIGURE V-31

HORIZONTAL FLIGHT, THEN VERTICAL DESCENT

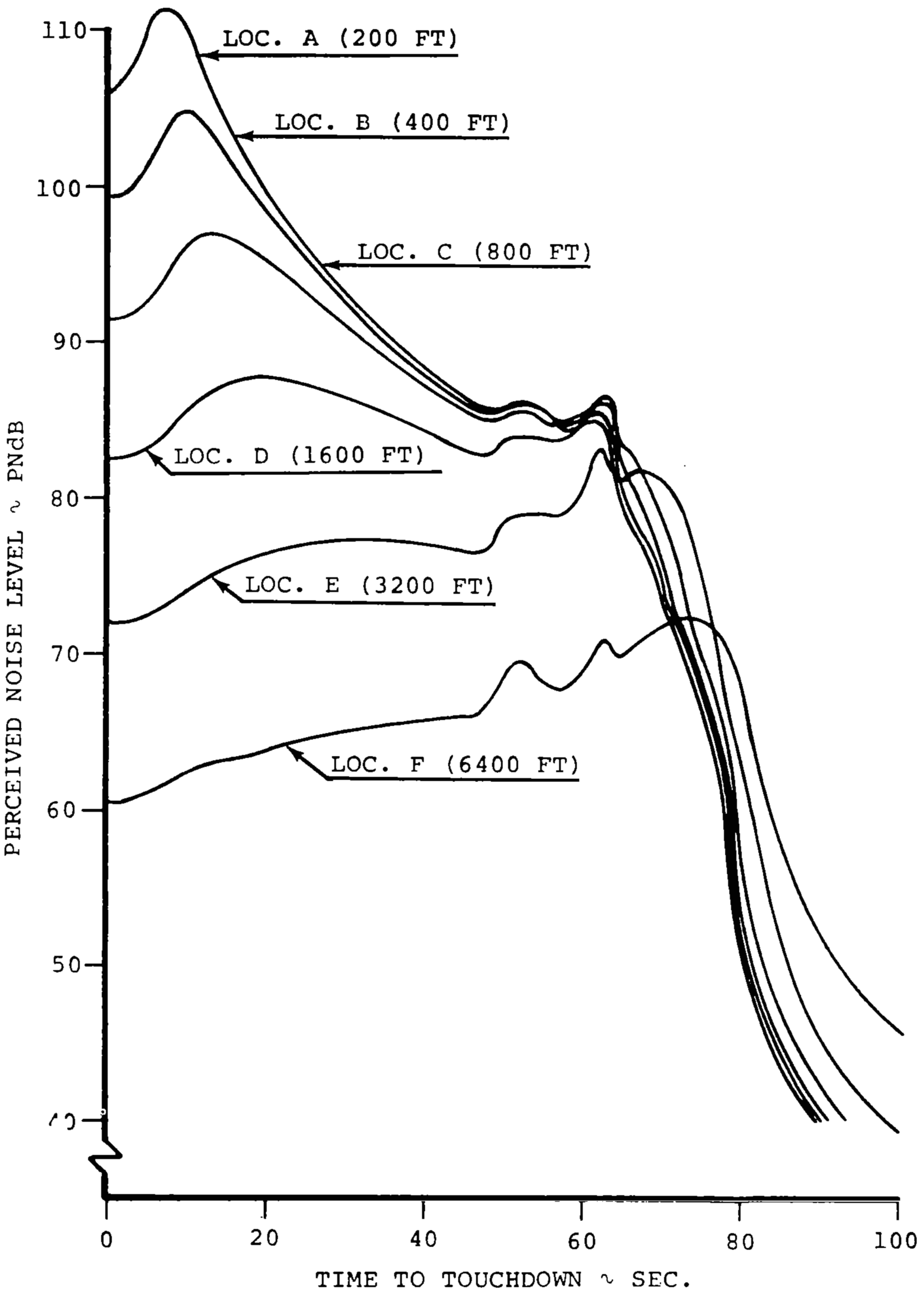

FIGURE V-32

HORIZONTAL FLIGHT, THEN VERTICAL DESCENT

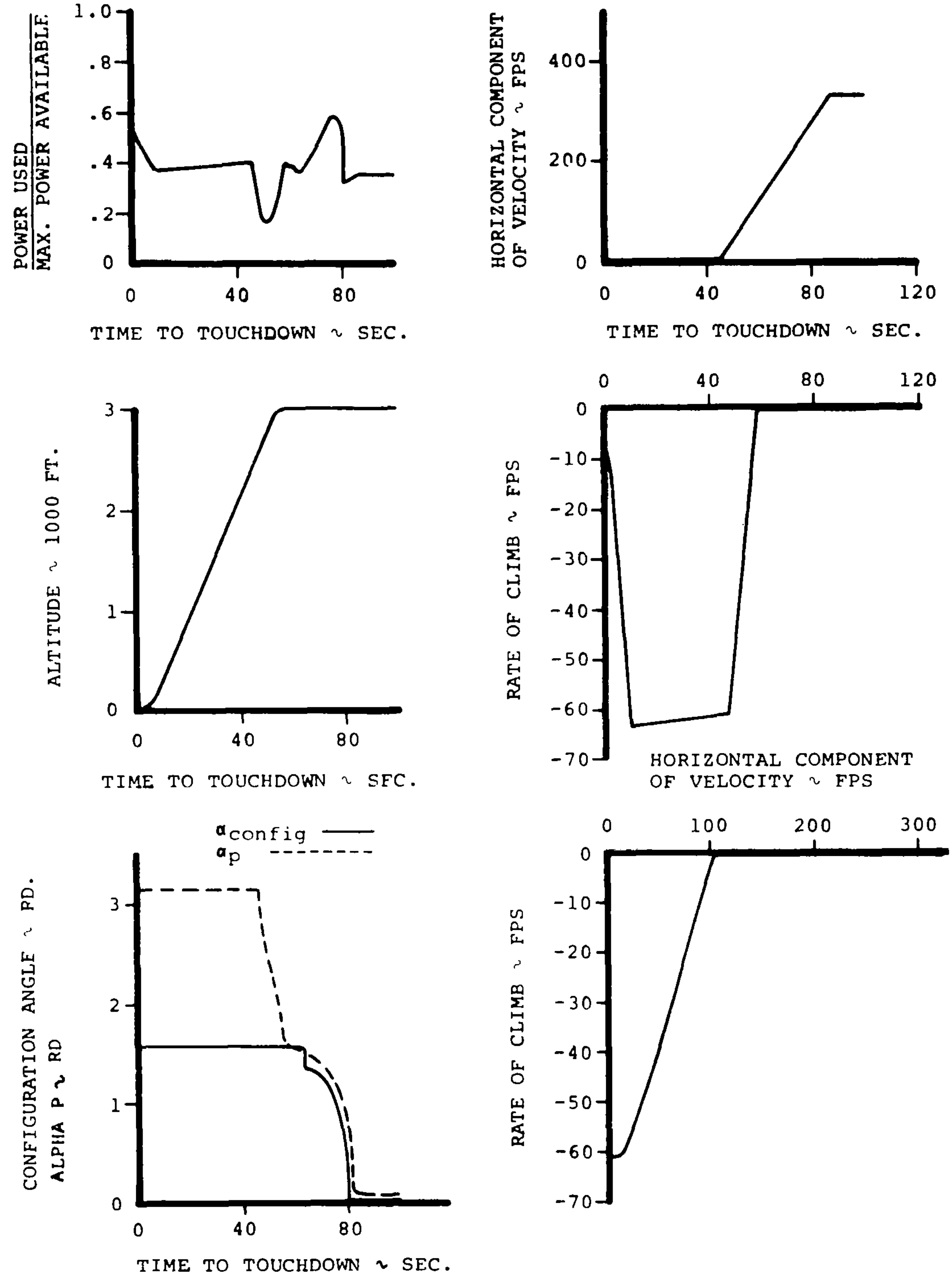

FIGURE V-33

HORIZONTAL FLIGHT, THEN VERTICAL DESCENT

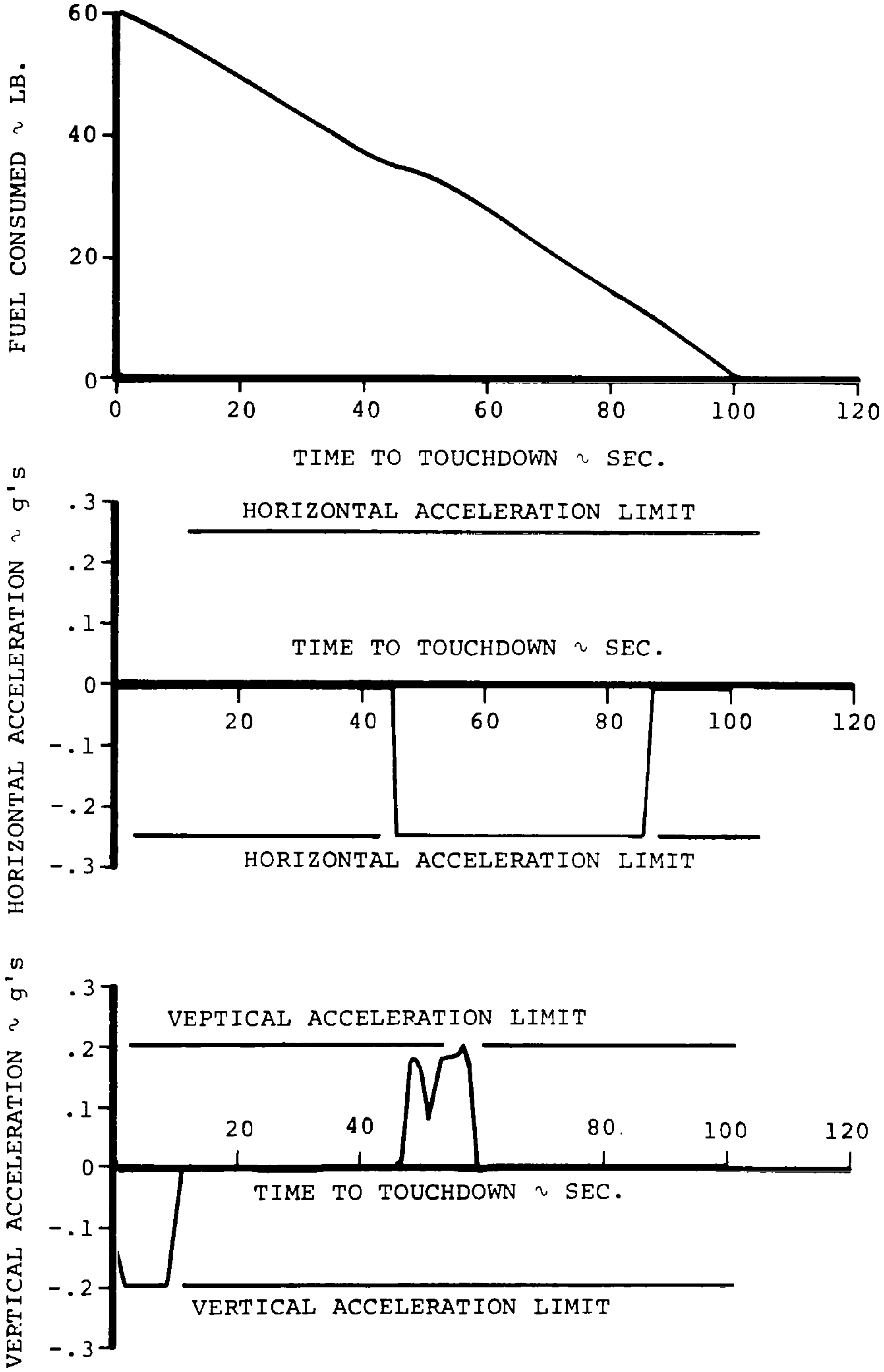

FIGURE VI-34

Maximum Performance Trajectory followed by a Near Vertical Descent (A Nonoptimum Noise Performance Descent): The third and last noise abatement profile which is considered is illustrated in Figures V-35 through V-38. It is almost identical to the constrained optimal trajectory which was presented in Figures V-23 through V-26. The only real difference between the two trajectories is that in this last trajectory, a near zero horizontal velocity is maintained during the last ten seconds of flight. During this time interval, high rates of sink are sustained because the applied power is at its minimum allowable limit. A near vertical flight path is generated for the last 1000 feet of descent (Figure V-35). The available power is increased near the terminal stage of descent in order to achieve the desired touchdown velocity.

The general characteristics of tilt-rotor noise which are generated by this flight profile are very similar to the acoustic characteristics of the restricted optimum trajectory. However, in this profile, higher altitudes near the landing point do significantly reduce the predicted perceived noise level at the first few ground locations. Unfortunately, no significant reduction in noise level was calculated at measuring locations which are located more than a mile away from the landing point.

MAXIMUM PERFORMANCE TRAJECTORY, THEN A NEAR-VERTICAL DESCENT

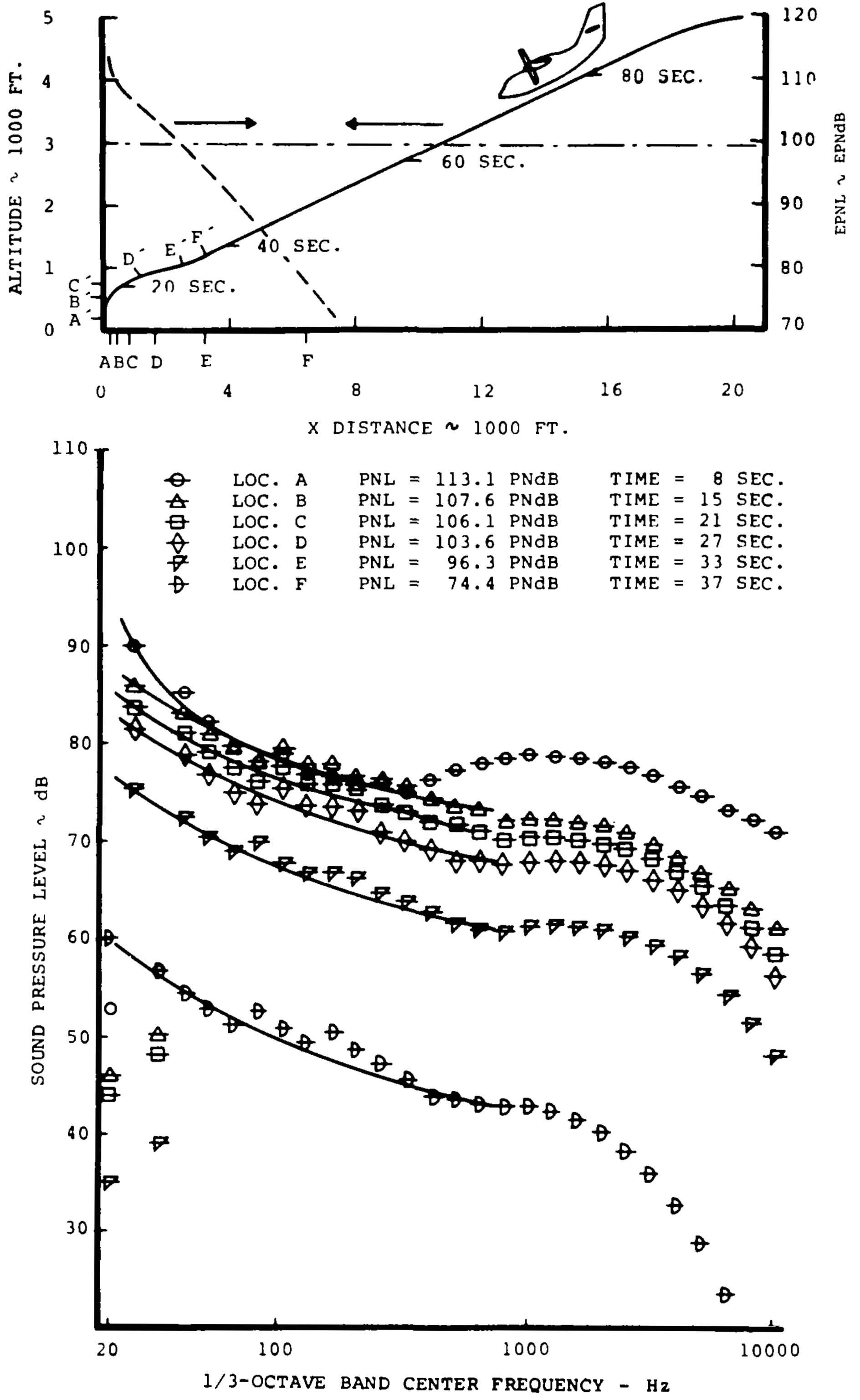

FIGURE V-35

MAXIMUM PERFORMANCE TRAJECTORY, THEN A NEAR-VERTICAL DESCENT

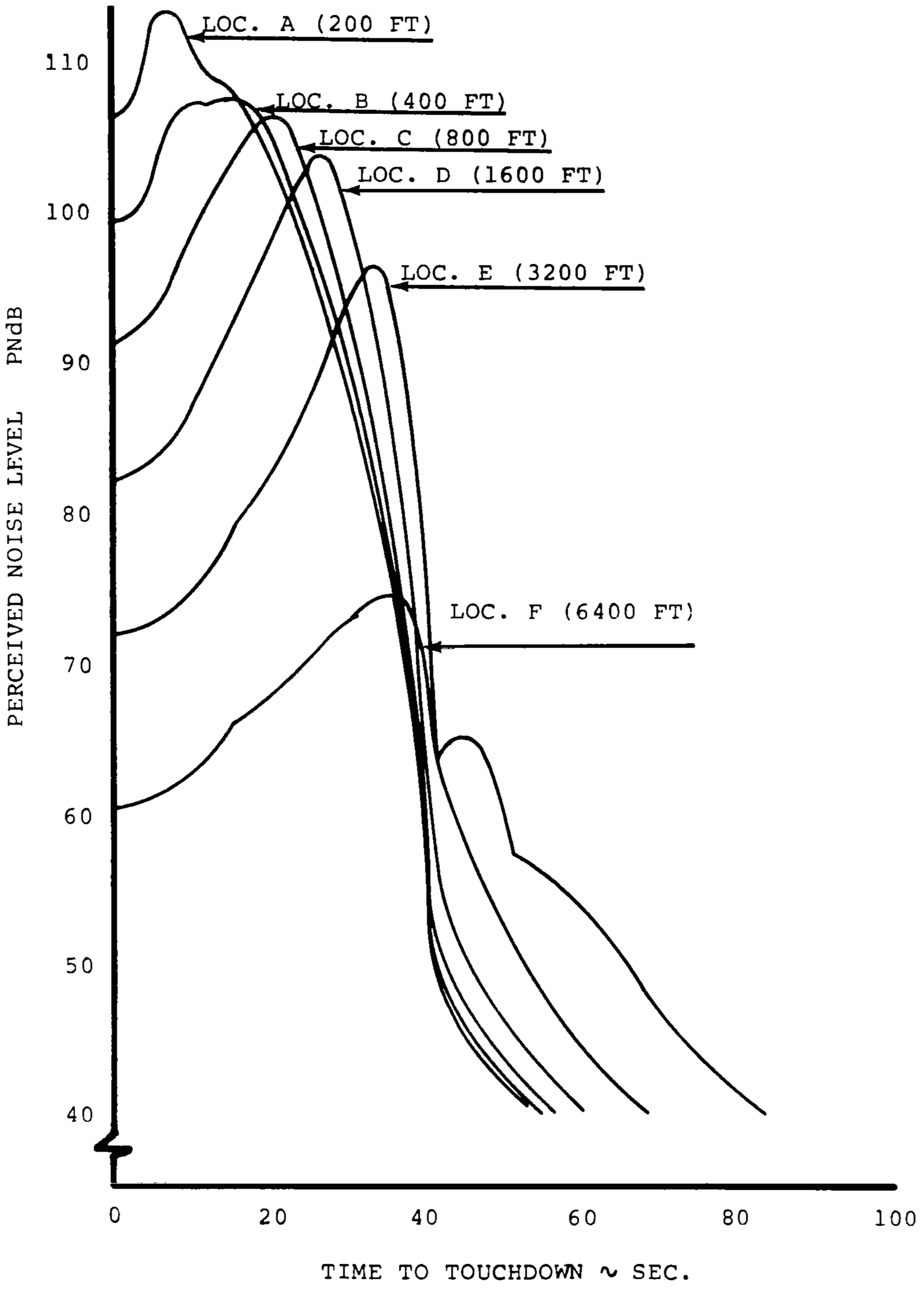

FIGURE V-36

MAXIMUM PERFORMANCE TRAJECTORY, THEN A NEAR-VERTICAL DESCENT

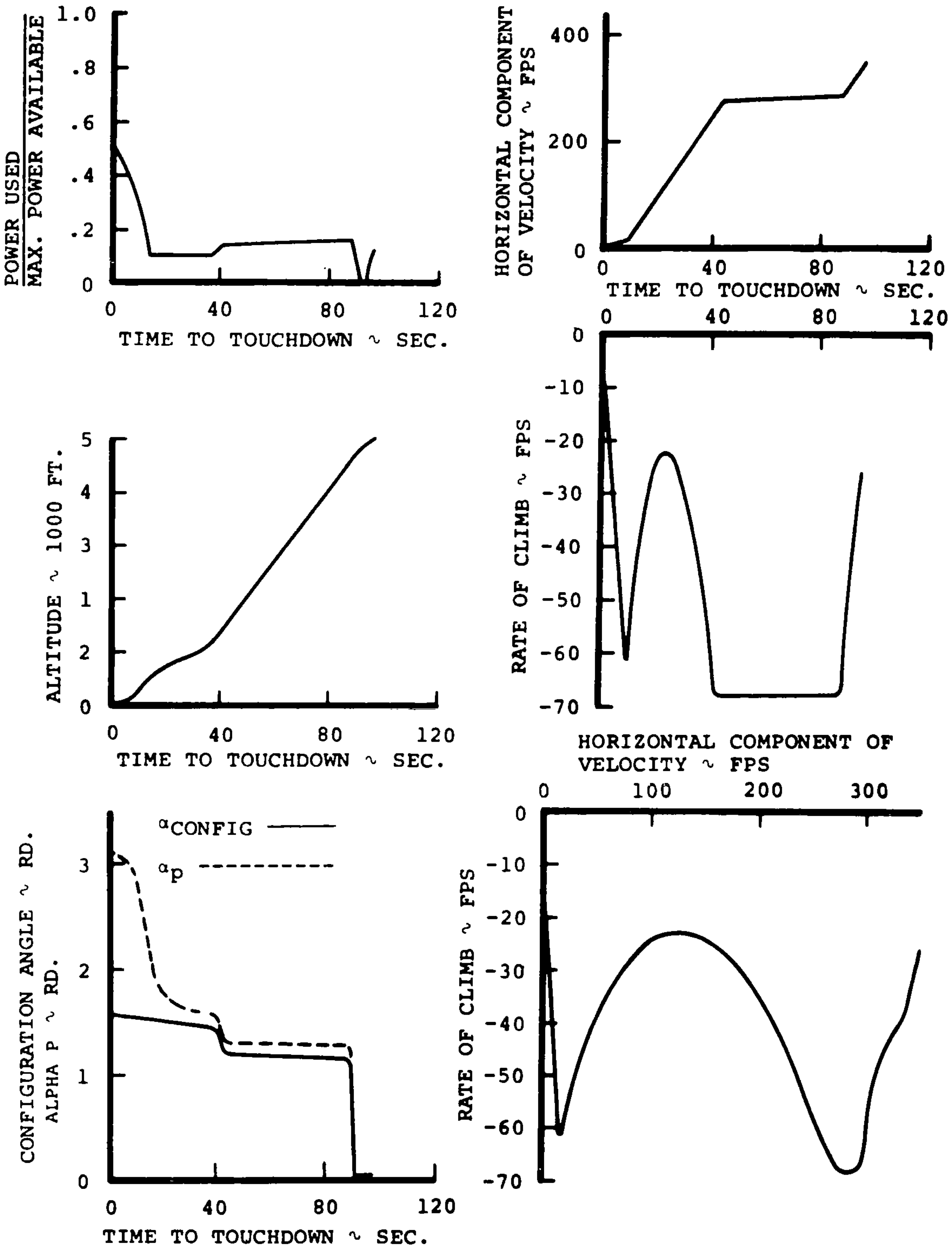

FIGURE V-37

MAXIMUM PERFORMANCE TRAJECTORY, THEN A NEAR-VERTICAL DESCENT

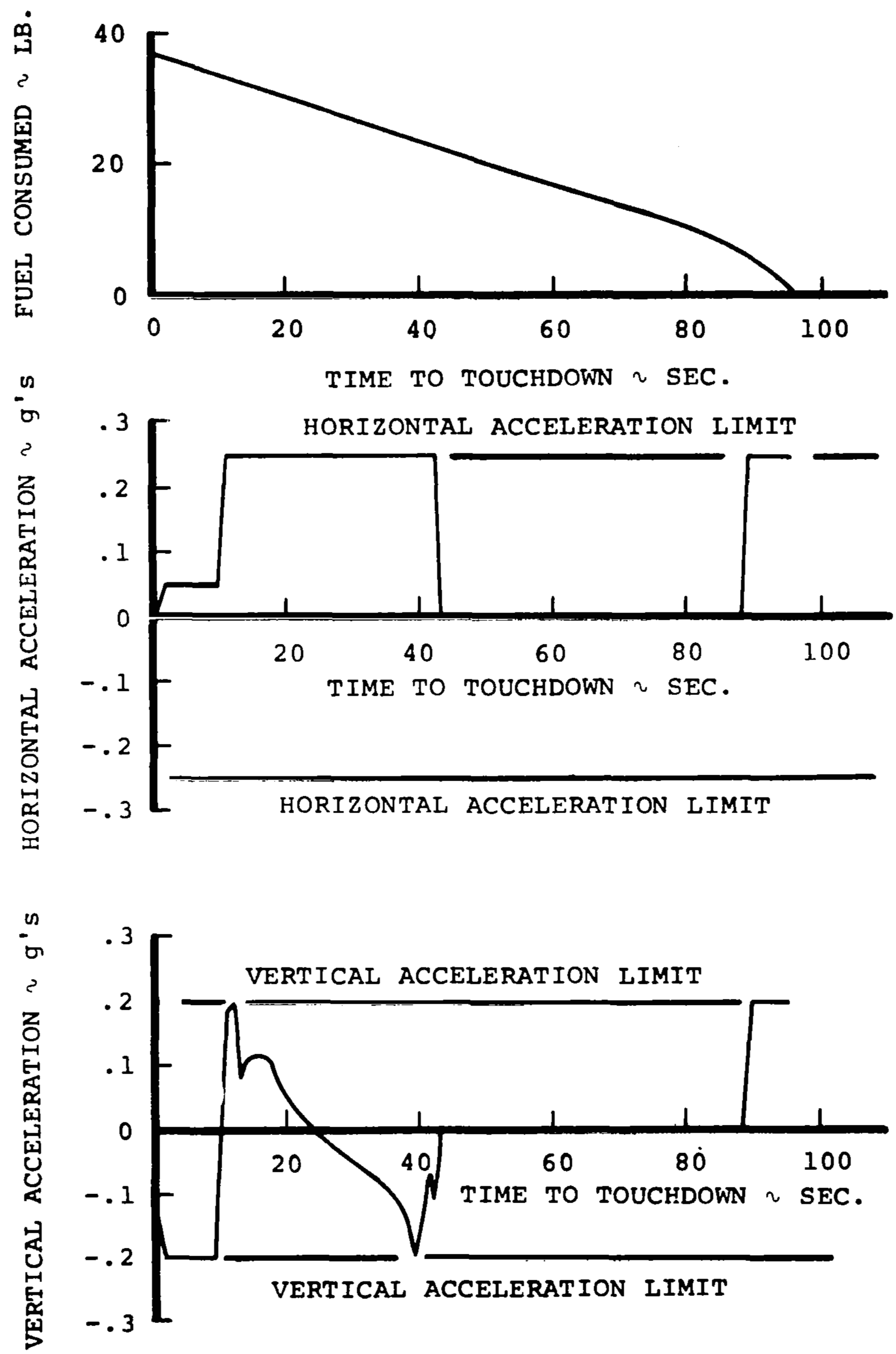

FIGURE V-38

## Review and Assessment of the Major Assumptions and Computational Techniques

The results which have been presented are really only as good as the performance and acoustical models which were used to generate them. Therefore, this section of the report presents a critical assessment of the major assumptions which were used in their development. For the purposes of this qualitative analysis, an assumption is considered to be "major" when it may significantly alter the final results presented.

The development of theoretical mathematical performance and acoustic models of a proposed tilt-rotor aircraft is admittedly a difficult task. Full-scale experiments which could be used to verify the predicted characteristics of the vehicle are not readily available. However, by using existing data from model tests and other full-scale data from vehicles which exhibit similar characteristics to the tilt-rotor aircraft in some mode of flight, a theoretical performance-acoustic model of a tilt-rotor aircraft was developed. Because experimental full-scale results could not be checked, the results which are presented more than likely contain some errors. However, the basic relationships between the noise and performance tradeoffs are thought to be correct. Therefore, it has been possible to draw some preliminary conclusions about the effectiveness of changing the flight path profile to maximize tilt-rotor performance and/or to reduce the noise measured near the landing point.

Performance Model. - Although accelerations parallel and perpendicular to the flight path have been used to bound the permissible flight envelope of the tilt-rotor aircraft, they have not been used directly in the performance equations. It has been assumed that a kinematic performance model predicts adequately tilt-rotor performance. Therefore, the power expended when the vehicle is accelerating from one equilibrium set of operating conditions to another is in error. However, it is analytically shown in Appendix D that this error is, in all probability, small and can be neglected for all practical performance considerations. Accelerations of less than, or equal to, .25g insure that in all flight trajectories of interest, the power required to accelerate the aircraft represents only a small fraction of the total. The assumption that accelerations do not directly affect the basic force balance equations also has some acoustical implications. Inaccurate thrust and drag computations will produce some inaccuracies in the calculated noise. However, because most of the calculated noise is produced when the rotor thrust-to-weight ratio is large, the relatively small difference between the thrust required in equilibrium flight and that required in accelerating flight cause small changes in the frequency content and overall level of the calculated sound (less than 2dB in most cases.

The descent performance of the tilt-rotor aircraft was governed entirely by performance limits. Unfortunately, the theoretical performance model presented in this report does not represent an in-depth study of those limits. Existing techniques were employed to predict, as well as possible, those critical constraints which govern tilt-rotor descent performance. But, more refined analysis and prediction techniques will undoubtedly change the magnitude of these very important constraints. However, the basic character of the rate of sink versus forward velocity curve will remain the same. Therefore, the results which have been presented do indicate the benefits that can be expected from flight path control. This study has not attempted to constrain tilt-rotor descent performance by pilot workload and aircraft handling qualities and a quantitative description of descent trajectories will await a more precise description of the tilt-rotor's constraints.

For simplicity in the development of the kinematic performance model, the flap deflection angle and the wing-lift to aircraft-weight ratio were programmed to be a function of horizontal velocity. These two inner loop controls were chosen to approximate the minimum power required of the tilt-rotor in steady level flight. However, these control settings are definitely not optimal in takeoff flight. High rates of climb create significant downloads at low forward speeds which degrade performance. Fortunately, only short periods of time are spent under these flight conditions. Therefore, gross errors in the determination of optimum flight profiles are unlikely. More optimal trajectories could be determined numerically by optimizing all four independent control variables ($\eta$, $\overline{U}$, $\delta_f$, $\theta$). However, the problem immediately becomes an order of magnitude more difficult.

Acoustic Model. - Many simplifying assumptions have been made which may affect the acoustic results which have been presented. Many of these assumptions have been made because a more accurate mathematical representation of tilt-rotor noise does not presently exist. Therefore, the preceding acoustic results should be interpreted as trends and should not be considered to represent absolute sound levels.

It has been assumed that rotor harmonic loading is dependent upon the rotor's operating state. An empirical relation between these operating states and a harmonic "loading law" was derived based upon a limited amount of preliminary data. This loading law was used to predict the rotational noise which was produced by the tilt-rotor aircraft. More accurate prediction of rotational noise is dependent upon further improvements in rotor harmonic loading prediction.

The empirical relation which was used in this report to predict vortex noise is currently under investigation. Its validity has been seriously questioned at small values of thrust. However, because most of the acoustic results which have been presented are calculated under high thrust conditions, this limitation is not considered to be too serious.

Subjective Assessment of Rotor Generated Noise. - The perceived noise level (PNdB) and the effective perceived noise level (EPNdB) are the two subjective assessments of VTOL annoyance which are employed in this report. An endorsement of these subjective noise measures is not intended. They are simply a commonly employed measure of annoyance.

Functional Expansion Approach Applied to Trajectory Optimization Problems. - The application of AESOP to determine optimum trajectories of the kinematic trajectory model of the tilt-rotor aircraft was more difficult than originally anticipated. Large amounts of computer time were expended as each iteration of AESOP gained very small increases in performance. Fortunately, many of the optimum trajectories could be located within engineering accuracy by using the graphical arguments which were outlined in Appendix D. Some of the hypotheses concerning the reasons why AESOP did not always efficiently optimize this parametric trajectory optimization problem are discussed below.

AESOP is basically a parameter optimization subroutine. In order to optimize the kinematic tilt-rotor mathematical performance model, the optimization problems were formulated as parameter optimization problems. A functional expansion of both independent control variables $\eta_c(t)$ and $\bar{u}(t)$ as a Fourier series with a finite number of coefficients was employed. (See Section IV, eqs. IV-2 and IV-3). A Fourier series was chosen because it possesses the property of orthogonality and the ability to represent sharp corners in control space with a reasonable number of harmonic constraints. Performance inequality constraints consist of control bounds which are a function of time only. When the Fourier series expansion of the control time histories violated an inequality constraint, the value of the constraint was directly used as the allowed control time history. Terminal boundary conditions upon the state were enforced by adding a weighted penalty function directly to the performance index.

The Fourier coefficients of the functional expansion were not independent of one another. Changes in one coefficient directly affected the optimum choice of other coefficients. However, the magnitude of the higher order coefficients began to decrease, indicating that only four terms of each control function were adequate to represent the optimal tilt-rotor takeoff trajectory. Unfortunately, no mathematical criteria was available to judge whether this observation is quantitatively correct.

The determination of optimum landing trajectories was more difficult than that of takeoff. Excessive computer time was required to determine trajectories which, in some cases, were less optimal than those computed by following the control time histories suggested in Appendix D. The apparent lack of success of this approach is believed to be caused by two factors: the minimum time constraint surface (the rate of sink curve, see Figure II-15) exhibits three possible local minima; and the control time history frequently intersected control inequality constraints. Both of these factors complicated the optimum performance problem to the point where the functional expansion approach did not appear to converge. Only slight decreases in the magnitude of the higher order expansion coefficients were noted. Furthermore, each optimum expansion coefficient appeared to be very sensitive to the optimum values determined for the other coefficients.

A better method to locate optimum landing trajectories was used toward the closing stages of this work. Engineering judgment and insight was first used to estimate the control time histories of the optimum trajectories. Once this first estimate was found, the functional expansion approach, together with AESOP were used to improve the estimate of the optimal trajectory. Convergence to an optimum, although not spectacular, was improved.

In general, it is definitely attractive to be able to use a generalized optimization tool like AESOP to solve optimization problems because the programming task is considerably lessened. However, because the pecularities of each specific problem formulation have not been included in the optimization procedure, rather long computer times are to be expected. Furthermore, if the performance surface is not smooth and well behaved, and additional inequality constraints must also be enforced, considerable difficulty may be experienced in finding optimal trajectories.

## VI. CONCLUSIONS AND RECOMMENDATIONS

1. System studies of noise and performance emphasize and explore the basic tradeoffs which are possible with proposed VTOL aircraft. They indicate potential operational and design methods to improve overall system performance.

2. Significant noise reductions (compared with optimal-performance trajectories) can be obtained by controlling the flight path of VTOL aircraft near the terminal area. For the tilt-rotor aircraft considered in this report, a reduction of up to 7 EPNdB is realized during takeoff (at ground positions located close to the takeoff point) if an almost-vertical

flight profile is flown. Up to a 10-EPNdB reduction during landing is also possible through flight path control.

3. Noise-abatement trajectories may significantly increase both the time of flight and total fuel consumed during takeoff and landing. However, because the tilt-rotor is basically a low-power-loading aircraft, the total fuel consumed is only a small fraction of the aircraft's useful load.

4. The highest level of noise generated by the tilt-rotor aircraft occurs in the helicopter mode of flight where the thrust is the largest. Furthermore, these high thrusting conditions are generated in close proximity to the takeoff and landing points. For example, in the "minimum time to climb to 3000 feet" (Figure V-3), the perceived noise level at all measuring locations is greater than 100 PNdB when the aircraft is less than 2000 feet from the takeoff point and below 1000 feet in altitude.

5. Increasing the applied power during takeoff effectively decreases the noise level heard on the ground by more rapidly increasing the distance between the sound source and the observer. Although the noise initially increases slightly at these higher power levels, the increasing distance resulting from higher integrated rates of climb dominates. Increasing the applied power during takeoff also reduces the total fuel and time required to attain a specified altitude.

6. Parametric optimization techniques can most easily be applied to dynamic optimization problems if relatively few inequality constraints are enforced. Introducing these constraints significantly reduces the rate of convergence to a global optimum.

7. To quantitatively define optimal-landing-performance trajectories, an accurate assessment of a VTOL's rate-of-descent boundaries is required. At the present time, additional experimental and theoretical efforts are necessary to more clearly define the descent limitations of the tilt-rotor aircraft.

8. Continuing theoretical and experimental research is needed to improve quantitative predictions of prop-rotor noise. In particular, a more thorough analysis and verification of the influence of the rotor's operating state on noise generation is required.

9. Methods of predicting subjective response to rotor noise warrant continued research so that a better means of establishing far-field subjective acoustic criteria for rotary-wing aircraft are provided.

# APPENDIX A

## DESIGN CHARACTERISTICS OF THE "VERTOL 160" TILT-ROTOR AIRCRAFT

### Rotor. -

| | |
|---|---|
| Number of Blades per Rotor | 3 |
| Rotor Diameter | 55 ft |
| Solidity at 0.75R | 0.0857 |
| Disc Loading | 9.7 lb/ft$^2$ |
| Tip Speed | 750 fps |
| Rotational Frequency | 27 radians/sec |

### Wing. -

| | |
|---|---|
| Area | 585 ft$^2$ |
| Airfoil | NACA $63_4421$(Modified) |
| Aspect Ratio | 7.9 |
| Wing Loading | 80 lb/ft$^2$ |
| Span | 67.8 ft |

### Horizontal Tail. -

| | |
|---|---|
| Area | 212.5 ft$^2$ |
| Airfoil | NACA 0015 |
| Aspect Ratio | 4.24 |
| Span | 30.0 ft |

### Vertical Tail. -

| | |
|---|---|
| Area | 138 ft$^2$ |
| Airfoil | NACA 0015 |
| Aspect Ratio | 1.02 |
| Span | 11.67 ft |

### Weight. -

| | |
|---|---|
| Gross Weight | 46 200 lb |
| Weight Empty | 29 220 lb |
| Fixed Useful Load | 669 lb |
| Fuel | 4 311 lb |
| Payload | 12 000 lb |

### Propulsion Characteristics. -

| | |
|---|---|
| Number of Engines | 2 |
| Type of Engines | Lycoming LTC4B-12 |
| Max. Rated hp (Static) at S.L. Std. | 4450 hp/engine |

This page intentionally
left blank

# APPENDIX B

# NUMERICAL SOLUTION OF THE KINEMATIC PERFORMANCE EQUATIONS

A solution to the kinematic performance equations (eqs. II-47 to II-55) is complicated by two major factors. The solution, if it exists, may or may not be unique due to the nonlinear nature of the performance equations. Secondly, some of the unknowns appear implicitly in the performance equations; therefore, it is impossible to analytically solve for some unknowns in terms of other known variables. Iterative solution techniques are required.

Fortunately, a solution to these equations can be approached in a very straightforward manner. The differential and algebraic equations are conceptually uncoupled from one another. At the first instant in time, the algebraic performance equations are iteratively solved. The differential equations are then numerically integrated to the next position in time and the algebraic equations are again iteratively solved. The initial values chosen for the new iteration are the final values of the previous one. This procedure continues until the chosen terminal condition is satisfied. A conceptual block diagram of this solution procedure is presented in Figure B-1.

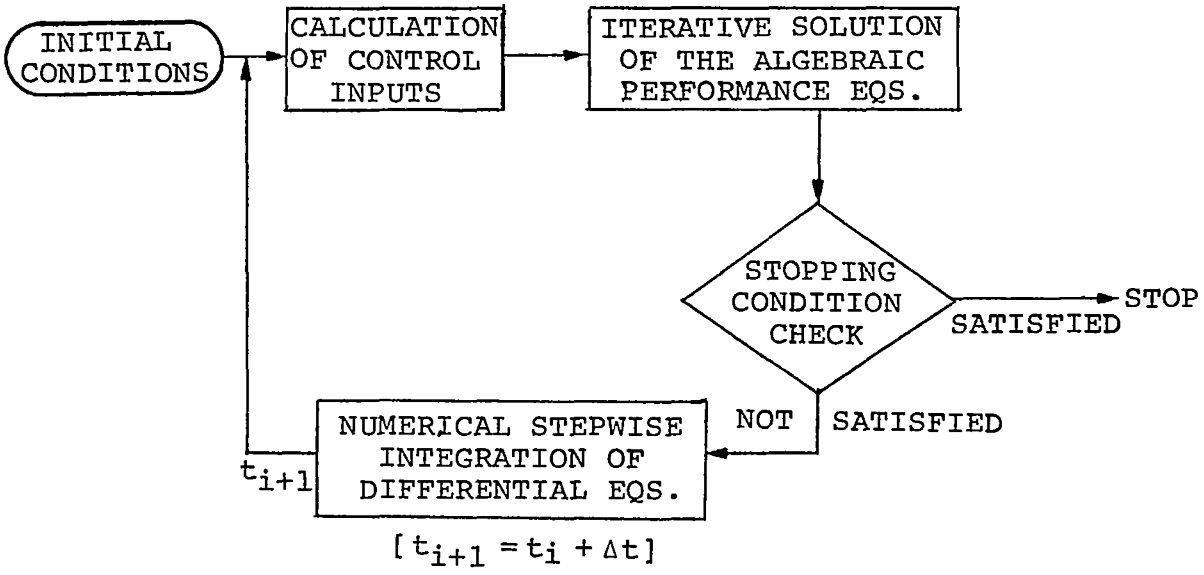
INITIAL CONDITIONS
CALCULATION OF CONTROL INPUTS
ITERATIVE SOLUTION OF THE ALGEBRAIC PERFORMANCE EQS.
STOPPING CONDITION CHECK
SATISFIED
STOP
NOT SATISFIED
NUMERICAL STEPWISE INTEGRATION OF DIFFERENTIAL EQS.
$t_{i+1}$
$[t_{i+1} = t_i + \Delta t]$

Figure B-1

Many well-known subroutines exist which will integrate a system of first order differential equations to a specified degree of accuracy (ref. 30). For simplicity, a trapezoidal rule integration routine is used in this analysis. A more accurate determination of the aircraft's flight path may be obtained by using a higher order integration subroutine.

The drag, lift, $C_L$, momentum and power balance equations must be solved at each discrete time step by iterative techniques. These five algebraic equations in ten unknowns are functionally represented by eqs. II-47 → 51. At an instant in time, the state variable H is specified along with the four control variables, $\overline{u}$, $\eta_c$, $\theta$, $\delta_f$. The remaining five unknowns are obtained by iteratively solving the five governing algebraic equations.

A numerical solution is facilitated by making the following assumption: the power control only influences the rate of climb or sink of the aircraft. This simplification allows the power equation to be uncoupled from the two force-balance equations, the $C_L$ equation, and the momentum equation.

The justification for assuming that the applied power only influences the steady-state rate of climb is made on purely physical grounds. If the horizontal velocity is specified along with the flap and attitude angles, an increase in applied energy per unit time must result in an added rate of climb. Notice that if the variables $\overline{V}$ and $\gamma$ had been retained as control variables, then an increase in the applied power at a chosen velocity in near-hovering conditions would never allow a power balance to exist. The total velocity vector, $\overline{V}$, would constrain the power available control, $\eta_c$. Thus, the assumption that both controls are independent would no longer be valid. Therefore, it is necessary to introduce the variable $\overline{w}$ and the independent control variable $\overline{u}$.

The independent control variables of the five algebraic performance equations are $\overline{u}$, $\eta_c$, $\theta$, and $\delta_f$. A diagramatic sketch of how a solution is found is given in fig. B-2. The iteration procedure is decoupled into two loops: an inner loop which satisfies the two force balance equations, the $C_L$ equation, and the momentum equation; and an outer loop which satisfies the power balance equation.

If an estimate of the vertical velocity ($\overline{w}$) is made, an inner loop solution can be found by iteratively solving the algebraic steady-state performance equations. Because the control variables $\overline{u}$, $\theta$, and $\delta_f$ are specified, a solution to the four equations in four unknowns can be found.

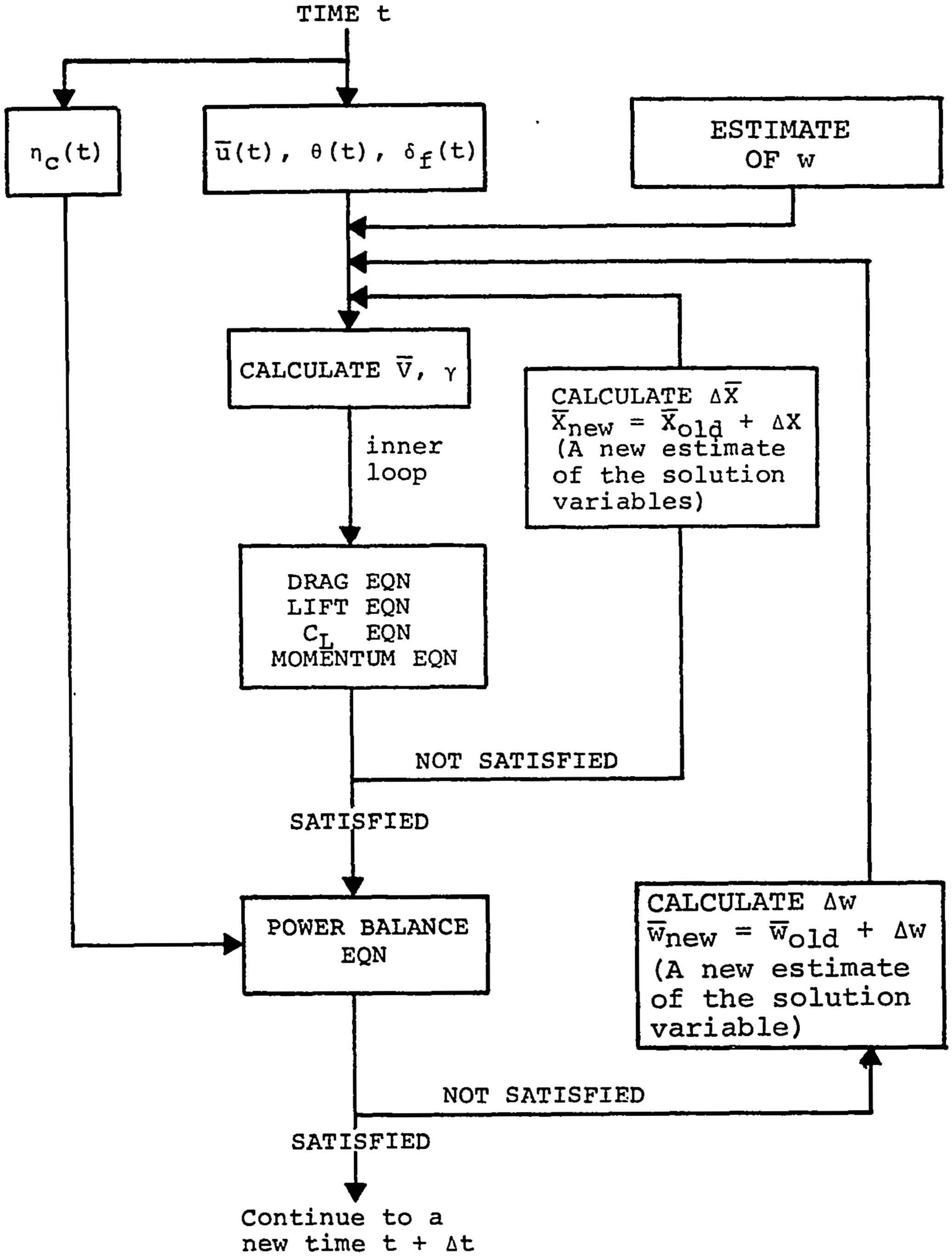
TIME t
$\eta_c(t)$
$\overline{u}(t)$, $\theta(t)$, $\delta_f(t)$
ESTIMATE OF w
CALCULATE $\overline{V}$, $\gamma$
inner loop
CALCULATE $\Delta\overline{X}$ $\overline{X}_{new} = \overline{X}_{old} + \Delta X$ (A new estimate of the solution variables)
DRAG EQN
LIFT EQN
$C_L$ EQN
MOMENTUM EQN
NOT SATISFIED
SATISFIED
POWER BALANCE EQN
CALCULATE $\Delta w$ $\overline{w}_{new} = \overline{w}_{old} + \Delta w$ (A new estimate of the solution variable)
NOT SATISFIED
SATISFIED
Continue to a new time t + Δt

Figure B-2

The power balance equation is depicted in the outer loop of Figure B-2. A Newton-Raphson procedure is used to improve the guess of the vertical velocity, $\overline{w}$, until the power equation (eq. II-51) is satisfied. The Newton-Raphson algorithm for this scalar becomes

$$\overline{w}_{new} = \overline{w}_{old} + \Delta\overline{w}$$

where $$\Delta\overline{w} = -Y/(\partial f_5/\partial\overline{w})\Big| .$$

The partial derivative $\partial f_5/\partial\overline{w}\Big|$ is evaluated numerically. When $\Delta w \rightarrow 0$ or $Y \rightarrow 0$, a solution to all five algebraic performance equations is obtained.

# APPENDIX C

## SOLUTIONS OF THE MOMENTUM EQUATION IN NONAXIAL FLIGHT

In Section II of this report, it was pointed out that finding numerical solutions to the five kinematic algebraic performance equations became difficult at high rates of sink and small horizontal velocities. The difficulty may be traced to the nonlinear characteristics of the momentum equation in this regime. An explanation of these numerical solution difficulties is presented in this appendix.

The momentum equation (eq. (eq (II-1)) for nonaxial flight of a prop-rotor in propulsive flight is developed in Section II. It is rewritten below in nondimensional form.

$$\{(\bar{V}\cos(\alpha_p) + \bar{v})^2 + (\bar{V}\sin(\alpha_p))^2\}^{1/2}\,\bar{v} - \lambda_T = 0$$

where

$$\bar{V} = V/V_r, \quad \bar{v} = v/V_r, \quad \lambda_T = T/W, \quad \text{and} \quad V_r = \sqrt{W/2\rho A}.$$

This equation relates the thrust-to-weight ratio ($\lambda_T$) to the nondimensional induced velocity ($\bar{v}$), the axial velocity ($\bar{V}$ cos ($\alpha_p$)), and the translational velocity ($\bar{V}$ sin($\alpha_p$)) of the prop-rotor. Figure C-1 illustrates how these variables are geometrically related.

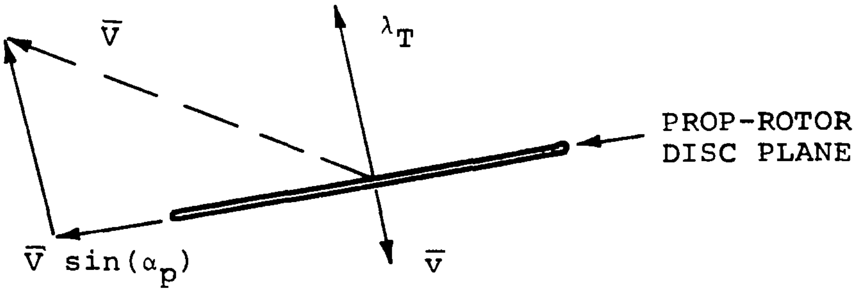

Figure C-1

The locus of possible solutions to the momentum equation for $\lambda_T = 1.0$ and $\overline{v} > 0$ is presented in Figure C-2. Each solution was found by graphical trial and error techniques.

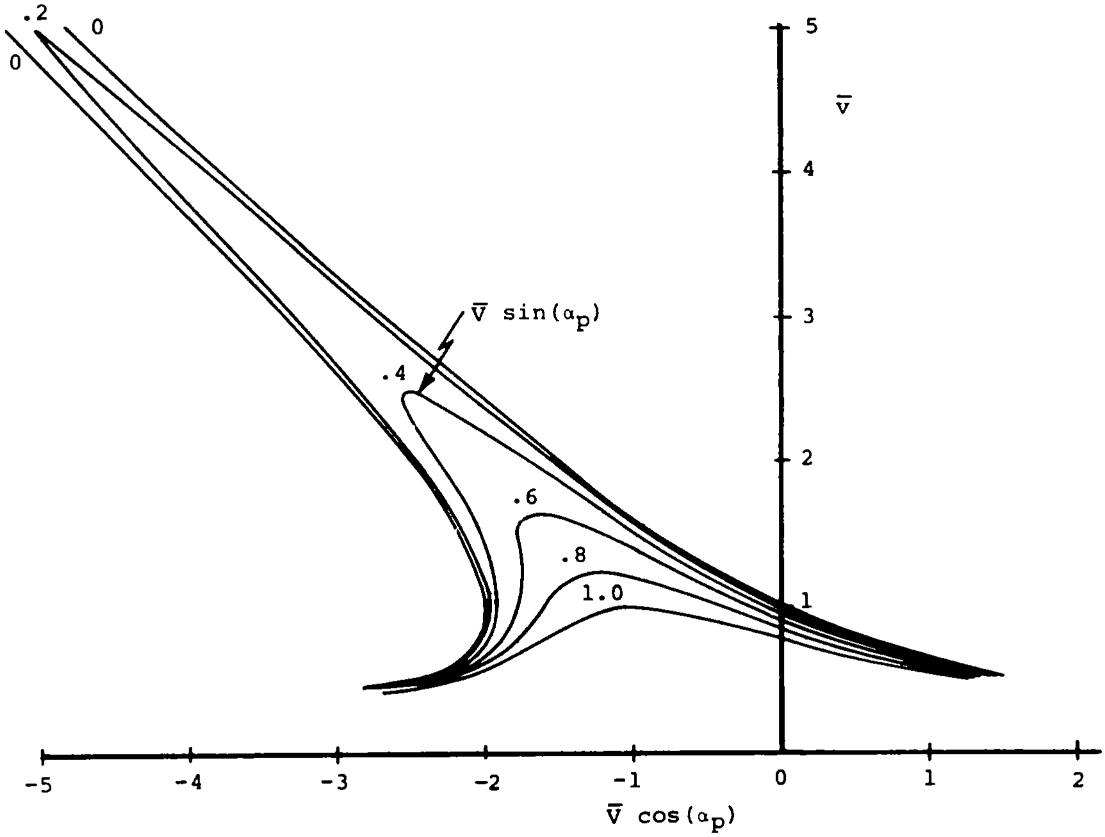

Figure C-2

If the axial velocity of the rotor is positive (i.e., $\overline{V}\cos(\alpha_p) > 0$), only one solution is possible for a given translational velocity. However, if the axial velocity of the rotor becomes sufficiently negative and the translational velocity of the prop-rotor is small ($\overline{V}\sin(\alpha_p) < 1.0$), multiple solutions to the momentum equation exist.

The regime where multiple solutions to the momentum equation exist plays havoc with the Newton-Raphson iteration procedure. This numerical algorithm may find any one of the possible roots to this equation at any given time. In most cases of interest, only one root has any physical significance. However, the particular root which is found is left to chance in this multiple solution regime. It is, therefore, desirable to locate and avoid the regime where multiple solutions are possible.

The locus of points where convergence of the Newton-Raphson algorithm was not attained is illustrated in Figure C-3. This figure is replotted on the rate of sink vs forward velocity map shown in Figure C-4. At small power settings, the "region of no convergence" is only a problem on very steep approach paths. As the translational velocity increases, the momentum equation is well behaved and unique realistic solutions are obtained. The suggested solution constraint boundary, shown in Figure C-4, prohibits descending flight in the "no-convergence" regimes.

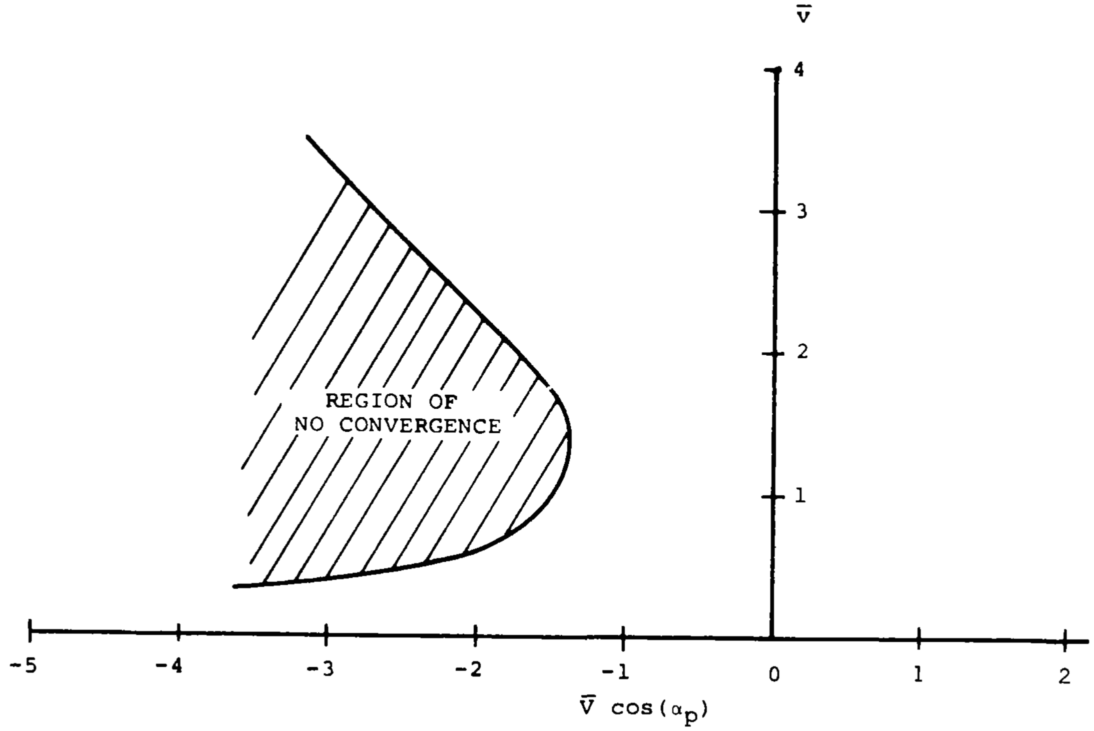

Figure C-3

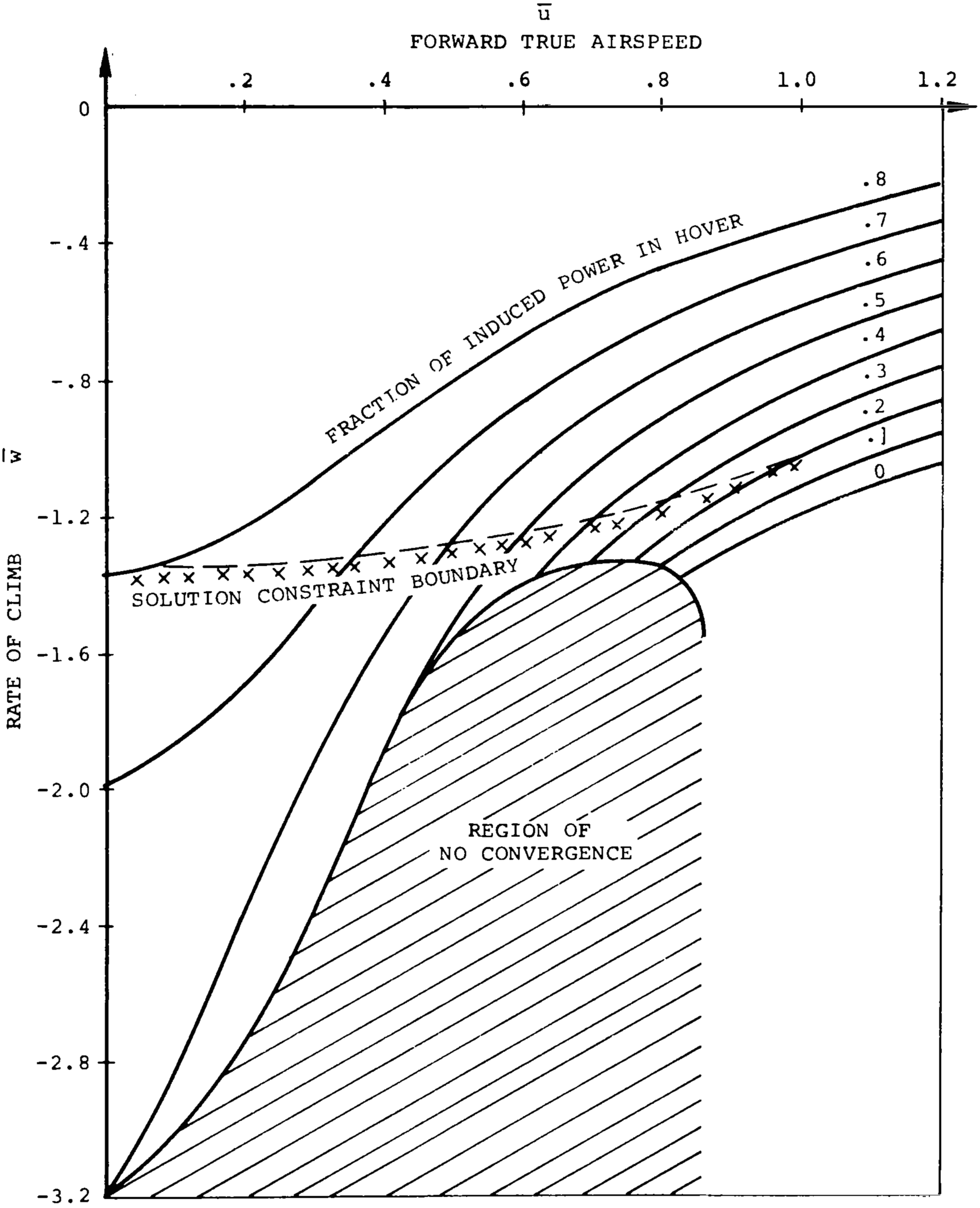

ū
FORWARD TRUE AIRSPEED
.2
.4
.6
.8
1.0
1.2
0
-.4
-.8
-1.2
-1.6
-2.0
-2.4
-2.8
-3.2
w̄
RATE OF CLIMB
.8
.7
.6
.5
.4
.3
.2
.1
0
FRACTION OF INDUCED POWER IN HOVER
SOLUTION CONSTRAINT BOUNDARY
REGION OF
NO CONVERGENCE

Figure C-4

# APPENDIX D

# TIME & FUEL MINIMIZATION USING A SIMPLIFIED KINEMATIC MODEL

Within the climb and descent performance boundaries, a simple graphical procedure is developed which permits the approximation of takeoff and landing trajectories minimizing time and/or fuel required in those maneuvers. This approach permits to visualize advantages and disadvantages of various flight strategies and thus, select those that appear optimum from the time and/or fuel point of view. In addition, the results of this simplified analysis can be used to choose first estimates of initial control time histories for the complete kinematic optimal performance problem as discussed in Section V. The development of the graphical optimization techniques is preceded by a brief analytical discussion.

## Task Definition and Model Description

The performance optimization task is defined as a requirement to minimize: (a) time and/or fuel required from vertical takeoff to reach a prescribed altitude, H, and (b) time and/or fuel needed to perform vertical landing with a defined touchdown velocity, $w_{td}$ (corresponding to $u = 0$) from initial flight conditions, as given by the flight speed $\vec{V}_o = \vec{u}_o + \vec{w}_o$ and flight altitude H.

In performing the above task, the so-called kinematic model of the aircraft is used. In this model, the permissible area of the w vs u relationship is limited on one hand, by the maximum rate of climb $[(R/C)_{max} \equiv w_{lim} = f(u)]$, while on the other, by the rate of descent $[(R/D)_{max} \equiv -w_{lim} = f(u)]$ curves. Figure D-1 shows typical boundaries as established in Section II. It is further assumed that the $(R/C)_{max}$ and $(R/D)_{max}$ limits remain the same throughout the whole altitude range.

Within the permissible operation area (fig. D-1), the following constraints are imposed:

$$|\dot{u}| \leq |a_x|$$

$$|\dot{w}| \leq |a_y|.$$

In the graphical optimization procedures, it will be assumed that within the whole permissible area, it is physically possible to achieve and maintain (when desired), both $|\dot{u}|$ and $|\dot{w}|$ up to their "legal" limits until the boundary of the region is reached. This means that acceleration could be controlled in the bang-bang manner.

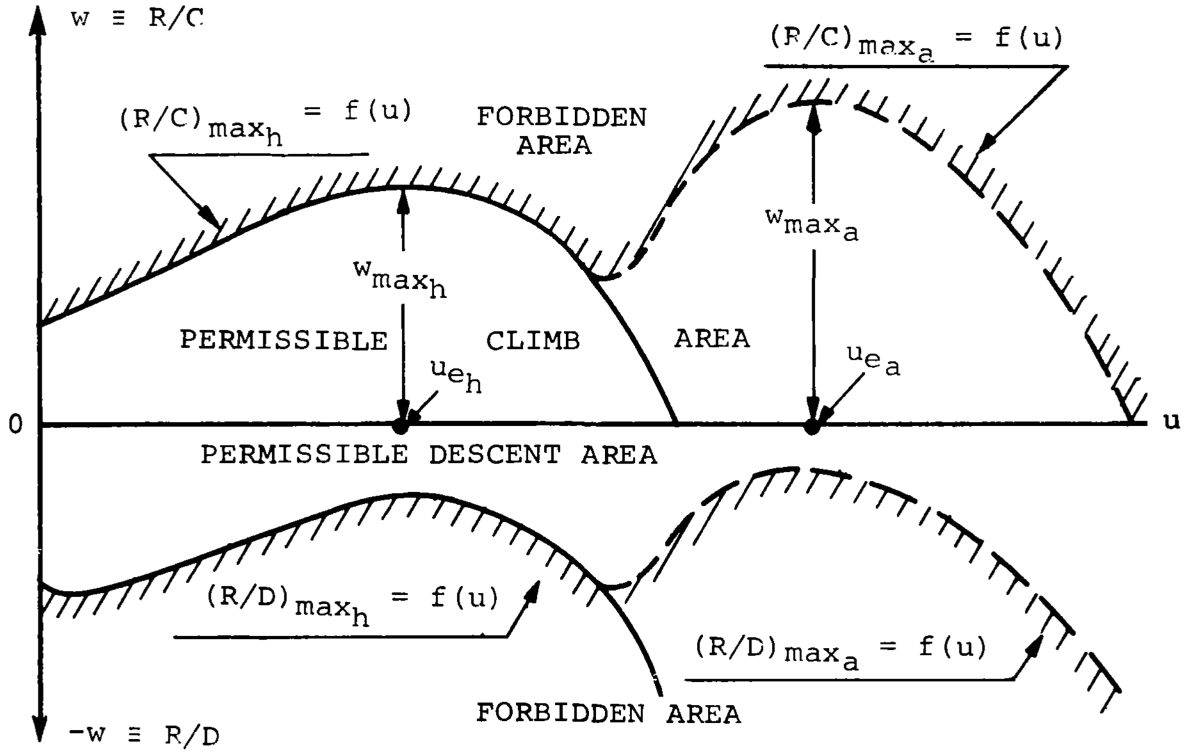

w ≡ R/C
(R/C)$_{max_a}$ = f(u)
(R/C)$_{max_h}$ = f(u)
FORBIDDEN AREA
$w_{max_a}$
$w_{max_h}$
PERMISSIBLE
CLIMB
AREA
$u_{e_a}$
$u_{e_h}$
0
u
PERMISSIBLE DESCENT AREA
(R/D)$_{max_h}$ = f(u)
(R/D)$_{max_a}$ = f(u)
FORBIDDEN AREA
-w ≡ R/D

Figure D-1

In reality, especially in ascent, when the permissible rate of climb boundary is approached at a constant u value, the vertical acceleration approaches zero in a gradual, and not a discontinuous manner.

$$\dot{w}|_{w \to w_{lim}} \to 0.$$

However, it will be shown later that even in the case of vertical climb, the bang-bang assumption regarding acceleration appears to introduce minor errors only.

The acceleration limits may also be encountered along the performance boundary itself and they can be evaluated, either graphically or analytically. In the first case, it suffices to have a graphical representation of $(R/C)_{max} = f(u)$ or $(R/D)_{max} = f(u)$, while in the second, an analytical relationship between $(R/C)_{max} = f(u)$ or $(R/D)_{max} = f(u)$ must be known.

Assuming a constant acceleration along one (say, the horizontal axis), the corresponding orthogonal (in this case, vertical) acceleration is given as:

$$d(R/C)_{max}/dt \equiv \dot{w} = (d/dt)[f(u \pm a_x\ t)]$$

or $$d(R/D)_{max}/dt \equiv -\dot{w} = (d/dt)[f_1(u \pm a_x\ t)].$$

## Vertical Climb

In order to develop a better feel regarding the importance of various parameters influencing the time and fuel minimization, as well as the validity of the bang-bang acceleration assumption, the case of vertical takeoff and vertical climb is considered first. Furthermore, since basic understanding of the physical aspects represent the chief aim of those considerations, the simplest possible approach based on the momentum theory is used. Attention is focused first, on the significance of the ratio of the shaft power delivered by the engines ($SP_{av}$) to that required in hovering ($SP_{hov}$), $k_p \equiv (SP_{av}/SP_{hov})$.

Initial vertical acceleration.- The initial vertical acceleration ($\dot{w}_{v_o}$) as a function of $k_p$ is investigated first. Within limits of the simple momentum theory, shaft power (in ft.lbs/sec) available can be expressed as follows (ref. 2):

$$SP_{av} \equiv k_p\ SP_h = (1/\zeta_A\ \zeta_{tr})k_p\ k_v\ W\sqrt{k_v(W/A)/2\rho} \qquad (D1)$$

where $\zeta_A$ is the aerodynamic efficiency (figure of merit), $\zeta_{tr}$ is the transmission efficiency (it also covers power requirements for driving accessories), $k_v$ is the ratio of the gross weight (W) plus the vertical drag ($D_v$) to gross weight. $[k_v \equiv (W + D_v)/W]$ and W/A is the nominal disc loading.

The ideal rotor power available ($RP_{id_{av}}$) for the static thrust generation is (ref. 2):

$$RP_{id_{av}} = \Big[(1/\zeta_A)k_p\ k_v\sqrt{k_v(W/A)/2\rho} - (3/4)k_v(\bar{c}_{d_o}/\bar{c}_{\ell_{hov}})V_t\Big](1/k_{ind})W \qquad (D2)$$

where $\overline{c}d_0$ is the average blade profile drag coefficient, $\overline{c}_{\ell hov} = 6k_vW/\sigma A\rho V_t^2$ is the average blade lift coefficient in hovering ($A$ = total disc area of the rotors), $V_t$ is the tip speed, and $k_{ind}$ is the ratio of the actual to the ideal induced power.

Knowing the ideal rotor horsepower available, the corresponding ideal induced velocity can be computed as:

$$v_{id_{av}} = (RP_{id_{av}}/2A\rho)^{1/3}. \tag{D3}$$

Consequently, the corresponding static thrust ($T_o$) will be

$$T_o = 2A\rho v^2{}_{id_{av}} \tag{D4}$$

and finally, the initial vertical acceleration:

$$\dot{w}_{v_o} = g[T_o/W) - k_v]. \tag{D5}$$

Substituting eq. (D2) into eq. (D3), then eq. (D3) into eq. (D4), and finally, eq. (D4) into eq. (D5), the following is obtained:

$$\begin{aligned}\dot{w}_{v_o} = g\Bigg\{&\Big[2\rho/(W/A)\Big]\Bigg\{\Big[(1/\zeta_A)k_p\ k_v\sqrt{k_v(W/A)/2\rho}\\ &- (3/4)\left(\overline{c}_{d_o}/\overline{c}_{\ell_h}\right)k_v\ V_t\Big](W/A)/2\rho\ k_{ind}\Bigg\}^{2/3} - k_v\Bigg\}\end{aligned} \tag{D6}$$

The initial vertical acceleration ($\dot{w}_{v_o}$) is calculated as a function of $k_p$ from eq. (D6) with the following values of various parameters, assumed as representative for the considered tilt-rotor aircraft with a disc loading of $W/A = 10$ psf; $\rho = \rho_o$; $\zeta_A = .78$; $k_v = 1.055$; $k_{ind} = 1.07$; $\overline{c}_{d_o}/\overline{c}_{\ell hov} = 0.55$ and $V_t = 700$ pfs.

Figure D-2 shows a plot of $\dot{w}_{v_o}/g = f(k_p)$ computed for the above values. A glance at this figure should give an idea regarding the magnitude of the initial vertical acceleration for various levels of the excess power as expressed by the $k_p$ ratio.

Rate of vertical climb. - Using the simple momentum approach, steady-state rate of climb in vertical ascent ($w_{vc}$)

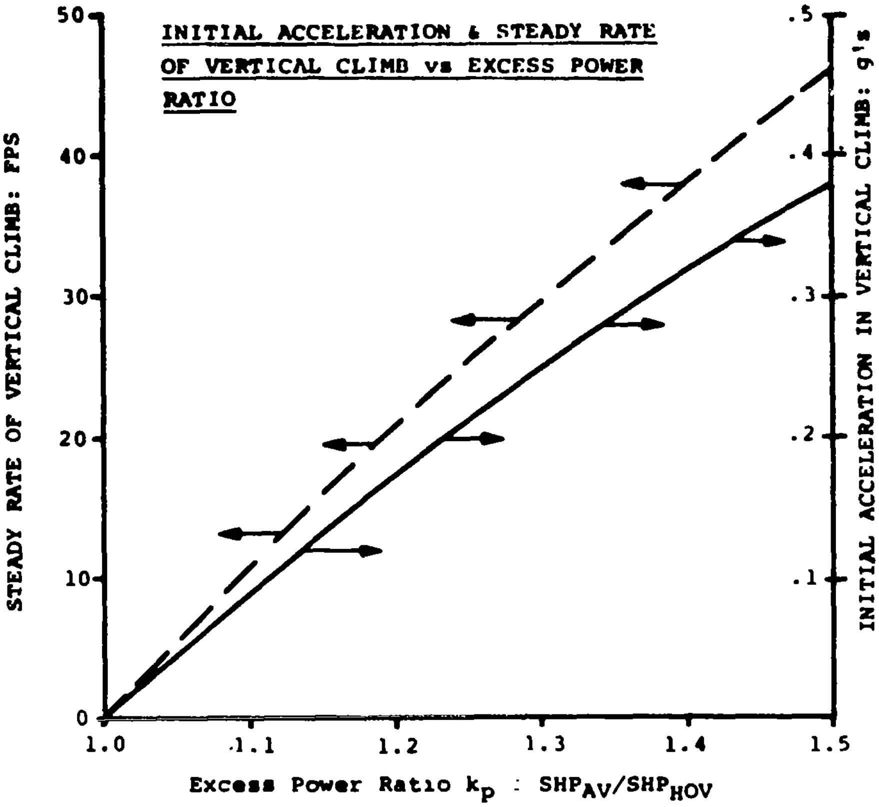

Figure D-2

can also be expressed in terms of the excess power ratio ($k_p$) (ref. 2):

$$w_{vc} = V'_{id} - v_{id} \tag{D7}$$

where $V'_{id}$ is the ideal total rate of flow through the rotor disc

$$V'_{id} = RP_{id_{av}}/k_v\ W \tag{D8}$$

and $v_{id}$ is the ideal induced velocity

$$v_{id} = k_v\ W/2\rho AV'_{id}. \tag{D9}$$

Assuming the same numerical values of various parameters as in the preceding case of initial acceleration, $w_{VC}$ vs $k_p$ computed from eq. (D9) is also shown in Figure D-2. In this way, levels of both the initial vertical acceleration as well as the steady rate of vertical climb can be easily assessed for various $k_p$ values.

Time of vertical climb. - It was indicated previously that as $w_V \rightarrow w_{VC}$, $\dot{w}_V \rightarrow 0$. Using basic relations of the momentum theory, it is possible to compute $\dot{w}_V$ at various $w_V$ values. However, for the sake of simplicity, it will be assumed that $\dot{w}_V$ varies linearly from its maximum level $\dot{w}_{V\max} \equiv a_{V_0}$ at $w_V = 0$ to $\dot{w}_V = 0$ at $w_V = w_{VC}$.

$$(dw_V/dt) = a_{V_0} - \alpha w_V = a_{V_0}(1 - w_V/w_{VC}) \qquad \text{(D10)}$$

where $\alpha \equiv a_{V_0}/w_{VC}$.

Under the above assumption, eq. (D10) can be integrated within limits from $w_V = 0$ to $w_{VC}$ and the following relationship between the rate of vertical climb and time is obtained:

$$w_V = w_{VC}(1 - e^{-t\alpha}). \qquad \text{(D11)}$$

For selected values of $k_p$, the corresponding values of $a_{V_0}$, $w_{VC}$ and thus $\alpha$, can easily be obtained from Figure D-2. Then $w_V = f(t)$ can be calculated. Figure D-3 shows this relationship.

Using eq. (D11), a relationship between altitude (H) reached in a vertical ascent and time required, can readily be obtained:

$$dy = w_V dt.$$

Substituting eq. (D11) into the above relationship and integrating from $y = 0$ to $y = H$, leads to the following expression:

$$H = w_{VC}\left[t + (e^{-t\alpha} - 1)/\alpha\right]. \qquad \text{(D12)}$$

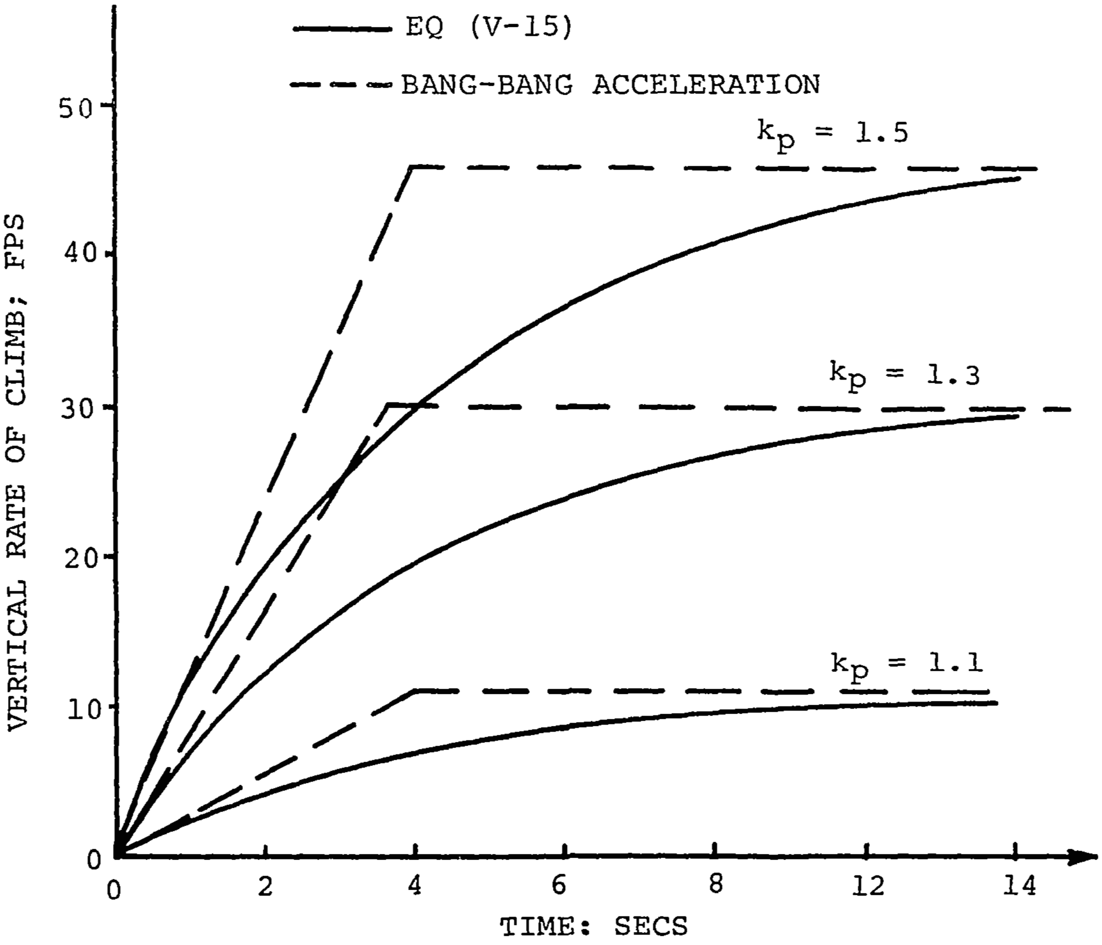

Figure D-3. Vertical Rate of Climb vs Time for 3 Excess Power Ratios

For several $k_p$ values (1.1; 1.3; and 1.5), the relationship between time and altitude reached is shown in Figure D-4, while Figure D-5 gives an example of time required in vertical climb vs $k_p$ for an assumed altitude of H = 1000 feet. These figures clearly indicate that high $k_p$ values are essential in reducing the time required to climb to a given altitude.

At this point, a question may be asked regarding the validity of the kinematic model which assumes that the ascent boundary (in this case, $w_v = w_{vc}$) may be approached in the bang-bang fashion at full acceleration value, which suddenly drops to zero when $w_v = w_{vc}$ is reached. In Figure D-3, a comparison is shown of $w_v = f(t)$ computed from eq. (D-11) with that based on a constant acceleration of $a_{v_o}$ up to time $t_a = w_{vc}/a_{v_o}$ when $\dot{w}_v$ suddenly becomes zero (broken lines in Figure D-3).

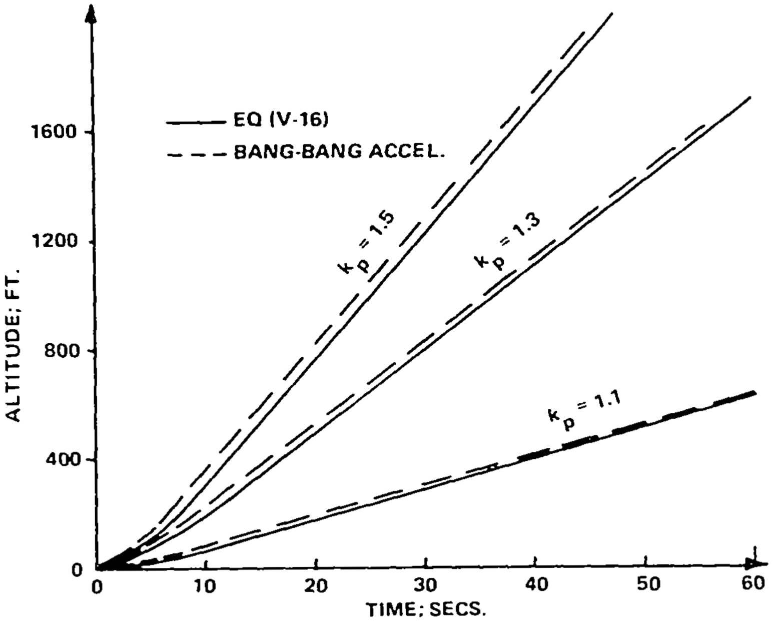

Figure D-4. Altitude vs Time in Vertical Climb

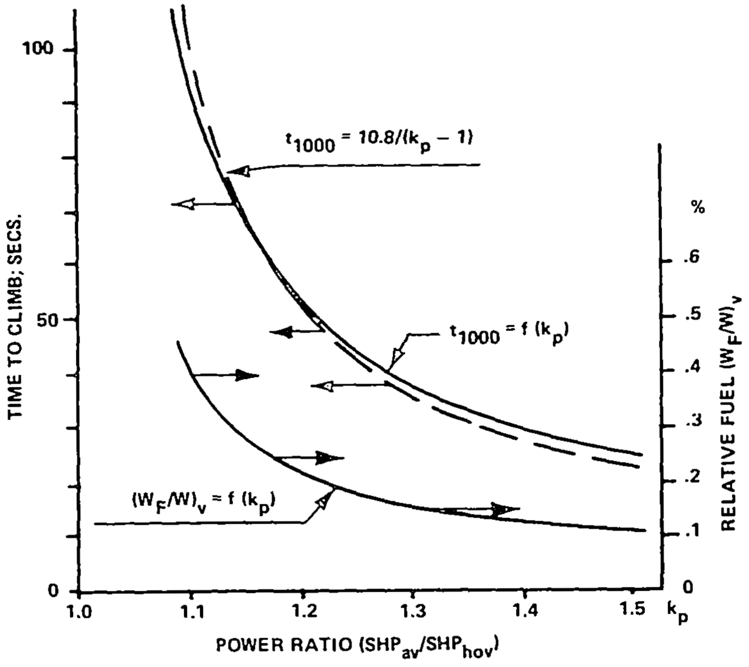

Figure D-5. Time & Fuel Required to Climb Vertically to 1000 Feet vs Excess Power Ratio

Figure D-4 shows a comparison between H = f(t) computed for a constant acceleration $a_{v_o}$ up to $t_a = w_{vc}/a_{v_o}$ and then, $a_{v_\rho} = 0$ (broken lines), vs those predicted by eq. (D11). It can be seen from Figure D-4 that at the altitudes of interest for the terminal operation ($H \geq 1000$ ft.), the differences are negligible. In view of this, it may be stated that for practical time minimization problems, approaches based on the bang-bang vertical acceleration are acceptable.

Fuel in vertical climb. - Assuming that during vertical climb to some altitude H, both the SHP of the engines ($SHP_{av} = k_p SHP_{hov}$) and the sfc remain constant, fuel consumed can be expressed as follows:

$$W_{F_H} = k_p \; SHP_{hov} \; sfc \; t_H/3600 \qquad \text{(D13)}$$

where the time of climb $t_H$ is in seconds.

Substituting for $SHP_{hov}$, its expression in terms of the ideal induced power, etc., the following expression for the relative fuel weight is obtained:

$$(W_{F_H}/W)_v = 5.05 \cdot 10^{-7} (k_p k_v/\zeta_A \zeta_{tr}) \sqrt{k_v (W/A)/2\rho} \; sfc \; t_H \; . \qquad \text{(D14)}$$

It may be expected from eq. (D14) that in general, a reduction in $t_H$ hsould be beneficial for the minimization of the $W_{F_H}/W$ ratio. But $t_H$ in turn, depends on $k_p$. In order to investigate whether the product of $k_p$ and $t_H$ will also decrease with increasing $k_p$, the following approximate relationship between $t_H$ and $k_p$ may be postulated for any fixed value of H:

$$t_H = \kappa/(k_p - 1) \qquad \text{(D15)}$$

where $\kappa$ is a constant associated with a given H value. It can be seen from Figure D-5 that, indeed for instance for H = 1000 feet, $\kappa = 10.8$ assures an acceptable fit for the $t_H = f(k_p)$ curve.

Substituting eq. (D15) into eq. (D14), the latter becomes:

$$(W_{F_H}/W)_v = 5.05 \cdot 10^{-7} (k_v/\zeta_A \zeta_{tr}) \sqrt{k_v (W/A)/2\rho} \; sfc \; \kappa/[1 - (1/k_p)] \; . \qquad \text{(D16)}$$

Now it is clear from eq. (D16) that in order to minimize the fuel required to climb vertically to a given altitude, the $k_p$ ratio should be kept as high as possible. As an example, relative fuel required to climb vertically to H = 1000 feet is computed from eq. (D16) (assuming $\zeta_{tr} = 0.95$ and sfc = 0.5 lbs/SHP-hr.), and plotted in Figure D-5. A glance at this figure will indicate that, indeed, minimization of time to climb in vertical ascent is identical with the minimization of the fuel used in that maneuver. Furthermore, since in the present model, power setting ($k_p$) is the only control available for optimization in vertical climb, it is clear that in order to minimize both time and fuel, the $k_p$ ratio should be at its maximum value (with due consideration of $\dot{w}_v$ constraints).

Climb in forward flight. - At high u values, as encountered at maximum rate of climb in forward flight, the influence of the additional inflow (due to climb) on the induced power, contrary to the case of vertical and near-vertical ascent, is usually negligible. Hence, it is legitimate to compute rate of climb at any high u (say, $u \geq 3v_{id_{hov}}$) on the basis of the excess of the actual rotor or propeller power over that required for a steady-state level flight at that speed, $\vec{V} = \vec{u} + \vec{0}$. For the helicopter regime of flight, rate of climb becomes:

$$w_f = (\zeta_{tr}/k_{ind})\ 550(SHP_{av} - SHP_u)/Wk_{v_f} \qquad \text{(D17)}$$

where $k_{v_f}$ is the download coefficient in forward flight.

For the aircraft configuration, $w_f$ will be:

$$w_f = \zeta_{tr}\zeta_{pr}\ 550(SHP_{av} - SHP_u)/W \qquad \text{(D18)}$$

where $\zeta_{pr}$ is the propulsive efficiency of the rotor-propeller.

Time: Time to climb to a given altitude H will be

$$t_{H_f} = \int_0^H \left[1/w_f(y)\right] dy. \qquad \text{(D19)}$$

In general, eq. (D19) represents a functional, where w(y) is, in turn, a function of the control u = f(y). Depending on the initial value of u and existing constraints, different strategies may be selected for the minimization of $t_{H_f}$. However, it can be deduced from eq. (D19), where $w_f(y)$ appears in the denominator, that in view of eqs. (D18) or (D19), the excess of the rotor or thrust power per pound of aircraft gross weight should be as high as possible.

As to the selection of the most-promising strategies leading to the time minimization in achieving a prescribed flight velocity and altitude from the initial condition represented by vertical takeoff ($u = 0$), this subject will be discussed later with the help of a graphical approach.

At present, in order to provide a better quantitative feel for the problem, a cursory analytical relationship will be developed for the helicopter configuration only.

Assuming $u$ and excess power ($SHP_{av} - SHP_u$) constant, eq. (D17) is substituted into eq. (D19) which, in turn, is integrated within the 0 to H limits:

$$t_{H_f} = \left[k_{v_f}\, k_{ind_f}/550\zeta_{tr}(SHP_{av} - SHP_u)\right] WH. \qquad (D20)$$

It can be seen from eq. (D20) that in order to minimize $t_{H_f}$, the difference between $SHP_{av}$ and $SHP_u$ should be as large as possible. This means that $SHP_{av}$ should represent maximum engine power available, while $SHP_u = SHP_{u_e} \equiv SHP_{min}$. Assuming that $u = u_e$ and consequently, $SHP_u = SHP_{min}$, eq. (D20) can be rewritten as follows:

$$t_{H_f} = \left[k_{v_f}\, k_{ind_f}/550\zeta_{tr}(k_{pf} - 1)\right](W/SHP_{min})H \qquad (D20a)$$

where $k_{pf} \equiv SHP_{av}/SHP_{min}$.

Assuming for the power loading at $SHP_{min}$, a representative value for the considered tilt-rotor aircraft of $W/SHP_{min} = 16.5$ lbs/hp, $t_{H_f}$ is computed for $H = 1000$ feet and plotted vs $k_{pf}$ in Figure D-6.

Fuel: In view of eq. (D17), total SHP required in the helicopter configuration in ascent with a rate of climb, $w_f$, will be:

$$SHP = SHP_u + (1/\zeta_{tr})k_{ind}\, k_{v_f}\, W\, w_f/550 \qquad (D21)$$

and for the aircraft configuration (in view of eq. (D18)):

$$SHP = SHP_u + (1/\zeta_{tr}\zeta_{pr})W\, w_f/550. \qquad (D22)$$

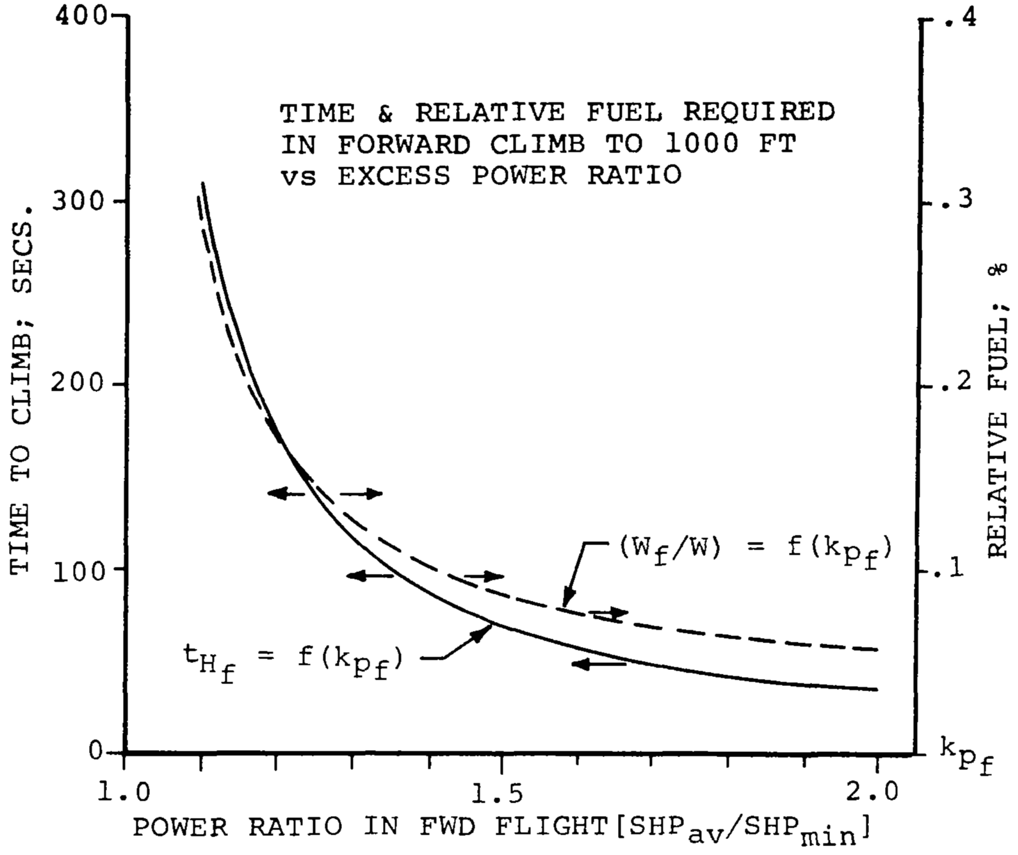

Figure D-6

Considering as an example the helicopter case, the elementary amount of fuel consumed can be expressed as follows:

$$dW_{F_f} = SHP_u\, sfc(1/3600\; w_f)dy$$

$$+ (1/1\,980\,000\; \zeta_{tr})k_{ind}\; k_{v_f}\; W\; sfc\; dy. \qquad \text{(D23)}$$

where $w_f$ is in fps.

In order to obtain a better quantitative feel of this process of optimization, the simplest possible case will be considered of $u$ = const and $w_f$ = const. Under these assumptions, eq. (D23) is integrated from $y = 0$ to $y = H$, and eq. (D18) is substituted for $w_f$. Furthermore, defining $k_{p_f} \equiv SHP_{av}/SHP_u$, eq. (D23) leads to the following expression of fuel as a percentage of the gross weight:

$$(W_{F_f}/W) = (k_{ind}k_{v_f}/19\ 800\zeta_{tr})\{[1/(k_{p_f} - 1)] + 1\}sfc\ H\ \%$$

(D24)

It is clear from eq. (D24) that in order to minimize the amount of fuel required in forward flight, $SHP_{av}/SHP_u$ should be maximized. This means that whenever there is a freedom of selecting u, its value should be $u_e$; i.e., that corresponding to $SHP_{min}$, while $SHP_{av}$ should be as high as possible. An additional benefit is realized from operating at high power settings since the lowest sfc values usually correspond to maximum continuous power.

Taking for example, H = 1000 feet and assuming the following values for other parameters; $k_{v_f} = 1.0$, $k_{ind_f} = 1.07$, $\zeta_{tr} = 0.95$ and sfc = 0.5 lb/hp/hr; $(W_{F_f})\%$ is computed and plotted vs $k_{p_f}$ in Figure D-6. A glance at this figure will indicate that similarly to the case of vertical ascent, trends in forward climb for both time and fuel minimization with $k_{p_f}$ are the same. This means that, in general, a flight management strategy that is beneficial for time minimization would also be beneficial as far as reduction of fuel required in climb is concerned.

With respect to the task of the whole ascent operation beginning with a vertical takeoff, it appears that from the moment of lift-off throughout the whole climb maneuver, the engines should operate at the highest possible values of $k_p$ first, and then $k_{p_f}$, as permitted by the power available and/or operational constraints of vertical and horizontal accelerations ($|a_y|$ and $|a_x|$). Furthermore, it appears that, in principle, u corresponding to the highest $k_{p_f}$ value (be it for the helicopter or airplane configuration) should be reached as soon as possible, and then the climb continued at that $k_{p_{max}}$ value. However, in some cases it may not be desirable to strive for u corresponding to the highest $k_{p_f}$ value within the whole envelope. For instance, for low terminal altitudes, it may not be advantageous to go through conversion and acceleration to u corresponding to $k_{p_{f_{max}}}$ in the airplane configuration, but to be satisfied with $k_{p_{f_{max}}}$ of the helicopter regime. All of these, as well as other aspects of selecting an optimum strategy of time and fuel minimization in an ascent to a given altitude (as well as in a descent from a given altitude) will become more clear through a graphical interpretation of the time and fuel optimization problem.

## Graphical Approach to Time and Fuel Minimization

Climb and descent envelopes developed in Section II are used in the definition of the kinematic performance model

(Figures D-7 and D-8). The task of optimization is formulated as a requirement to establish the optimum strategy of controlling u and w to yield minimum time and/or fuel trajectories in one of the following terminal maneuvers performed in the vertical plane (X,H).

(1) Climb from a vertical takeoff to a prescribed altitude (H). This requirement may incorporate no restrictions regarding the magnitude of the horizontal component of the flight velocity when altitude H is reached, or the desired $u_H$ may be specified à priori.

(2) Descent from a given altitude (H) and a given initial velocity of flight $\vec{V}_0 = \vec{u}_0 + \vec{w}_0$ to vertical landing ($u_{td} = 0$) with a prescribed touchdown velocity ($0 \leq w_{td}$).

Climb. - Vertical takeoff is specified as the only initial condition. As to the terminal consideration at the altitude H, let it be assumed that there is no à priori defined value of the u component that must be achieved when the prescribed altitude H is reached in the shortest possible time. Under these conditions, it may be anticipated that the best general strategy would be based on reaching, as quickly as possible,

$$\vec{V} = \vec{u}_{e_h} + \vec{w}_{max_h} \text{ or } \vec{V} = \vec{u}_{e_a} + \vec{w}_{max_a}$$

corresponding to the maximum rate of climb, either in the helicopter or airplane regime and maintaining it all the way up to the desired altitude H (Figure D-7).* But in any case, minimum time required to reach that $u = u_e$ and $w = w_{max}$ velocity will correspond to the longer of the two times required to accelerate the aircraft, either at the rate $a_x$ to $u_e$ or at the rate $a_y$ to $w_{max}$. Since in all practical cases, the $u_e$ values (especially for the aircraft configuration) would probably be much higher than those of $w_{max}$, it may be expected that

$$t_{e_x} = u_e/a_x > t_{e_y} = w_{max}/a_y.$$

In order to give some idea as to how selection of approximately optimum strategies can be performed, the following 3 cases are presented (Figure D-7):

(1) From a vertical takeoff, the aircraft is accelerated along the x and y axes at such rates that at the time $t_e$, both velocities $u_{e_h}$ and $w_{max_h}$, for the helicopter regime, are achieved simultaneously.

---

*Zooming trajectories are, by definition, not considered in this kinematic analysis.

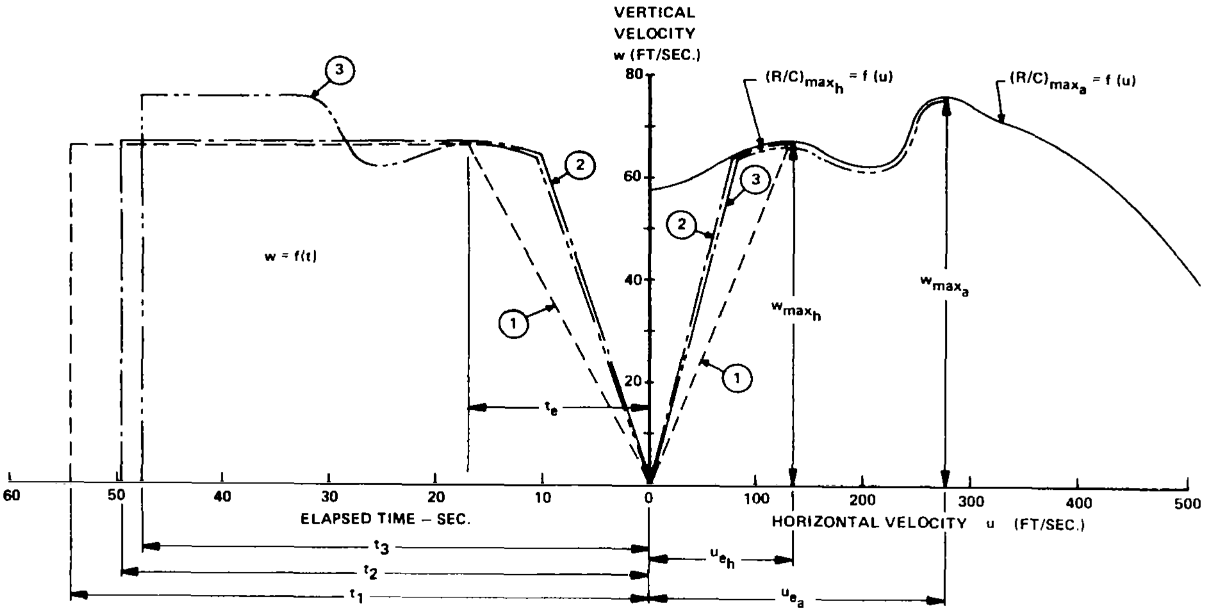

Figure D-7

(2) From the same type of takeoff as in (1), the aircraft is accelerated along both axes at the maximum permissible rate ($\vec{a} = \vec{a}_x + \vec{a}_y$) until the $(R/C)_{max}$ boundary is reached. Then it continues to accelerate at the rate $a_x$ along the x axis up to $u = u_{eh}$. From this moment, it climbs at $w_{max_h}$ up to the altitude H. During this part of the maneuver preceding the reaching of the steady rate of climb, a check should be made as to whether the vertical acceleration resulting from the $w = f(u)$ relationship does not exceed the permissible $\dot{w}$ limits.

(3) The beginning of the maneuver is the same as in (2). However, after the $(R/C)_{max}$ boundary has been reached, the aircraft stays on that boundary while accelerating at $\dot{u} = a_x$ until the horizontal velocity component becomes $u_{e_a}$. From this point, it climbs at $w_{max_a}$ up to the desired altitude H. As in the previous case, it must be continuously checked as to whether riding of the $(R/C)_{max}$ boundary, when u increases at the rate $a_x$, the $\dot{w}$ does not violate the $|a_y|$ constraint.

In the first case (see Figure D-7, dash line), the vertical acceleration along the y axis will be

$$\dot{w} = a_x(w_{max_h}/u_{eh})$$

and the vertical distance ($H_e$) covered in time $t_e$ would be:

$$H_e = (1/2) w_{max_h} t_e.$$

The rest of altitude equal to $H - H_e$ will be covered at a constant rate of climb ($w_{max_h}$) and hence, the corresponding additional time ($\Delta t_1$) will be

$$\Delta t_1 = (H - H_e)/w_{max_h}$$

and the total time to climb (Figure D-7)

$$t_1 = t_e + \Delta t_1$$

becomes $\quad t_1 = (u_{e_h}/a_x) + [(H/w_{max_h}) - (1/2)(u_{e_h}/a_x)].$

In the second case (see Figure D-7, dot-dash line), the proposed strategy is more beneficial as, at time $t_e$, a larger area (higher altitude) is under the curve than in the first case.

It appears, hence, that for the helicopter configuration, the optimum climb strategy for the minimum time to climb to an altitude H would consist (under somewhat idealized conditions) of accelerating at $\vec{a} = \vec{a}_x + \vec{a}_y$ until the $(R/C)_{max}$ boundary is reached and then riding that boundary up to $\vec{V} = \vec{u}_{eh} + \vec{w}_{max_h}$ and then climbing at the maximum rate of climb of $w_{max_h}$.

In the third case (dash-double-dot line in Figure D-7), the desirability of the proposed strategy will depend on the magnitude of the terminal altitude (H). Should H be relatively low, then loss of the rate of climb while riding the 'valley' connecting the helicopter $(R/C)_{max}$ boundary with that of the airplane, would not be compensated by the eventually higher $w = w_{max_a}$ values. It is clear that in addition to the altitude aspects, such factors as: (a) depth of the valley in the $(R/C)_{max}$ boundary, (b) relative magnitudes of $u_{e_a}$ vs $u_{eh}$, and (c) relative magnitudes of $w_{max_a}$ vs $w_{max_h}$ would influence the desirability of either the second or third strategy.

For some particular shapes of the $(R/C)_{max}$ boundary for the whole aircraft (from helicopter to airplane configuration), it may be desirable to accelerate as fast as permissible to the bottom of the valley and then to ride the $(R/C)_{max}$ boundary up to $w_{max_a}$ and then to climb at that speed.

Once the $(R/C)_{max}$ boundaries are known for a given aircraft, it is easy to investigate graphically the above discussed (and possibly some other) strategies and evaluate them from the point of view of the time-to-climb minimization.

Since time minimization in climb is synonymous with fuel minimization, the above graphical procedures applicable to the task of time-of-climb optimization could equally serve as roadmaps for the fuel-in-climb minimization.

Descent. - In this case, the permissible area for the w vs u relationships is limited by the u axis and the maximum rate of descent $(R/D)_{max} \equiv w_{lim} = f(u)$ curve. The above curve also permits checking (either analytically or graphically) of the orthogonal acceleration resulting from 'sliding' along the $(R/D)_{max}$ boundary with one velocity changing at its maximum legal rate.

With respect to the initial conditions, it is assumed for simplicity, that the initial altitude is $y_o = H$ and the gate velocity at that altitude is horizontal ($w_o = 0$), while its value is $u_o$. Terminal conditions are defined as $y_t = 0$; $u = 0$ and $w = w_{td}$ where $w_{td}$ is the permissible touchdown speed. It is further assumed (as in the case of climb) that within the whole permissible descent area, it is possible to reach and maintain the horizontal and vertical accelerations and decelerations at their maximum values of $|a_x|$ and $|a_y|$ up to the boundaries of that region in the bang-bang fashion. This means that power available, control response, etc., are sufficient to produce, whenever required, a vertical deceleration up to its maximum 'legal' limit.

In the case of landing with both acceleration and velocity constraints, optimum descent strategies can be worked out within the whole region limited by the u axis and the (R/D) $(R/D)_{max} = f(u)$ boundary.

For the sake of simplicity and brevity, only part of the helicopter regime $(R/D)_{max}$ curve is considered. However, it is believed that the reader who will familiarize himself with this example should have no difficulty in dealing with more complicated cases incorporating the whole $(R/D)_{max}$ boundary (helicopter and airplane) of a tilt-rotor aircraft.

Initial conditions are assumed: $u_o = 250$ fps, $w_o = 0$, $H_o = 3000$ feet. Terminal conditions are: $u_t = 0$, $w_t = 0$, $H_t = 0$. $|a_x| \leq 0.25g \equiv 8\ \text{ft/sec}^2$; $|a_y| \leq 0.2g \equiv 6.4\ \text{ft/sec}^2$; $(R/D)_{max} = f(u)$ as shown on the right side of Figure D-8.

Under the above assumptions, minimum time to reduce horizontal component to zero would be:

$$t_{x_{min}} \approx 31 \text{ secs.}$$

Minimum time to accelerate at $|a_y|$ and then decelerate at the same level to $w = 0$ within 3000 feet with no $(R/D)_{max}$ constraints would be:

$$t_{y_{min}} \approx 43 \text{ secs.}$$

It is apparent, hence, that proper management of the vertical component of flight velocity becomes of prime importance in the minimization of time of descent.

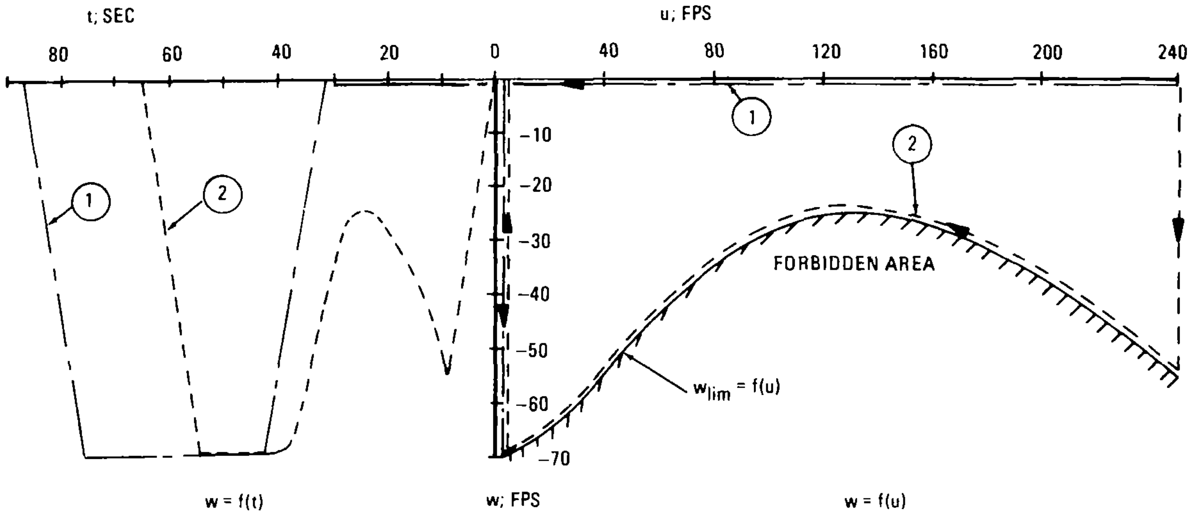

Figure D-8

Due to the $-w = f(u)$ constraints, the actual time of descent will be longer than 43 seconds. Therefore, it may be anticipated that the optimum strategy should be based on getting as quickly as possible to the area of large negative w values. Subsequently, this high rate of descent should be maintained until the lowest possible altitude required for reduction of $-w$ to zero (at $-\dot{w} = a_y$) is reached. Since, in the considered example, the highest rate of descent occurs at $u = 0$, it becomes desirable to reach $V(u = 0; -w = 70 \text{ fps})$ as quickly as possible. Should there be $|-w| > |-w_{u=0}|$ at some other u value, then of course, it might be desirable to reach as quickly as possible, that particular combination of $-w$ and u, and descend in that condition as long as possible before proceeding to the reduction of the u value to 0.

At first glance, it may appear that the following strategy (1) could be beneficial (dash-dot line, Figure D-8): First, reduce the horizontal component (u) at the maximum permissible rate $|a_x| = |0.25g|$ and then descend vertically, first accelerating and then decelerating at $|a_y| = |1.2g|$. However, a glance at Figure D-8 will indicate that the resulting time of 87 seconds is not optimum. This is obviously due to the 31 seconds "lost" in horizontal flight with no decrease in altitude. To correct this aspect, Strategy (2) is shown as a better approach (dotted line in Figure D-8): (a) keeping $u = u_o$ constant, accelerate vertically at the maximum permissible rate down to the $(R/D)_{max} = f(u)$ boundary; (b) follow this boundary, reducing u at the $-a_x$ rate until u = 0, and the corresponding maximum permissible rate of vertical descent is reached; (c) maintain that rate of descent, then recover at $|a_y|$ from the critical altitude. It can be seen that the time corresponding to Strategy (2) is t = 65 seconds, and it probably either represents an optimum or is close to it. However, should the permissible rate of descent at u corresponding to the gate speed be higher than at u = 0, it would be more beneficial to execute the minimum-time landing maneuver by staying at that speed ($u_o$) and the corresponding maximum permissible rate of descent until an altitude is reached that is sufficient to perform a maneuver consisting of "riding" the $(R/D)_{max} = f(u)$ boundary and then reducing the rate of descent to w = 0 at $|a_y|$.

Fuel Minimization: Fuel minimization problems throughout the whole descent maneuver are (as in climb) synonymous with those of time minimization - total weight of fuel used in descent from a given altitude (H) and a given initial flight velocity $\vec{V}_o = \vec{u}_o + \vec{w}_o$ to vertical landing at a permissible touchdown speed $w_{td}$ can be expressed as the following functional:

$$W_F = -\int_H^o SHP(y)\ sfc(y)\ [1/w(y)]dy$$

where dy/w(y) is substituted for dt.

An inspection of the above equation will immediately indicate that since, in all practical cases, the rate of total fuel consumption, as expressed by the product of SHP·sfc* decreases with reduction of SHP, optimum strategy for fuel minimization in descent should be based on maintaining the rate of descent as high as possible, while keeping the power level as low as possible. This obviously, means that upon selecting $(R/D)_{max}$ boundary corresponding to the lowest permissible power setting, a strategy leading to the minimum time of descent should be worked out.

---

*In spite of the increase of sfc, the total fuel flow as given by this product decreases.

However, if the landing problem is further constrained by specifying the horizontal gate position ($X_g$) in addition to the gate velocity and altitude, the minimum time and fuel trajectories may not be identical. For clarification, the parameter $X^*$ is introduced to represent the horizontal distance traversed by the tilt-rotor aircraft while performing a minimum time descent with an unspecified gate position. (In this case, minimum time and fuel trajectories are synonymous.) The resulting optimal trajectory has associated with it, a time $t^*$ and the fuel consumed $W_F^*$.

If a horizontal gate position ($X_g$) is chosen which is less than $X^*$, then the time to descend ($t_g$) from this new gate position will be larger than $t^*$. Furthermore, the fuel consumed will also be greater. However, because the power level of the aircraft is maintained at its smallest value, the minimum time and fuel trajectories for this further constrained problem formulation remain synonymous.

If a gate position ($X_g$) is chosen which is larger than $X^*$, minimum time and fuel trajectories are no longer identical. In both the minimum time and fuel trajectories which result, $t_g \geq t^*$ and $W_{F_g} \geq W_F^*$.

However, at these large horizontal gate distances, less fuel is expended by maintaining aerodynamically efficient flight conditions at low power levels. For example, if $X_g >> X^*$, a minimum fuel trajectory from a prescribed altitude and gate velocity would have a rather long segment of steady-state flight at or near the best range velocity of the aircraft. A minimum time trajectory, from the same set of initial conditions would have a segment of flight at, or near, the maximum velocity limits of the aircraft.

This short discussion of the factors which are important in the determination of optimal tilt-rotor trajectories has been presented for the reader's convenience. Many of the aerodynamic considerations of the complete tilt-rotor model (Section II) have been omitted or simplified to help develop the analytical train of thought necessary to analyze the results of the complete kinematic model which is presented in Section V.

The Boeing Company
Vertol Division
Philadelphia, Pa., 17 January 1972

# APPENDIX E

## LIST OF SYMBOLS

| | |
|---|---|
| A | total disc area of the rotors, $ft^2$ |
| AR | aspect ratio |
| B | number of blades, or |
| B | vortex noise bandwidth Doppler correction factor, dB |
| C | wing chord, ft, or |
| C | complex Fourier coefficient of sound pressure, or |
| C | airload coefficient |
| $C_D$ | drag coefficient |
| $CF_1$ | change in $C_{L_{max}}$ when flap deflection = 90° |
| $CF_2$ | change in the drag coefficient due to reduction of the wing planform area when the flap deflection angle ($\delta_f$) = 0 |
| $CF_3$ | profile drag coefficient when angle of attack of the wing ($\alpha_W$) = ±90°, flap deflection angle ($\delta_f$) = 0° |
| $C_L$ | lift coefficient |
| D | drag, lbs., or |
| D | vortex noise directivity factor, dB |
| F | harmonic airload |
| H | altitude, ft, or |
| H | rotor inplane drag force, lbs |
| J | payoff function, or |
| J | Bessel function of the first kind |
| J' | derivative of Bessell function |
| K | weighting factor, or |
| K | empirical vortex noise constant |

| | |
|---|---|
| L | lift, lbs |
| M | Mach number = translational velocity with respect to air/speed of sound |
| $M_t$ | rotor blade tip rotational Mach number |
| N | noise level in general |
| P | power, ft.lbs/sec |
| $P_r$ | ideal induced power to hover without download, ft.lbs/sec |
| $\bar{P}$ | nondimensional power ($P/P_r$) |
| PNL | perceived noise level, PNdB |
| R | rotor radius, ft, or |
| R | universal gas constant, 53.3 ft.lb/slug °R |
| R/C | rate of climb,ft/sec |
| R/D | rate of descent, ft/sec |
| RP | rotor power, ft.lbs/sec |
| S | vortex noise spectrum shape factor, dB |
| $S_b$ | total blade area, $ft^2$ |
| SHP | total shaft horsepower |
| SP | total shaft power, ft.lbs/sec |
| T | thrust, lbs, or |
| T | temperature, °F |
| V | flight velocity, ft/sec |
| V' | total rate of flow through rotor disc, ft/sec |
| V" | rotor slipstream velocity, ft/sec |
| $V_E$ | effective rotor tip speed, ft/sec |
| $V_r$ | reference velocity; ideal induced velccity in hover, ft/sec = $\sqrt{W/2\rho A}$ |

| | |
|---|---|
| $V_t$ | tip speed of the rotors, ft/sec |
| $W$ | weight of the aircraft, lbs |
| $W_F$ | weight of fuel, lbs |
| $W_f$ | fuel flow, lbs/hr |
| $W/A$ | nominal disc loading, lbs/ft$^2$ |
| $X$ | horizontal distance measured in a ground-based axis system, ft |
| $a$ | acceleration, ft/sec$^2$, or |
| $a$ | lift curve slope of the wing, rad$^{-1}$ |
| $a$, $b$ | Fourier coefficients |
| $a_o$ | speed of sound in air, ft/sec |
| $a_x=\dot{u}_{max}$ | maximum permissible horizontal acceleration, ft/sec$^2$ |
| $a_y=\dot{w}_{max}$ | maximum permissible vertical acceleration, ft/sec$^2$ |
| $b$ | wing span, ft |
| $c$ | rotor blade chord, ft |
| $\bar{c}_{d_o}$ | average blade profile drag coefficient |
| $\bar{c}_{\ell hov}$ | average blade lift coefficient in hover |
| dB | decibels |
| $e$ | Oswald's efficiency factor |
| $f$ | frequency, Hz |
| $f_C$ | band center frequency, Hz |
| $f_H$ | upper band frequency limit, Hz |
| $f_L$ | lower band frequency limit, Hz |
| $f'_1$ | normalized lower band frequency limit, Hz |
| $f'_2$ | normalized upper band frequency limit, Hz |
| $f_o$ | peak vortex noise frequency, Hz |

| | |
|---|---|
| $f_{1-5}$ | generalized functional expressions |
| $f_{o0}$ | profile drag coefficient of the wing in Regime I with zero degrees of flap deflection |
| $f_{o2}$ | second-partial derivatives of the profile drag with respect to flap deflection ($\delta_f$) in Regime I |
| $f_{s_1}$ | second partial derivative of the profile drag with respect to flap coefficient in Regimes II and III |
| g | acceleration of gravity, 32.2 ft/sec$^2$ |
| i | $\sqrt{-1}$ |
| $i_p$ | angle between the thrusting line and the mean aerodynamic chord of the wing, rad |
| $k_p$ | power ratio in vertical climb ($SHP_{av}/SHP_{hov}$) |
| $k_{pf}$ | power ratio in forward flight ($SHP_{av}/SHP_{min}$) |
| $k_v$ | (gross weight + vertical drag)/gross weight |
| m | sound harmonic number |
| n | sound harmonic number, ($n = mB$) |
| q | freestream dynamic pressure, lb/ft$^2$ |
| q" | slipstream dynamic pressure, lb/ft$^2$ |
| r | blade radial station, ft |
| r | phase radius, ft |
| s | distance from rotor hub to observer, ft |
| sfc | specific fuel consumption, lbs/hr;hr |
| t | time |
| $t_r$ | reference time: $V_r/g$ |
| u | horizontal component of flight velocity, ft/sec |
| v | induced velocity, ft/sec |
| $v_i$ | induced velocity at the disc, ft/sec |
| w | vertical component of flight velocity, ft/sec |

| | |
|---|---|
| $\alpha$ | slope of vertical acceleration vs $(R/C)_V$, $sec^{-1}$ |
| $\alpha_C$ | $= \theta - \gamma$, fuselage attitude - flight path angle, rad |
| $\alpha_{OL}$ | angle of zero lift, rad |
| $\alpha_P$ | angle between the thrust vector & velocity vector, rad |
| $\alpha_V$ | induced angle of attack change, rad |
| $\alpha_W$ | angle of attack of the wing, rad |
| $\Gamma$ | total vorticity of rotor system |
| $\gamma$ | flight path angle, rad |
| $\Delta$ | incremental quantity |
| $\Delta C_D$ | change in drag coefficient |
| $\Delta I_\ell$ | higher harmonic induced force on one rotor blade |
| $\delta_f$ | flap deflection angle, rad |
| $\zeta$ | phase angle of Fourier series, rad |
| $\zeta_A$ | aerodynamic efficiency (Figure of Merit) |
| $\zeta_{pr}$ | propulsive efficiency of propeller |
| $\zeta_{tr}$ | transmission efficiency (also reflecting accessory & installation losses) |
| $\eta_c$ | control variable $\equiv$ fraction of maximum available HP |
| $\theta$ | attitude angle of the wing, rad |
| $\kappa$ | constant in curve fitting |
| $\lambda$ | indicates blade air loading harmonic number |
| $\lambda_{Df}$ | fuselage drag/weight |
| $\lambda_{D_{NAC}}$ | nacelle drag/weight |
| $\lambda_{Ds}$ | slipstream drag/weight |
| $\lambda_H$ | H-force/weight, or |
| $\lambda_H$ | rotor inflow ratio |

| | |
|---|---|
| $\lambda_{L_S}$ | slipstream lift/weight |
| $\lambda_T$ | thrust/weight |
| $\mu$ | rotor advance ratio ≡ flight speed $\sin(\alpha_p)$/tip speed |
| $\pi$ | 3.14159 |
| $\rho$ | air density, slugs/ft$^3$ |
| $\rho_o$ | $2.37 \cdot 10^{-3}$ slug/ft$^3$ |
| $\Sigma$ | denotes summation over the limits shown |
| $\sigma$ | $\rho/\rho_o$, or |
| $\sigma$ | rotor solidity ratio ≡ blade area/disc area |
| $\phi$ | angle measured from rotor shaft axis, degree |
| $\Omega$ | rotor rotational speed, rad/sec |
| $\omega$ | frequency of Fourier series, CPS |

Subscripts

| | |
|---|---|
| A | aerodynamic |
| C | radial force |
| D | drag |
| H | at altitude H |
| NAC | nacelle |
| T | thrust |
| a | during acceleration, or airplane configuration |
| av | available |
| d | during deceleration |
| e | corresponding to minimum SHP required |
| f | in forward flight |
| h | helicopter configuration |
| hov | hovering |

| | |
|---|---|
| id | ideal |
| ind | induced |
| n | fixed axis system |
| o | original (initial) |
| p | point source |
| pro | caused by profile drag |
| r | reference |
| s | in the slipstream of the rotor |
| t | terminal, or tip |
| td | touch-down |
| u | at speed of flight with horizontal component u |
| v | in vertical flight |
| vc | in steady-state vertical climb |
| w | wind axis system, or |
| w | at speed of flight with vertical component w |
| x | along horizontal axis |
| y | along vertical axis |
| 0 | steady airload |

### Superscript

| | |
|---|---|
| $(\bar{\ })$ | denotes nondimensionalization with respect to $V_r$ |

# REFERENCES

1. Halwes, D.R.: Flight Operations to Minimize Noise. Vertiflite, Vol. 17, No. 2, Feb. 1971, pp. 4-10.

2. Stepniewski, W.Z.: Introduction to Helicopter Aerodynamics. Rotorcraft Publishing Committee, Morton, Pa., 1959.

3. Kassianides, G.: Model 160 Full-Scale Download Test Analysis Report. Boeing Document No. D8-0995, Philadelphia, Pa., Jan. 20, 1969.

4. McVeigh, M. A.: Summary and Analysis of the Results of a Wind-Tunnel Test on an Unpowered Model of the Boeing-Vertol Model 150 Tilt-Wing/Tilt-Rotor Airplane in the University of Maryland Wind Tunnel. Boeing Document No. D8-0572, Philadelphia, Pa., Dec. 8, 1966.

5. Preliminary Performance Data AVCO Lycoming Model LTC4B-12 Turboshaft Engine. Lycoming Div., AVCO, Technical Brochure No. 1214.34, Dec. 1, 1967.

6. Schmitz, F.H.; Gibs, J.; Hinterkeuser, E.; and Stepniewski, W.Z.: Trajectory Analysis of a Tilt-Rotor Aircraft. Boeing Document No. D210-10276-1, Work performed under Phase V of Contract NAS2-5025, April, 1971.

7. Gessow A.; and Myers, G.C.: Aerodynamics of the Helicopter. Frederick Ungar Publishing Company, 1967.

8. Washizu, K.; Azuma, A; Koo, J.; and F. Oka: Vertical Descent Rotor Tests, University of Tokyo, Japan, Jan. 1964.

9. Gutin, L.: On the Sound Field of a Rotating Propeller. Langley Aeronautical Laboratory, NACA TM-1195, Oct. 1948.

10. Garrick, I.E.; and Watkins, C.E.: A Theoretical Study of the Effect of Forward Speed on the Free-Space Sound-Pressure Field around Propellers. NACA Report 1198, 1954.

11. Lowson, M.V.; and Ollerhead, J.B.: Studies of Helicopter Rotor Noise. USA AVLABS, TR68-60, Jan. 1969.

12. Ollerhead, J.B.; and Lowson, M.V.: Problems of Helicopter Noise Estimation and Reduction. AIAA Paper No. 69-195, Feb. 1969.

13. J. Scheiman: A Tabulation of Helicopter Rotor-Blade Differential Pressures, Stresses and Motions as Measured in Flight, Langley Res. Ctr. Report NASA TMX-952, Mar. 1954.

14. Burpo, F.B.; and Lynn, R.R.: Measurement of Dynamic Airloads on a Full-Scale, Semi-Rigid Rotor. Bell Helicopter Co., AVLABS Report TCREC TR-62-42, Dec. 1962.

15. Morse, P.M.; and Ingard, K.V.: Theoretical Acoustics. Chapter 10, McGraw-Hill Book Company, 1968.

16. Hinterkeuser, E.: A Preliminary Investigation of the Acoustical Properties of a Model Rotor in Non-Axial Flight. The Boeing Co. Vertol Division Addendum to Contract NAS 2-5473, April 1971.

17. Yudin, E.Y.: On the Vortex Sound from Rotating Rods. NACA TM No. 1136, Washington, D.C., March 1947.

18. Schlegel, R.; King, R.; and Mull, H.: Helicopter Rotor Noise Generation and Propagation. USA AVLABS Technical Report 66-4, Fort Eustis, Va., Oct. 1966.

19. Sternfeld, H.; Spencer, R.H.; and Schairer, J.O.: An Investigation of Noise Generation on a Hovering Rotor. The Boeing Company Vertol Division Document No. D210-10229-1, for U.S. Army Research Office, Durham, N.C. under Contract DAHC04-69-C-0087, Jan. 1971.

20. Mangiarotty, R.A.; and Turner, B.A.: Wave Radiation Doppler Effect Correction for Motion of a Source, Observer and the Surrounding Medium. Journal of Sound and Vibration, Vol. 6, No. 1, July 1967, pp. 110-116.

21. Standard Values of Atmospheric Absorption as a Function of Temperature and Humidity for Use in Evaluating Aircraft Flyover Noise. Aerospace Recommended Practice ARP 866, Society of Automotive Engineers, Aug. 31, 1964.

22. Method for Calculating the Attenuation of Aircraft Ground-to-Ground Noise Propagation during Takeoff and Landing. Aerospace Information Report AIR 923, Society of Automotive Engineers, Aug. 15, 1966.

23. Loewy, R.G.: Aural Detection of Helicopters in Tactical Situations. Institute for Defense Analysis Research Paper P-25, AD 409535, Alexandria, Va., May 1963.

24. Kryter, K.D.: Scaling Human Reactions to the Sound from Aircraft. Journal of the Acoustical Society of America, Vol. 31, 1959, pp. 1415-1429.

25. Pinker, R.A.: Mathematical Formulation of the Noy Tables. Journal of Sound and Vibration, Vol. 8, No. 3, 1968, pp. 488-493.

26. Evaluation of the Absolute Subjective Acceptability of VTOL Aircraft Noise. The Boeing Co. Vertol Div. Document No. D210-10392-1 dtd. January 10, 1972.

27. Hague, D.S.; and Glatt, C.R.: A Guide to the Automated Engineering and Scientific Optimization Program. Boeing Document No. D2-114271-1, June 1968 (CR-73201).

28. Stepniewski, W.Z.; and Kalmbach, Jr., C.F.: Multi-variable Search and Its Application to Aircraft Design Optimization. The Boeing Company & Princeton University, for the Aeronautical Journal of the Royal Aeronautical Society, London, England, Vol. 74, No. 713, May 1970.

29. Ignagni, M.: Determination of Optimum Climb Trajectories. Honeywell, Inc., Aerospace Div. Document No. T-231, Feb. 1969.

30. Conte, S.D.: Elementary Numerical Analysis - An Algorithmic Approach. McGraw-Hill Book Company, 1965.

## Bibliography

Hague, D.S.; and Glatt, C.R.: An Introduction to Multi-Variable Search Techniques for Parameter Optimization and Program AESOP. Boeing Document No. D2-114271-2, April 1968.

Magee, J.; Maisel, M.; and Davenport, F.: The Design and Performance Prediction of Propeller/Rotors for VTOL Applications. AHS No. 325, May 1969.

Masson, A.: Test of Three Convertiplane Propellers in the S1 Wind Tunnel for The Boeing Company. ONERA Document No. 1/481GY, 1968.

Perkins, C.D.; and Hage, R.E.: Airplane Performance Stability and Control. John Wiley & Sons, Inc., 1949.

Smith, M.C.: University of Maryland Wind Tunnel Test #489 - Force, Moment and Downwash Measurements on a Rigid Rotor and Semi-Span Wing. Boeing Document No. D8-1062-1 thru D8-1062-4, Philadelphia, Pa. , October 16, 1968.

Tompkins, J.; Mirandy, L.; and Freeman, A.: Model Rotor Blade Loads, Blade Motions and Performance Study (8-Foot Diameter CH-47B and AGB Rotors - UMWT 516). Boeing Document No. D8-2338-1, April 25, 1969.